

# D4.3



## Experimental work on bentonite evolution in the frame of BEACON – final report of WP4

### DELIVERABLE D4.3 Report

Author(s): Fabien Bernachy-Barbe, José A. Bosch, Gemma Campos, Beatriz Carbonell, Katherine A. Daniels, Alessio Ferrari, Caroline C. Graham, William Guillot, Carlos Gutiérrez-Álvarez, Jon F. Harrington, Rubén J. Iglesias, Markku Kataja, Klaus-Peter Kröhn, Michael Kröhn, David Mašín, Jan Najser, Janis Leon Pingel, Elena Real, Thorsten Schäfer, Jiří Svoboda, Haiquan Sun, Joni Tanttu, María Victoria Villar, Klaus Wieczorek

Reporting period: 01/06/2020 – 31/05/2022

Date of issue of this report: **31/01/22**

Start date of project: **01/06/17**

Duration: 60 Months

This project receives funding from the Euratom research and training programme 2014-2018 under grant agreement No 745 942		
<b>Dissemination Level</b>		
<b>PU</b>	Public	<b>X</b>

**REVIEW**

<b>Name</b>	<b>Internal/Project/External</b>	<b>Comments</b>

**DISTRIBUTION LIST**

<b>Name</b>	<b>Number of copies</b>	<b>Comments</b>
Seifallah BEN HADJ HASSINE(EC)	Digital	
Beacon partners	Digital	

## Abstract

The objectives of the Beacon experimental studies have been to provide input data and parameters for development and validation of models and to reduce uncertainties about conditions and phenomena influencing bentonite homogenisation. Both the homogenisation of an initially inhomogeneous bentonite system and the persistence or development of inhomogeneities in the bentonite system under various mechanical and hydraulic conditions have been investigated. Eight experiment teams perform tests involving different bentonite materials and different hydraulic and mechanical boundary conditions. This report is the final Beacon WP4 deliverable on experimental work.

The Beacon partners BGS, CEA, CIEMAT, CTU, CU, EPFL, JYU, KIT, and GRS devised and carried out a wide range of experiments to provide the data needed. Experiments addressed the influence of hydro-mechanical path and aggregate size distribution for several macroscopically homogeneous bentonite materials, the gap filling behaviour of swelling bentonite for numerous different configurations and conditions, the hydration-induced homogenisation of different binary systems like block/pellet and block/powder systems or systems of two blocks with different initial densities, and the shearing behaviour at a bentonite/steel interface.

Unsaturated inhomogeneous bentonite systems tend to evolve to more homogeneous systems. In particular, bentonite exhibits an extremely well gap filling behaviour. However, once full saturation is reached, the current density distribution seems to remain fixed – at least in the laboratory time scale. Natural analogue studies performed in Beacon (Deliverable D4.2) do not show any hint that this changes even in the very long term.

Homogenisation depends on many parameters. Experimental results suggest that a critical one is the hydration velocity – fast hydration seems to result in irreversible swelling close to the hydration front, resulting in an overall inhomogeneous density.

Bentonite behaviour was characterised in many experiments, some of them successfully using new developed methods. Several experiments were selected for modelling cases in the work packages WP3 and WP5. Still, there is more experimental output to be used for future simulation activities, which will improve both the understanding of the experimental results and the confidence in the models.

# Content

<b>1</b>	<b>Introduction</b> .....	<b>7</b>
<b>2</b>	<b>Overview of Work Package 4</b> .....	<b>9</b>
<b>3</b>	<b>Hydro-mechanical behaviour of macroscopically homogeneous bentonite material</b> .....	<b>13</b>
3.1	Influence of initial granulometry on swelling behaviour (EPFL) .....	13
3.1.1	Tested material .....	13
3.1.2	Experimental setup .....	14
3.1.3	Testing procedure .....	15
3.1.4	Results .....	16
3.1.4.1.	Isochoric saturation .....	16
3.1.4.2.	Vertical swelling tests .....	20
3.1.5	Conclusion .....	22
3.2	Influence of different hydro-mechanical paths on final macroscopic properties and local homogeneity of compacted samples (EPFL) .....	22
3.2.1	Experimental setup .....	23
3.2.2	Tested material .....	23
3.2.3	Test procedure .....	23
3.2.4	Results .....	24
3.2.5	Microstructural analysis .....	25
3.2.5.1.	Mercury Intrusion Porosimetry .....	25
3.2.5.2.	Scanning Electron Microscopy .....	30
3.2.6	Conclusions and recommendations .....	32
3.3	Hydraulic and mechanical properties of Czech bentonite (CU, CTU) .....	32
3.3.1	Constant load tests (CU) .....	32
3.3.1.1.	Outline of the tests .....	32
3.3.1.2.	Constant load swelling .....	33
3.3.1.3.	Water retention properties .....	36
3.3.1.4.	Mercury intrusion porosimetry .....	40
3.3.1.5.	Environmental scanning electron microscopy .....	42
3.3.1.6.	Conclusions .....	44
3.3.2	Constant volume tests in "MPC" cells (CU) .....	48
3.3.2.1.	Outline of the tests .....	48
3.3.2.2.	Single density tests .....	48
3.3.2.3.	Dual density tests .....	50
3.3.2.4.	Conclusions .....	54
3.3.3	Constant volume tests (CTU) .....	55
3.3.3.1.	Homogenous samples .....	57
3.3.3.2.	Dual density samples .....	60
3.3.3.3.	Pellets .....	61
3.3.4	Stress path investigation (CTU) .....	64
3.3.4.1.	Homogenous samples .....	64
3.3.4.2.	Pellets .....	67
3.3.4.3.	Conclusion .....	69
<b>4</b>	<b>Swelling into limited void</b> .....	<b>70</b>
4.1	Swelling into a void as function of sample/void ratio, orientation and temperature (BGS) .....	70
4.1.1	Tested material .....	70
4.1.2	Experimental set-up .....	70
4.1.3	Testing procedure .....	75
4.1.4	Results .....	76
4.1.4.1.	Experiments conducted .....	76
4.1.4.2.	Testing under ambient conditions .....	77
4.1.4.3.	Testing under elevated temperature conditions .....	83
4.1.4.4.	Testing under high salinity conditions .....	89
4.1.4.5.	CT data .....	91

4.1.4.6.	Discussion .....	93
4.1.5	Conclusions .....	97
4.2	Swelling into a void under suction control or flow control (CIEMAT) .....	98
4.2.1	Material.....	98
4.2.2	Methodology .....	99
4.2.2.1.	GAP-vapour tests .....	99
4.2.2.2.	GAP-liquid tests .....	100
4.2.2.3.	Postmortem tests.....	101
4.2.3	Results.....	103
4.2.3.1.	GAP-vapour tests .....	103
4.2.3.2.	GAP-liquid tests .....	112
4.2.4	Conclusions .....	121
4.3	Swelling into a limited void (CTU) .....	122
4.4	X-ray imaging and wetting of semi-free swelling bentonite in a sample chamber (JYU) .....	126
4.4.1	Setup and methods.....	126
4.4.2	Experiments .....	127
4.4.3	Results and conclusions .....	128
4.5	Pellet-scale investigations (KIT/GRS) .....	131
4.5.1	Material.....	131
4.5.2	Pre-tests with a preliminary cell design .....	132
4.5.3	Single-pellet tests.....	132
4.5.3.1.	Test setup and components .....	132
4.5.3.2.	Test procedure .....	134
4.5.3.3.	Test results .....	135
4.5.3.4.	Discussion of results.....	139
4.5.4	Pellet-cluster test .....	139
4.5.4.1.	Test setup and preparations .....	139
4.5.4.2.	Simple pre-tests .....	142
4.5.4.3.	Test procedure .....	146
4.5.4.4.	Discussion of the results.....	148
4.5.5	Data comparison.....	153
4.5.5.1.	Test conditions.....	153
4.5.5.2.	Test results.....	153
4.5.6	Summary, conclusions and recommendations.....	156
4.5.6.1.	Summary .....	156
4.5.6.2.	Conclusions.....	157
4.5.6.3.	Recommendations.....	158
<b>5</b>	<b>Binary mixtures or artificial inhomogeneities .....</b>	<b>159</b>
5.1	Saturation of pellet/block systems under isochoric conditions (CIEMAT) .....	159
5.1.1	Material.....	159
5.1.1.1.	FEBEX bentonite .....	159
5.1.1.2.	MX-80 bentonite .....	160
5.1.2	Methodology .....	161
5.1.2.1.	Tests with FEBEX bentonite.....	161
5.1.2.2.	Tests with MX-80 bentonite.....	166
5.1.3	Results.....	168
5.1.3.1.	Large-scale oedometer (FEBEX) .....	168
5.1.3.2.	Transparent cell (FEBEX).....	180
5.1.3.3.	Thermo-hydraulic cell (MX-80).....	191
5.1.4	Discussion.....	192
5.1.5	Conclusions .....	197
5.2	Stress field evolution and final state of heterogeneous samples saturated under isochoric conditions (CEA).....	198
5.2.1	Objectives and methods.....	198
5.2.2	Investigated test cases and global measurements .....	199
5.2.3	Stress field evolution .....	202
5.2.4	Characterization of the final states .....	205
5.2.5	Conclusions and perspectives .....	208

5.2.5.1.	Analysis of the hydro-mechanical behaviour of the different experiments .....	208
5.2.5.2.	Perspectives and improvements suggested for new experiments .....	209
5.3	X-ray tomographic imaging of pellet/powder mixes saturated under isochoric conditions (CEA) .....	210
5.3.1	Objectives and methods .....	210
5.3.2	Testing and improvements .....	211
5.3.2.1.	Experiment TOMO_1 (Tomobento_1) .....	211
5.3.2.2.	Experiment TOMO_2 (Tomobento_2) .....	213
5.3.2.3.	Experiment Tomo_3 (Tomobento_3) .....	213
5.3.3	Conclusions and perspectives .....	217
<b>6</b>	<b>Influence of the degree of saturation on the shearing behaviour at the bentonite – steel interface (EPFL) .....</b>	<b>218</b>
6.1	Background .....	218
6.2	Materials and methods .....	218
6.2.1	Tested material .....	218
6.2.2	Experimental setup .....	218
6.2.2.1.	Experimental set-up for the internal shearing .....	218
6.2.2.2.	Testing set-up for the interface shearing .....	219
6.2.3	Sample preparation .....	220
6.2.4	Testing procedure .....	220
6.3	Results .....	221
6.3.1	Influence of the granulation on the internal shearing and interface shearing .....	221
6.3.2	Influence of water content and suction on the response upon shearing .....	224
6.3.3	Discussion .....	226
6.3.3.1.	Influence of the granulation on the response of the material on internal and interface shearing .....	226
6.3.3.2.	Influence of water content on the response on the interface shearing .....	226
6.3.4	Conclusions .....	227
<b>7</b>	<b>Conclusions and future work .....</b>	<b>228</b>
7.1	Results summary and conclusions .....	228
7.2	Remaining questions and recommendations for future work .....	231
<b>8</b>	<b>References .....</b>	<b>232</b>

# 1 Introduction

Bentonite plays an important role in the engineered barrier system (EBS) concept in many radioactive waste management programmes. Understanding of the fundamental processes governing bentonite barrier evolution is therefore essential. The Beacon project aims at an increased understanding and modelling capability of the bentonite mechanical evolution, especially with respect to material homogenisation. The key work packages of model development (work package WP3) and model validation (WP5) have been using existing experimental data which have been compiled for this purpose in WP2.

The existing database was, however, limited, because the focus of earlier experimental work has generally been on hydration, and the mechanical part was not always captured or evaluated. Therefore, additional laboratory testing has been performed in WP4.

The objectives of the Beacon experimental studies have been to provide input data and parameters for development and validation of models and to reduce uncertainties about conditions and phenomena influencing bentonite homogenisation. Both the homogenisation of an initially inhomogeneous bentonite system and the persistence or development of inhomogeneities in the bentonite system under various mechanical and hydraulic conditions were investigated.

The important variables in terms of bentonite buffer safety function are swelling pressure and permeability. They are both directly related to bentonite dry density. For a fully saturated buffer, homogeneous dry density implies homogeneity of swelling pressure and permeability. Therefore, homogeneity in the context of this report basically means homogeneity of density.

Obviously, a system with gaps or a binary system of, e.g., bentonite blocks and pellets is not homogeneous, but density will evolve in the direction of a more homogeneous system when hydrated. On the other hand, a homogeneous unsaturated bentonite can become inhomogeneous with respect to its density distribution during hydration, because not all the material will be in contact with water (at least not in the early hydration phase), and the wetted part will swell first and compress the still dry part of the bentonite. If this early phase swelling is irreversible (and there is respective experimental evidence), then a completely homogeneous system is not realistic. Instead, a system with a density bandwidth which is “homogeneous enough” will be the design target.

In the frame of WP4 of the Beacon project, eight experiment teams have performed laboratory tests involving different bentonite materials, different setups, and different hydraulic and mechanical boundary conditions. The results and conclusions of these experiments are presented in this report, which represents deliverable D4.3 of the project. It is the sequel and completion of deliverable D4.1 “Bentonite mechanical evolution – experimental work for the support of model development and validation” (Baryla et al., 2019) which documented the state of the experimental work after two years of Beacon. Note that the numbering of deliverables changed because D4.1 evolved from the originally planned two deliverables D4.1 “Homogenisation of an initially inhomogeneous bentonite system – experimental input to model development and validation” and D4.2 “Persistence or development of inhomogeneities in the bentonite system – experimental input to model development and validation”.

Deliverable D4.2 (originally D4.3) “Creep in bentonite – a natural analogue study” (Sellin & Villar, 2020) was issued in April 2020. It represents the final report on a self-contained part of WP4 that does not include new experimental work, but evaluation of earlier drill core studies with respect to the question whether density gradients in bentonite materials will disappear in the very long term. Thus, D4.2 and D4.3 together represent the complete output of Beacon WP4.

## 2 Overview of Work Package 4

Evolution of a bentonite EBS will be influenced by a whole range of conditions and phenomena. The most important are

1. Initial state of the EBS: For bentonite homogenisation or, on the other hand, the evolution of heterogeneity, there will be a difference between initially single density (i.e., a bentonite block) or multi-density (pellets, blocks/gaps, blocks/pellets) systems. In this context, the scale of observation is important (a pellet system might be considered as homogeneous in the large scale, while being highly inhomogeneous on the pellet scale).
2. Hydration conditions and history: Solution composition, thermal and mechanical load and hydration history (water availability and hydration velocity, hydration via a vapour or liquid phase) will have an impact on the evolution of buffer texture, swelling pressure and hydraulic properties.
3. Mechanical boundary conditions: Free swelling will definitely lead to a different material than constant volume hydration. These are the end points on the scale of a variety of potential mechanical boundary conditions.
4. Interplay between heterogeneity and swelling pressure as well as mechanical properties: Evolution of heterogeneities in the buffer will possibly affect the overall swelling pressure and mechanical properties, e.g., shear strength. Especially at interfaces, e.g., between buffer and waste package, shearing behaviour can be relevant with respect to the homogenisation process.

The experiments were designed to investigate the relevant phenomena. Different bentonites were investigated to broaden the spectrum of observations. Different analysis techniques have been applied by different partners, so that a more complete and reliable characterization of bentonite behaviour is obtained, improving the reliability of results. The experimental observations should feed into calibration and improvement of the constitutive laws performed in WP3. Therefore, all the experiments planned and performed in WP4, together with information on the setup, material, experiment conditions, and expected outcome, have been assembled early in the project in an experiment table (Table 2-1) which was meant as a help for WP3/WP5 to facilitate the selection of tests and data suitable for each modeller's development and validation task. The experiment table is available to the project participants as an excel file on the project web server. Not all experiments have been or were suitable to be modelled, but some of them were selected as modelling cases for both WP3 (model development) and WP5 (testing, verification and validation of the models).

The experiments performed within Beacon are presented in the chapters 3 to 6. The organisation is as follows:

1. Hydro-mechanical behaviour of macroscopically homogeneous bentonite material: Experiments of EPFL addressing the influence of initial granulometry and of the hydro-mechanical path on the final properties of MX-80 as well as constant load and constant volume tests, performed by CU and CTU, on the Czech Cerny vrch bentonite are found in Chapter 3.
2. Swelling into limited void: Chapter 4 includes experiments performed in constant volume cells partially filled with bentonite. BGS, CIEMAT, CTU, and JYU performed respective tests at different scales and with different emphases. Also pellet-scale and pellet cluster tests of KIT and GRS are found in this chapter, because the inter-pellet space can be considered as a void
3. Binary mixtures or artificial inhomogeneities: Experiments of CIEMAT and CEA using bentonite block/pellet systems or pellet/powder mixtures as well as block/powder systems are presented in Chapter 5.

4. Chapter 6 deals with EPFL's experiments on the influence of the degree of saturation on the shearing behaviour at a bentonite – steel interface

In fact, the organisation of experiments in the different chapters is not entirely as strict as described above. As an example, tests with two blocks of different densities performed by CU are presented in Chapter 3 (although the system is not initially homogeneous), while similar tests of CEA are found in Chapter 5. However, it would have been rather complicated to further break down and classify all the contributions of the experiment teams. In any case, an attempt to bring all the results together and draw some overall conclusions is made in Chapter 7, which also contains some recommendations for future experimental investigations.

**Table 2-1. WP4 experiment table**

Identification			Setup		Material				Experiment conditions				Outcome		
Partner in charge	Experiment name	Main objective	Type of experiment	Sample size	Bentonite	Block/granular	Dry density	Initial degree of saturation / water content	Solution	Mechanical boundary conditions	Hydraulic boundary conditions	Temperature	Measurements	Data resolution	Remarks
EPFL		the influence of initial granulometry on final as-compacted state	Isochoric saturation followed by compaction	h:12,5mm x D:35mm	MX-80	granular	various	hygroscopic water content and $w_{lim} \approx 20\%$	distilled water	oedometer cell, radial displacement prevented	two-sided saturation	ambient	final void ratio, final granulation	displacement: micron; swelling pressure: 0.6MPa, saturation pressure 1kPa	
EPFL		the influence of the different hydro-mechanical paths on final macroscopic properties and local homogeneity of compacted samples	free swelling; free swelling followed by compaction; isochoric saturation followed by compaction	h:12,5mm x D:35mm	MX-80	granular	1.4 Mg/m <sup>3</sup>	hygroscopic water content	distilled water	oedometer cell, radial displacement prevented	two-sided saturation	ambient	final void ratio after each type of experiment, final pore size distribution, swelling pressure in case of isochoric saturation test	displacement: micron; swelling pressure: 0.6MPa, saturation pressure 1kPa	
CU	investigation of microstructure, hydraulic and mechanical properties of the Czech bentonite	description of microstructural changes under different hydraulic paths and mechanical response on the saturation of compacted samples	WRC, MIP, ESEM, swelling experiments in oedometer	5 cm diameter, 1 cm height (oedometer tests)	BCV	block (oedometer tests)	1.27; 1.6 and 1.9 g/cm <sup>3</sup> for WRC, MIP and ESEM. Dry densities for oedometer tests will be determined.	corresponding to initial wc of bentonite powder (app. 10%)	distilled water	constant load swelling + compression (oedometer tests)	one-side saturation (oedometer tests)	ambient	swelling under constant load, swelling pressure after re-compression		
CTU	hydraulic and mechanical properties of the Czech bentonite	hydraulic properties, density distribution, total pressure	swelling tests - constant volume and constant load	constant volume - 3 cm diameter, 2 cm height; constant load - 5 cm diameter, 1 cm initial height	BCV, B75	blocks, pellets	dual density - 1.3 & 1.7 for constant volume; 1.3 - 1.8 for constant volume; initial 1.27; 1.6 and 1.9 g/cm <sup>3</sup> for constant load	10%	water	constant volume cell (attached to permeameter); constant load swelling + compression (oedometer tests)	one side saturation	ambient and 60°C	constant volume cells - water intake, total pressure at one end, density distribution at the end; swelling under constant load ("deformation" on each load step)		
BGS	SITS (Swelling in to voids)	evolution in swelling pressure, porosity and density as different height blocks of bentonite swell into a fixed volume. Tests repeated with ambient and elevated temperatures at with two different salinities.	Swelling test into fixed volume	diameter 60mm, vessel length 120 mm. Sample length variable.	MX-80	Blocks	will be determined axially and radially to determine variations after swelling	will be measured but blocks will start at "100%" to reduce test times	distilled and NaCl balance to Swedish groundwater	constant volume with multiple stress measurements	resaturation from both ends of the vessel	ambient and 90°C	spatially resolved: swelling pressure; porosity, water content, density, etc, plus potentially bulk permeability	around 10mm for post-mortem sub sampling	
CIEMAT	GAP vapour	Follow density changes in a block sample saturated under limited axial swelling conditions	Hydration of a block sample with vapour water allowing limited axial swelling (initial gap). Perforated cell	cylinder, 38x28 mm	FESEX	block	1.7-1.5 g/cm <sup>3</sup>	14%	water vapour	limited axial swelling (depending on the size of the gap)	saturation from the gap surface	20°C	Water intake, postmortem (density, water content, MIP)	mm	
CIEMAT	GAP liquid	Follow density changes in a block sample saturated under limited axial swelling conditions	Hydration of a block sample with liquid water allowing limited axial swelling (initial gap)	cylinder, 50x25 mm	FESEX (MX-80?)	block	1.65 g/cm <sup>3</sup>	13.5%	Deionised water	limited axial swelling (depending on the size of the gap)	saturation from the surface opposite to the gap	ambient	Water intake, postmortem (density, water content, MIP)	mm	

**Table 2-1. WP4 experiment table (continuation)**



CTU	swelling into limited void	Follow dry density and water content evolution for different bentonite/gap ratios	Hydration of a block sample with liquid water allowing limited axial swelling (initial gap)	h: 120 mm x D: 120 mm	BCV	block				Constant volume cell, limited volume increase of block	one-sided re-saturation	ambient			
JYU	Partly constricted swelling experiment - preliminary title	Dry density and water content profiles and axial swelling pressures from both ends of the chamber as a function of time during wetting.	swelling test, limited volume increase (initial sample 10mm high with 4 mm gap)	20 mm	Bara Kade	Block	Initially 15 to 17 g/cm <sup>3</sup>	*17% water content	Will be determined	Constant volume cell, limited volume increase of block	one-sided re-saturation	ambient	1D water content and dry density distributions and axial swelling pressure from both ends of the chamber	sub mm	Full measurement series to be started soon
KIT	SPT (Single-Pellet Test)	Swelling pressure / density / porosity distribution evolution on pellet-scale	swelling test, limited volume increase	h: 20 mm x D: 25 mm	MX-80	single pellet + fragments	1.0 g/cm <sup>3</sup>	12.3% water content	Pearson water	constant volume cell, limited volume increase of pellet	one-sided re-saturation	ambient	spatially resolved swelling pressure	mm	
GRS	PCT (Pellet-Cluster Test)	Swelling pressure / water content evolution and comparison to SPT (single-pellet test)	swelling test, constant volume cell	h: 50 mm x D: 50 mm	MX-80	pellets	1.0 g/cm <sup>3</sup>	12.3% water content	Pearson water	constant volume cell, limited volume increase of pellets into inter-pellet space	one-sided re-saturation	ambient	swelling pressure, water intake		
CIEMAT	MGR	Check density homogenisation upon saturation of two materials initially different (pellets/block)	Hydration at constant volume in an oedometer	cylinder, 100x100 mm	FESEX	Combination of block/granular	1.6 g/cm <sup>3</sup> (block) / 1.3 g/cm <sup>3</sup> (pellets)	13.5% (block) / 10.1% (pellets)	Deionised water	Constant volume	Saturation through the pellets surface under controlled low flow	ambient	Water intake, swelling pressure, postmortem (density, water content, MIP, XRD)		
CIEMAT	Window	Check density homogenisation upon saturation of two materials initially different (pellets/block)	Hydration at constant volume in a transparent cell	12x12x20 mm	FESEX	Combination of block/granular	1.6 g/cm <sup>3</sup> (block) / 1.3 g/cm <sup>3</sup> (pellets)	13.5% (block) / 10.1% (pellets)	Deionised water	Constant volume	Saturation through the pellets surface under low pressure	ambient	Water intake, images, postmortem (density, water content, MIP, XRD)	mm	complementary to MGR, qualitative
CIEMAT		Check density homogenisation upon saturation of two materials initially different (pellets/block)	Hydration at constant volume in thermo-hydraulic cell	h: 14.5 mm x D: 15 mm	MX-80	Combination of block/granular	1.49 g/cm <sup>3</sup> (block) / 1.5 g/cm <sup>3</sup> (pellets/powder mixture)	initial saturation 23% (block) / 23% (pellets/powder)	Deionised water	Constant volume	Saturation through the pellets/powder surface	ambient	RH/T, lateral pressure, pore pressure		
CEA	Stress Field evolution during Bentonite Homogenization (preliminary title)	density evolution and pressure field on simplified heterogeneities	isochoric swelling test	diam. 57 mm	MX-80	Several configurations	average around 1.5 g/cm <sup>3</sup>	will be determined	LSMHM synthetic site water	constant volume cell	one-sided / two-sided re-saturation	ambient	axial stress, 9 local pressure sensors (3 heights, 3 rad. positions), 3 RH sensors (3 heights)		post-mortem density and water content local measurements, some MIP
CEA	Tomobento	qualitative evaluation of the homogenisation of a pellet/powder mix using in-situ X-ray tomography	swelling test, limited volume increase	diam. 57 mm	MX-80	single pellet + powder	will be determined	will be determined	LSMHM synthetic site water	quasi-constant volume cell	one-sided re-saturation	ambient	3D X-ray absorption coefficient field	30 µm	
EPFL		influence of the degree of saturation on the shearing behaviour at the bentonite - steel interface	isochoric saturation using vapour equilibrium technique followed by shearing test	h: ~15mm, 30x30mm	MX-80; FEBEX	MX-80; granular; FEBEX; blocs	to be determined	to be determined	various	direct shear apparatus	two sided saturation with vapour equilibrium technique	ambient; (60°C)	swelling pressure; interface friction angle; interface adhesion	displacement: micron; swelling pressure: to be determined, saturation pressure: to be determined	

### 3 Hydro-mechanical behaviour of macroscopically homogeneous bentonite material

#### 3.1 Influence of initial granulometry on swelling behaviour (EPFL)

Segregation during bentonite emplacement is one of the issues that could be encountered in nuclear waste repositories that consider granular bentonite as a sealing material. This would lead to an initial heterogeneity in bentonite grain size distribution (GSD) within a given section in the repository. In order to determine the influence of the initial GSD on the final (as-saturated) state of granular MX80 bentonite, a series of laboratory tests were conducted at EPFL. Three granulations were tested and compared. The hydration process, as well as saturated states as a function of the initial states were studied.

##### 3.1.1 Tested material

The tested material is granular MX-80 bentonite. Some basic and index properties are reported in Table 3-1 (after Seiphoori et al. 2014). Dry density of the grains is approximately equal to 2.1 Mg/m<sup>3</sup>.

**Table 3-1. Basic properties of the MX80 bentonite used in the tests**

Smectite content	Specific surface	Specific gravity	Liquid limit	Plastic limit
85%	523 m <sup>2</sup> /g	2.74	420%	65%

Samples characterised by three types of GSD, corresponding to Fuller-type, unifractional and bifractional, as shown in Figure 3-1, were tested.

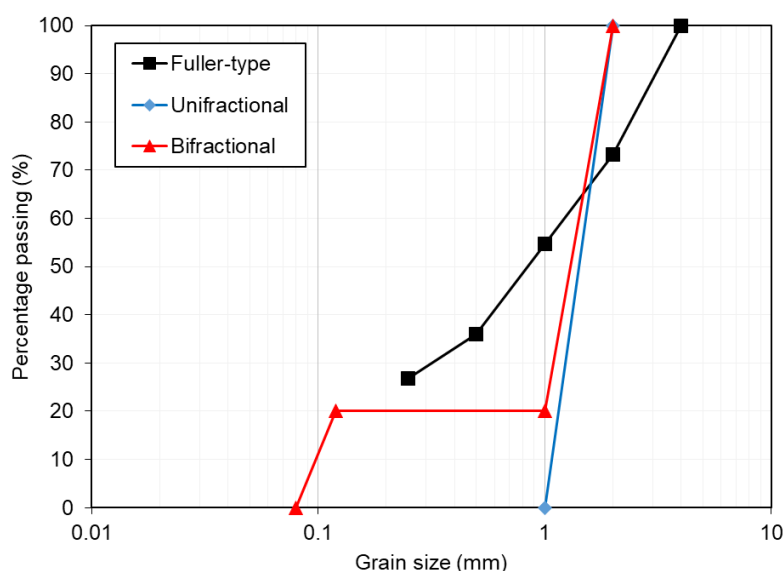


**Figure 3-1. Grain size distribution (GSD) curves of the samples tested**

The Fuller-type GSD is characterised by a curvature coefficient  $C_c=1.5$  and uniformity coefficient  $CU = 6$  and corresponds to the recommended site granulation to be used in the Swiss concept of high-level radioactive waste disposal (Plötze and Weber, 2007). In the as-poured state, the dry density of the samples characterized by this granulometry is around  $1.50 \text{ Mg/m}^3$ . The unifractional GSD consists 100% of the fraction 1-2 mm, characterised by a curvature coefficient  $C_c=0.77$  and uniformity coefficient  $CU = 1.43$ , leading to a dry density in the as-poured state of around  $1.30 \text{ Mg/m}^3$ . The bi-fractional granulation is composed by 80% of the fraction 1-2 mm and 20% of the fraction 0.08-0.125 mm, a curvature coefficient  $C_c=7.87$  and a uniformity coefficient  $CU = 14$ , resulting in a dry density around  $1.45 \text{ Mg/m}^3$  at as-poured state.

### 3.1.2 Experimental setup

Tests were performed using a high-pressure oedometric cell. A complete description of the apparatus is provided in Ferrari et al. (2016). The cell is made of stainless steel and holds an oedometric ring with height of 12.5 mm and diameter of 35.0 mm. This ring is inserted into a high-rigidity cylindrical cell (Figure 3-2a). The top and the bottom of the sample are in contact with metallic porous plates, which are connected to the drainage lines (Figure 3-2b).

The cell is placed in a high-stiffness frame equipped with a hydraulic jack, which allows to control the axial total stress up to 100 MPa (resolution of 0.06 MPa) (Figure 3-3). The vertical displacement is measured by LVDTs (resolution of  $1 \mu\text{m}$ ) fixed on the upper part of the oedometric cell.

Water is supplied with a Pressure/Volume (PV) controller (resolution of pressure control of 1kPa), from the bottom and top bases of the oedometric cell (Figure 3-2b).

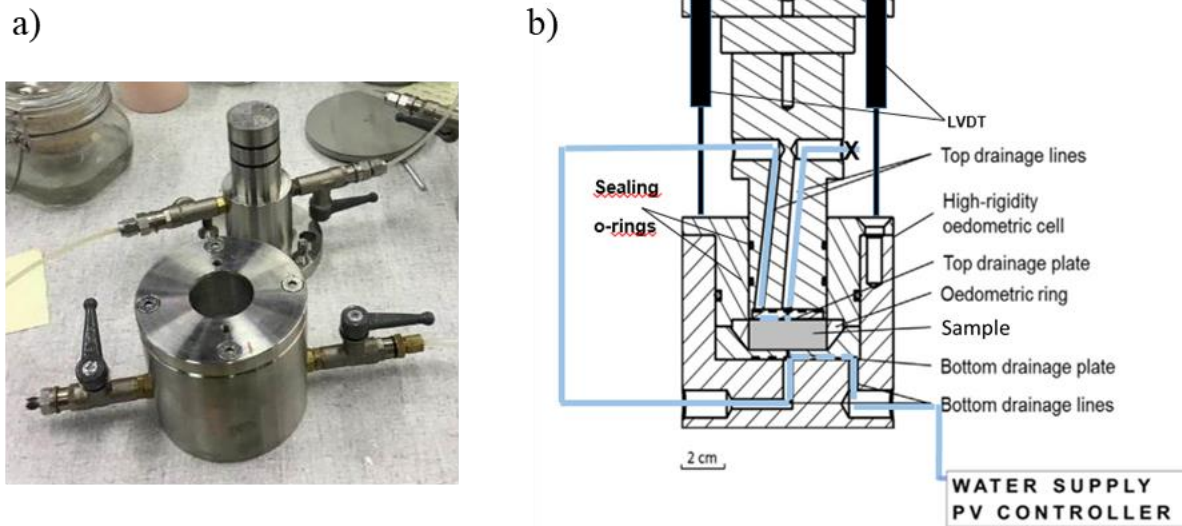


**Figure 3-2. (a) High-rigidity oedometric cell. (b) Schematic layout of the cell showing the drainage system**

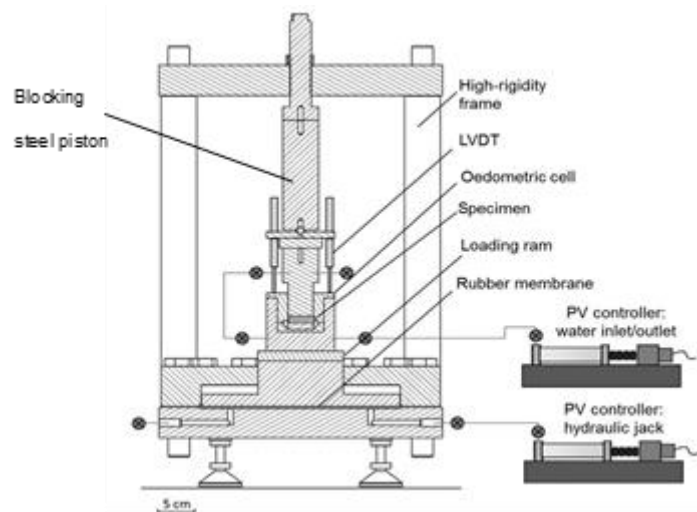


**Figure 3-3. Schematic layout of the test for saturating the sample with liquid water in isochoric conditions**

### 3.1.3 Testing procedure

The granular MX80 bentonite at hygroscopic conditions was poured into the oedometric cell. As in the Swiss concept of repository, this corresponded to the initial state.

Inside the oedometer, samples were hydrated up to equilibration with distilled water in liquid phase following two different paths as shown in Figure 3-4; point A corresponds to the initial state of the samples (as poured state). Water pressure applied in both cases was constant at 20 kPa.

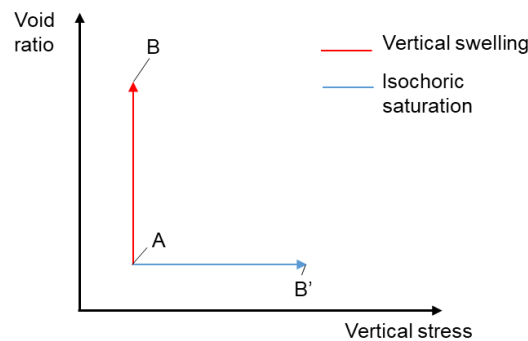


**Figure 3-4. Hydro-mechanical paths followed to study the influence of initial granulation**

The first wetting scenario (wetting path A-B) included saturation in oedometric conditions (radial displacement prevented) with a low constant vertical load of 21 kPa, allowing free vertical (axial) swelling conditions. To minimize friction effects, the surfaces in contact with the samples, as well as all sealing rings of the oedometric cell, were lubricated with grease.

The second wetting scenario (path A-B') involved isochoric hydration. To prevent volume changes during hydration, vertical displacement was constantly monitored and controlled. The maximum vertical displacement was 0.6%, corresponding to a maximum variation of dry density of 0.01 Mg/m<sup>3</sup>.

Initial state of the samples tested are summarized in Table 3-2 (isochoric saturation) and Table 3-3 (free swelling saturation). Total suction at hygroscopic conditions was measured using a chilled-mirror WP4c psychrometer. Of particular interest is the dependency of the initial dry density on granulation. Samples of the Fuller-type (series P) were further used to study the stress path dependency response (see Section 3.2).

**Table 3-2. Nomenclature, grain size distribution and initial state of the samples subjected to isochoric hydration**

	Grain size distribution	Degree of saturation (-)	Water content (-)	Total suction (MPa)	Dry density (Mg/m <sup>3</sup> )	Void ratio (-)
P2-1	Fuller-type	0.20	0.06	104.20	1.49	0.85
P2-2		0.20	0.06	106.36	1.49	0.84
GU-1	Unifractional	0.14	0.06	92.98	1.31	1.10
GU-2		0.16	0.07	101.28	1.30	1.12
GB-1	Bifractional	0.21	0.07	97.41	1.44	0.91
GB-2		0.22	0.07	91.07	1.45	0.90

**Table 3-3. Nomenclature, grain size distribution and initial state of the samples subjected to hydration allowing vertical swelling**

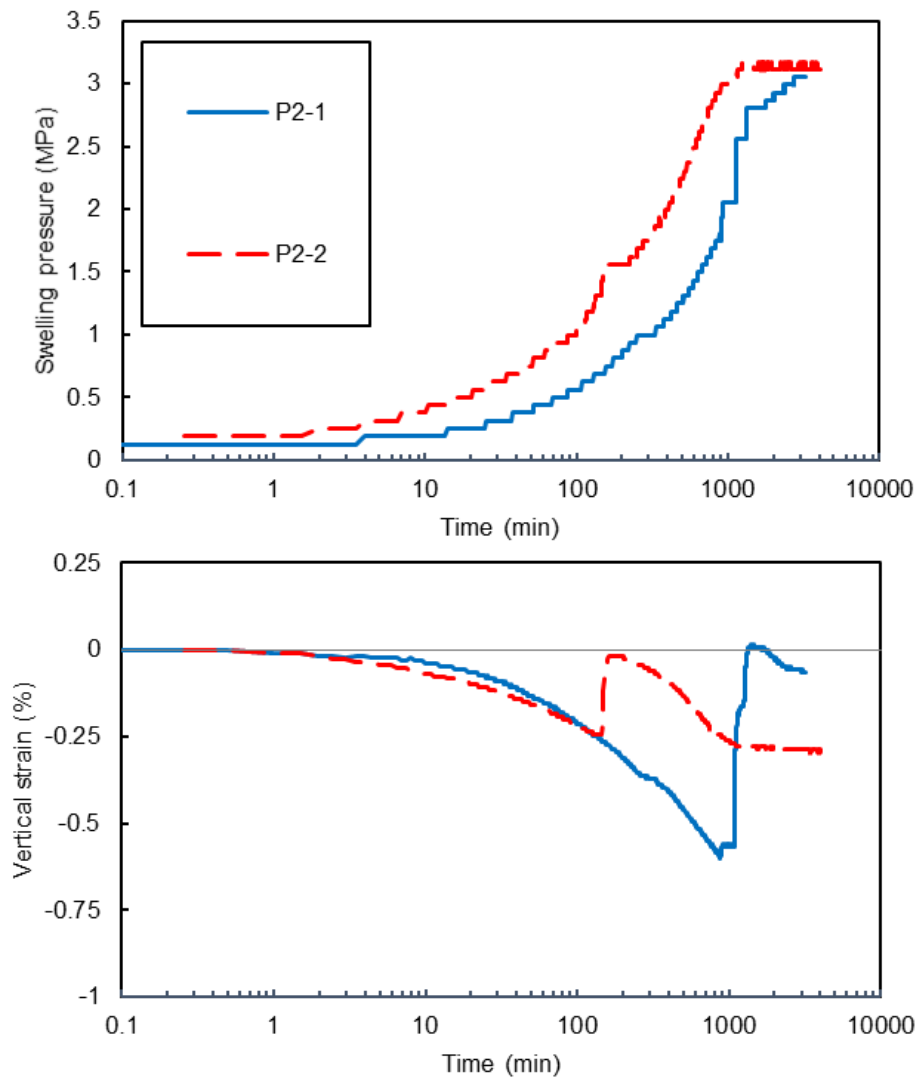
	Grain size distribution	Degree of saturation (-)	Water content (-)	Total suction (MPa)	Dry density (Mg/m <sup>3</sup> )	Void ratio (-)
P1-1	Fuller-type	0.20	0.06	99.49	1.48	0.86
P1-2		0.19	0.06	98.73	1.47	0.87
P1-3		0.23	0.07	90.45	1.50	0.83
GU-3	Unifractional	0.15	0.07	101.28	1.27	1.16
GU-4		0.16	0.07	94.04	1.27	1.16
GB-3	Bifractional	0.18	0.07	91.07	1.44	0.91
GB-4		0.25	0.08	90.86	1.45	0.89

### 3.1.4 Results

In the following sections the results obtained are summarised. The sign convention used is negative for expansion strains and tensile stress, and positive for contractive strains and compression stress.

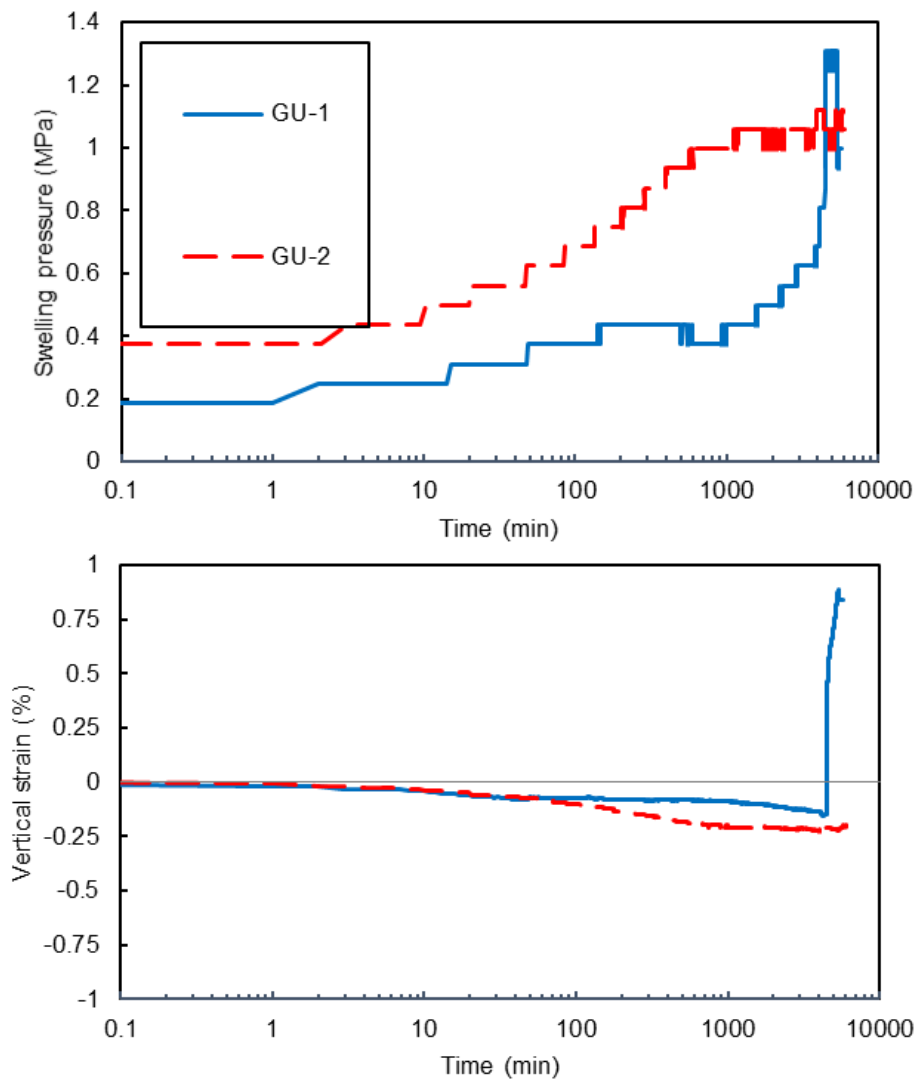
#### 3.1.4.1. Isochoric saturation

The applied vertical strains and development of swelling pressure for two samples with Fuller-type GSD, upon hydration under isochoric conditions is represented in Figure 3-5. Before hydration, a total axial stress of 0.19 MPa was applied in order to ensure contact of the sample with the set up.



**Figure 3-5. Evolution of swelling pressure and vertical strain applied in time during isochoric saturation of samples characterized by a Fuller-type grain size distribution**

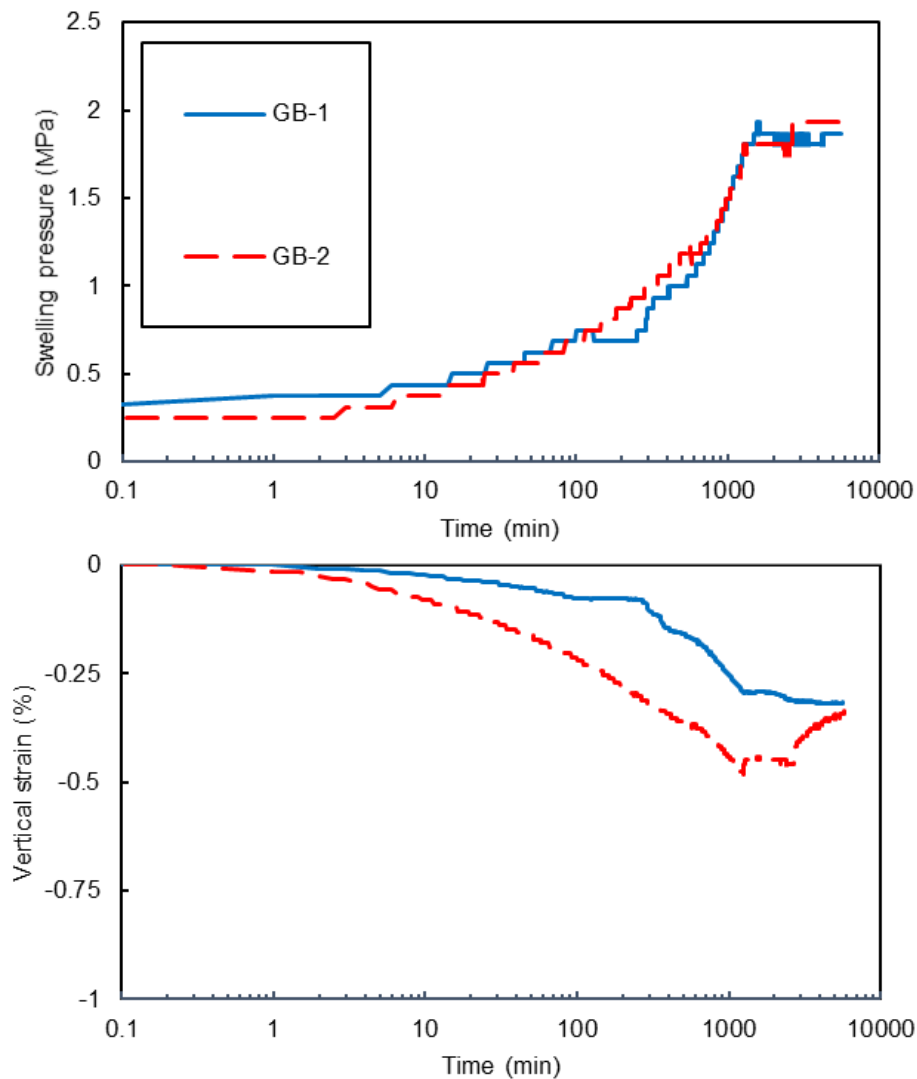
The vertical strains and swelling pressure in time of the samples with unifractal GSD, upon hydration under isochoric conditions is represented in Figure 3-6.



**Figure 3-6. Evolution of swelling pressure and vertical strain applied in time during isochoric saturation of samples characterized by a unifractal GSD**

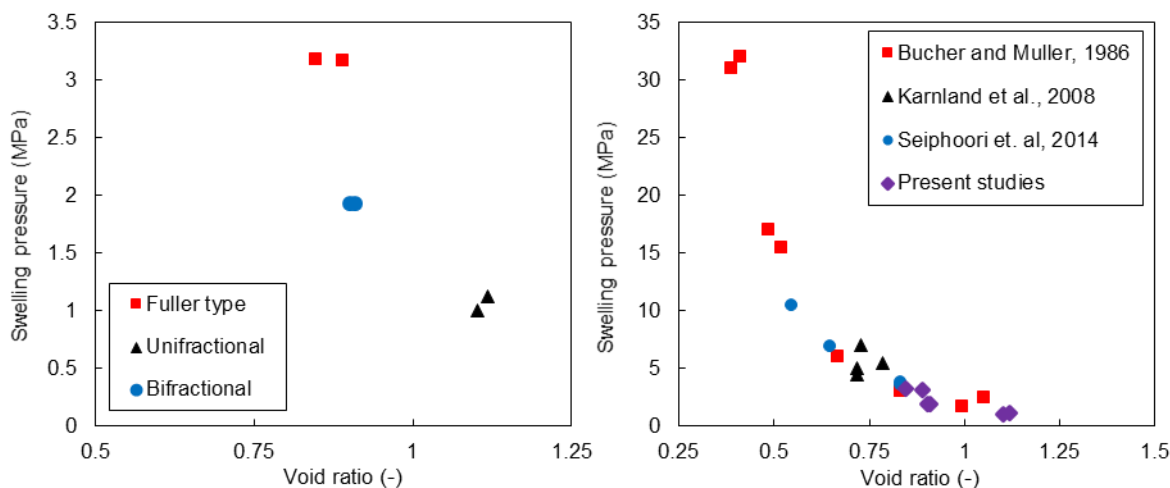
The applied vertical strains and corresponding development of swelling pressure upon hydration for two samples with bifractional GSD, is represented in Figure 3-7.

The swelling pressure developed in a slightly different way for each sample. An important factor influencing the course of wetting process was the manual increase of the swelling pressure. The time of the intervention and the value of pressure increment affected the stabilization time of the saturation process as well as the axial swelling. Nevertheless, final values of swelling pressure at equilibrium were fairly similar for samples having the same granulation.



**Figure 3-7. Evolution of swelling pressure and vertical strain applied in time during isochoric saturation of samples characterized by a bifractional grain size distribution**

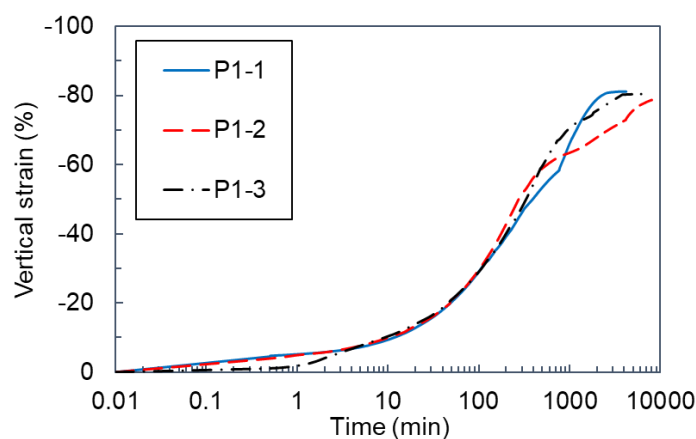
A dependency between final value of swelling pressure and granulation can be observed. Unifractional samples reached the lowest values of swelling pressure. This can be explained by the different dry densities achieved upon pouring the granular material with different granulations. Overall, the obtained values of swelling pressure as a function of dry density are in agreement with the tendency reported in the literature for MX80 bentonite (Figure 3-8).



**Figure 3-8. Left: Relationship between void ratio and swelling pressure of tested samples. Right: comparison with the values reported in the literature (data from Bucher and Müller-Vonmoos, 1989; Karnland et al., 2008; Seiphoori, 2014)**

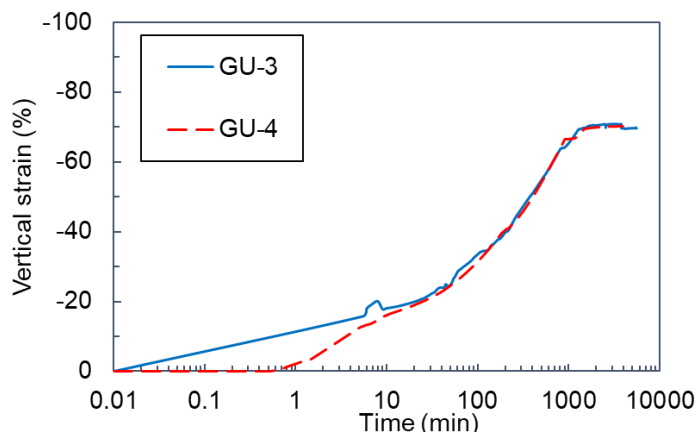
### 3.1.4.2. Vertical swelling tests

Figure 3-9 shows the evolution of axial displacement of the samples with Fuller-type GSD hydrated under vertical-free swelling conditions. Initially all samples swelled with the same rate, up to vertical strains around 50%. After around 300 minutes of hydration, the swelling process developed slightly different for each sample. Nevertheless, the final value of vertical strain stabilized at 80% for all samples.



**Figure 3-9. Evolution of vertical (axial) strain in time during free swelling saturation of samples characterized by a Fuller – type GSD**

The hydration of two samples with unifractional GSD developed in a very similar trend (Figure 3-10). The process stabilized after around 1700 minutes.



**Figure 3-10. Evolution of vertical (axial) strain in time during free swelling hydration of samples characterized by a unifractal GSD**

The development of swelling strains upon hydration for two samples with a bifractal GSD is presented in Figure 3-11. Initially both specimens swelled with similar increment rate. Afterwards, swelling trends differed significantly. Although the saturation process of both samples reached the stabilization after a similar time, the final values of vertical strains differed by 10%.

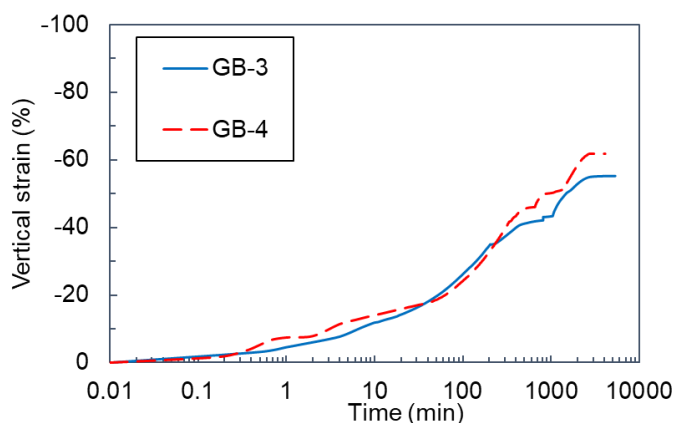


**Figure 3-11. Evolution of vertical (axial) strain in time during free swelling saturation of samples characterized by a bifractal GSD**

As with swelling pressure tests, the swelling process developed slightly different manner for each bentonite sample. In Figure 3-12 the final vertical strains are presented as a function of initial dry density for all tested samples.

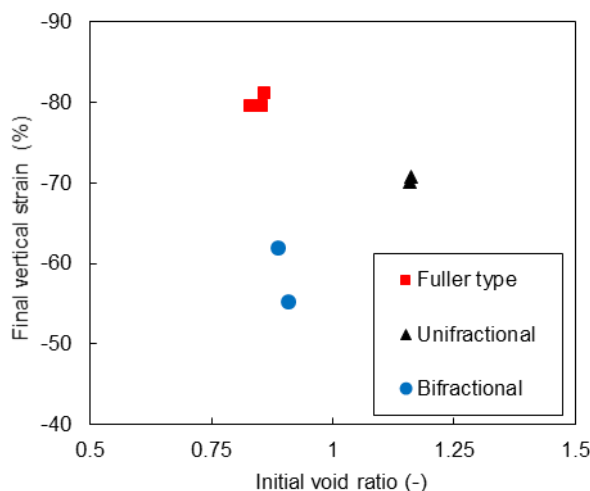


**Figure 3-12. Final axial strain upon free swelling as a function of void ratio for different gain size distributions**

Data in Figure 3-12 suggests that there is not a direct relationship between initial void ratio and swelling potential when different granulations are compared. The initial dry density of the samples characterised by a unifractional granulation ( $1.27 \text{ Mg/m}^3$ ) was lower than for a bifractional granulation ( $1.45 \text{ Mg/m}^3$ ); however, final values of vertical strains of the former granulation are 10-15% higher. This result indicates that not only dry density, but also initial granulation, should be considered when analysing swelling phenomenon. As shown in Figure 3-11, the swelling process for the samples with a bifractional granulation presented a transition zone, with some perturbations, which most likely affected the final value of swelling strains. It is also remarkable the higher dispersion of vertical strains of the samples with a bifractional granulation with respect to the other two granulations.

### 3.1.5 Conclusion

EPFL investigated the influence of initial grain size distribution on the final state of resaturated bentonite samples. While swelling pressure of confined samples was only influenced by the differences in initial dry density of the differently grained samples, free swelling experiments showed a higher volume increase of unifractional grain samples (lower density) compared to bifractional grain samples (higher density). This result indicates that not only dry density, but also initial grain size distribution should be considered when analysing swelling phenomena.

## 3.2 Influence of different hydro-mechanical paths on final macroscopic properties and local homogeneity of compacted samples (EPFL)

Mechanical behaviour of active clays is highly stress-path dependent. For instance, the swelling pressure measured after wetting under isochoric conditions from the as-compacted state is usually different from that obtained after free swelling and compression to the initial density. It is commonly accepted that microstructural evolution is the main cause of such observations (Gens & Alonso 1992). In this section, a set of experiments at the laboratory scale with the objective of assessing the influence of different hydro-mechanical paths on the final state of bentonite is presented. These tests have been complemented with microstructural

observations at different stages by means of Mercury Intrusion Porosimetry (MIP) and scanning electron microscopy (SEM) techniques.

### 3.2.1 Experimental setup

The high pressure oedometric set-up described in section 1.2 was used to perform the tests. Vertical stress was applied by means of a hydraulic jack, in which the pressure is maintained by a pressure/volume controller. The application of high confining stress is not instantaneous and depends on the performance of pressure/volume controller, compressibility of the apparatus and compressibility of the tested material itself (Ferrari et al., 2016). Measured deformations were corrected accounting for these factors.

### 3.2.2 Tested material

The tested material is granular MX-80 bentonite, as presented in Section 3.1.1. All tests have been performed on samples with an initial grain size distribution corresponding to the Fuller-type distribution (see Figure 3-1).

### 3.2.3 Test procedure

The samples reported in Section 3.1.1 with a Fuller-type granulation saturated at constant volume and free axial swelling were further subjected to compression stages. A schematic view of the testing paths followed is shown in the “void ratio – vertical stress” plane in Figure 3-13, including the points at which microstructural testing with MIP and SEM were performed.

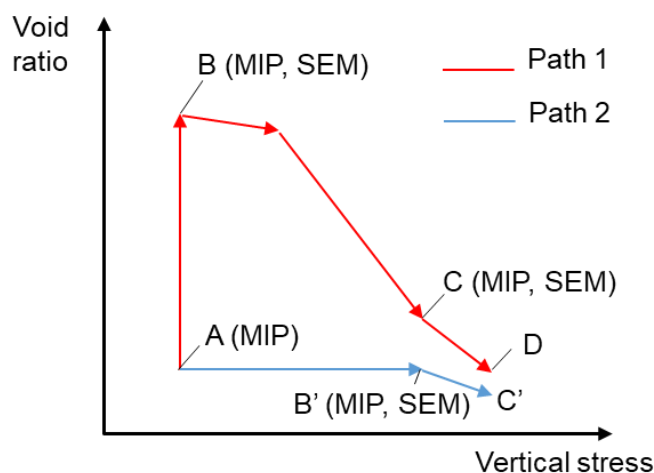


**Figure 3-13. Schematic view of the testing program in terms of void ratio and vertical stress. Initial point is in both cases denoted by A and corresponds to the as-poured, hygroscopic state. The points at which MIP tests and SEM observations were performed are also shown**

The initial state of the samples corresponded to the as-poured and hygroscopic condition, with void ratios around 0.85, water content in the range of 0.06-0.07 and a total suction between 150 MPa and 170 MPa; the specific initial conditions of the tested samples are given in Table 3-2 and Table 3-3 (series “P”).

Deaired, deionized water at a constant pore water pressure of 20 kPa was applied in all the stages of the experiments (saturation and loading).

Path 1 (A–B–C–D) consisted in the following two stages:

- A–B: Hydration under a constant vertical stress of 21 kPa. The stage finished once swelling strains stabilized with time.
- B–C–D: Increase of vertical stress in steps up to 20 MPa.

Path 2 (A–B'–C') consisted in following two stages:

- A–B': Hydration in constant-volume conditions. Vertical stress was increased according to the observed displacements in order to maintain as much as possible isochoric conditions. This stage finished once swelling pressure stabilized with time.
- B'–C': Increase of vertical stress in steps up to 20 MPa.

Three samples were prepared for each of the two paths; this allowed to perform MIP analyses at intermediate states of the hydro-mechanical loadings. The applied sequence for each sample is summarised in Table 3-4.

**Table 3-4. Nomenclature for the samples involved in the experimental program**

	Sample	Sequence (see Fig. 6)	MIP and SEM
Path 1	P1-1	A-B	At point B
	P1-2	A-B-C	At point C
	P1-3	A-B-C-D	No
Path 2	P2-1	A-B'-C'	No
	P2-2	A-B'	At point B'
	P2-3	A-B'	No

### 3.2.4 Results

The results of the two paths in terms of void ratio and total vertical stress are shown in Figure 3-14 for the samples P1-3 and P2-1. The evolutions of void ratio (Path 1, stage A-B) and vertical stress (Path 2, stage A-B') during the previous stages are also shown in the figure. Void ratios are computed accounting for the displacement recorded for each load increment, corrected to take into account the deformation of the set-up. Vertical effective stress can be computed considering that a constant back-pressure of 20 kPa was maintained during all the experiments.

MIP is available at point C (vertical stress of 3.24 MPa) from sample P1-2.

A clear effect of the stress path followed is observed comparing the final state of samples P1-2 and P2-1. Despite having the same degree of saturation and being subjected to the same final value of vertical stress, a difference in void ratio of 0.13 (15% of initial void ratio) between the two samples was obtained.

Nevertheless, upon further compression this difference seems to decrease, as it can be seen comparing the compression curves of samples P2-1 and P1-3. Both samples followed the same asymptotic line once vertical stress exceeded 12 MPa. At the final state, at a vertical pressure of 20 MPa, both samples reached the same void ratio.

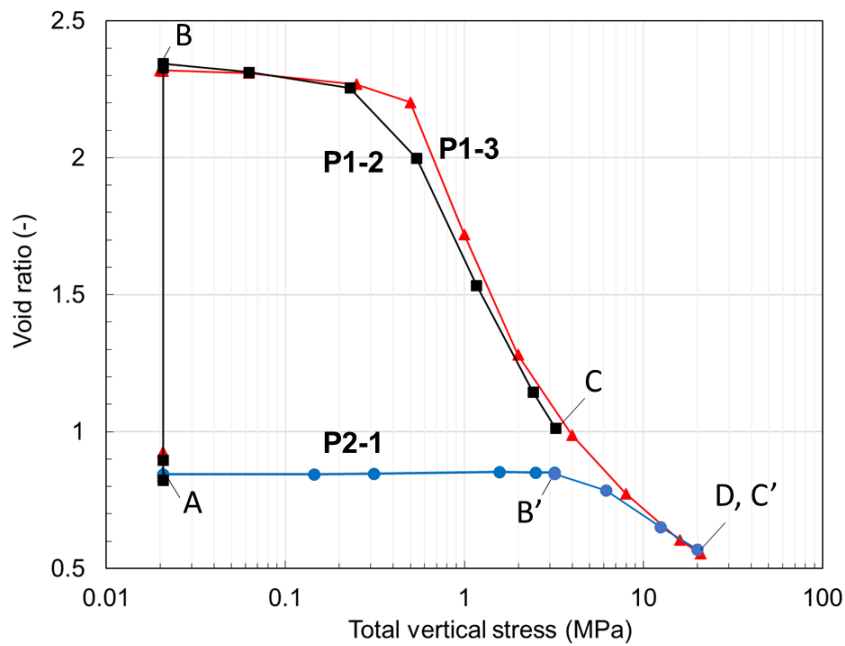


**Figure 3-14. Results of the oedometric compression tests after saturation under constant axial stress (P1-2 and P1-3) and constant volume conditions (P2-1)**

### 3.2.5 Microstructural analysis

The microstructure of the MX-80 granular bentonite was analysed by three techniques: Micro Intrusion Porosimetry (MIP), Scanning Electron Microscopy (SEM) and Micro Computed Tomography MCT. MIP was used to analyse the microstructure of all tested samples. The SEM observations were conducted for samples with Fuller-type GSD subjected to different hydro-mechanical conditions. Results of MIP and SEM are presented in the following.

#### 3.2.5.1. Mercury Intrusion Porosimetry

##### **Samples preparation**

MIP technique requires full removal of the pore liquid. To minimize shrinkage effects upon drying, freeze drying technique was applied. Saturated samples were sub-cored by means of a cutting rod and dry. Sub-cored specimens were subsequently frozen in liquid nitrogen (boiling point of  $-196^{\circ}\text{C}$ ) and dried by sublimation inside a vacuum chamber (at 0.06 mbar and  $-52^{\circ}\text{C}$ ) for 24 hours. In Figure 3-15, the saturated sub-cored specimens and samples during freeze drying are presented.



**Figure 3-15. Sub-cored samples before (left) and during (right) freeze drying**

### **Testing procedure**

Freeze-dried specimens were placed inside the dilatometer which was directly inserted into the MIP apparatus. Tests were carried out using a Thermo Electron Corporation MIP apparatus.

Two levels of porosity are usually distinguished from MIP tests in double-structured clayey materials. These are commonly classified between intra-aggregate (micropores) and inter-aggregates (micropores). Several criteria have been proposed in the literature to separate between the two levels. In the present study the distinction between the inter-aggregate and intra-aggregate porosity is done based on the observation of intrusion/extrusion cycles, following the method proposed by (Delage and Lefebvre, 1984). The main idea of the method is that the first intrusion of mercury fills all the accessible and interconnected pore space, giving the distribution of total porosity. After complete release of the intrusion pressure, due to the ‘ink-bottle’ effect caused by clay aggregates, only some portion of the mercury is released out of the non-constricted pores. A second intrusion will follow approximately the same extrusion path, thus defining the free porosity (Romero et al., 1999). The difference between the porosity recovered by the mercury intrusion and extrusion describes the entrapped porosity, related to the inter-aggregate porosity. The free porosity is consequently associated with the intra-aggregate porosity.

### **Influence of hydro-mechanical path on the microstructure of saturated MX80 bentonite**

In Figure 3-16, the Pore Size Distribution (PSD) of the as-poured state (Seiphoori, 2014) obtained from MIP can be compared with the PSD of the sample P2-3 saturated in isochoric conditions. Both samples were prepared according to the Fuller-type granulometry.

In the as-poured state the PSD has a bimodal character with peaks around 0.01  $\mu\text{m}$  (intra-grain) and 14  $\mu\text{m}$  (inter-grain porosity). The PSD of the sample saturated in isochoric conditions has several modes. Upon saturation, assemblages with intra-aggregate pores with a diameter around 0.03  $\mu\text{m}$  were identified. Some larger aggregates were created with a dominant inter-aggregate pore size around 0.3  $\mu\text{m}$ . A third peak, around 30  $\mu\text{m}$ , suggests that some of the initial pores were preserved upon saturation. The pores larger than 80  $\mu\text{m}$  are probably artefacts of sample preparation (freeze drying technique application) and were not totally resolved by MIP analysis.

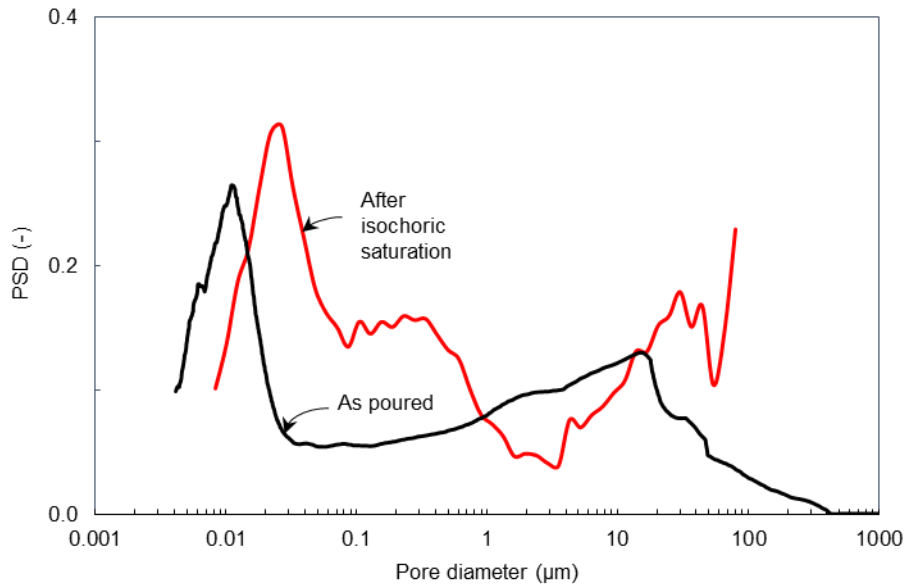


**Figure 3-16. Pore size distribution function of P2-3 sample saturated in isochoric conditions, comparison with as-poured state (Seiphoori, 2014)**

In Figure 3-17, the influence of the hydro-mechanical path on the intra-aggregate porosity can be observed. All PSDs depicted correspond to samples with the same initial Fuller-type granulation. Sample P1-1 was saturated in free swelling conditions, sample P2-3 in isochoric conditions and sample P1-2 was saturated in free swelling conditions and further compressed to the swelling pressure measured from sample P2-3.

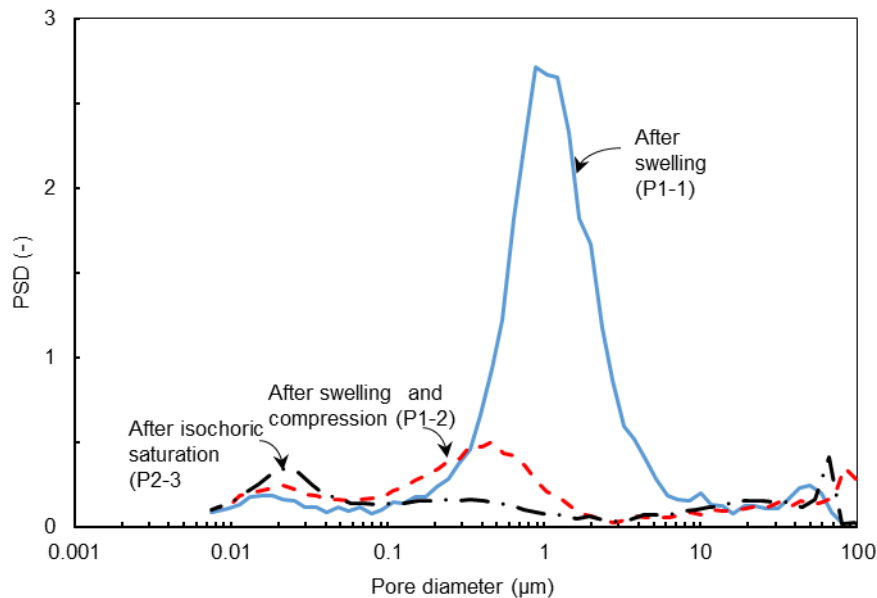


**Figure 3-17. Pore size distribution of the samples with Fuller-type GSD subjected to different hydro-mechanical paths. The legend indicates the sample tested (see Table 3-4)**

The PSD of the sample saturated in free swelling conditions had three visible modes with peak values of around 0.02  $\mu\text{m}$ , 1  $\mu\text{m}$  and 50  $\mu\text{m}$ . The first peak is related to the intra-aggregate porosity, whereas the second and third to the inter-aggregate porosity. The entrance pore size delimiting inter-aggregate and intra-aggregate porosities (determined by analysing intrusion/extrusion cycles) is around 0.2  $\mu\text{m}$ . After free swelling, the inter-aggregate porosity prevailed, with the intra-aggregate porosity being 8% of the total resolved porosity.

Interestingly, the PSD of sample P1-2, saturated in free swelling conditions and compressed, suggests a transition from the PSD of sample P1-1 to that of sample P2-3. The pore size delimiting inter-aggregate and intra-aggregate porosities is around 0.05  $\mu\text{m}$ . The peak value within the inter-aggregate porosity decreased to 0.4  $\mu\text{m}$  while the peak value of the intra-aggregate remained at the same level of around 0.2  $\mu\text{m}$ . The intra-aggregate porosity made up to 18% of the total resolved porosity. As a result of freeze drying, fissures with a size larger than 80  $\mu\text{m}$  developed.

Since volume change was prevented during hydration of sample P2-3, the creation of aggregates seemed to be hindered. The inter-aggregate pores are much smaller (with the dominant value of pore size of 0.3  $\mu\text{m}$ ), and less pronounced than in case of samples saturated in free swelling conditions. For this sample, the intra-aggregate porosity amounted 21% of the total resolved porosity.

### ***Influence of initial grain size distribution on the microstructure of the saturated samples***

The results of MIP tests for the three samples with different grain size distributions saturated in free swelling conditions are presented in Figure 3-18. The PSD functions of all tested samples have the same three main modes. Regardless initial grain size distribution, a peak around 0.02 $\mu\text{m}$ , corresponding to the intra-aggregate porosity is revealed. The second peak, related to the inter-aggregate porosity, varies slightly depending on the initial grain size distribution. The value of pore size delimiting intra and inter-aggregate porosities determined analysing intrusion/extrusion cycles is around 0.2  $\mu\text{m}$  for all samples. The inter-aggregate porosity prevailed in case of free swelling saturation, independently of the initial granulometry.

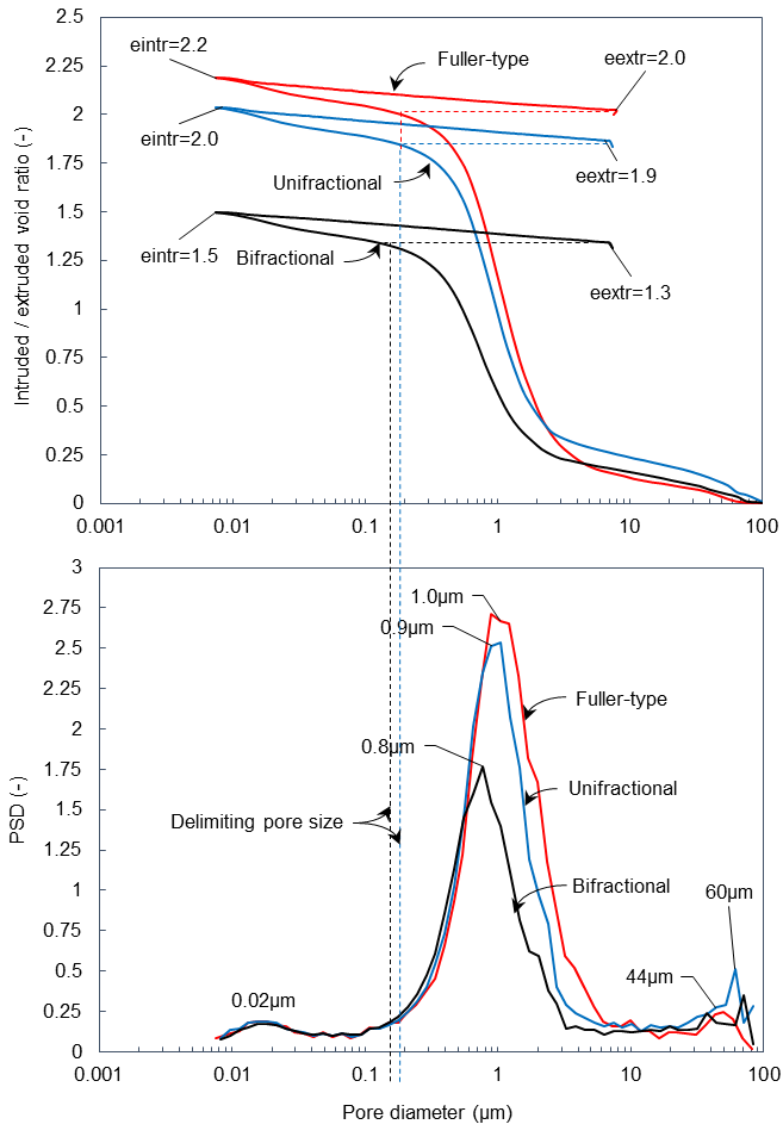


**Figure 3-18. Cumulative intruded and extruded void ratio (up) and pore size distribution (down) of the samples saturated in free swelling conditions with different initial granulations**

In Figure 3-19 the results of MIP tests for three samples with different grain size distributions saturated in isochoric conditions are presented. Since changes in volume were prevented upon wetting, initial porosity was preserved. The PSD functions of the samples characterized by unifractional and bifractional granulations have a bimodal distribution with peaks around 0.02  $\mu\text{m}$  (related to intra aggregate porosity) and around 60  $\mu\text{m}$ . The second mode of the PSD might be correlated with the pores that were not filled with low density material during saturation or, to some extent, with fissures created upon freeze drying.

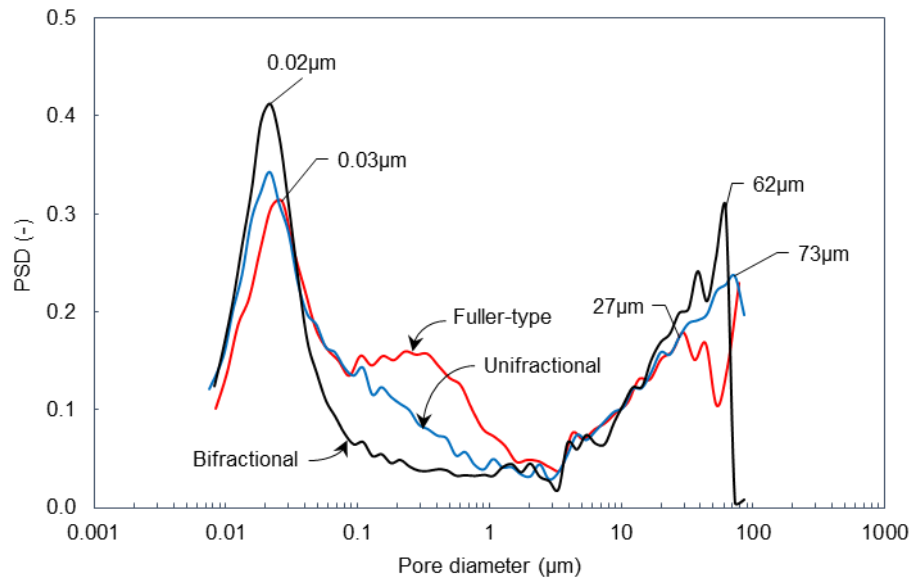


**Figure 3-19. Pore size density function of the samples saturated in isochoric conditions differing in initial granulations (indicated with arrows)**

### 3.2.5.2. Scanning Electron Microscopy

#### **Samples preparation**

Scanning Electron Microscopy Technique was applied to analyse the microstructure of the samples characterised by the Fuller type granulation after being subjected to three different hydro-mechanical paths (see Table 5). As for the MIP tests, the SEM requires full removal of the pore liquid; the extraction of the pore fluid from the samples was done by freeze-drying.

#### **Testing procedure**

The basic operating principle of the SEM involves the creation of a finely focused beam of energetic electrons by means of emission from an electron source (Goldstein, 2017). The electrons interact with atoms in the material and produce various signals that can be detected. This signal contains information about the material's surface topography and compositions. The electron beam is usually scanned in a raster scan pattern, and the position of the beam is combined with the detected signal in order to generate an image.

All tests were performed in a high-performance scanning electron microscope FEI Quanta 200f. Observations were carried out in high vacuum mode (HV) using the Secondary electron (SE) detector (spot 3.0) at an accelerating voltage between 20 and 30 kV. The applied working distance (WD) was up to 10-20 mm. SEM magnifications were in the range 15-50000X.

#### **Results: Influence of hydro-mechanical paths**

In Figure 3-20 the SEM microphotographs of samples subjected to different hydro-mechanical paths are summarized. In Figure 3-20a, the SEM picture for the sample saturated in free swelling conditions (P1-1) are presented. No outlines of the initial granular structure are distinguished. The distance between observed aggregates is in the range of 0.5 - 2.5  $\mu\text{m}$ . In Figure 3-20b the SEM picture of the sample saturated in isochoric conditions is presented (P2-2). Possible outlines

of initial grains and some connections can be noticed. In Figure 3-21c, the SEM pictures of the sample saturated in free swelling conditions (P1-2) and compacted are presented. The area is homogeneously filled with the clay. The outlines of aggregates are visible, but no pore space between the aggregates is noticed. The distance measured between aggregate layers is in the range of 0.5 – 1  $\mu\text{m}$ .

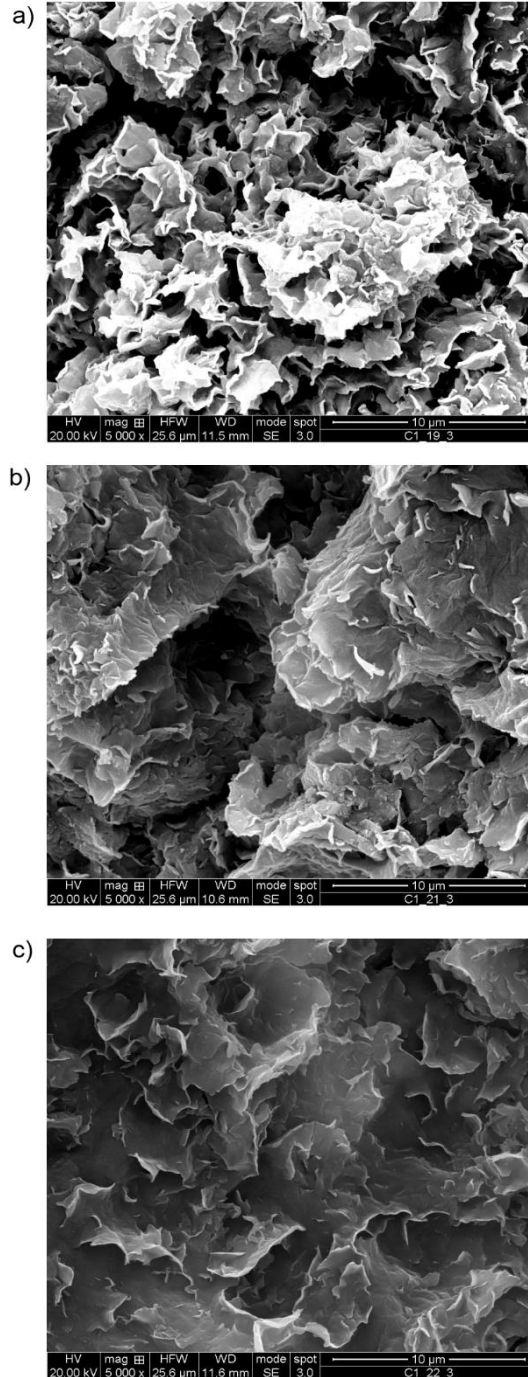


**Figure 3-20. SEM photomicrographs of (a) sample P1-1 (b) Sample P2-2 and (c) Sample P1-2. The total width of the pictures corresponds to 25.6  $\mu\text{m}$**

The results of MIP analysis combined with additional SEM observations complement the interpretation of MX80 bentonite behaviour in various hydro-mechanical states.

For all tested granulations, the dominant size of micro porosity is in similar range regardless of the stress path. The applied hydro-mechanical paths as well as the initial granulation influenced mostly the inter-aggregate (macro) porosity. The microstructure of the material saturated in free swelling conditions seems to be noticeably modified in comparison with the material in initial hygroscopic state. After free swelling saturation, no outlines of initial grains were visible. For the case of isochoric saturation, full development of clay aggregates was not possible. The grains swelled in limited range. The initial structure characterised by the compacted grains was rather preserved after full saturation and outlines of the as – poured state can be distinguished.

### **3.2.6 Conclusions and recommendations**

The experiments addressed the Influence of different hydro-mechanical paths on final state of the bentonite. Granular bentonite with a fuller-type granulation was either (a) hydrated under constant low stress (nearly free swelling), and stress was afterwards increased, or (b) hydration was performed at constant volume conditions, and stress was afterwards increased to the same value as in (a). A clear effect of the stress path followed was observed comparing the final state of samples. Despite having the same degree of saturation and being subjected to the same final value of vertical stress, a difference in void ratio of 0.13 (15% of initial void ratio) between the two samples was obtained.

For all tested granulations, the dominant size of micro-porosity is in similar range regardless of applied wetting scenario or stress level. The applied hydro-mechanical paths as well as the initial granulation influenced mostly the inter-aggregate (macro-) porosity. The microstructure of the material saturated in free swelling conditions seems to be noticeably modified with respect to the initial hygroscopic state. After free swelling saturation, no outlines of initial grains were visible. For the case of isochoric saturation, the initial structure characterised by the compacted grains was rather preserved after full saturation and outlines of the as-poured state can be distinguished.

All the results regarding the volume change behaviour and the microstructure evolution correspond to tests performed under oedometric conditions in which radial stresses were not measured. In order to complement the present work, the effects of radial stress developed during wetting on the stress path dependent behaviour could be studied. Future work could also focus on the final pore size distribution at the same void ratio-vertical stress reached from different stress paths.

## **3.3 Hydraulic and mechanical properties of Czech bentonite (CU, CTU)**

### **3.3.1 Constant load tests (CU)**

#### **3.3.1.1. Outline of the tests**

Laboratory tests were carried out on Czech bentonite (BCV) from Cerny vrch deposit (north western region of the Czech Republic). Compacted samples were prepared from bentonite powder of its original water content (10-11%). Three different initial dry densities of 1.27, 1.60 and 1.90 g/cm<sup>3</sup> were investigated. The one-dimensional swelling behaviour, water retention properties and microstructure characteristics were studied. The one-dimensional swelling behaviour under constant load was performed using the conventional oedometer cell. The water retention properties were investigated on samples, which were first equilibrated either at highest (286.7 MPa) or lowest (0.001 MPa) suction and then suction change was analysed at wetting and drying path. Furthermore, retention tests on directly equilibrated samples (from the

initial water content) were performed under both free swelling and constant volume conditions.

Mercury intrusion porosimetry was used to analyse the pore size distribution curves at different initial dry densities and suction levels. The environmental scanning electron microscopy (ESEM) was applied to analyse the deformation of bentonite aggregate at different hydration paths including the wetting-drying-wetting (WDW) and drying-wetting-drying (DWD) paths starting from the initial state of bentonite.

### 3.3.1.2. Constant load swelling

The conventional oedometer apparatus shown in Figure 3-21 was used for measuring the swelling deformation of the bentonite BCV. The compacted bentonite was tested in the standard fixed stainless-steel ring, 50 mm inside diameter and 20 mm height. Silicone grease was applied to the inner wall of the stainless-steel ring to reduce friction between the specimen and the wall. The filter papers were placed between the specimen and porous stones.

Considering the porous stone placement and the swelling deformation, the samples were prepared with the initial height of 8-10 mm. Once the compacted bentonite was introduced in the stainless-steel ring, the vertical stress was applied. For each initial dry density, 4-7 different loads were applied (Table 3.5). Then the specimen was flooded by distilled water. The vertical deformation and time required to reach constant deformation were recorded. The ASTM D2435/D2435M standard recommends the correction for oedometer apparatus compressibility. The deflection of the apparatus was measured for all loads applied during the tests by substituting the soil specimen by a smooth hard steel disk.

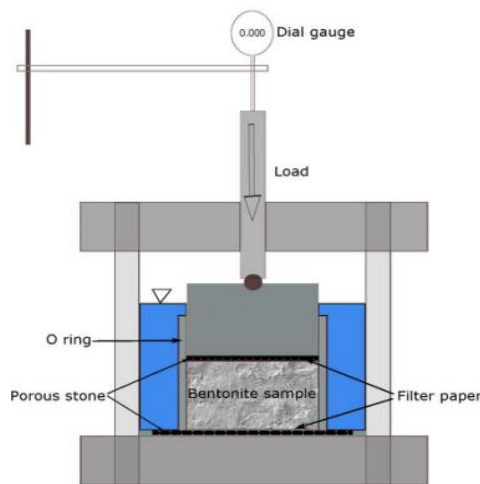


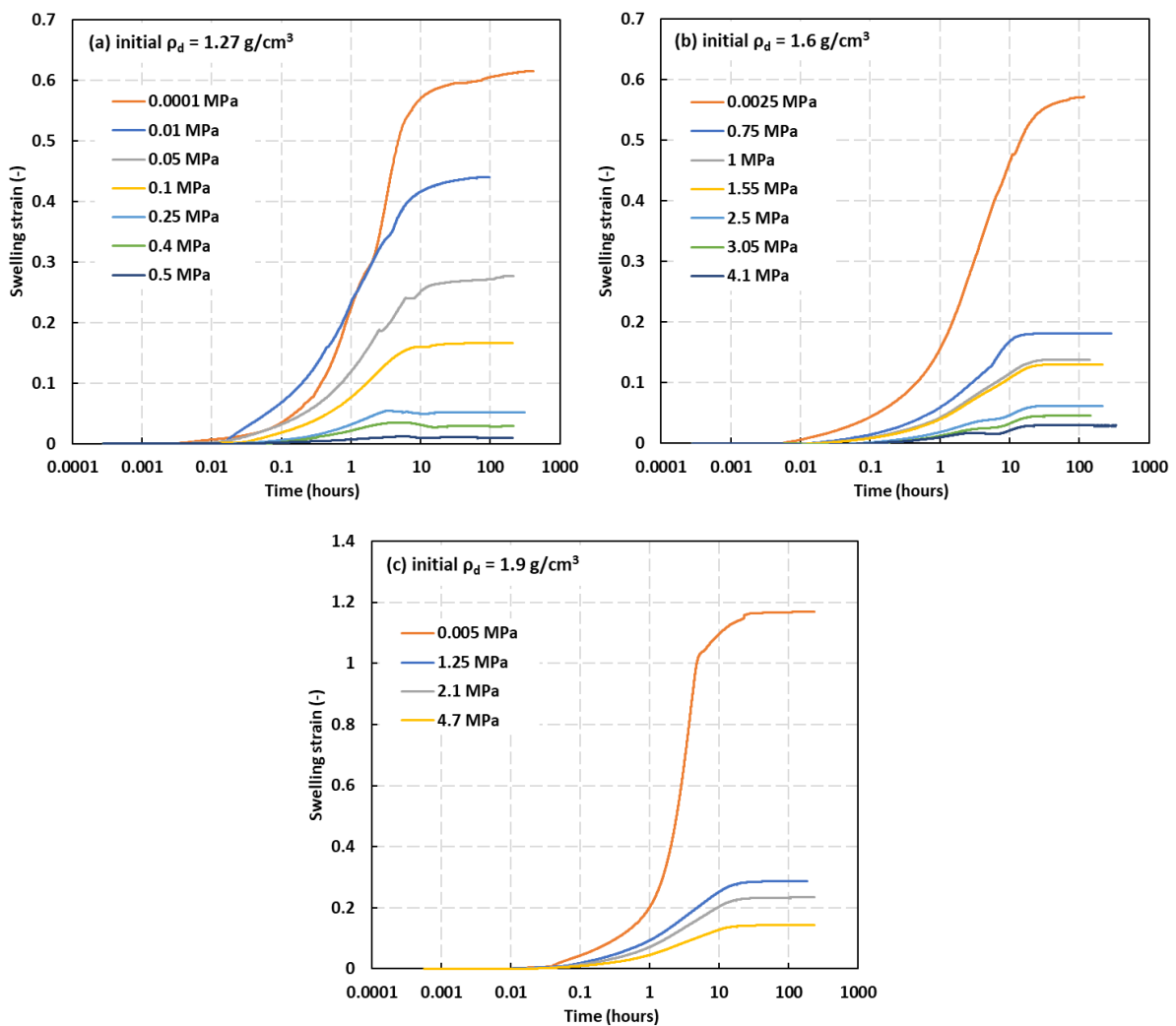
**Figure3-21. Measurement of constant load swelling**

**Table 3-5. Initial dry densities and vertical stresses applied in constant load swelling tests**

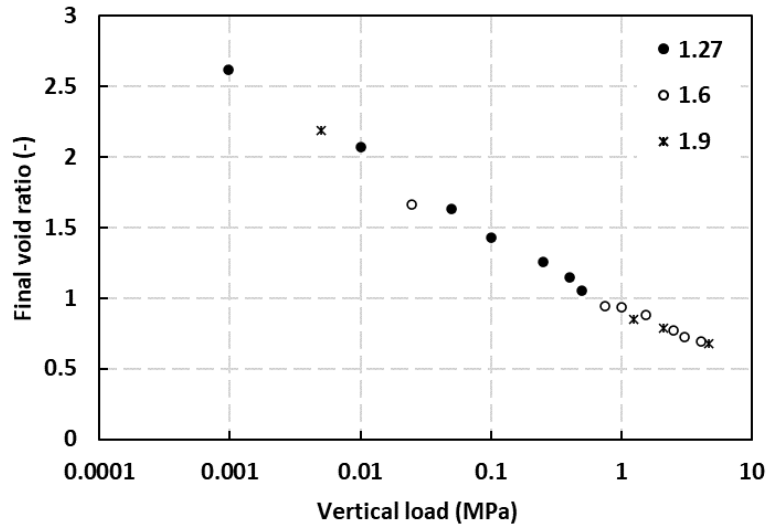
$\rho_d = 1.27 \text{ g/cm}^3$	$\rho_d = 1.6 \text{ g/cm}^3$	$\rho_d = 1.9 \text{ g/cm}^3$
0.001 MPa	0,025 MPa	0.005 MPa
0.01 MPa	0,75 MPa	1.25 MPa
0.05 MPa	1 MPa	2.1 MPa
0.1 MPa	1,55 MPa	4.7 MPa
0.25 MPa	2.5 MPa	
0.4 MPa	3.05 MPa	
0.5 MPa	4.1 MPa	

Figure 3-22 shows the evolution of the constant load swelling with time for initial dry densities of 1.27, 1.6 and 1.9 g/cm<sup>3</sup> for all the applied constant loads. Swelling strain equals to the ratio of swelling deformation and initial height. It increased rapidly in the initial stage after flooding. For the lowest vertical load of 0.98 kPa, which corresponds to the weight of top plate, the equilibration of the final swelling strain took longer time (over 100 hours), while for higher loads, the time of equilibration was shorter (e.g., 50-60 hours). After the final state was reached, the final swelling strain was recorded and the final void ratio was calculated from the final water content, specific gravity and final dry density.

Figure 3-23 shows the final void ratio versus applied vertical load for all tested initial dry densities. It shows that final void ratio decreases with increasing vertical load linearly in semi-logarithmic scale. The presented trends are independent of the initial dry density. It indicates that initial compaction has no effect on final void ratio.



**Figure 3-22. Development of swelling strain with time for dry density (a) 1.27 g/cm<sup>3</sup> and (b) 1.6 g/cm<sup>3</sup>**



**Figure 3-23. Final void ratios versus vertical load in constant load tests for initial dry densities of 1.27, 1.60 and 1.9 g/cm<sup>3</sup>**

Two specimens (with initial  $\rho_d = 1.27 \text{ g/cm}^3$  and applied stress of 10 kPa and with initial  $\rho_d = 1.6 \text{ g/cm}^3$  and applied stress of 25 kPa) were selected for more complex investigation of mechanical behaviour during loading – unloading cycle. After reaching constant swelling strain, both specimens were subjected to incremental loading up to the vertical stress of 4,8 and 5,7 MPa, respectively. Loading stage was followed by incremental unloading. Both unloading-reloading curves including initial constant load swelling stages are presented in Figure 3-24. It indicates that during loading stage, both loading curves converge and unloading lines are identical for both specimens. It suggests that application of high vertical load removed the effect of different initial conditions given by different compaction efforts.

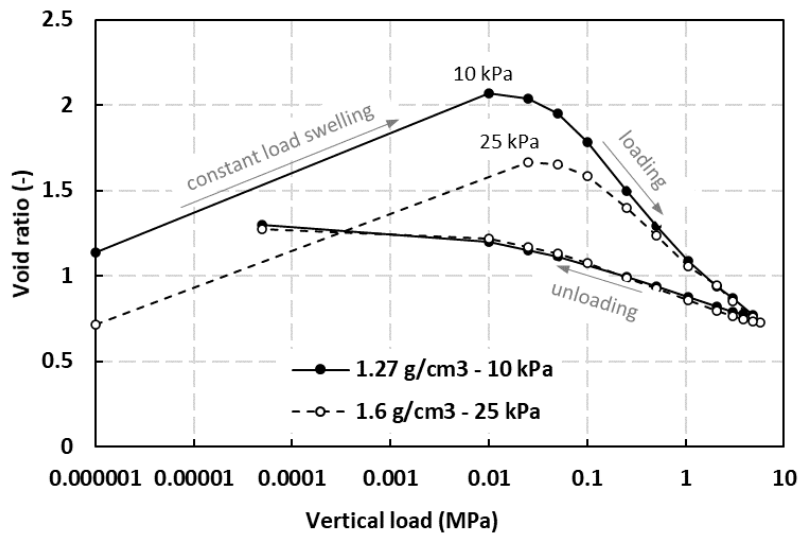


**Figure 3-24. Constant load swelling tests followed by loading-unloading cycle**

### 3.3.1.3. Water retention properties

The vapor equilibrium technique (Delage et al., 1998) was used to control suction in sealed desiccators. The relative humidity in the sealed desiccators was imposed by different saturated chemical solutions. The total suction can be calculated from Kelvin's equation by knowing the relative humidity. The desiccators with saturated solutions were placed in a room with controlled temperature to ensure constant suction. Eight different salt solutions were used generating total suction in a range from 3.29 to 286.7 MPa as shown in Table 3-6. The desiccator with distilled water (assumed suction of 0.001 MPa) was used to prepare the samples for drying path.

**Table 3-6. Characterisation of salt solutions used for vapor equilibrium method measurements (at temperature of 20 °C)**

Salt solutions	Relative humidity (%)	Suction (MPa)
Lithium Chloride Monohydrate (LiCl·H <sub>2</sub> O)	12.0	286.7
Potassium Acetate (CH <sub>3</sub> COOK)	23.1	198.14
Magnesium Chloride Hexahydrate (MgCl <sub>2</sub> ·6H <sub>2</sub> O)	33.1	149.51
Potassium Carbonate (K <sub>2</sub> CO <sub>3</sub> )	43.2	113.50
Sodium Bromide (NaBr)	59.1	71.12
Sodium Chloride (NaCl)	75.5	38.00
Potassium Chloride (KCl)	85.1	21.82
Potassium Sulphate (K <sub>2</sub> SO <sub>4</sub> )	97.6	3.29

Several different test series with variable dry density, hydraulic path and confining conditions were performed for complex evaluation of retention properties of the bentonite. The compacted bentonites with three different initial dry densities (1,27, 1,6 and 1,9 g/cm<sup>3</sup>) were first broken into several small pieces with weight ranging from 1.5 to 8 grams.

The samples for determination of wetting path were placed into the highest suction desiccator (LiCl solution) to equilibrate. The samples for measurement of drying path were placed into the lowest suction desiccator (distilled water). After equilibration, the samples were distributed to other desiccators to determine wetting and drying path. Third set of the samples was directly distributed to the desiccators immediately after compaction without any equilibration (initial water content corresponded to hygroscopic water content of approximately 10%). All three series of tests were performed under unconfined conditions, so the samples could freely swell during water content equilibration.

Furthermore, additional test series was performed under constant volume conditions. The samples were compacted into the constant volume cells (Figure 3-25) and placed in the desiccators with salt solutions without any equilibration. Only wetting path (from initial hygroscopic water content) could be analysed as during drying constant volume conditions cannot be kept due to shrinking of the samples. The summary of the performed tests is presented in Table 3-7.

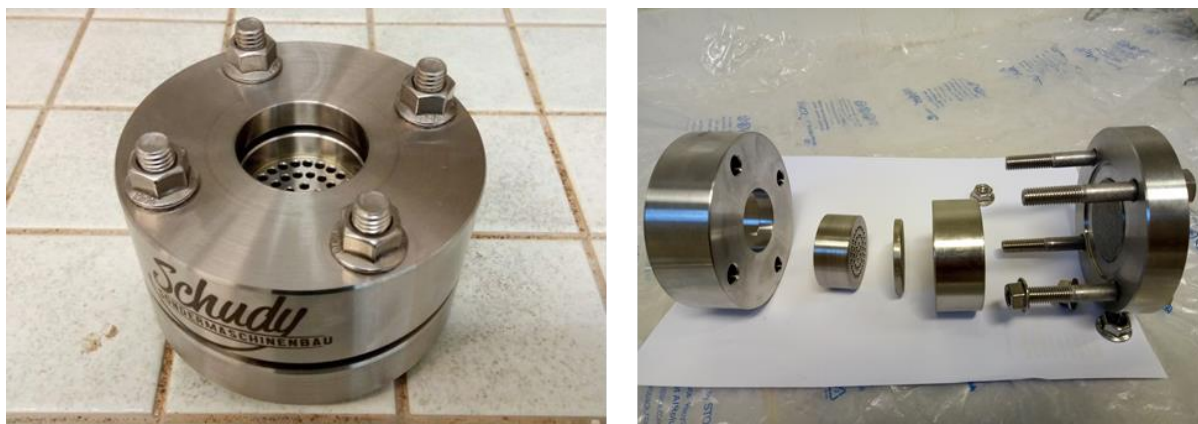


**Figure 3-25. Constant volume cells for measurement of retention curves**

**Table 3-7. Summary of all retention curves**

Dry density $\rho_d$ (g/cm <sup>3</sup> )	Unconfined conditions			Constant volume
	Drying path	Wetting path	From hygroscopic water content	From hygroscopic water content
1.27	X	X	X	X
1.6	X	X	X	X
1.9	X	X	X	X

The example of equilibration of unconfined samples compacted to 1.27 g/cm<sup>3</sup> and tested at wetting path is presented in Figure 3-26. The time of equilibration took over 2 months for the samples exposed to biggest change of suction (lowest suction in Figure 3-26).

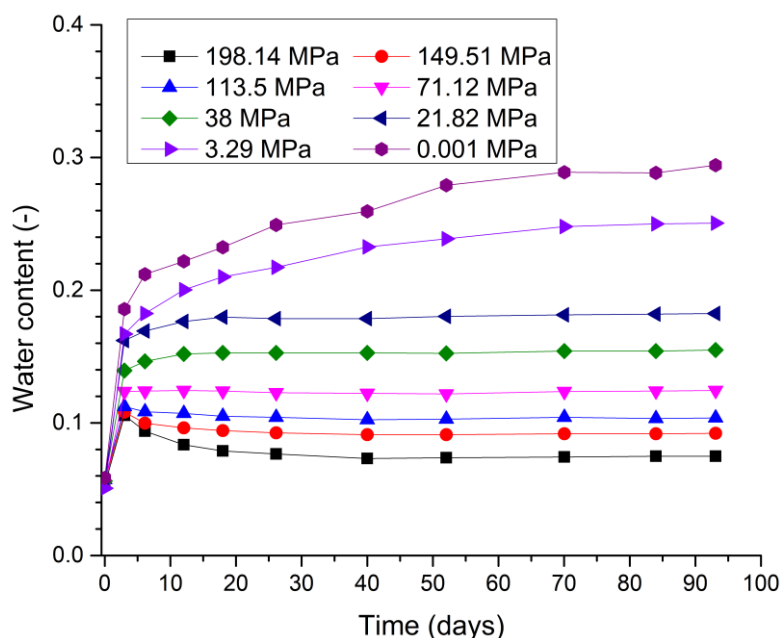


**Figure 3-26. Example of water content evolution with time for different suctions obtained by vapor equilibrium method (initial dry density of 1.27 g/cm<sup>3</sup>)**

Once the equilibrium was reached, one part of the samples was taken from each desiccator and used for the determination of water content. Another part (4 to 6 pieces) was immediately weighted and then covered by wax to determine their volume. The volume was measured using the wax immersion method following the ASTM C914-95 (ASTM, 2004) procedure. The final void ratio value was determined as the average value from those obtained on all pieces from the same desiccator. The degree of saturation was calculated from the obtained values of water content and void ratio.

Figure 3-27(a) shows the water retention curves of three different initial dry densities and both wetting and drying paths. The water content has almost linear relationship with suction in semi-logarithmic scale and creates only narrow hysteretic loop between wetting and drying paths. It can be concluded that the initial dry density had little influence on the water content. With the assumption that most water is concentrated in the micropores at high suctions (Sun et al. 2018), these results suggest that micropores are only little influenced by the compaction pressures, as if their volume was to be affected, their water retention capacity (which is known to be porosity dependent) would also change.

Contrarily, quite a remarkable effect of the initial dry density was found on the degree of saturation through its effect on void ratio (Figure 3-27(b) and (c)). The results consistently show an increase in the global degree of saturation with increasing dry density.

Water retention curves determined from hygroscopic water content are presented in Figure 3-28. Similar to Figure 3-27(a), no effect of initial dry densities is observed. Position of unconfined water retention curves is consistent with wetting and drying paths and lies inside the hysteretic loop presented in Figure 3-27(a). Results of retention curves measured at constant volume exhibit slightly higher water contents for given suction compared to unconfined tests. Lower water contents of 1.9 g/cm<sup>3</sup> curve at low suctions is associated with low porosity of the constant volume sample, which reached full saturation and could not absorb more water.

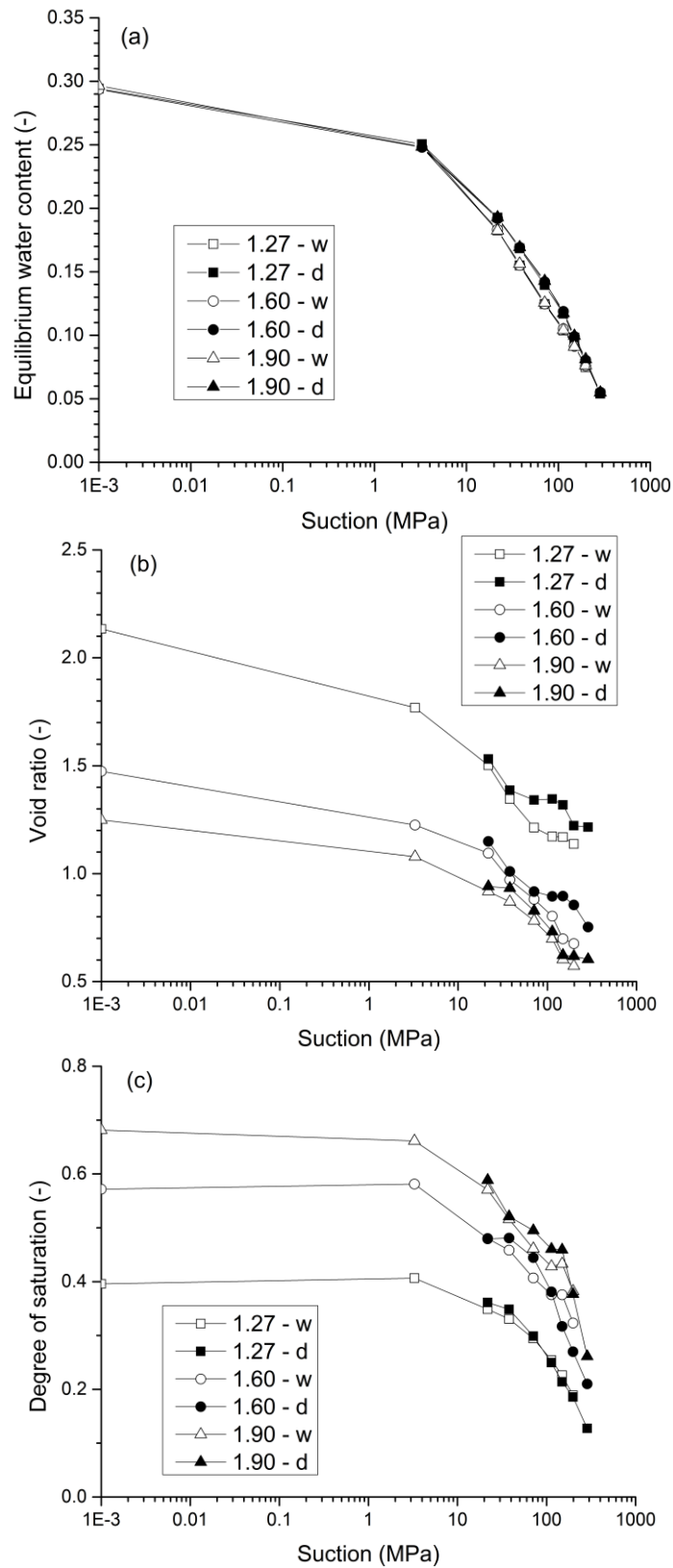


**Figure 3-27. Water content (a), void ratio (b) and degree of saturation (c) with respect to suction along wetting and drying path at dry densities of 1.27, 1.60 and 1.90 g/cm<sup>3</sup>**

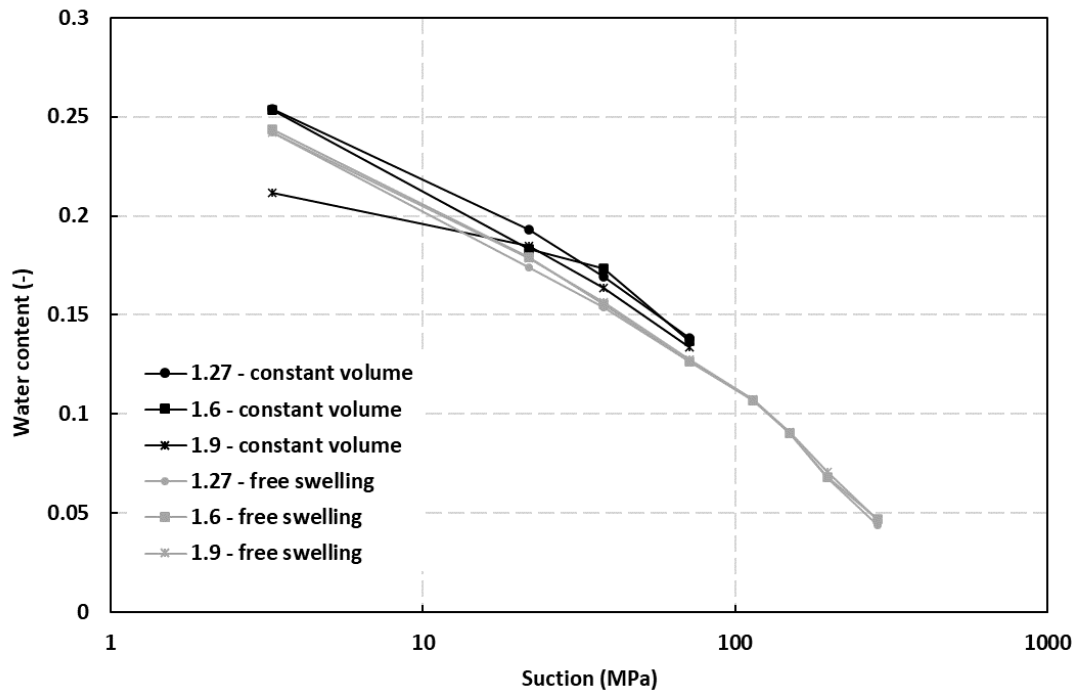


**Figure 3-28. Comparison of water retention curves determined from hygroscopic water content at “constant volume” and “unconfined” conditions**

### 3.3.1.4. Mercury intrusion porosimetry

Mercury intrusion porosimetry is based on the capillary law governing non-wetting liquid penetration into small pores. The pore entrance diameter can be calculated from the applied mercury pressure by assuming that the cylindrical pores exist in soil according to the Washburn equation (Juang and Holtz, 1986)

$$D = -(4\sigma_{Hg} \cos \theta_{nw})/P \quad [3.1]$$

where  $D$  is the entrance pore diameter;  $\sigma_{Hg}$  is the surface tension of mercury;  $\theta_{nw}$  is the contact angle between the mercury and the soil surface; and  $P$  is the intrusion pressure. In this study, the values  $\theta_{nw} = 130^\circ$  and  $\sigma_{Hg} = 0.484 \text{ N/m}$  at  $25^\circ\text{C}$  were considered in the pore diameter calculation.

The tests were performed at the Department of Inorganic Technology at the University of Chemistry and Technology Prague (Apparatus Autopore IV, Micromeritics). The measurement was carried out in two regimes, one was a low-pressure regime from 0.01 to 0.2 MPa (corresponding to the pore radius between 100 and 3  $\mu\text{m}$ ); the other one is the high-pressure regime from 0.2 to 400 MPa (corresponding to the pore radius between 3  $\mu\text{m}$  and 1.5 nm). MIP tests were conducted on freeze-dried samples to retain the original microstructure. In freeze-drying methods, the samples were first immersed in liquid nitrogen and then the frozen samples were placed under a deep vacuum. Finally, the samples went through sublimation in the vacuum chamber of a freeze dryer (Delage et al., 1996). In the tests, samples of three different initial dry densities of the compacted bentonite were first equilibrated at the suction of 286.7 MPa (LiCl) and then distributed to desiccators to reach suctions of 113.5, 38, 21.82 and 3.29 MPa (wetting path). The samples equilibrated at these suction levels were used for MIP tests. Figure 3-29 shows the MIP results of three dry densities samples (1.27, 1.60 and 1.90  $\text{g/cm}^3$ )

at each suction level. The comparison of different dry densities demonstrates that compaction has big influence on the predominant pore radius represented by the highest peak. An increase of dry density leads to the reduction of the peak and shifting the predominant pore size towards smaller pores. This trend is independent on the value of applied suction.

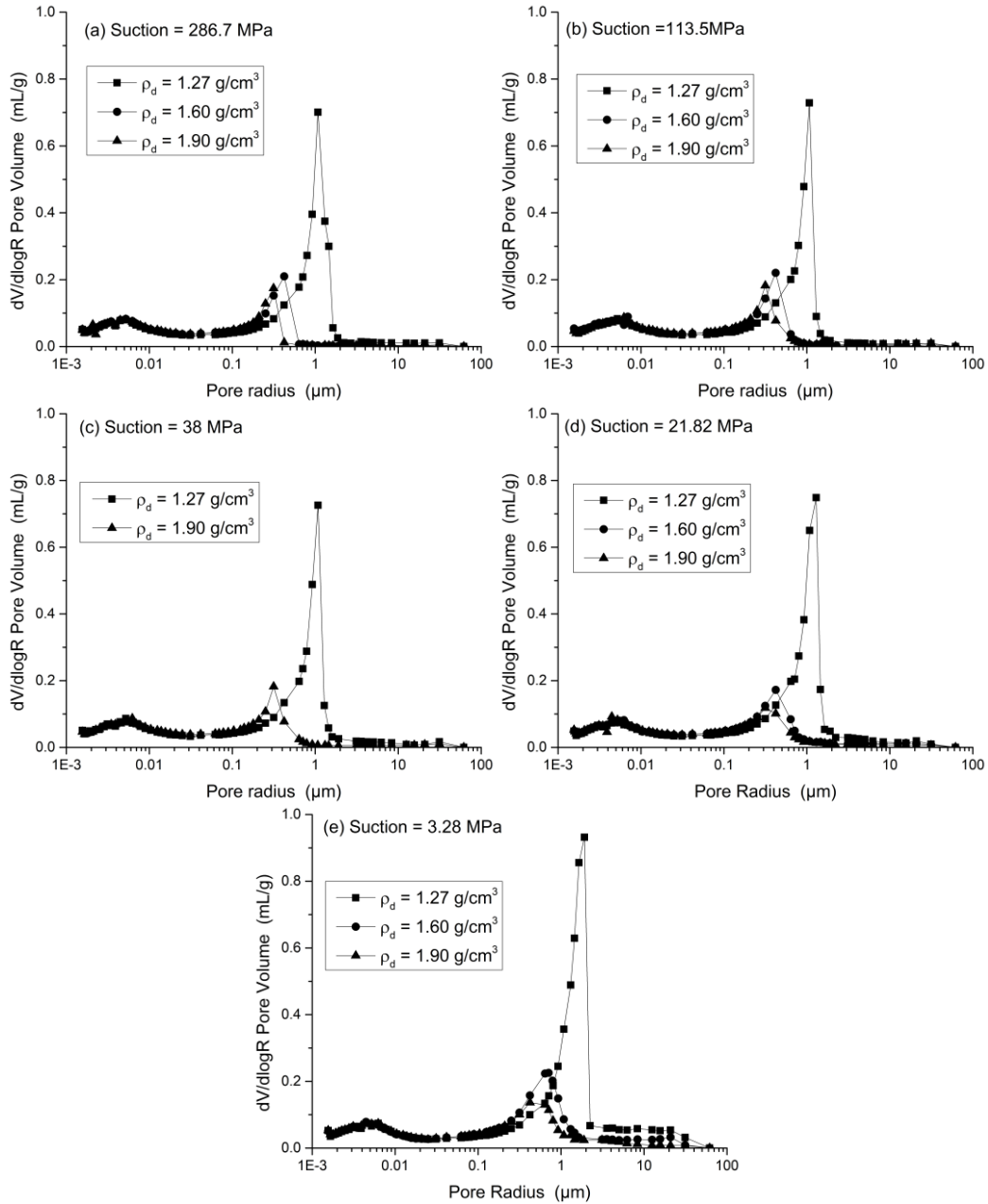


**Figure 3-29. Pore size distribution curves of samples with different dry densities at constant suction**

Figure 3-30 presents the same results, replotted to identify the effect of suction on pore size distribution. It shows that the peaks representing predominant pore radius are slightly affected by applied suction. With increase of suction, peak is shifted towards smaller pore radius. This effect is more obvious for high initial dry density samples (Figure 11c). Compared to the effect of initial dry density, suction has significantly smaller influence on predominant pore size.

According to the criteria to discriminate the macro and micro pore presented in Romero et al., (2011), the transition pore radius boundary between macropores and micropores is around 0.05-0.07  $\mu\text{m}$ . The pore size distribution curves show that the compacted bentonites have double structure pore system, which consists of macropores (represented by pore radius around 1-2  $\mu\text{m}$ ) and micropores (represented by peak at approximately 5-6 nm). Pore size distribution curves show that suction and especially compaction have significant influence on the macropores. The influence on the micropores was found to be insignificant.

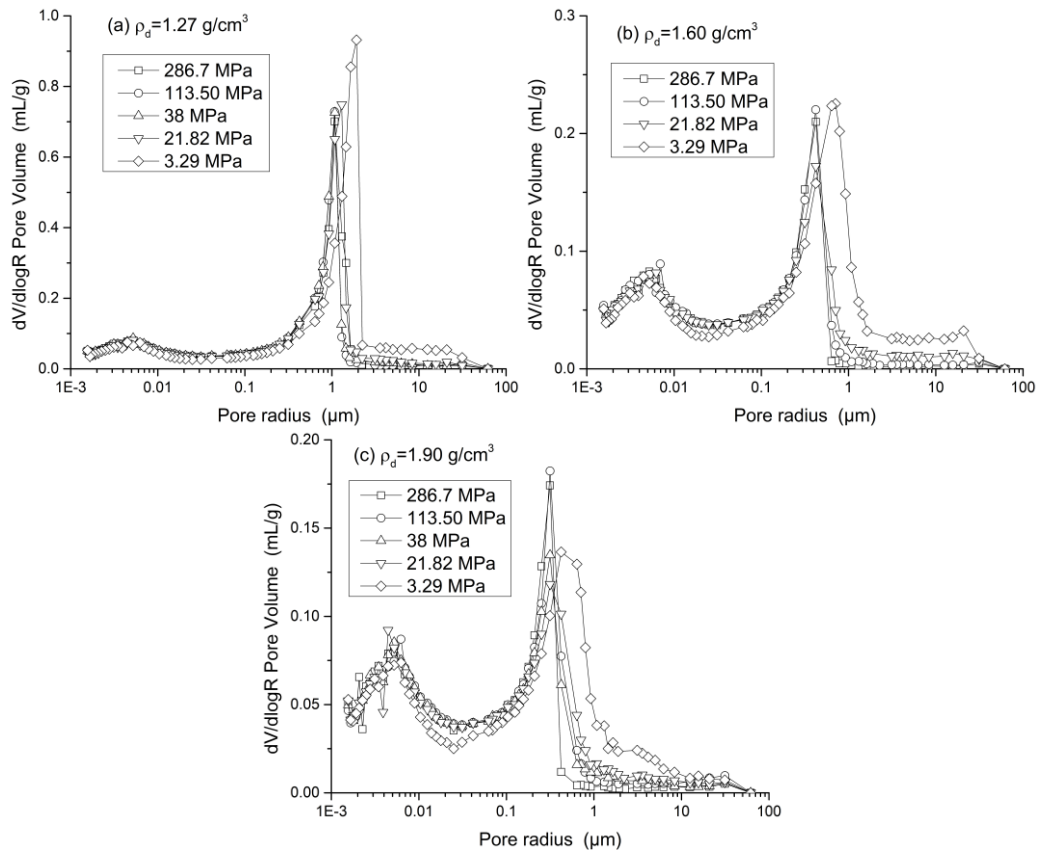


**Figure 3-30. Pore size density distribution curves of three different initial dry densities with different suction**

### 3.3.1.5. Environmental scanning electron microscopy

The environmental scanning electron microscopy (ESEM) was used to directly analyse the bentonite samples. The ESEM tests were performed using a Quanta 650 FEG scanning electron microscope at the Institute of Scientific Instruments of the Czech Academy of Sciences, Brno. The compacted samples with initial dry density of 1.27, 1.60 and 1.90  $\text{g}/\text{cm}^3$  were used for the ESEM observations. No cutting tool was used to prepare the sample surface; instead, following the procedures of Lin & Cerato (2014), the specimen was fractured in order to expose a fresh, undisturbed section of the sample. Figure 3-31 shows the microphotos of compacted bentonite with initial dry density of 1.27  $\text{g}/\text{cm}^3$  at various magnifications. Figure 3-31 (a) shows the general view of the studied sample. With the magnification increased, more detailed observation including distinct aggregates and the macropores between them can be performed (Figure 3-31 (c,d,e)). Figure 3-31 (g) and (h) show the micropores within the aggregates. Double structure pore system, which was identified on MIP distribution curves can be confirmed by direct observation.

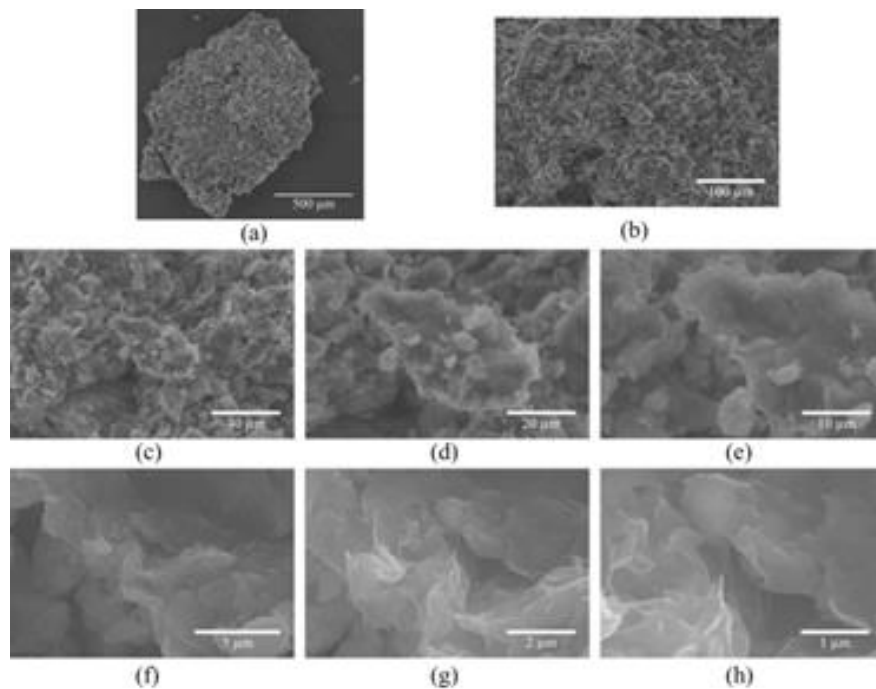


**Figure 3-31. Micro-photos of compacted bentonite ( $1.27 \text{ g/cm}^3$ ) with different magnification: (a) general view; (b) 1000x; (c) 2500x; (d) 5000x; (e) 10000x; (f) 25000x; (g) 50000x; (h) 100000x**

A series of ESEM observations was performed on the bentonite samples exposed to different relative humidity. The tests were carried out at constant temperature of  $3^\circ\text{C}$ ; the water vapor pressure was imposed directly in the ESEM chamber, which made it possible to observe directly the microstructure response to suction changes. From the water retention curves obtained on similar bentonite B75 (Sun et al., 2018) and the initial water content of the samples, the water vapor pressure of 559.8 Pa (corresponding to relative humidity of 73.9 % and suction of 38 MPa) was determined as the optimal initial state for the experiment. Two hydraulic paths were applied: drying-wetting-drying path (DWD) with suction path  $38 \rightarrow 287 \rightarrow 3 \rightarrow 38$  MPa, and wetting-drying-wetting path (WDW) with suctions  $38 \rightarrow 3 \rightarrow 287 \rightarrow 38$  MPa. A detailed plan of the imposed suction levels and test conditions is shown in Table 4. The interval between vapor pressure changes was 15 min. A similar interval was used also by other researchers (Montes-H, 2005; Lin & Cerato, 2014).

**Table 3-8. Water vapour pressure, relative humidity, total suction adopted in ESEM measurements**

Temperature = 3°C					
Drying-wetting-drying path (DWD)			Wetting-drying-wetting path (WDW)		
Relative humidity (%)	Water vapor pressure (Pa)	Total suction (MPa)	Relative humidity (%)	Water vapor pressure (Pa)	Total suction (MPa)
73.9	559.8	38.00	73.9	559.8	38.00
56.7	429.8	71.13	84.0	636.9	21.81
40.4	306.5	113.50	87.0	659.5	17.46
30.3	230.0	149.52	91.0	689.8	11.82
20.6	156.0	198.18	94.0	712.5	7.76
10.2	77.0	286.67	97.4	738.3	3.30
20.6	156.0	198.18	91.0	689.8	11.82
30.3	230.0	149.52	87.0	659.5	17.46
40.4	306.5	113.50	84.0	636.9	21.81
56.7	429.8	71.13	73.9	559.8	38.00
73.9	559.8	38.00	56.7	429.8	71.13
84.0	636.9	21.81	40.4	306.5	113.50
87.0	659.5	17.46	30.3	230.0	149.52
91.0	689.8	11.82	20.6	156.0	198.18
97.4	738.3	3.29	10.2	77.0	286.67
91.0	689.8	11.82	20.6	156.0	198.18
87.0	659.5	17.46	30.3	230.0	149.52
84.0	636.7	21.86	40.4	306.5	113.50
73.9	559.8	38.00	56.7	429.8	71.13
			73.9	559.8	38.00

Figure 3-32 show the example of low dry density samples exposed to wetting-drying-wetting path (WDW). During the first wetting path (Figure 3-32(a→f), (38→3.29 MPa)), the volume of aggregates slightly increased. Macropores remained dry, except of the lowest suction. At 3.29 MPa, water entered the macropores, which can be seen in Figure 3-32(f).

In order to quantitatively analyse the aggregates volume change upon WDW and DWD paths, the digital image analysis (Sun et al., 2019) was used to calculate volume strain of the selected aggregates. Figures 3-33 and 3-34 show the selected aggregates and their volume strain on both WDW and DWD paths respectively for low initial dry density. The volume strain shows a hysteretic behaviour between wetting/drying or drying/wetting path. The volume increased sharply near the lowest suction (3.29 MPa). This effect is caused by water, which entered the macropores and caused the aggregate boundaries to be less clearly defined in the photographs. In the higher suction range (>30 MPa), the volume strain shows a linear change with the suction and hysteretic loop appears to be quite narrow. At DWD paths, this linear slope is different for the four aggregates, but the difference is quite minor. At WDW paths, suction vs. volumetric strain relationship gives almost parallel lines for all studied aggregates (Figure 3-33). The aggregate volumetric response appears to be reversible with suction at higher values. The same results were obtained also for medium and high initial dry density samples.

**3.3.1.6. Conclusions**

Constant load swelling tests showed that initial compaction of bentonite has no effect on final void ratio. Further, loading-unloading cycles applied to selected samples after constant load swelling test indicate that application of high vertical load removed the effect of different initial compaction.

Water retention data showed similar results obtained from both constant volume and free swelling tests. Water content for the given suction is not affected by initial dry density. This is explained by distribution of water inside the bentonite structure. For the suctions higher than 3 MPa, water is concentrated in the micropores, which are only little influenced by compaction pressures. This conclusion was supported by MIP distribution curves and ESEM observations.

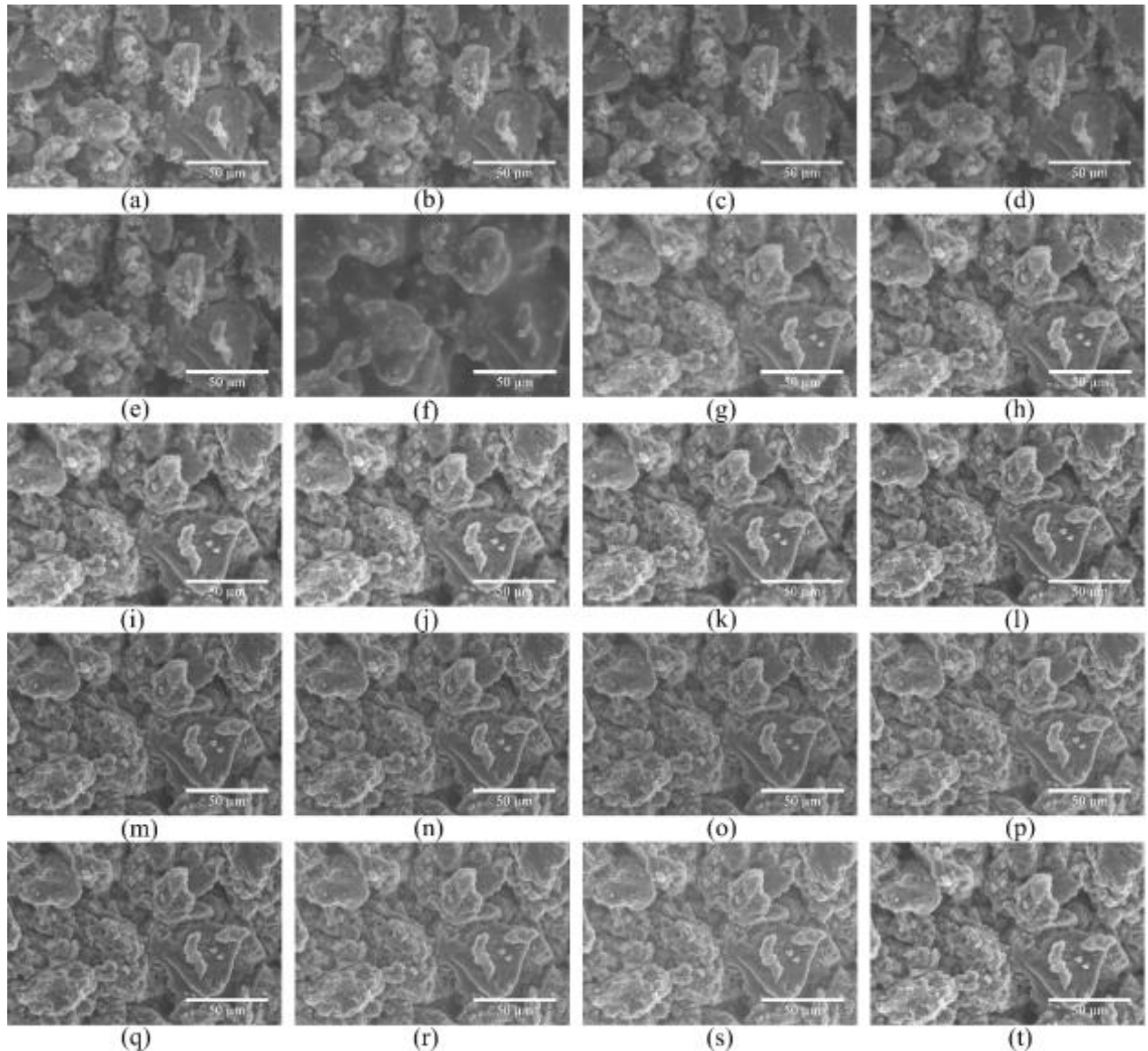


**Figure 3-32.2 ESEM microphotos of compacted bentonite with a dry density of  $1.27 \text{ g/cm}^3$  under the wetting–drying–wetting path (WDW): (a) 38 MPa; (b) 21.81 MPa; (c) 17.65 MPa; (d) 11.82 MPa; (e) 7.76 MPa; (f) 3.29 MPa; (g) 11.82 MPa; (h) 17.46 MPa; (i) 21.86 MPa; (j) 38 MPa; (k) 71.13 MPa; (l) 113.5 MPa; (m) 149.52 MPa; (n) 198.18 MPa; (o) 286.67 MPa; (p) 198.18 MPa; (q) 149.52 MPa; (r) 113.5 MPa; (s) 71.13 MPa; (t) 38 MPa**

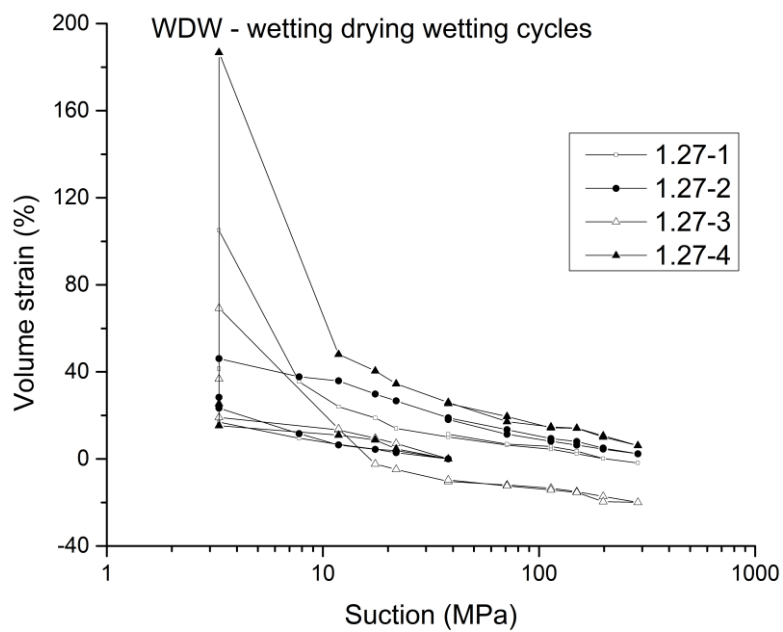
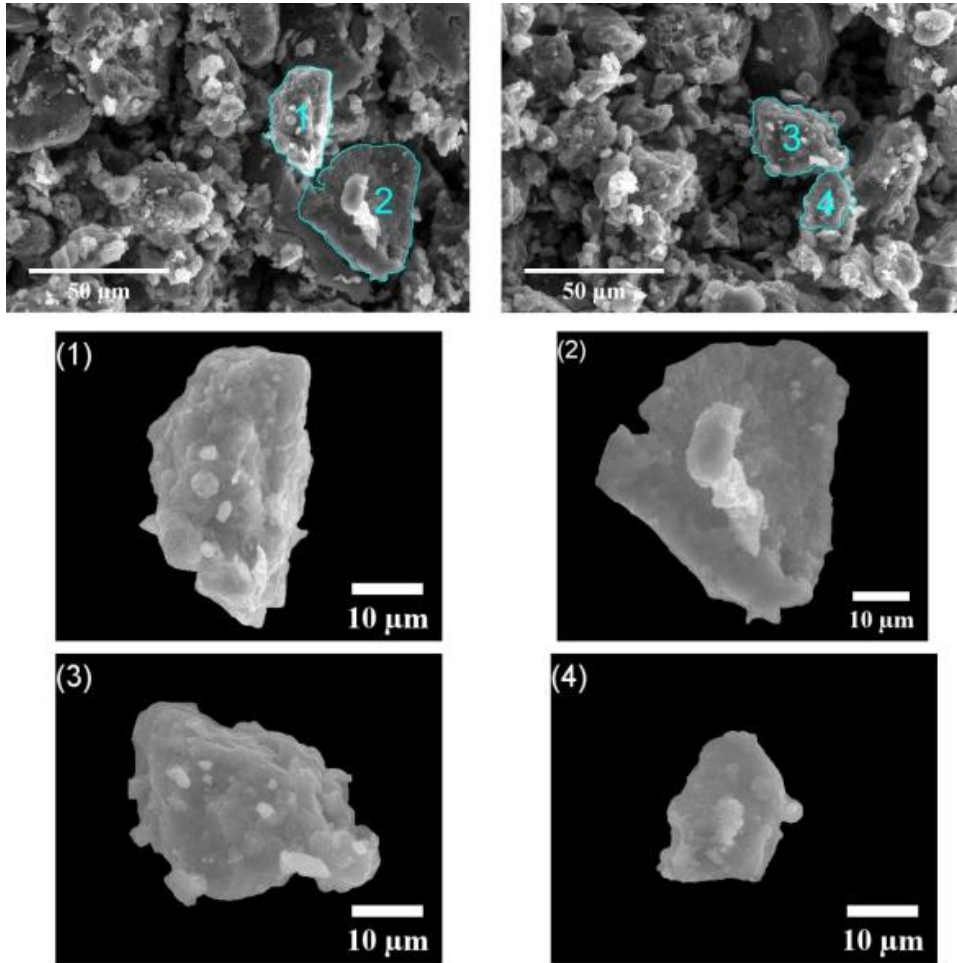


**Figure 3-33. Aggregates of the initial dry density 1.27 g/cm<sup>3</sup> samples selected for calculation of volume strain at wetting-drying-wetting path (WDW)**

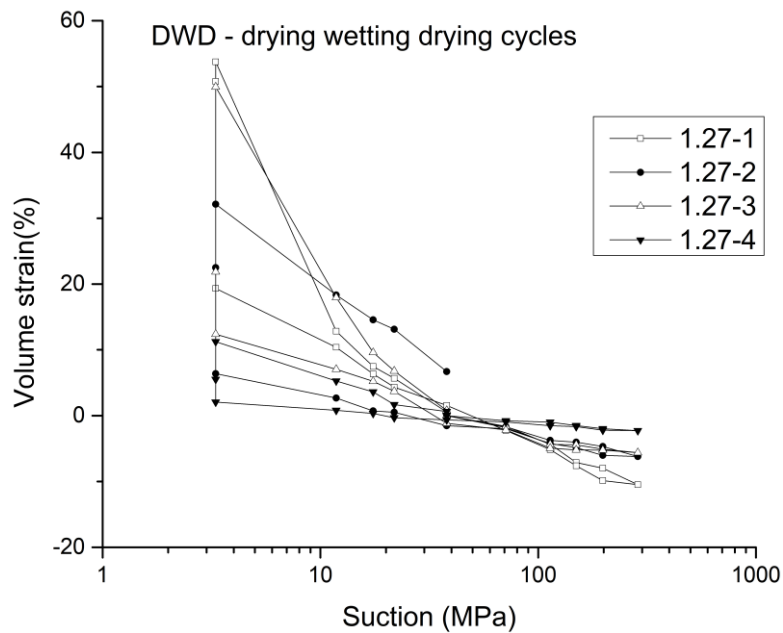
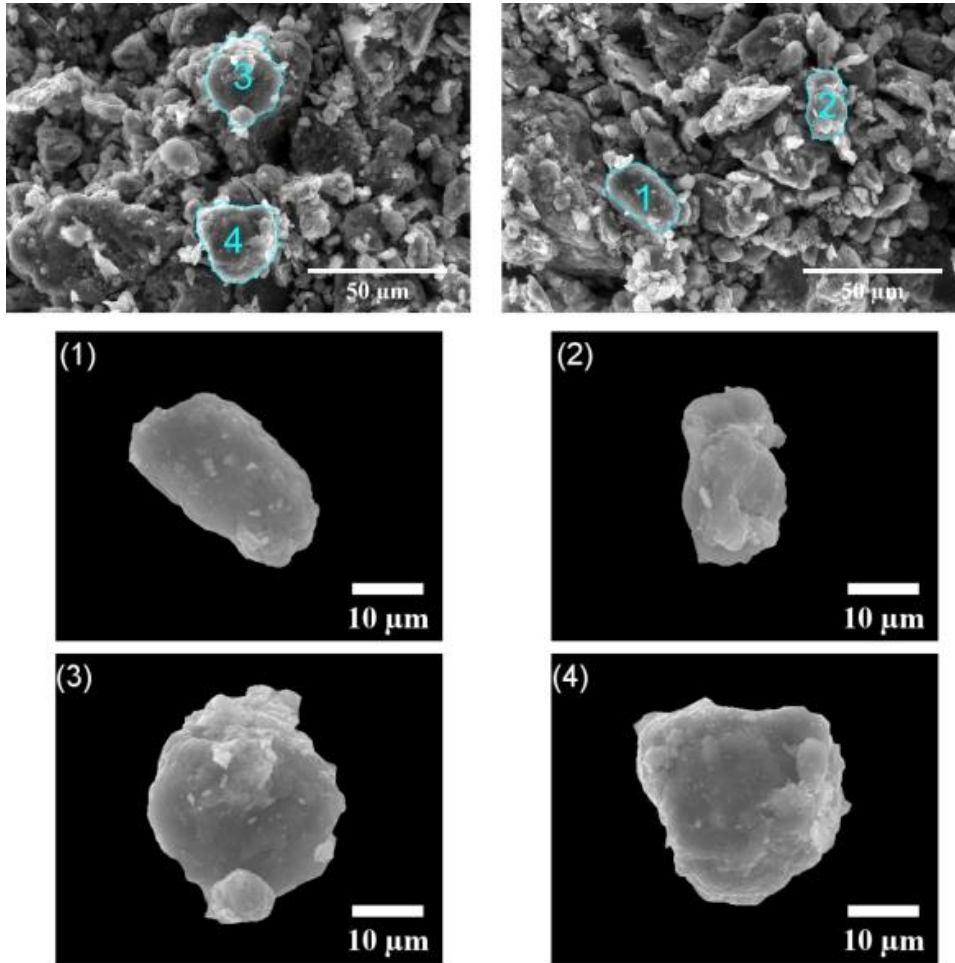


**Figure 3-34. Aggregates of the initial dry density 1.27 g/cm<sup>3</sup> samples selected for calculation of volume strain at drying-wetting-drying path (DWD)**

### 3.3.2 Constant volume tests in "MPC" cells (CU)

#### 3.3.2.1. Outline of the tests

The aim of the constant volume tests performed in MPC cells was to evaluate the homogenisation process of the samples composed of two bentonite layers compacted to different dry densities. The programme of the tests included four swelling pressure tests on homogeneous (single density) samples to determine behaviour of individual layers for later dual density tests. The single density samples were prepared in two individually compacted layers to keep a density profile as uniform as possible. Each layer was prepared from 36 grams of the bentonite powder of its original water content (approximately 11%).

Dual density tests included six experiments carried out on three pairs of different initial dry densities. The samples were prepared in the same way as single density samples with different compaction force for each sample layer. For each combination of dry densities, two tests were performed with different direction of saturation. The summary of the tests is presented in Table3-9.

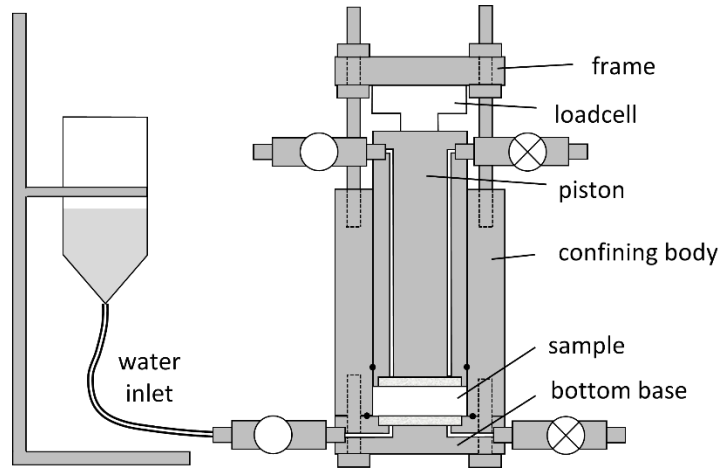
**Table 3-9. Summary of constant volume test performed in MPC cells**

Type of test	Initial dry density (g/cm <sup>3</sup> )	
	Top layer	Bottom layer (saturation base)
Single density tests:	1.3	1.3
	1.5	1.5
	1.7	1.7
	1.85	1.85
Dual density tests	1.7	1.3
	1.3	1.7
	1.85	1.3
	1.3	1.85
	1.85	1.5
	1.5	1.85

#### 3.3.2.2. Single density tests

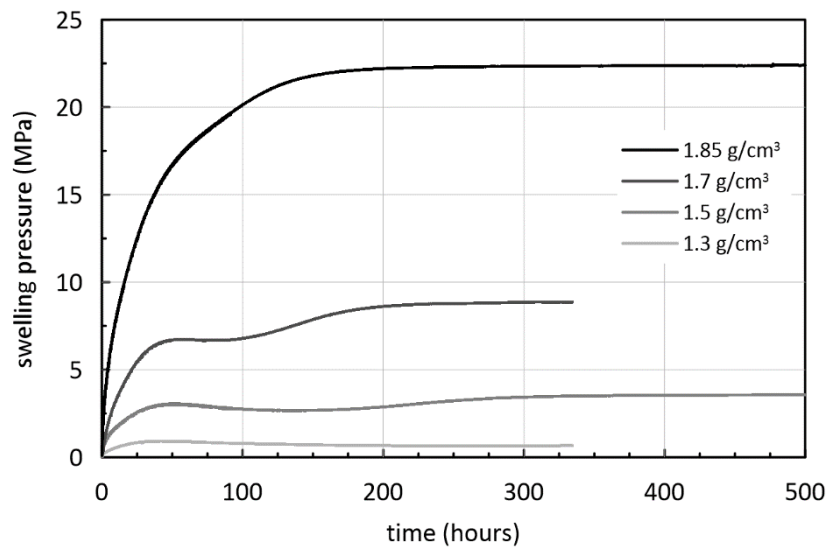
Single density tests were performed in stainless steel constant volume cells composed of a confining ring, lower base and piston, which was held in a fixed position by a rigid frame. A small loadcell was placed between the piston and the frame.

The metal porous plates connected to drainage lines were integrated into the bottom base and the piston allowing saturation of the sample. The bentonite sample of 50mm diameter was compacted directly to the cell. Total height of the samples varied in the range 18-26 mm based on initial dry density. The sample was saturated with distilled water through the bottom base. No water pressure was applied during saturation (test setup is presented in Figure 3-35). The increase of swelling pressure was monitored until constant value was reached.

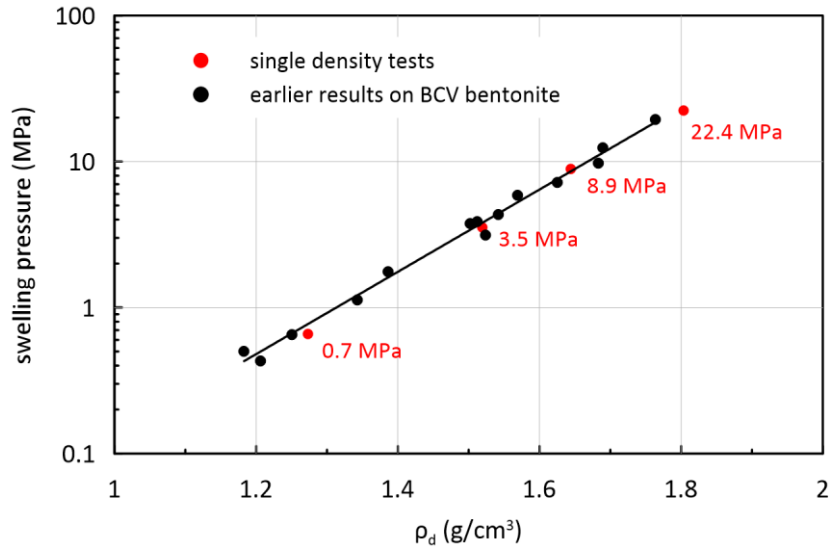


**Figure 3-35. Setup of MPC cells for swelling pressure measurement of single density samples**

The evolution of swelling pressures with time is presented in Figure 3-36. It shows that swelling pressure fully stabilised after approximately 300 hours. The final swelling pressures exhibit linear increase with initial dry density in semilogarithmic scale. Figure 3-37 shows the results of the single density tests in comparison with earlier BCV test results obtained for another research project. The comparison shows that the results follow the same trend and confirms consistency of the results.



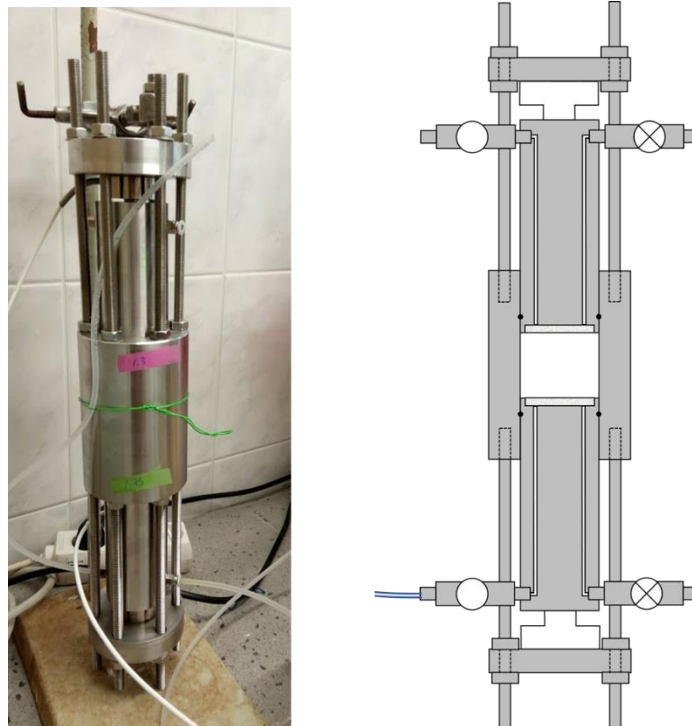
**Figure 3-36. Evolution of swelling pressure with time during single density tests**



**Figure 3-37** Dependency of swelling pressure on dry density

### 3.3.2.3. Dual density tests

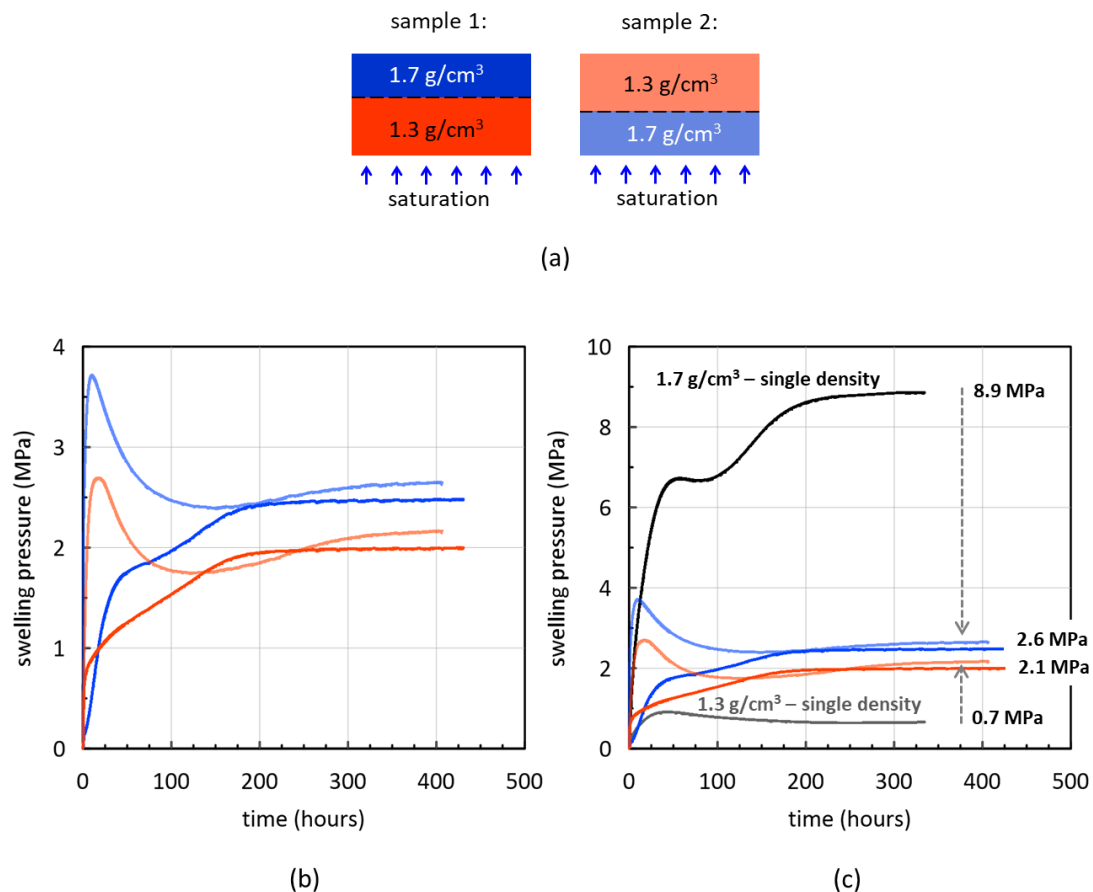
In dual density experiments, swelling pressure was monitored on both bases of the sample. Therefore, the setup of the MPC constant volume cell was modified. Bottom base was replaced by another piston held in its position by a rigid frame with another loadcell which resulted in a symmetrical arrangement of the cell (Figure 3-38).



**Figure 3-38.** Arrangement of MPC cells for dual density tests

The results of the dual density experiments combining initial dry densities 1.7 and 1.3 g/cm<sup>3</sup> are presented in Figure 3-39. Figure 3-39(a) shows sections of both samples with colours of individual layers corresponding to lines in Figures 3-39(b) and (c). The increase of swelling pressure with time was significantly different for both tested samples (Figure 3-39(b)). The sample 2, which was saturated from the high dry density base, exhibited rapid increase of swelling pressure on both bases in the initial phase of the saturation due to the high swelling potential of the high-density layer. As the saturation proceeded to the other layer, a homogenisation of the whole sample took place and swelling pressure on both bases decreased. Development of swelling pressures in sample 1, saturated from the low-density layer, is significantly slower with no peak on swelling pressure curves. It can be explained by swelling of the high-density layer during its saturation and resulting compression (densification) of the low-density layer, which was already saturated and behaved in a plastic and more deformable manner.

The swelling pressures reached steady values after approximately 400 hours in sample 2, while saturation of sample 1 was significantly faster (200 hours). This is associated with higher hydraulic conductivity of the sample's 1 bottom base, while the saturation base of sample 2 was less permeable.



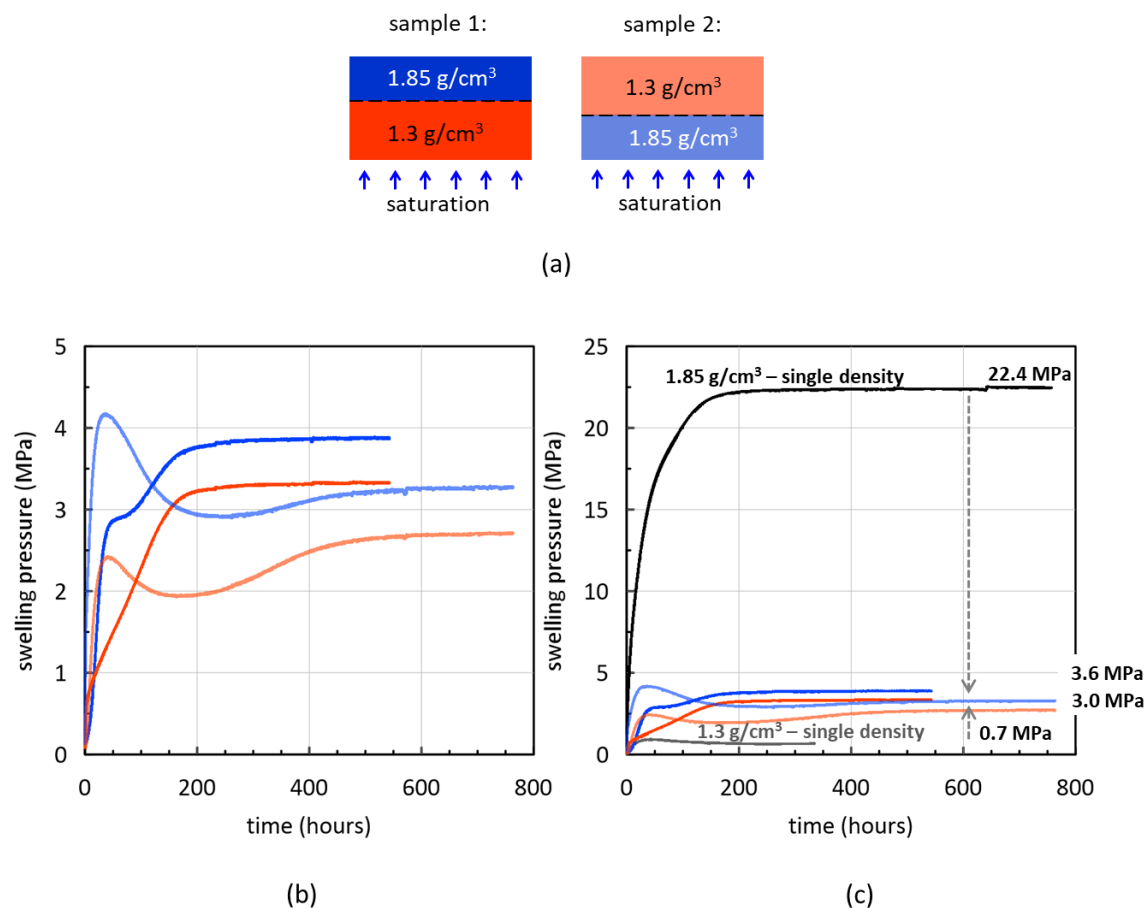
**Figure 3-39. Swelling pressures of dual density samples composed of layers with initial dry densities 1.3 and 1.7 g/cm<sup>3</sup>**

Figure 3-39(c) shows the comparison of swelling pressures with single density samples of dry densities 1.3 and 1.7 g/cm<sup>3</sup>, representing the behaviour of individual layers. This comparison demonstrates the homogenisation process inside dual density samples, which is represented

by dashed lines. It reveals that swelling pressures, which are 8.9 and 0.7 MPa for individual layers, reached 2.6 and 2.1 MPa on the respective bases of dual density samples. Thus, the measured difference is only 0.5 MPa. Despite significantly different evolution of swelling pressures in both dual density samples, the final values are almost identical for both tests. It indicates that direction of saturation has no effect on homogenisation and final swelling pressures.

Second set of dual density tests with layers of initial dry densities of 1.85 and 1.3 g/cm<sup>3</sup> is summarized in Figure 3-40. Time development of swelling pressures (Figure 3-40(b)) followed the trends described in Figure 3-39(b). Sample 2 exhibited a faster increase of swelling pressures followed by drop. The equilibration of swelling pressure took over 600 hours due to low hydraulic conductivity. Sample 1 stabilized faster despite a slower initial increase of swelling pressures. Final swelling pressures are slightly different for both samples, which may be due to small difference in initial dry densities of both samples. Nevertheless, the same final difference of swelling pressures between top and bottom base (0.6 MPa) was identified.

A comparison with single density samples (Figure 3-40(c)) demonstrates significant homogenisation of the samples during saturation and shows that the difference in final swelling pressure between both dual density samples is quite small in comparison with the swelling pressures of individual layers. Values 3.6 (3.0) MPa represents average final pressures on high (low) dry density base of both dual density samples.



**Figure 3-40. Swelling pressures of dual density samples composed of layers with initial dry densities 1.3 and 1.85 g/cm<sup>3</sup>**

The last set of dual density tests combined layers of initial dry densities of 1.85 and 1.5 g/cm<sup>3</sup>. The results are presented in Figure 3-41. Final swelling pressures of both samples differed by 0.8 MPa on the lower base and 1.2 MPa on the upper base. Difference between both bases of the same sample reached 1.2 MPa for sample 1 and 0.8 MPa for sample 2 with an average difference of 1 MPa (Figure 3-41(c)). However, despite the biggest measured difference in comparison of all three sets of samples, the results indicate a significant degree of homogenisation.

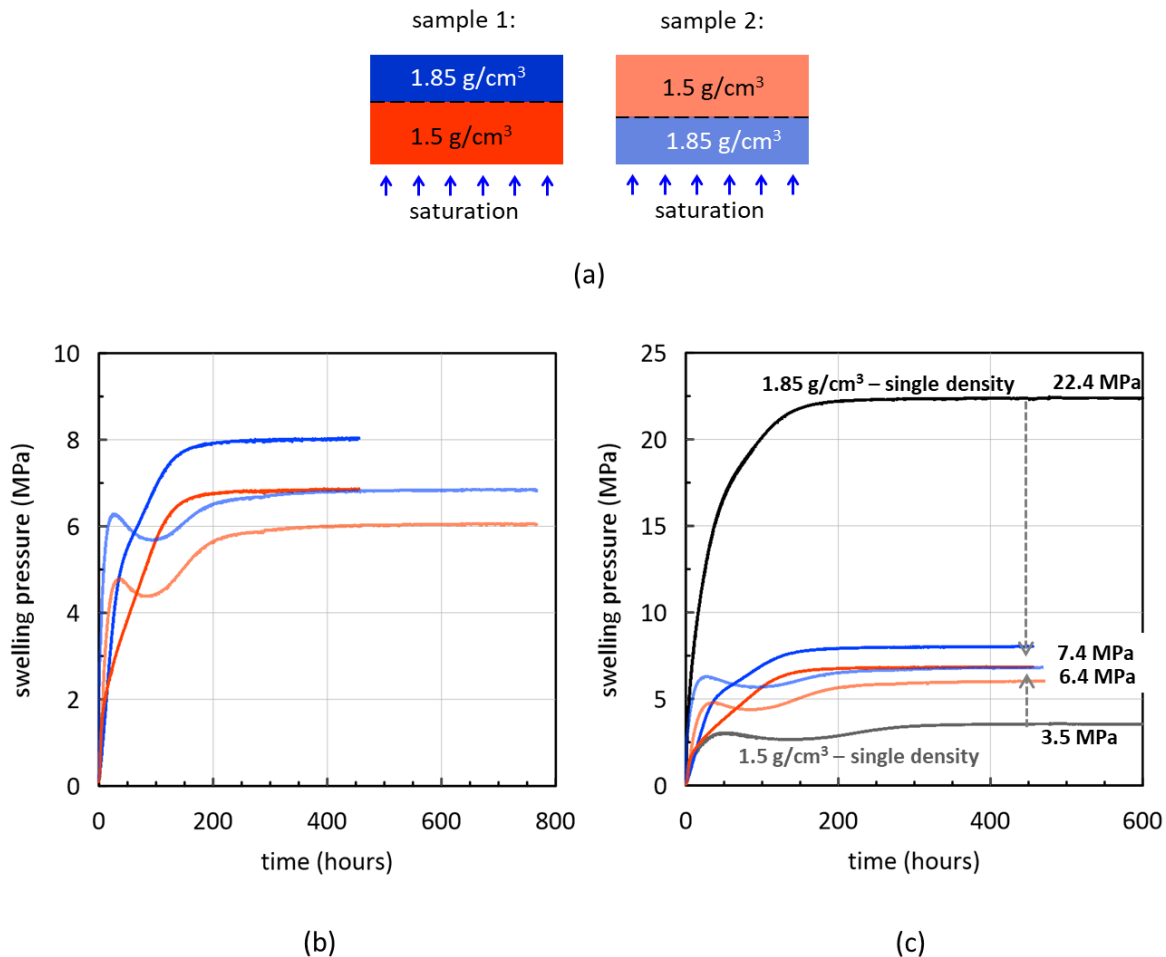


**Figure 3-41. Swelling pressures of dual density samples composed of layers with initial dry densities 1.5 and 1.85 g/cm<sup>3</sup>**

The study of the homogenisation process was supported by direct measurement of final density profiles of selected dual density samples. Both samples with 1.3 and 1.75 g/cm<sup>3</sup> layers were carefully extracted from MPC cells and cut to approximately 3 mm thick slices parallel to sample bases. Dry density profiles of the samples were calculated from measured water content with the assumption that samples reached full saturation. The layers, which were in contact with the saturation base, were affected by suction of water from porous stones during dismantling of the cells and swelled. Therefore, the outer layers were excluded from the analysis.

Both samples gave quite consistent dry density profiles as shown in Figure 3-42. Black lines represent the initial state before saturation and indicate significant homogenisation with the maximum difference of approximately 0.1 g/cm<sup>3</sup> between top and bottom base. Further, the dry density profiles indicate a gradual change over the sample's height with no distinct border between both layers.

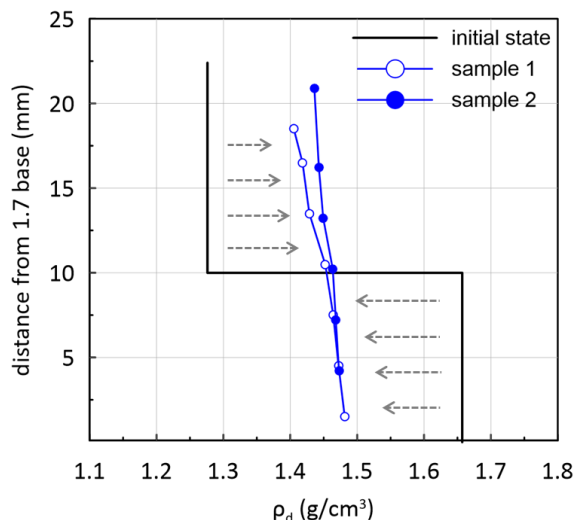


**Figure 3-42. Distribution of final dry densities in both samples with 1.3 / 1.7 g/cm<sup>3</sup> initial dry densities**

### 3.3.2.4. Conclusions

Three sets of dual density experiments, each combining two different initial dry densities, were carried out. Within each set, two identical samples were tested with different directions of saturation.

The measurement of swelling pressures showed a different evolution of swelling pressures based on the direction of saturation. A faster increase of swelling pressures followed by drop was observed on samples saturated from the high-density bases. Samples saturated from the low-density bases reached stable values faster due to higher hydraulic conductivity of the bottom layer, despite slower initial development of swelling pressures. However, both samples tested within each set reached similar final swelling pressures and no major influence of different development of swelling pressures was identified.

A significant homogenisation was observed in all dual density samples compared to swelling pressures of the individual layers. Average final differences for all three sets reached 0.5, 0.6 and 1.0 MPa, while differences in swelling pressures of the original layers tested within each set were 8.2, 21.7 and 18.9 MPa, respectively. A study of homogenisation in vertical profile was carried out by direct determination of dry density in vertical profile on selected set of samples. The results gave consistent dry density profiles with maximum difference of 0.1 g/cm<sup>3</sup> on both bases and indicate a gradual trend across the samples.

A considerable degree of homogenisation was observed in all experiments. The small final inhomogeneities may be partially attributed to the boundary conditions, especially wall friction, during the homogenisation process.

### 3.3.3 Constant volume tests (CTU)

Total pressure evolution, hydraulic conductivity (water flow), saturation evolution and final density (density changes) & water content distribution were investigated in constant volume cell apparatus. The aim was to obtain calibration data for mathematical model development.

The apparatus consists of cylinder with compressed argon, pressure regulator, gas water exchanger, flow meter and test cell (Figure 3-43). In the test cell the sample is on circumference confined into solid steel ring and at the top bottom by permeable plates from sintered steel. Bottom plate is fixed by steel support and top plate is supported by free floating piston. Other side of piston is fixed via force transducer (total pressure measurement) in fixed steel plate. Water is injected through the bottom permeable plate and collected via piston.

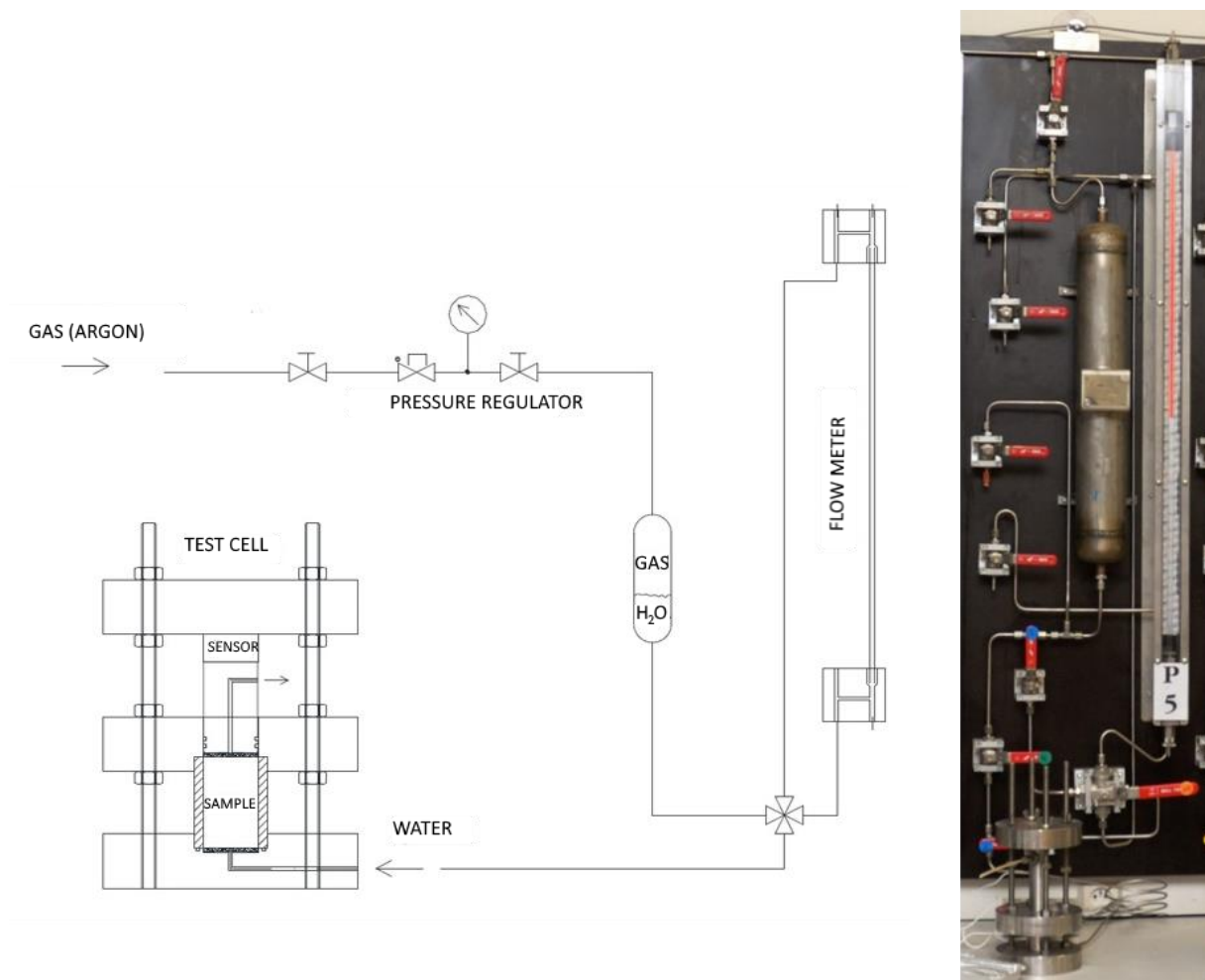


**Figure 3-43. Constant volume test apparatus**

The tests were performed on B75 a BCV material (Hausmannová et al., 2018). Both materials are Czech bentonites produced by Keramost a.s. with similar composition and properties. The switch from B75 (used initially) to BCV ("new" material) was made due to BCV selection new research reference material for Czech programme.

Three types of samples were investigated – homogenous samples from compacted powder bentonite, dual density samples (stack of two half height samples on top of each other with different density) and pellets. If not mentioned otherwise the total sample height was 20 mm and diameter 30 mm with exception for pellets where diameter 120 mm was used for some of the test to accommodate for larger grains.

The exact height and weight of the samples were determined via measurement and weighing following the completion of the sample preparation stage. The initial water content was determined before the preparation of the samples via the gravimetric method using the same material.

The test procedure was as follows:

1. Samples were compacted into permeameter ring
2. Test apparatus was assembled and zero measurement recorded
3. Water was injected into sample and test begun. If water was freely flowing through the sample (typical for pellets) saturation was temporarily turned off
4. Samples were continuously (or in pulses for leaking samples) saturated by water pressure ~1 MPa. Evolution of total pressure, flow and temperature was recorded
5. Once total pressure and hydraulic conductivity were stabilised the saturation was turned off
6. Once total pressure was stabilised (no saturation pressure → swelling pressure can be determined) the test was terminated and disassembled.
7. Water content and dry density of sample was determined. Selected samples were sliced perpendicular to vertical axis when pushed out from ring. Slices were used to determine water content and rough estimated of density (exact volume of the slice could not be controlled/measured therefore the estimate is quite imprecise)

The following tests in constant volume cells were carried out:

- Homogenous samples
  - Material B75
    - Standard test - top only measurement of total pressure – 4 tests
    - Influence of temperature (20/60/20 °C) – 3 tests
  - Material BCV
    - Standard test - top only measurement of total pressure – 3 tests
    - Standard test - top and bottom measurement of total pressure – 4 tests
    - Saturation development – 5 tests
- Dual density samples
  - Material B75
    - Standard test & slicing - top only measurement of total pressure – 2 tests
  - Material BCV
    - Standard test & slicing - top only measurement of total pressure – 2 tests
- Pellets
  - Material BCV\_PM2018
    - Standard test - top only measurement of total pressure – 3 tests
    - Standard test - top and bottom measurement of total pressure – 1 test
  - Material BCV\_PM2019
    - Standard test - top only measurement of total pressure – 2 tests
    - Standard test - top and bottom measurement of total pressure – 3 tests

### 3.3.3.1. Homogenous samples

Both materials (B75 and BCV) were tested in homogenous form. Four tests were performed on compacted B75 powder. The samples were compacted directly into test rings with no additional processing. Dry density of samples was 1300 – 1762 kg/m<sup>3</sup>. Evolution of total pressure and estimated hydraulic conductivity is shown in Figure 3-44.

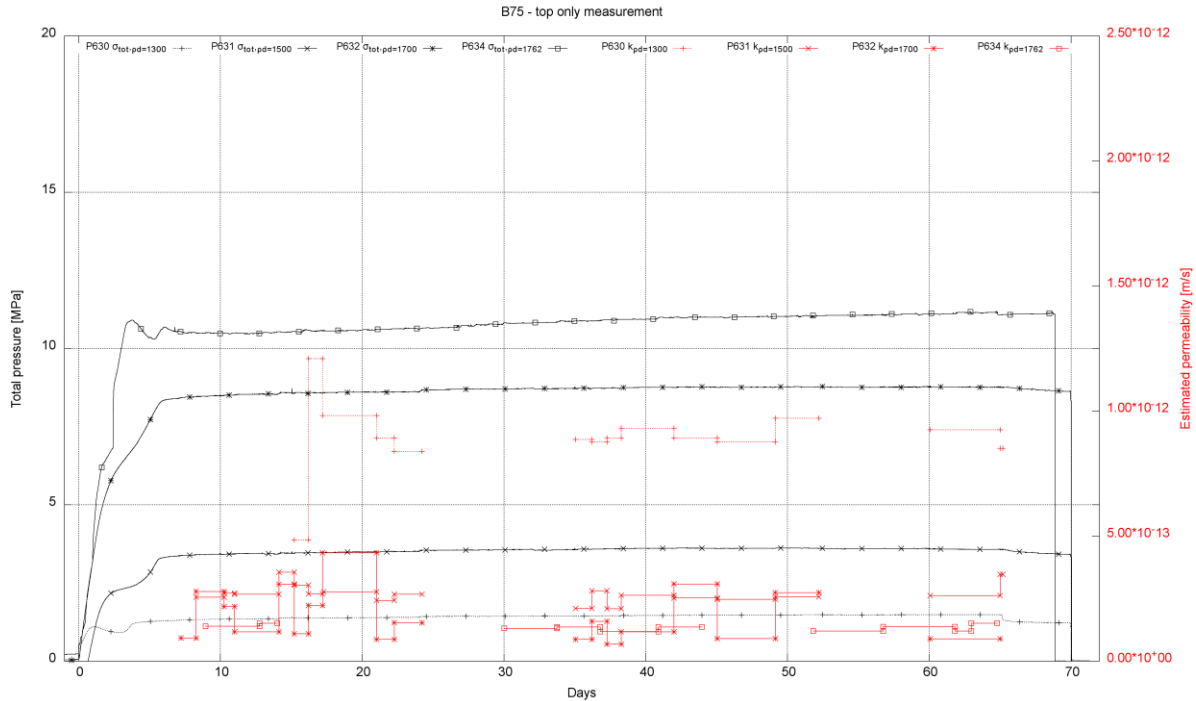


**Figure3-44. B75 homogenous samples (top only measurement)**

Three additional samples of B75 (dry density 1300-1800 kg/m<sup>3</sup>) were used to investigate the influence of temperature on total pressure and hydraulic conductivity evolution. Test begun at laboratory temperature (approx. 20 °C) with forced saturation phase followed by saturation shut off. After 6 months test cells were placed into 60 °C until hydraulic conductivity stabilised. At last the samples were moved back to laboratory temperature. The results (Figure 3-45) show that change of temperature has effect on hydraulic conductivity but after sufficient time the hydraulic conductivity stabilises at the same level as before temperature change.

BCV material was investigated more thoroughly. The standard top only measurement of total pressure was for selected samples altered into top & bottom measurement by adding bottom piston and transducer. Results of standard method for samples of dry density 1250, 1500 and 1900 kg/m<sup>3</sup> are shown in Figure 3-46.

Following the discussion at the internal WP4 workshop top and bottom measurement of total pressure was performed for four samples of dry density 1350, 1525, 1580 and 1750 kg/m<sup>3</sup>. Results (Figure 3-47) show that there is indeed difference in total pressure evolution on both sides of sample and it should be considered while developing the model.

By request from modelling team a temporal evolution of saturation was investigated. Series of samples with dry density of 1600 kg/m<sup>3</sup> was saturated and in predetermined intervals dismantling has been performed. During dismantling the sample was sliced into pieces approximately 2 mm thin and water content of each slice was determined by gravimetric method. Figure 3-48 shows saturation development over time.

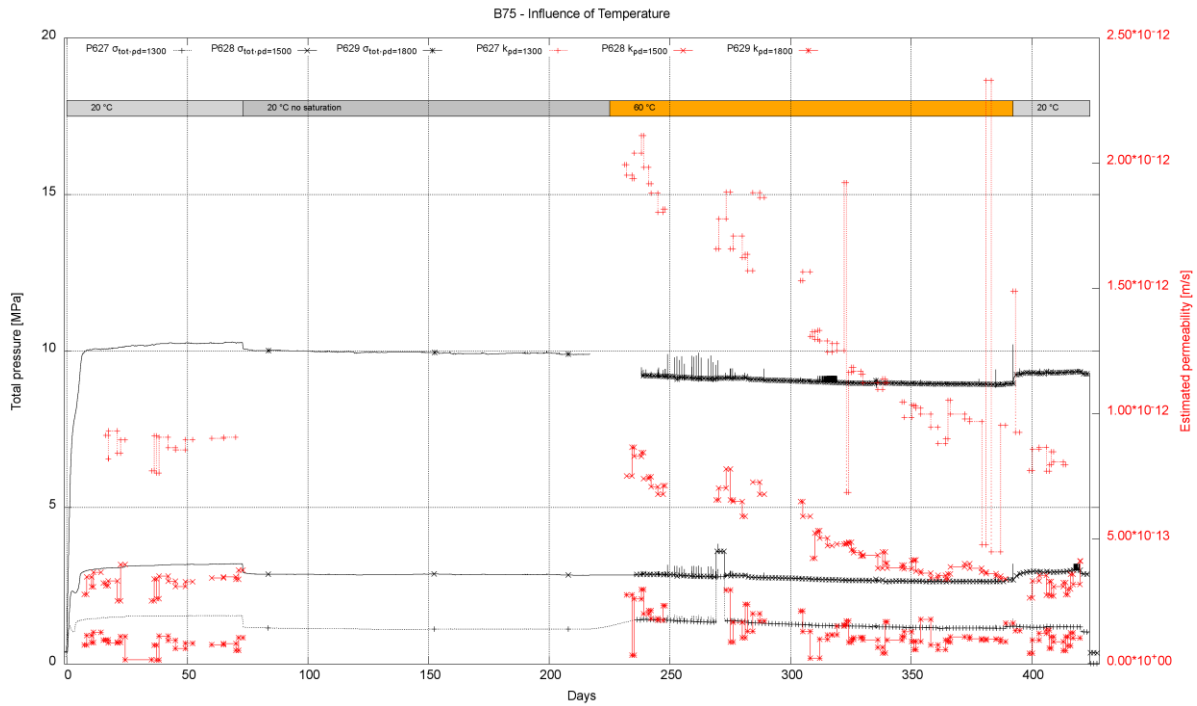


**Figure 3-45. B75 Influence of temperature**

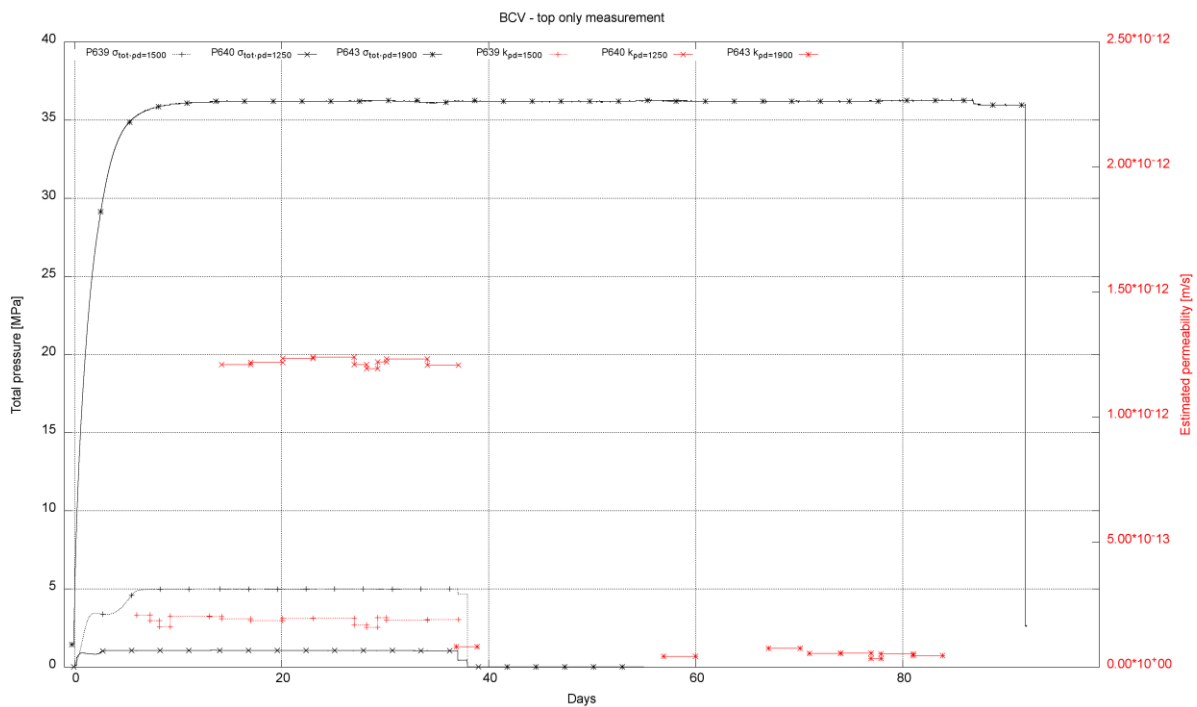


**Figure 3-46. BCV homogenous samples (top only measurement)**

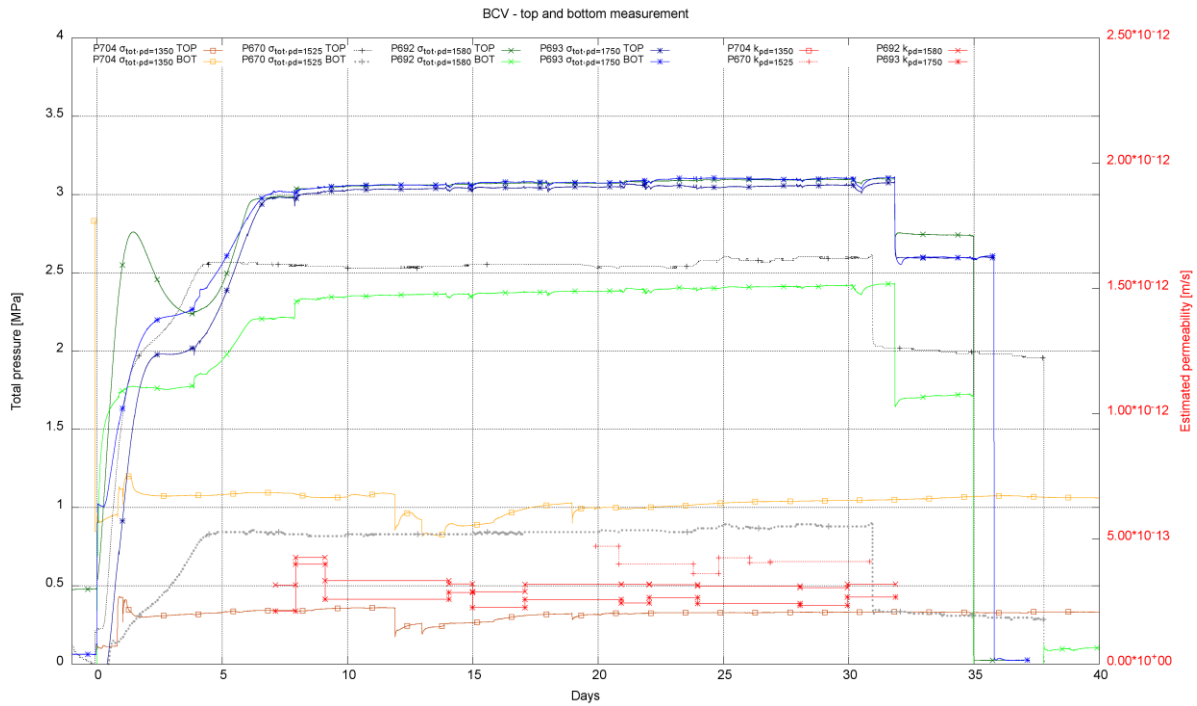


**Figure 3-47. BCV homogenous samples (top & bottom measurement)**

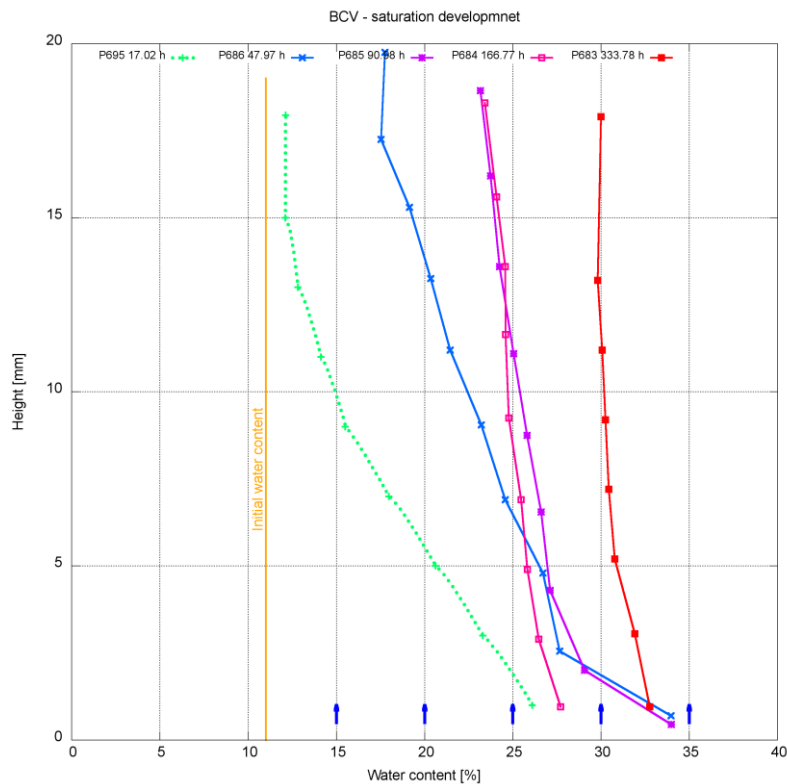


**Figure 3-48. BCV Saturation development**

### 3.3.3.2. Dual density samples

Density distribution changes have been investigated for BCV a B75 using dual density samples. In these test lower and upper part (half) of the sample had different initial dry density. The overall dimensions were same as for homogeneous samples. After the test was finished the sample was always sliced and water content distribution determined. At the same time dry density has been determined however due to irregular size of the slice its value is only indicative (more precise value of density can be calculated from water content/density at full saturation curve).

For each material two samples were tested. One sample with higher density in the upper part and the other in lower part. This allowed to observe the influence of flow direction in the cell. Results for B75 are shown in Figure 3-49 and for BCV in Figure 3-50. The results show that significant difference for each density configuration. When the low-density part is at the top there are significant changes in density distribution. This is probably caused by highly compacted part compressing the lower density part – the high-density parts get access to the water first and starts swelling thus compacting still dry lower density part (moreover the water pressure gradient helps the compression). On the contrary when lower density part is at the bottom it swells first and resists compression from upper part which starts to swell later (moreover the water pressure gradient helps the prevent compression of lower density layer).

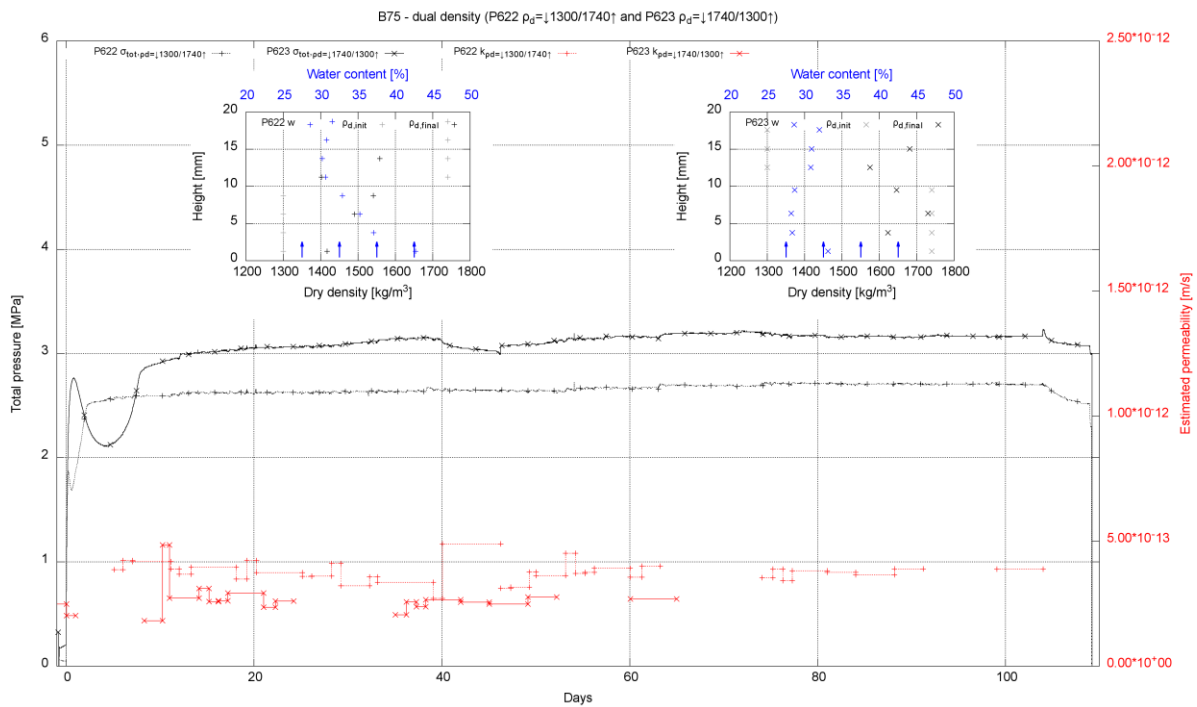


**Figure 3-49. B75 dual density samples**

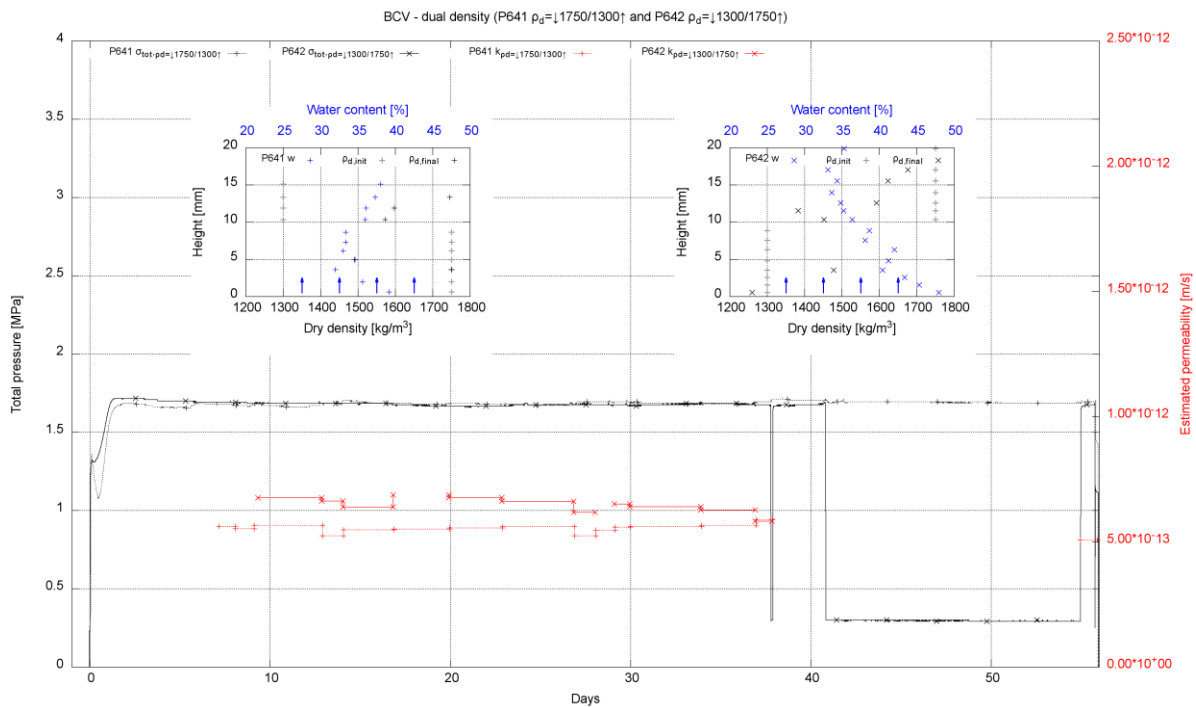


**Figure 3-50. BCV dual density samples**

### 3.3.3.3. Pellets

BCV pellets (Figure 3-51) were investigated in standard 30 mm diameter cells and in larger e.g. 120 mm diameter cells. For smaller cells fraction bellow 6 mm was used, for 120 mm cells no sieving was necessary.



**Figure 3-51. BCV pellets**

Test procedure for the pellets had to be modified for some samples. At the beginning of the test the saturation cannot be continuous due to voids between pellets. These voids create continuous pathway for water flow causing high water flow through the sample. Therefore, initially the water is introduced to the sample and then shut off (several times if necessary). This can be observed on fluctuation of total pressure. Once the major voids are closed full water gradient is applied and hydraulic conductivity is measured on periodic basis.

Two pelletized material were investigated. Both are based on BCV material. First marked as BCV 2018 is produced by roller compactor followed by crusher. The second one marked as BCV PM 2019 is of same produce but only fraction of grain size bellow 6 mm is always used in tests.

Results for top only measurement (small and big cells) of BCV 2018 is shown in Figure 3-52. Based on results of discussion at WP workshop top and bottom measurement of total pressure was carried out for one sample. Results are shown in Figure 3-53. Equivalent results for BCV 2019 are shown in Figure 3-54 and Figure 3-55. Samples from top & bottom measurement were sliced after the test in same manner as in temporal investigation of saturation.

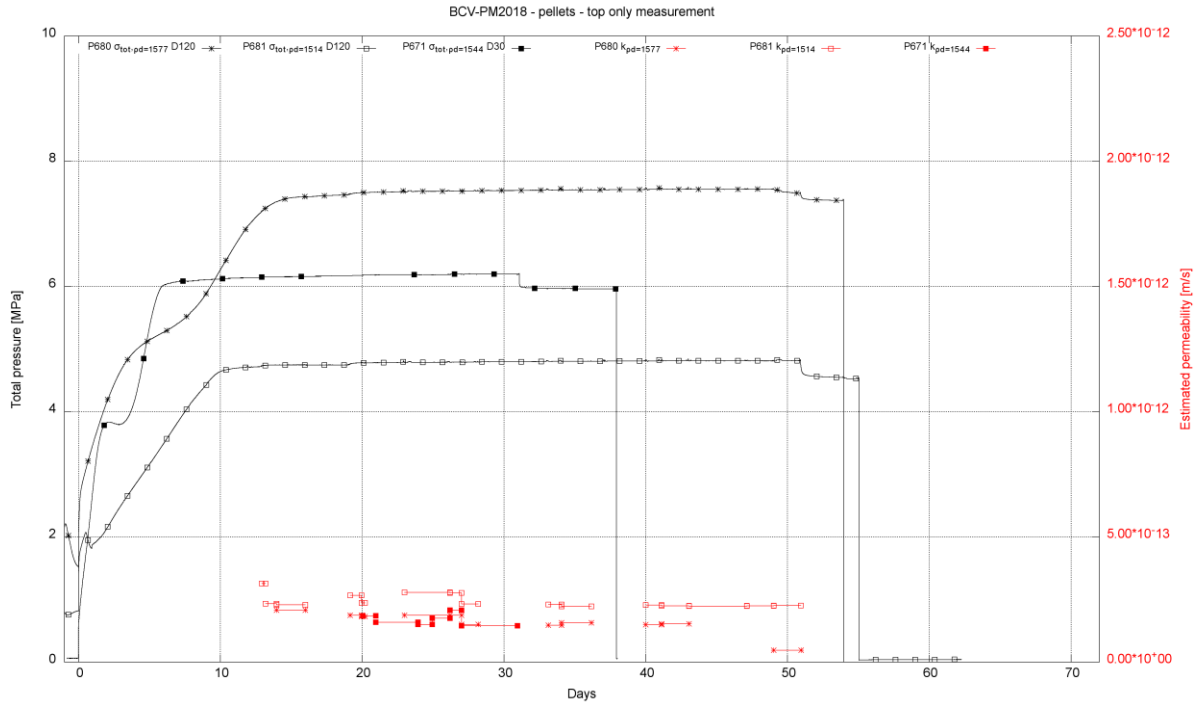


**Figure 3-52. BCV PM 2018 pellets (top only measurement)**

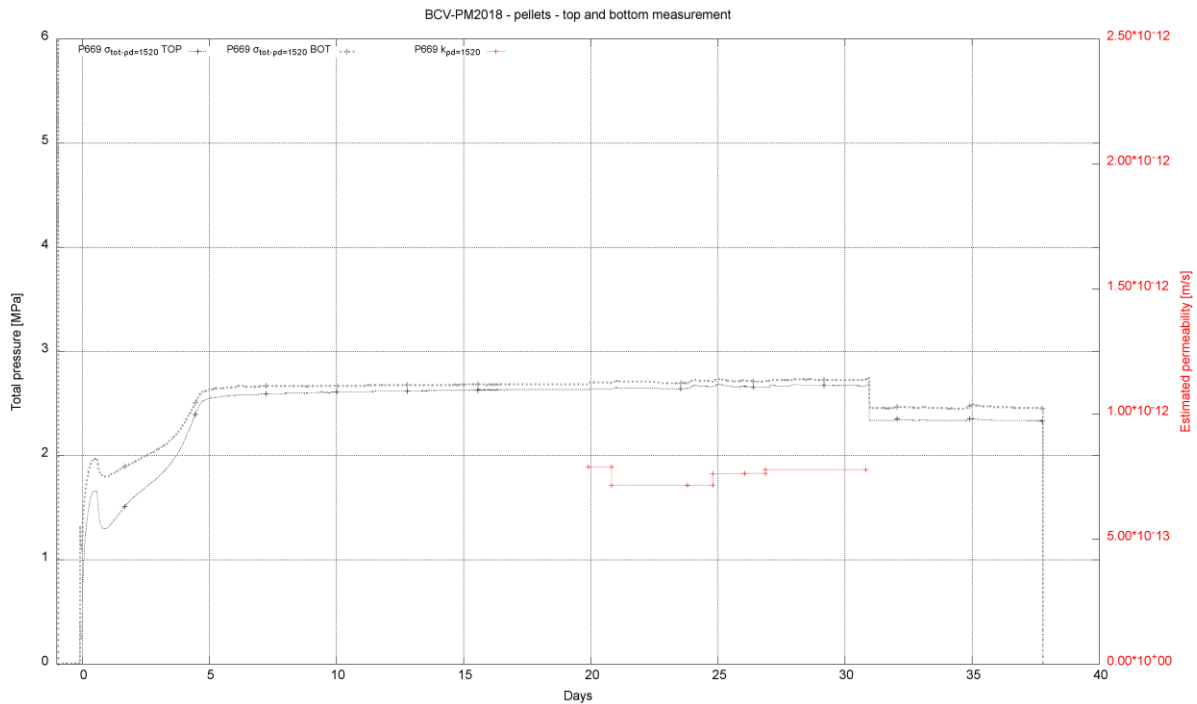


**Figure 3-53. BCV PM 2018 pellets (top & bottom measurement)**

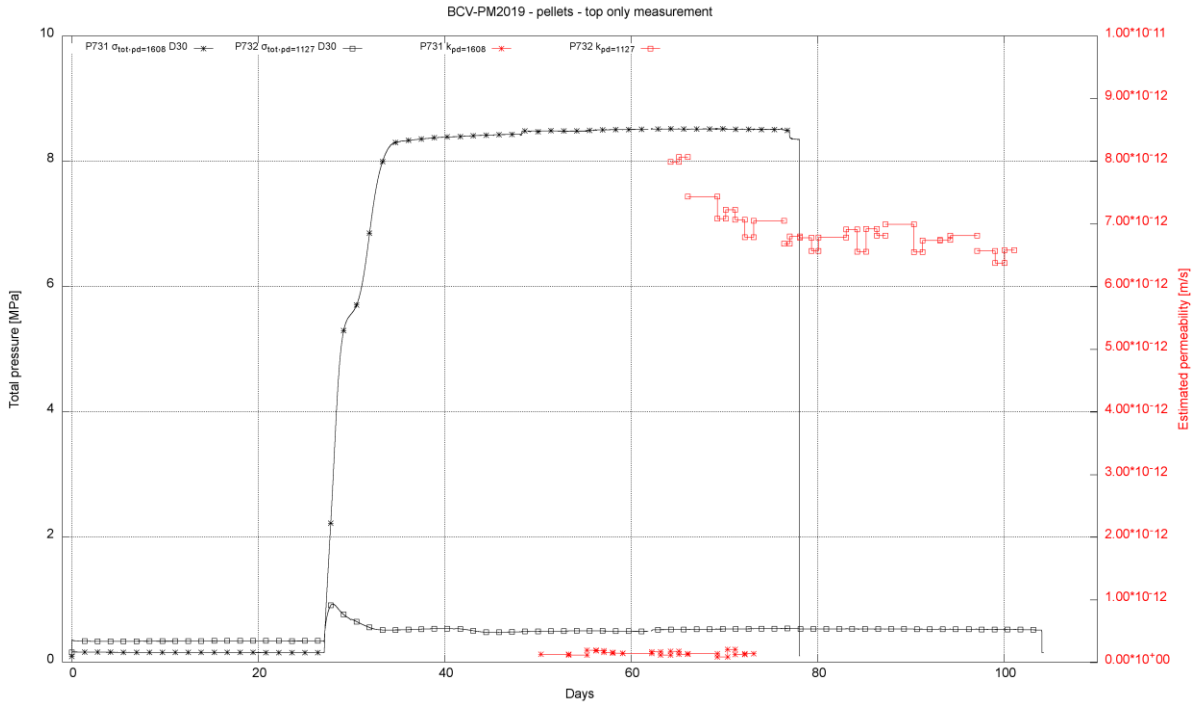


Figure 3-54. BCV PM 2019 pellets (top only measurement)

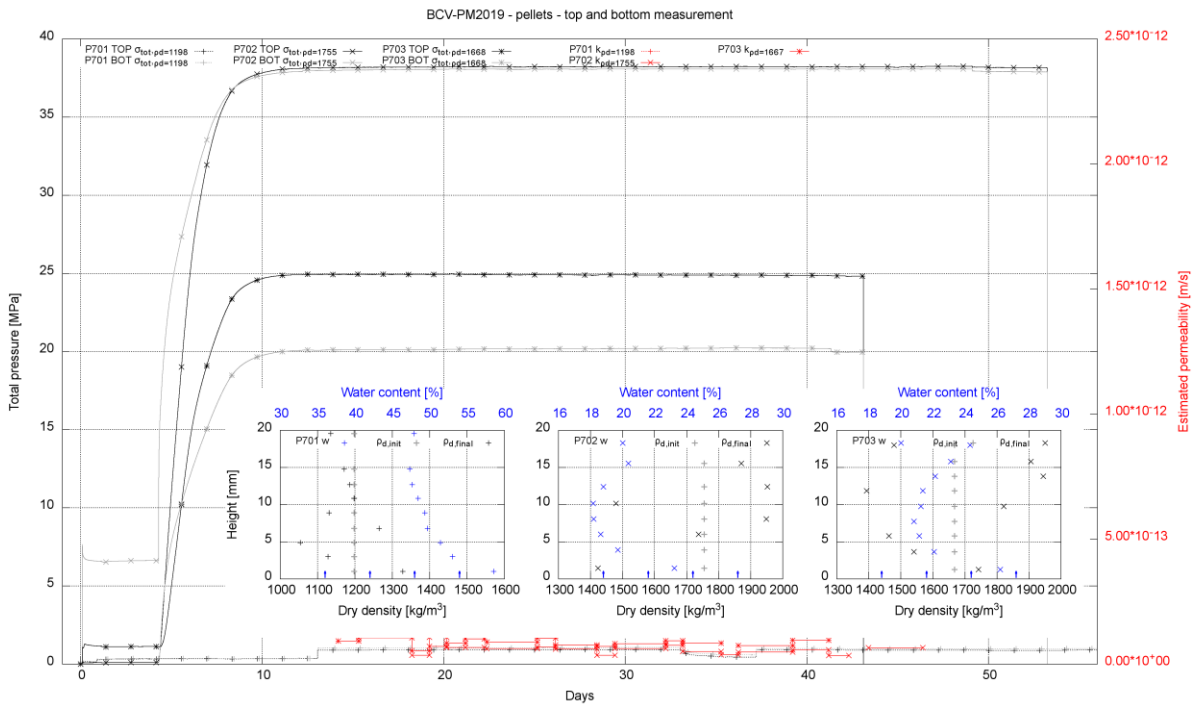


Figure 3-55. BCV PM 2019 pellets (top & bottom measurement)

### 3.3.4 Stress path investigation (CTU)

A stress path and saturation dependence of BCV mechanical behaviour has been investigated in oedometric cells. The intent of the research is to investigate typical load and saturation scenario in order to obtain data for mathematical model calibration and verification.

The BCV samples of various initial densities were fitted into oedometric ring of diameter 120 mm. Typically initial sample height 30 mm was used. The test was pressure controlled with free movement (deformation) along vertical axis (Figure 3-56). The pressure was stepwisely amended with each step taking up to 3 months until deformation was stabilised. Water was introduced at predefined stage.

Three scenarios were investigated:

- Scenario I - Saturation first (without load) than stepwise loading and unloading
- Scenario II - Dry material step wisely loaded than unloaded. Saturated without load and step wisely loaded + unloaded
- Scenario III - Dry material stepwisely loaded than saturated at full load and stepwisely unloaded + loaded

Both BCV (compacted) powder and pellets were investigated.

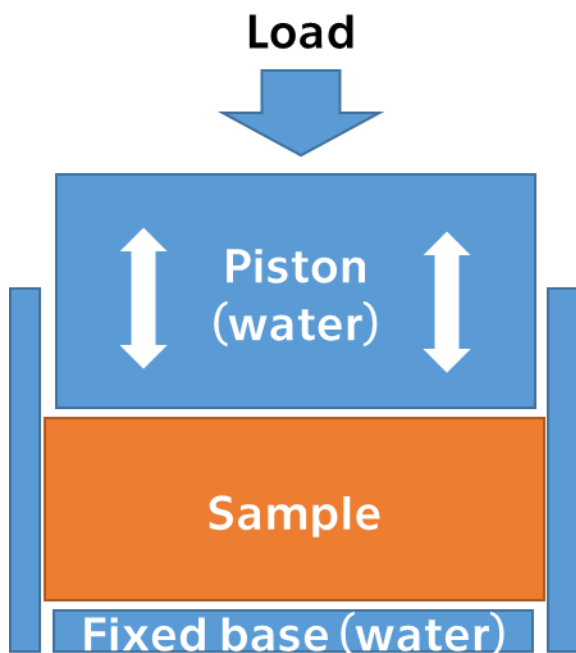


**Figure 3-56. BCV oedometric setup**

#### 3.3.4.1. Homogenous samples

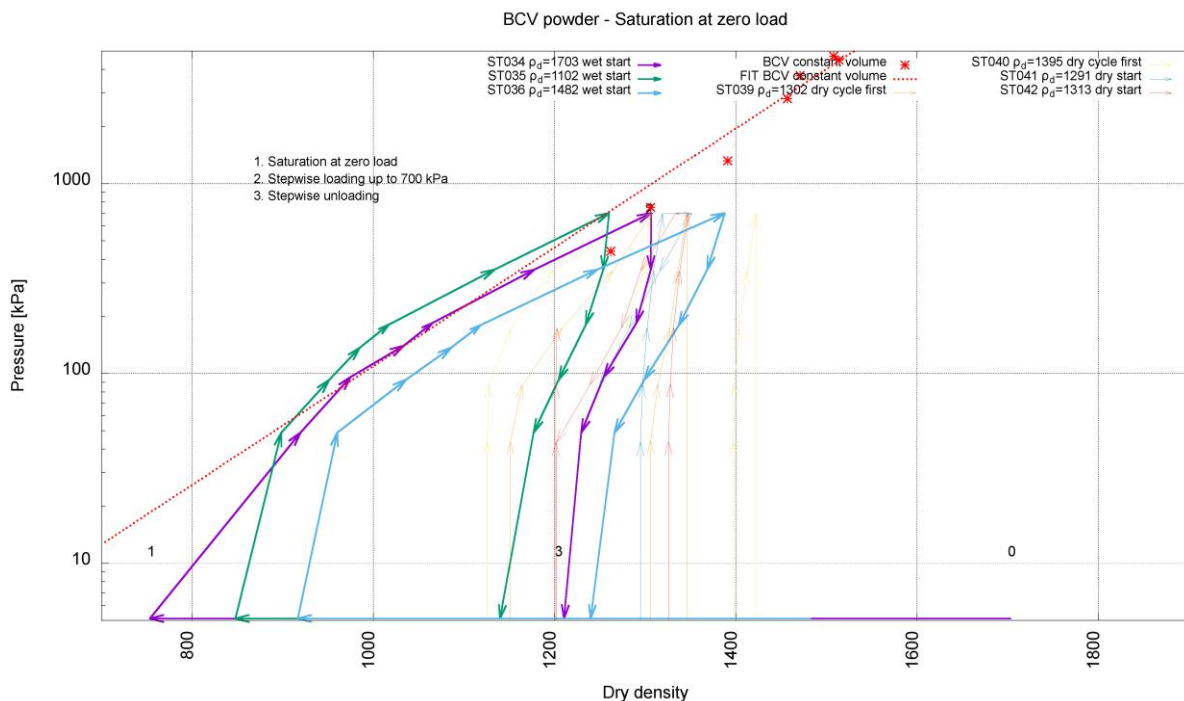
All 3 scenarios have been investigated on (compacted) powder material. The samples ranged dry density from 1102 kg/m<sup>3</sup> to 1703 kg/m<sup>3</sup>.

Figure 3-57 shows results from Scenario I. The initial dry density of samples was 1102, 1482 and 1703 kg/m<sup>3</sup>. The behaviour of samples is very similar regardless the initial dry density. There is clear stress path dependence as the dry density during unloading phase is much higher than the dry density reached during the initial free swelling during saturation.

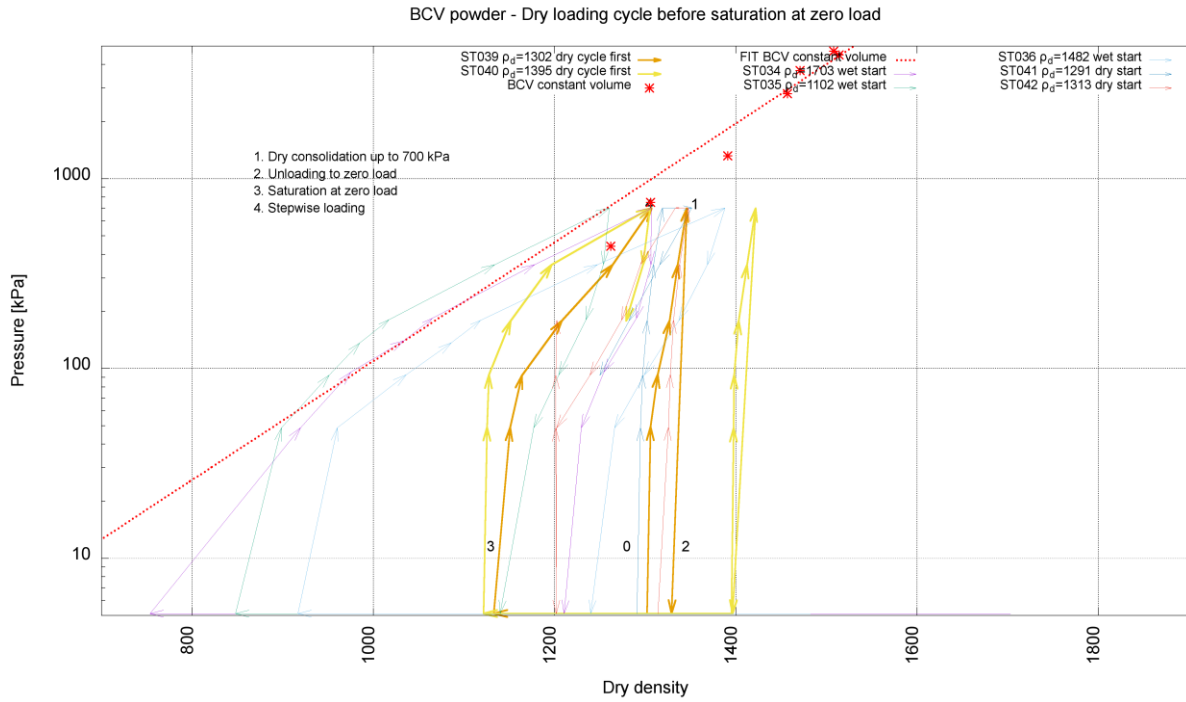
Figure 3-58 shows scenario II. The initial dry density of the samples was 1302 and 1395 kg/m<sup>3</sup>. Important observation has been made – while the saturation has been made at zero load the density after swelling is higher than in scenario I. The reason of that behaviour is not known and it needs further investigation. The unloading path (fully saturated) seems to follow same trajectory as for other scenarios.

Figure 3-59 shows results of scenario III. Two samples of density 1291 and 1313 kg/m<sup>3</sup> were investigated. The behaviour after saturation seems to be consistent with other scenarios (note there may be mechanical problem with test ST042 – stuck piston at last leg of unloading).

An overview of the BCV powder tests is given in Figure 3-60.



**Figure 3-57. BCV powder oedometric test – scenario I**



**Figure 3-58. BCV powder oedometric test – scenario II**

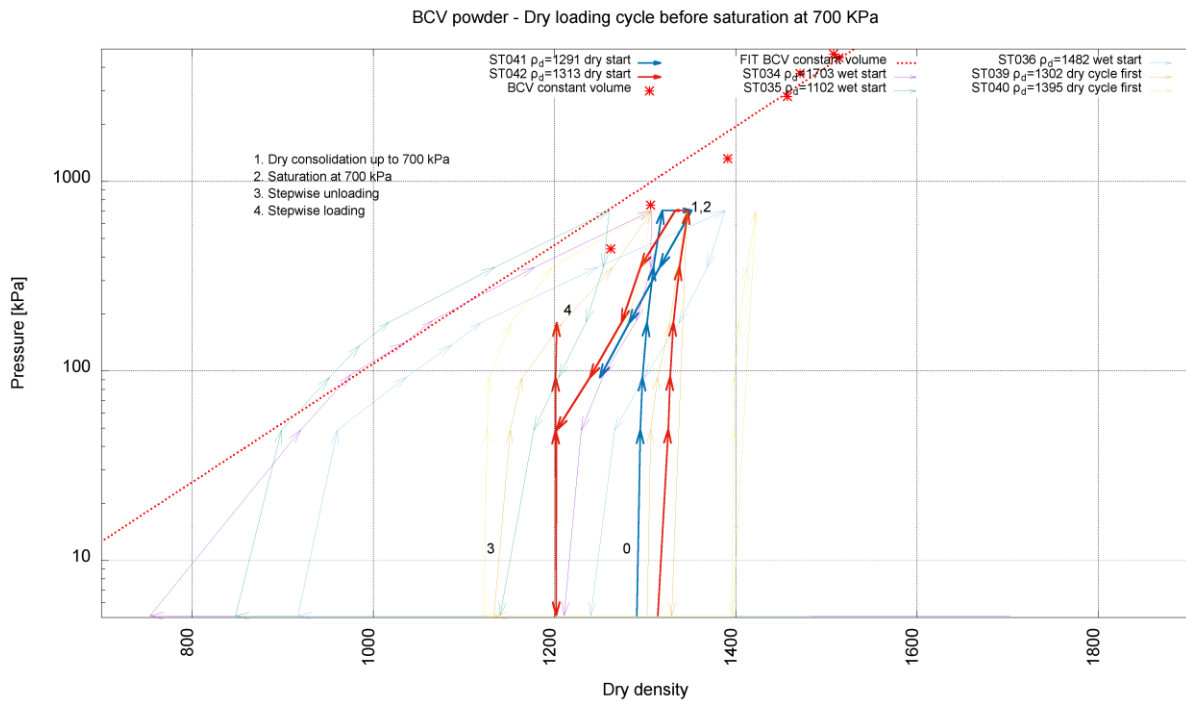


**Figure 3-59. BCV powder oedometric test – scenario III**

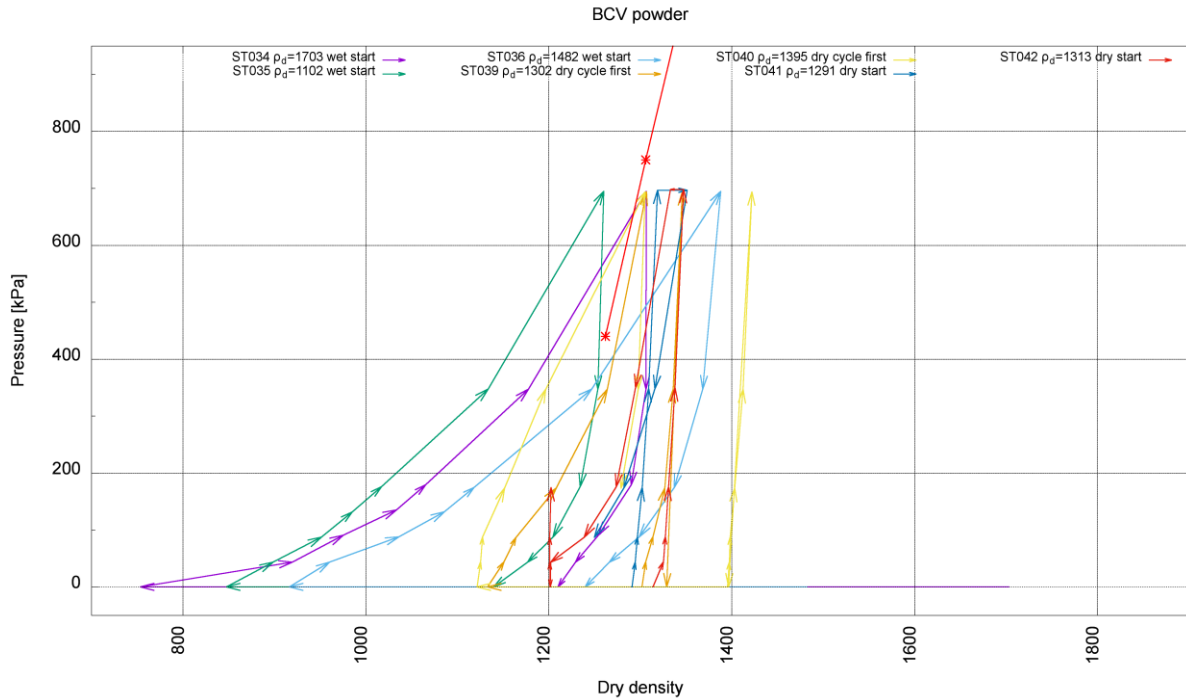


**Figure 3-60. BCV powder oedometric test – overview**

### 3.3.4.2. Pellets

Two scenarios (I&III, Figure 3-61) were investigated on pelletised material.

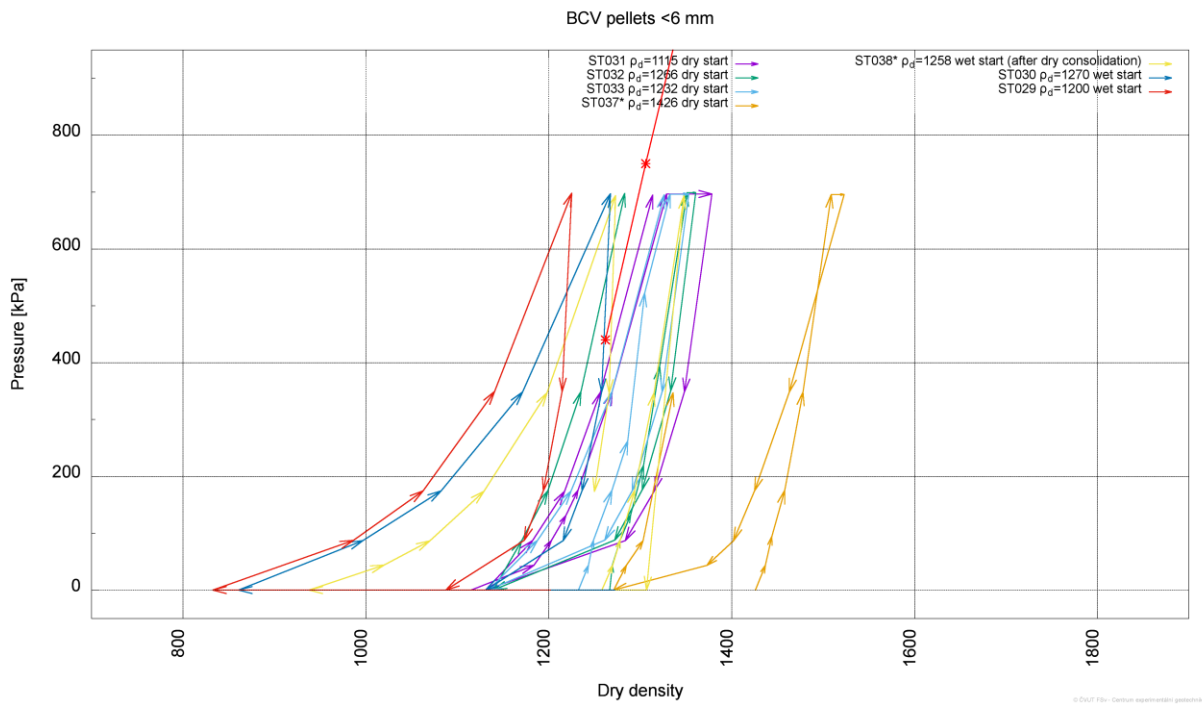


**Figure 3-61. BCV pellets oedometric test – overview**

Figure 3-62 shows results of scenario I and Figure 3-63 shows results of scenario III. An observation has been made in scenario III during saturation – the density change direction was different between samples. It indicates that there could be collapse of material structure.

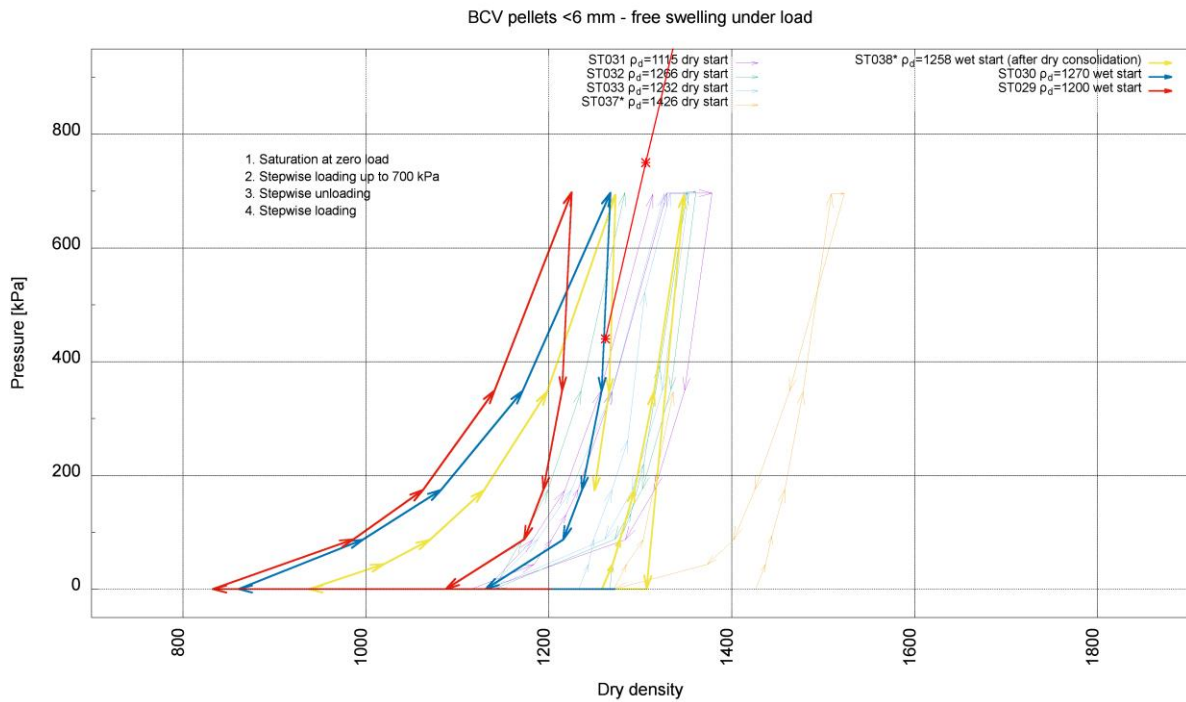


**Figure 3-62. BCV pellets oedometric test – scenario I**

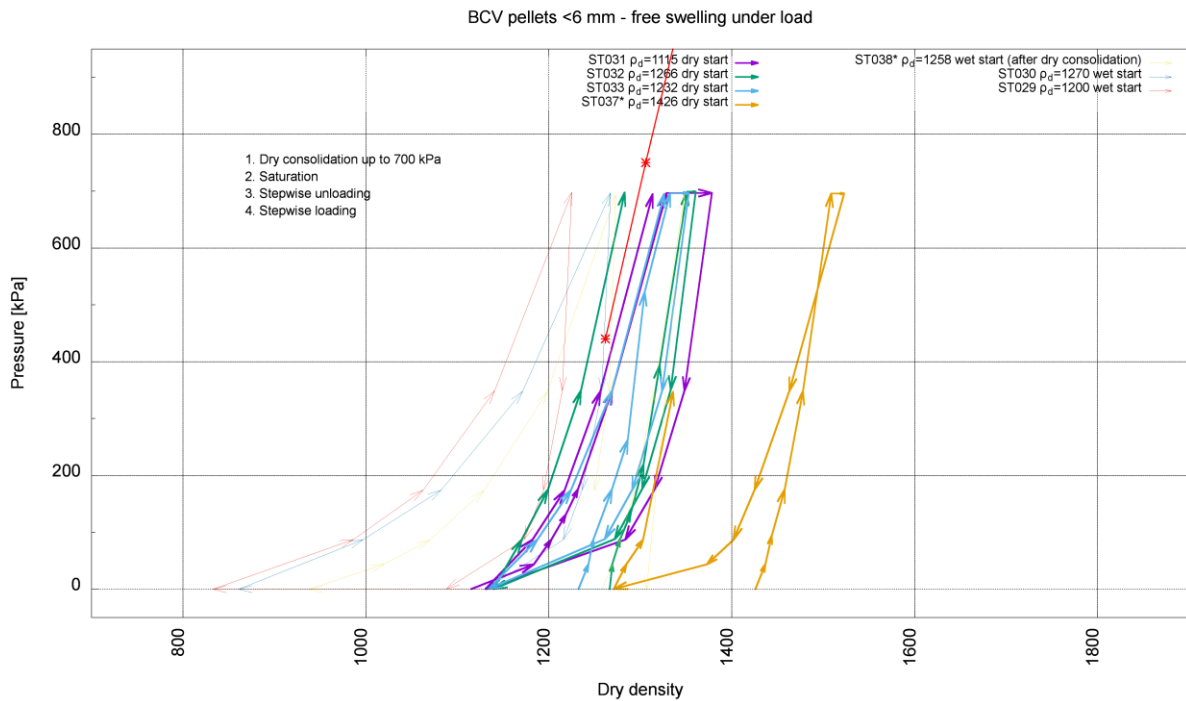


**Figure 3-63. BCV pellets oedometric test – scenario III**

### 3.3.4.3. Conclusion

The results of oedometric tests on powder material and pellets shows that there is a strong stress/saturation path dependency and stress at saturation is important. It indicates that there is continuous development of macro- & micro-structure of material. However, after full load and unload cycle in saturated state stress path stabilises.

There has been found a difference between (compacted) powder and pelletised material:

- Pellets can “collapse” at low densities when water is introduced (load capacity in dry state is higher than swelling pressure)
- Powder (even compacted) is more sensitive to dry load cycle
- Both pellets and powder converge to the similar/same stress path eventually

## 4 Swelling into limited void

### 4.1 Swelling into a void as function of sample/void ratio, orientation and temperature (BGS)

#### 4.1.1 Tested material

Engineered clays selected for testing comprise MX-80 Bentonite (VolClay) and a calcium-activated Bulgarian bentonite. The VolClay (Svensson et al. 2017) bentonite samples are compacted at the BGS from powder supplied by the American Colloid Company (now Mineral Technologies Inc.) through Sibelco Nordic, who crushed and dried the material. Ca-bentonite samples are compacted from powder supplied by Imerys through Svensk Karnslebrahantering (SKB). Detailed information about the composition of the two different bentonite test materials can be found in Table 4-1 below. In both cases, granular MX-80 is mixed with deionised water and compacted at 80MPa for 24 hours to produce the test sample. The sample is then turned down in a machine lathe to precisely fit the pressure vessel interiors used during testing.

**Table 4-1. Summary of clay used to form test samples. [BGS (C) UKRI]**

Name	MX-80 VolClay	Imerys Ca-Bentonite
Origin/Producer	American Colloid Company (now Mineral Technologies Inc.) through Sibelco Nordic.	Ca-bentonite from Bulgaria supplied by Imerys and provided by SKB Sweden.
Description	Granular Na-bentonite, crushed and dried. Average particle size ranges from 16 to 200 micron. This material is composed of predominantly montmorillonite (>90%), with small amounts of feldspar, biotite, selenite etc. At a 5% solids dispersion in distilled water the pH of the mixture ranges between 8.5 and 10.5.	Granular Ca-activated bentonite from Bulgaria, industrially homogenised and milled to a granular powder. The material contents are predominantly montmorillonite (>80%), with calcite, quartz, mica and trace gypsum.

#### 4.1.2 Experimental set-up

The primary objective of this test programme was to examine the impact of various controls on the swelling behaviour of bentonite in the presence of a void. Samples of varying length were used to examine the influence of permitted axial strain on homogenisation and swelling pressure development. It should be noted that the full internal dimensions within each pressure cell were not all the same and were, therefore, taking into account when calculating axial strain for each test.

Three experimental apparatus were used for the swelling tests. These are all constant volume apparatus, which constrain the sample in a radial direction, but allow axial swelling until the clay fills the full length of the pressure cell interior. A summary of the key apparatus features is given in Table 4-2 and a brief description for each is given below.

**Table 4-2. Summary of differences between test apparatuses. [BGS (C) UKRI]**

<b>Apparatus</b>	<b>Ambient or elevated T?</b>	<b>No. of pore pressure sensors</b>	<b>No. of stress sensors</b>	<b>Vessel interior length (mm)</b>
<b>1</b>	Elevated T	3 radial transducer arrays	5 (2 axial, 3 radial)	116
<b>2</b>	Both	None	12 (4 axial and 8 radial)	120
<b>3</b>	Ambient	3 radial transducer arrays	5 (2 axial, 3 radial)	116

### **Test apparatus 1**

This constant volume apparatus was used to conduct swelling tests under elevated temperature conditions. This is a bespoke set-up that has been designed and built at the BGS (Figure 4-1) and consists of (1) a thick-walled, dual-closure pressure vessel; (2) an injection pressure system; (3) a backpressure system; (4) 5 bespoke pressure transducers measuring radial and axial total stress; (5) 3 port-arrays with transducers for porewater pressure measurement; and (6) a microcomputer-based high-speed data acquisition system. The pressure vessel is comprised of a dual-closure tubular vessel manufactured from 316-stainless steel, pressure-rated to 70 MPa, with the internal surfaces hard-chromed to prevent damage. Large axial sintered filters (were also recessed into the end closures to ensure an even distribution of fluid entering the vessel at each of its ends; the test fluid was supplied to the sample using high precision syringe pumps (Teledyne ISCO D-Series 260D).

This apparatus has an internal length of 116 mm and a diameter of 60 mm. It was instrumented with 5 load cells (2 axial and 3 radial) and 3 transducer arrays to measure the total stress and pore pressure respectively. The load cells used were button-type XF2041–3-2kN temperature-compensated devices supplied by StrainSense Ltd. The load cells were positioned on the outside of the pressure vessel and held in stainless steel housings. The force was translated from the clay to the load cells via tungsten carbide pushrods, chosen for their hardness and incompressibility. The pressure measurements made by the load cells can be considered accurate to  $\pm 80$  kPa, whilst the porewater pressure transducers were accurate to  $\pm 0.25\%$  full scale range. The whole pressure vessel assembly (excluding the syringe pumps) was stationed inside an oven (BINDER GmbH, Tuttlingen, Germany, Series FED 400) that had a temperature range of 5°C above room temperature to 300°C. A detailed description of this apparatus is given by Daniels et al. (2021).

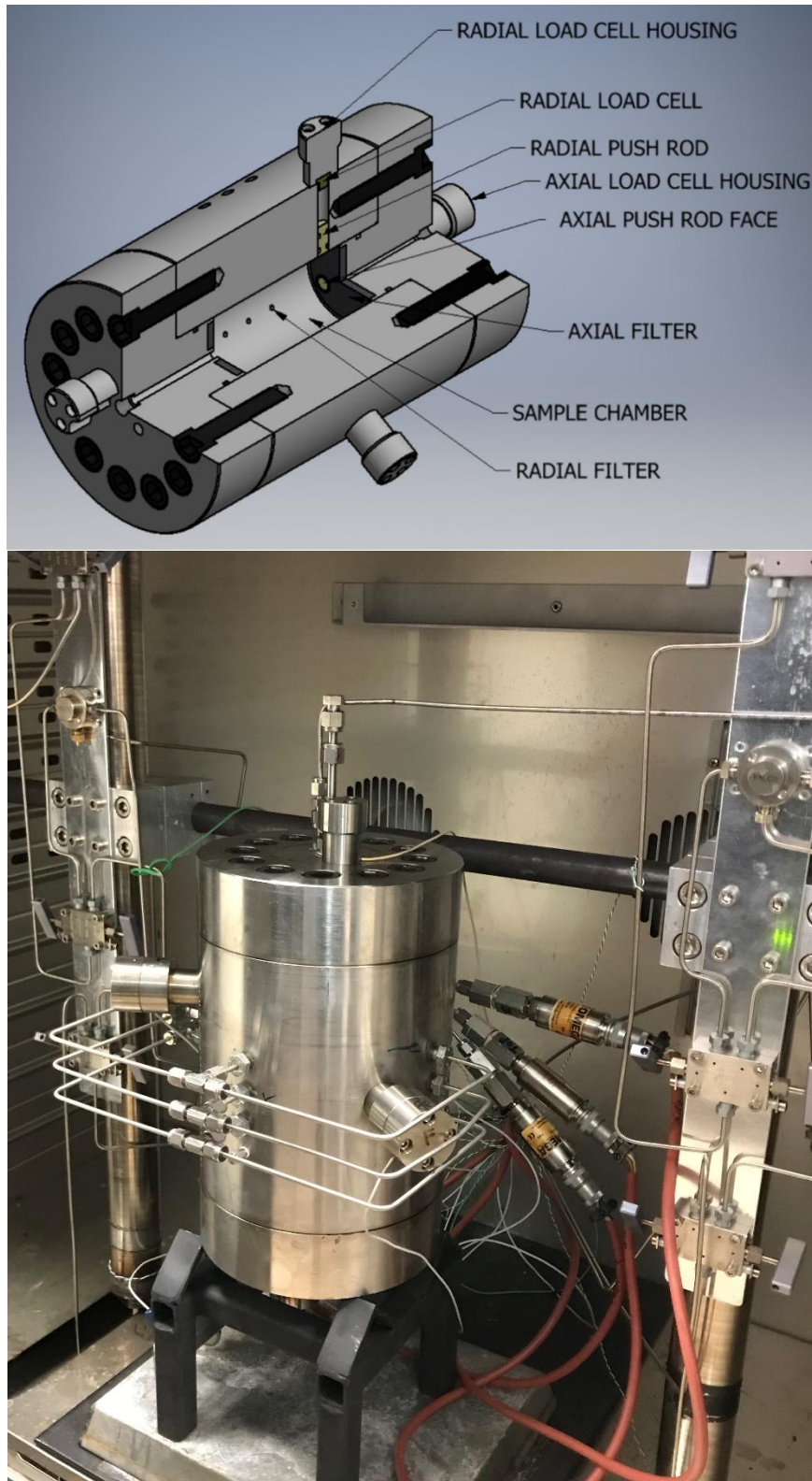


**Figure 4-1. Top: Cut-away diagram of the apparatus for the permeability evolution tests showing positioning of the total stress sensor locations and load cell housings, and the locations of the porewater pressure filters. Bottom: Photograph of the apparatus inside the large experimental oven. [BGS (C) UKRI]**

**Test apparatus 2**

This is also a bespoke apparatus that has been designed and built at the BGS (Figure 4-2). It consists of (1) a thick-walled, dual-closure pressure vessel; (2) an injection pressure system; (3) a backpressure system; (4) 12 bespoke pressure transducers measuring radial and axial total stress; and (5) a microcomputer-based high-speed data acquisition system. The pressure vessel is comprised of a dual-closure tubular vessel manufactured from Invar Alloy 36 steel, pressure-rated to 70 MPa, with the internal surfaces hard-chromed to prevent damage. Samples can be hydrated and/or a backpressure can be applied through two porous filters mounted on the end-closures. Samples are constrained radially, by the rigid stainless-steel cell, resulting in the development of a swelling pressure on hydration. The test fluid was applied to the sample using high precision syringe pumps (Teledyne ISCO D-Series 260D).

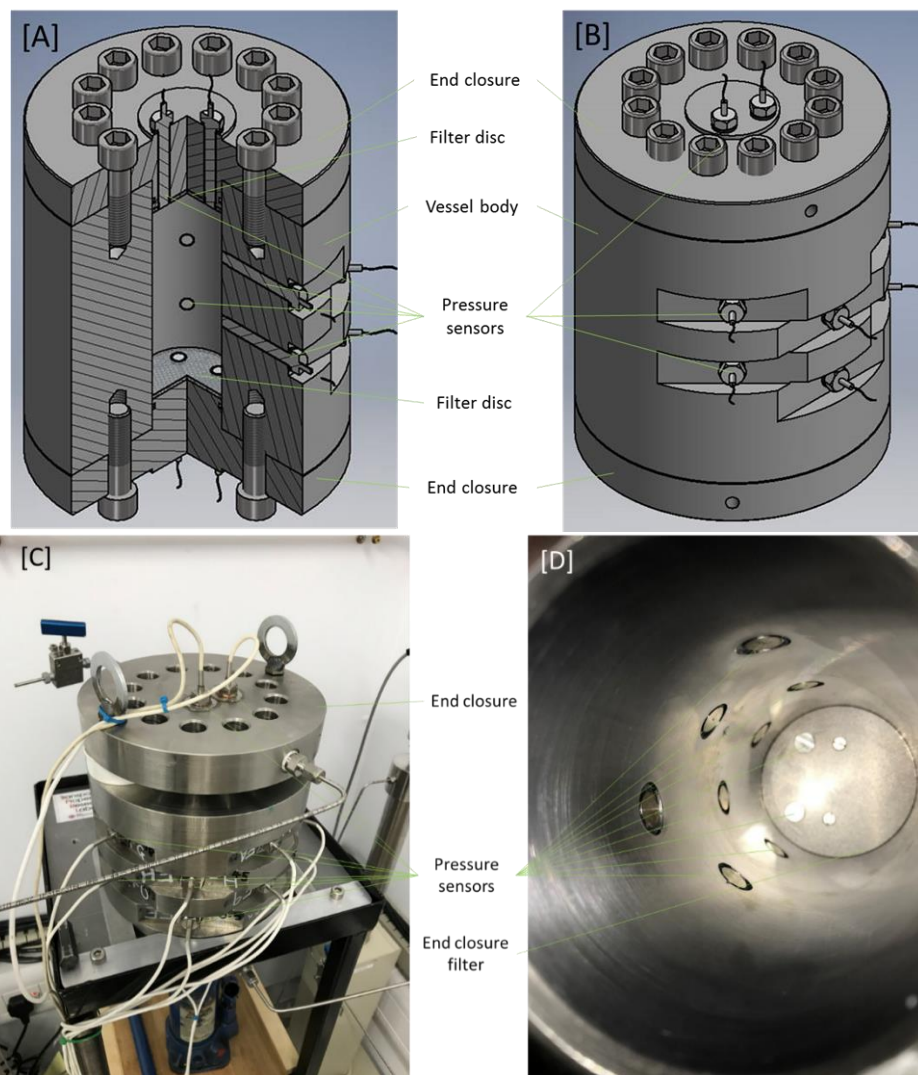


**Figure 4-2. [A] cut-away diagram and [B] schematic of the apparatus for the swelling pressure development tests showing the positioning of the pressure sensors and axial filter discs; [C] photo of the experimental set up including vessel, end closures and pressure sensors. This part of the assembly will be situated in the large oven; [D] internal view showing the eight radial and two axial pressure sensors. The axial sensors are embedded in the end closure filter. [BGS (C) UKRI]**

This apparatus uses 12 pressure sensors to measure total pressure (4 axial and 8 radial), but has no pore pressure sensors. The total pressure sensors used in this vessel are XP1147-200BS temperature-compensated custom sensors supplied by StrainSense Ltd. They do not require pushrods to translate the pressure from the clay to the outside of the vessel. Instead the instruments are screwed into the vessel and their face (containing a deformable membrane) touches the surface of the clay. The pressure measurements made by these sensors can be considered accurate to  $\pm 15$  kPa. When testing at elevated conditions, the whole pressure vessel assembly (excluding the syringe pumps) was stationed inside an oven (BINDER GmbH, Tuttlingen, Germany, Series FED 400) that had a temperature range of 5°C above room temperature to 300°C. A detailed description of this second apparatus is given by Harrington et al. (2020).

### **Test apparatus 3**

This constant volume apparatus was used to conduct swelling tests under ambient temperature conditions and for high salinity fluids. This is a bespoke set-up that has been designed and built at the BGS (Figure 4-3) and consists of (1) a thick-walled, dual-closure pressure vessel; (2) an injection pressure system; (3) a backpressure system; (4) 5 bespoke pressure transducers measuring radial and axial total stress; (5) 12 radial pore pressure transducers to monitor local evolution along around the sample; and (6) a microcomputer-based high-speed data acquisition system. The pressure vessel is comprised of a dual-closure tubular vessel manufactured from 316-stainless steel, pressure-rated to 70 MPa, with the internal surfaces hard-chromed to prevent damage. Large axial sintered filters (were also recessed into the end closures to ensure an even distribution of fluid entering the vessel at each of its ends; the test fluid was supplied to the sample using high precision syringe pumps (Teledyne ISCO D-Series 260D).

This apparatus has an internal length of 116 mm and a diameter of 60 mm. It was instrumented with 5 load cells (2 axial and 3 radial) and 3 transducer arrays to measure the total stress and pore pressure respectively. The load cells in this apparatus are button-type XF2041-3-2kN load cells supplied by StrainSense Ltd. The cells are housed on the outside of the vessel, with a tungsten carbide pushrod running from the internal face of the vessel to the housing on the outside. This configuration allowed the swelling stress of the clay to be translated to the load cell, but due to the indirect nature of the measurement, meant that the data were slightly more prone to hysteresis. The load cell measurements can only be considered as accurate to  $\pm 80$  kPa. The pore pressure measured with this should be considered accurate to  $\pm 15$  kPa. A detailed description of this apparatus is given by Harrington et al. (2020).

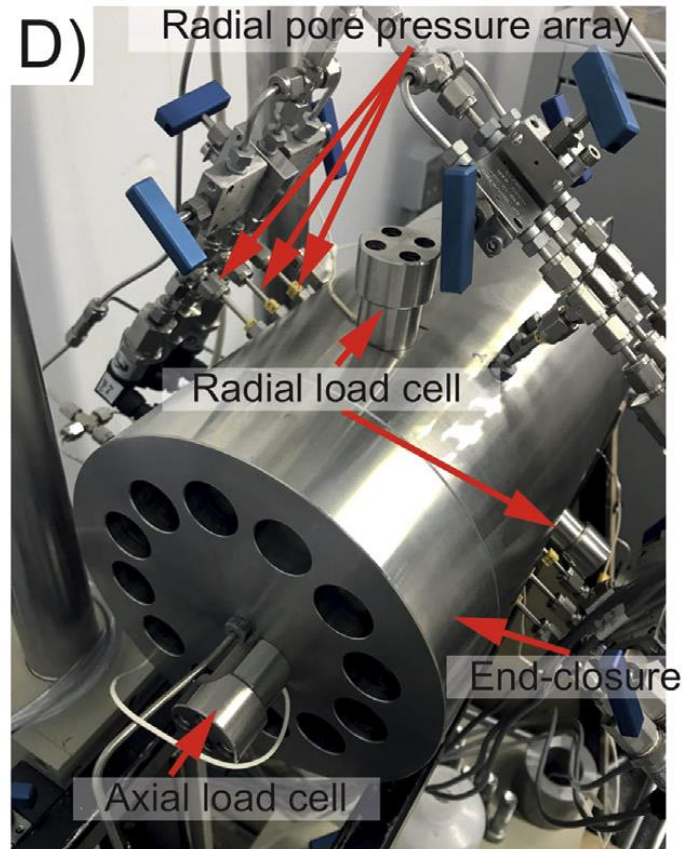


**Figure 4-3. Test apparatus 3 showing locations of the porewater pressure transducers and load cell housings. [BGS (C) UKRI]**

#### 4.1.3 Testing procedure

Testing at ambient temperature conditions was conducted inside an air-conditioned environmental chamber, which maintained conditions to within  $\pm 1^\circ\text{C}$ . Where elevated temperatures were required, the whole pressure vessel assembly (excluding the syringe pumps) was stationed inside an oven (BINDER GmbH, Tuttlingen, Germany, Series FED 400) which has a temperature range of  $5^\circ\text{C}$  above room temperature to  $300^\circ\text{C}$ . At the start of each experiment the apparatus was calibrated. The calibration was carried out by placing a steel bung in the bore of the test vessel and filling the apparatus with the test fluid (distilled water). All of the tubework was carefully flushed with the test fluid through each available port to ensure no residual air remained, and the apparatus was operated at ambient or heated to the selected testing temperature. A constant water pressure was then applied by one of the syringe pumps in 1 MPa increments from 1 to 7 MPa and back to 1 MPa. At each pressure increment, the pressure was held constant and the response on each of the sensors and on a Druck pressure calibration instrument was measured. This data was then used to provide a calibrated pressure output for each sensor. After calibration, where heating had occurred the oven temperature was reduced to ambient. For all calibrations the steel bung was then removed from the vessel and the tubework was carefully flushed again.

Before commencement of the first test, the apparatus was either left at ambient or heated to the appropriate testing temperature. The sample was pushed to the base of the void inside the apparatus and the remaining void space above the sample was filled with distilled water; the

sample was not heated in advance of insertion because this would have affected the pre-test saturation.

Testing was carried out at an applied water pressure of 4500 kPa, which was selected as a suitable value for the Swedish radioactive waste repository concept, as provided by SKB. Water pressure was then applied alternately to each end of the sample in incremental steps to the target value, starting at the end of the apparatus that was originally void space. This kept the sample fixed against the other end of the apparatus interior and prevented it from sliding along the bore of the vessel before the sample swelling began. The pore pressure reference value was chosen for comparability with Swedish plans for a disposal facility, as outlined by SKB.

The flow rate into and/or out of the sample was controlled and monitored using the syringe pumps and a single digital control unit. Each pump was operated in a constant pressure mode (except in Test 9 where a constant flow rate was used) and thus the flow rate and direction were not prescribed. Inflow or outflow could therefore occur at either end of the test vessel. Once the pore pressure had been applied to the sample, no external hydraulic gradient was then applied to the clay at any further point in the test. FieldPoint™ and cRIO logging hardware and the LabVIEW™ data acquisition software (National Instruments Corporation, Austin, TX, USA) were used to log the flow rate, total stress and pore pressure at 2 min intervals, providing a detailed time series dataset. Over the duration of each test, the sample was able to swell in an axial direction, into the remaining interior void space.

Upon completion of testing, the samples were carefully extruded from the apparatus and cut in approximately 10 mm thick samples. These were then weighed, placed in an oven at 105 °C and dried to determine the moisture content.

#### **4.1.4 Results**

The following sections summarise the test programme that has been conducted during BEACON, as well as the experimental results under ambient conditions and elevated temperatures and salinities. The influence of sample orientation and test material is also considered. Finally, the implications for the homogenisation process in bentonite are discussed.

##### **4.1.4.1. Experiments conducted**

A large suite of swelling experiments have been carried out within this subtask. Each individual test is carried out at a fixed temperature, for a duration of up to 100 days. A full summary of the experiments is given in Table 4-3. Tests investigating the influence of temperature were conducted at room ambient temperature (20°C) and 90°C. The influence of salinity at ambient temperatures has also been investigated for NaCl solutions of 1Molar and 3Molar. To investigate the influence of permitted axial strain, comparable tests have also been conducted with sample lengths ranging between 65 and 95mm.

For the purposes of enhanced interpretation in the discussion section (Section 4.1.4.2) test results have been combined with the initial few experiments conducted as part of the EURAD HITEC test programme, which includes experiments conducted at 100 and 150°C. Results from Test 13 are included in Section 4.1.4.3. Results from this and the other HITEC tests are incorporated into the discussion Section 4.1.4.6 and a more detailed description of these other tests can also be found in HITEC, 2021.

**Table 4-3. Test programme summary. N.b. Tests 13, 14 and 15 were conducted as part of the EURAD HITEC test programme. [BGS (C) UKRI]**

Test	Sample number	Apparatus number	Dry density	Fluid composition	Orientation	Temp (°C)	Water uptake method	Initial sample length (mm)	Material
1, 5, 7	FPR-BE-1; FPR-BE-5; FPR-BE-7	2, 2, 2	1.7, 1.7, 1.7	Deionised water (DI)	Vertical	20	Constant Pressure	65, 75, 85	MX80
2, 4, 8	FPR-BE-2; FPR-BE-4; FPR-BE-8	1, 1, 1	1.7, 1.7, 1.7	DI	Vertical	90	Constant Pressure	65, 75, 85	MX80
3, 6	FPR-BE-3; FPR-BE-6	3, 3	1.7, unknown	DI	Horizontal	20	Constant Pressure	65	MX80, Ca-bentonite
9	FPR-19-004	-	-	DI	Vertical	20	Constant Flow	90	MX80
10, 11, 12	FPR-20-001; FPR-20-018; FPR-20-026	3, 3, 3	1.7, 1.7, 1.7	1M NaCl sol.	Vertical	20	Constant Pressure	65, 85, 75	MX80
13, 14, 15	FPR-20-008; FPR-20-24; FPR-21-010	2, 2, 2	1.7, 1.5, 1.7	DI	Vertical	100, 100, 150	Constant Pressure	95, 95, 95	MX80
16	FPR_21_023	2	1.7	3M NaCl sol.	Vertical	20	Constant Pressure	65	MX80

#### 4.1.4.2. Testing under ambient conditions

Tests 1, 3, 5, 6, 7 and 9 were conducted at room temperature, using deionised water to enable resaturation and swelling. Of these experiments, samples 1, 5, 7 and 9 were vertically orientated, whilst samples 3 and 6 were horizontally orientated. It should also be noted that all experiments were conducted on MX80 bentonite, except for Test 6, where a Ca-bentonite was used instead. All experiments were allowed to resaturate and swell under a constant applied water pressure, except for Test 9, where a constant flow rate was used, so as to examine the influence of the hydration boundary condition. Test 9 isn't described further in this report. Finally, Tests 1, 5 and 7 were conducted on samples of varying length, so as to examine the influence of void size on the swelling behaviour of the clay. It should be noted that Tests 1, 5 and 7 were conducted Apparatus 2, whilst Apparatus 3 was used for Tests 3 and 6. As a result, the geometry of the total stress measurements differs somewhat. Tests 13, 14 and 15 were reported as part of the EURAD project (HITEC work package). They are complementary to the work conducted in BEACON, however, and Test 13 is discussed with the other elevated temperature experiments in Section 4.1.4.3. Tests 13-15 are also referred to in some of the discussion on elevated temperatures. A further description of these experiments and their findings can be found in HITEC, 2021.

#### Development of stress

##### Tests 1, 2 and 3 (vertical tests)

Swelling pressure was calculated as the difference between the measured total stress and the average applied water pressure. The resulting swelling pressure distributions are shown for Tests 1, 5 and 7 in Figure 4-4. A detailed examination of the test data from each of these experiments is given by Harrington et al. (2020). In all cases, the development of pressure is a spatially complex and time-consuming process, with significant variance still existing at the time of test

termination (a day 100). Given that the rate of pressure change observed during the latter stages of testing is very small, extrapolation of the results suggests that homogenisation of the bentonite would not occur for many years. However, it is clear that bentonite, under zero hydraulic gradient, is able to swell and ultimately fill the start void, creating a small but measurable swelling pressure in the axial sensors above the sample (where a void was initially present).

Whilst some minor changes in local stress field measurements may be interpreted as the result of stick-slip behaviour along the sides of the pressure vessel, it is possible that this behaviour may also result from localised yielding of the clay to accommodate high differential stresses. More strikingly, the smooth evolution of the pressure traces throughout the majority of testing is contrary to classic stick-slip friction behaviour, which is signified by abrupt changes in response and indicates that the majority of the observed behaviour is continuous process resulting from the gradual swelling of the clay sample.

Comparison of peak stresses between tests indicates that increasingly higher values were detected for increasing sample length. It is also interesting to note that the residual pressures measured at day 100 persist over a wider range of values as initial void size reduces (i.e. moving from Tests 1, through 7 and 5). This observation is considered further in the discussion Section (4.1.4.6).

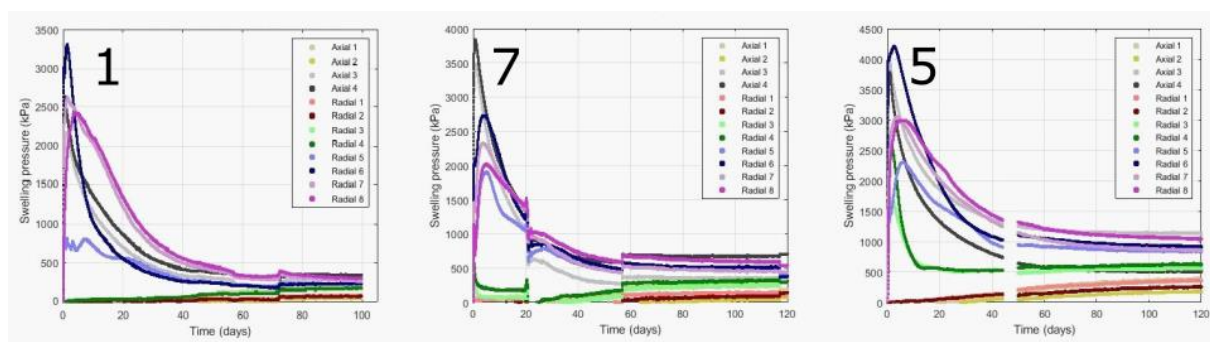


**Figure 4-4. Left to right: Development of swelling pressure during Tests 1, 7 and 5, with initial sample lengths of (65, 75 and 85mm, respectively). [BGS (C) UKRI]**

### Tests 3 and 6 (horizontal tests)

To examine the possible effect of gravity segregation on the swelling behaviour of bentonite, two tests were undertaken in which the samples were horizontally mounted within the apparatus. Except for this geometric change, all other aspects of Tests 3 and 6 were the same as Tests 1, 5 and 7. In Test 6, the role of clay composition was also examined by using a calcium-rich bentonite from Bulgaria. A detailed examination of the test data from each of these experiments is given by Harrington et al. (2020). As with the vertical experiments, the void next to the sample was completely filled with distilled water (in both tests) by carefully tilting the apparatus during the assembly procedure. Once the end-closure were in place, a water pressure of 4500 kPa was applied to both ends of the vessel, as before. Figure 4-5 shows the swelling pressure development for Tests 3 and 6 alongside the vertical test with an equivalent sample length of 65mm (Test 1). As with previous experiments, swelling pressure was calculated as the difference between the measured total pressures and the applied water pressure. For both horizontally orientated tests, measured values again show an initial peak, followed by a gradual convergence, the rate of which reduces to very small levels by day 100. In both cases, a substantially greater spread in the final swelling pressure distribution was noted. Test 3 also

saw a period where swelling pressures begin to rise again, before dropping to lower values. It is not clear whether these differences are reflective of the horizontal orientation, or is at least partially related to the different sensor arrangement used in Apparatus 3 for these experiments.

Comparison of the peak swelling pressures generated in both horizontal tests with the equivalent vertically orientated test (Test 1) also shows some differences. Peak pressures were substantially lower for the horizontally orientated Mx80 bentonite sample (Test 3) and the residual swelling pressures at the end of testing remained noticeably higher than for Test 1. In contrast, peak stresses were substantially higher for the calcium bentonite test sample (Test 6), with the final values in the sub-100kPa range, as with Test 3.

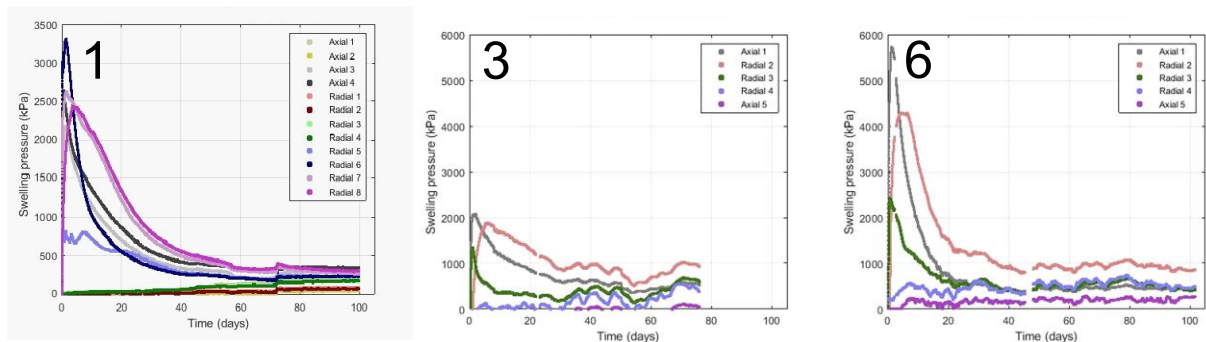


**Figure 4-5. Left: Swelling pressure evolution in a vertical orientation for a Na-bentonite sample (Test 1). Centre: Swelling pressure evolution in a horizontal orientation for a Na-bentonite sample (Test 3). Right: Swelling pressure evolution in a horizontal orientation for a Ca-bentonite sample (Test 6). Test samples 1, 3 and 6 were all 65mm long. [BGS (C) UKRI]**

## Water uptake

### Tests 1, 5 and 7 (vertical tests)

In each test the cumulative flow of water through the base of the sample (inflow) and from the top of the vessel (outflow) were closely monitored as a function of time, using a pair of highly accurate digital syringe pumps. A well-defined flow transient was measured for all tests (Figure 4-6, left), where inflow and outflow were roughly symmetrical, suggesting minimal net volume change of fluid within the vessel (<6 ml). This is not unexpected, given the void above the sample was completely filled with water immediately after installation of each sample before the end-closure was fitted. Based on comparison of the transient behaviour and asymptotic values, flux into and out of the vessel also appears proportional to the start volume of clay, with cumulative flux declining with increasing sample length. This indicates a progressive reduction in swelling strain, which is supported by the higher measurements of swelling pressure noted in Figure 4-4. The data in Figure 4-6 also provide a useful measure with which to crudely apportion swelling strains within the sample.

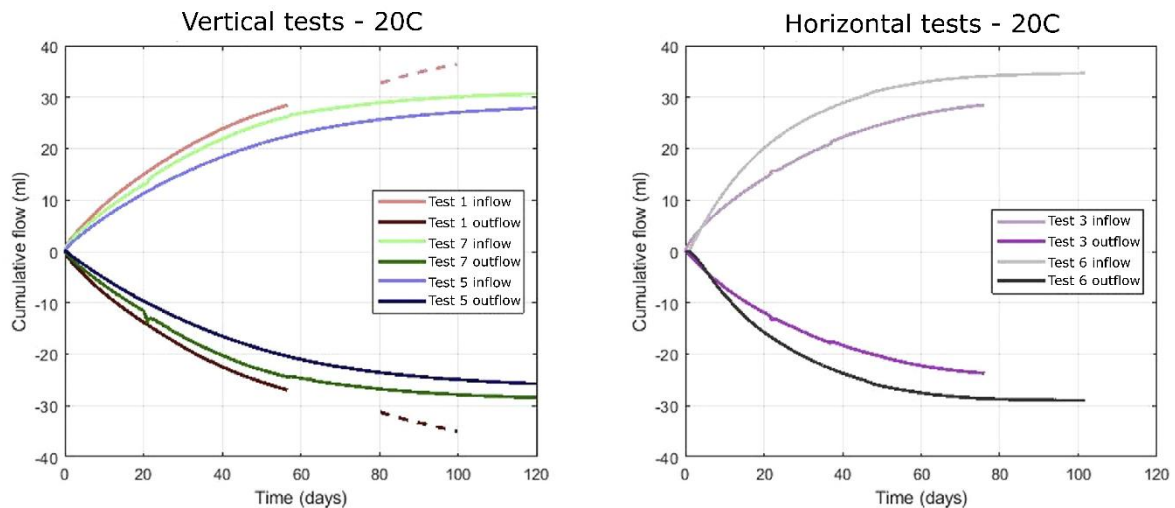


**Figure 4-6. Left: Cumulative flow into and out of the vessel from below and above the core, for Tests 1, 5 and 7. The flux in Test 1 from day 80 to the end of the test is marked by a dashed line because it is approximate and should be taken with caution. Right: Cumulative flow into and out of the vessel from below and above the core, for Tests 3 and 6. [BGS (C) UKRI]**

Examination of the data suggests around 36 ml of water entered the sample through the base of the vessel in Test 1. This quantity is relatively small, compared to the start void volume of 144.2 ml, suggesting that swelling, driven by water inflow through the base of the clay, accounted for approximately 23.4% of the volume change required to close the void. As such, the bulk of the sample expansion clearly occurred through unconstrained swelling through the upper face of the clay. This accounted for around 76.6% of the swelling strains required to close the void. A similar result occurred in Tests 5 and 7. Here, the proportion of swelling that occurred through water inflow from the base filter (below the sample) was 24.3% and 28.4% respectively. These values indicate that as the void length above the sample decreases, swelling above the sample is contributing less to the closure of the void.

#### **Tests 3 and 6 (horizontal tests)**

The cumulative flow response for Tests 3 and 6 exhibited the same general behaviour as that seen in Test 1, (Figure 4-6). Examination of the Test 3 data suggests around 26 ml of water entered/left the sample through the vessel filters by the end of testing at day 76. This test was curtailed as the rate of stress change was minimal and provided an opportunity to look at potential gravity segregation effects. By the end of testing, inflow to the sample was 28.5 ml, which compared to the same point in time, was marginally smaller than in Test 1. Using the value from Test 3, swelling through water inflow at the base of the clay, accounted for around 19.8% of the volume change required to close the void. While this value cannot be directly compared to those from Tests 1, 5 and 7, it clearly shows that, as before, the bulk of sample expansion occurred through unconstrained swelling from the upper face of the clay. This accounted for around 80.2% of the swelling strains required to close the void. Unlike in the Na-bentonite experiments with similar dimensions (Tests 1 and 3), the rate of water uptake was substantially quicker in the Ca bentonite test. This led to a well-defined asymptotic transient marking the end of hydration, which is consistent with the more rapid reduction in elevated swelling pressures observed for this test (Figure 4-5).

### Development of porewater pressure

Apparatus 3 allowed the monitoring of porewater pressure development as a function of time both within the void space of the apparatus and in the sample. Figure 4-7 shows the development of porewater pressure during Test 3. Here, water pressure can be seen to have evolved in a uniform way with the exception of filter 'PT6' which is atypical of the general response. While some minor anisotropy can be seen in the arrival times of the 'flood front' to each filter, the subsequent development of water pressure is similar in form and magnitude between each filter. The reason for the inflection in the pressure response is unknown, however, the fact it occurs in all measurement filters strongly indicates a material response to the ingress of water.

The development of porewater pressure in Test 6, performed on Ca-bentonite clay, exhibits a higher degree of anisotropy compared to that of Test 3 (Test 3, Figure 4-7). The development of water pressure is substantially delayed, compared to the Na-bentonite test. Even in these small-scale experiments, the permeation of water through the clay is non-uniform resulting in considerable heterogeneity in the development of porewater pressure. Upscaling these observations suggests that localisation of flow is likely in field experiments and, as a consequence, the development of swelling pressure may be equally impacted.

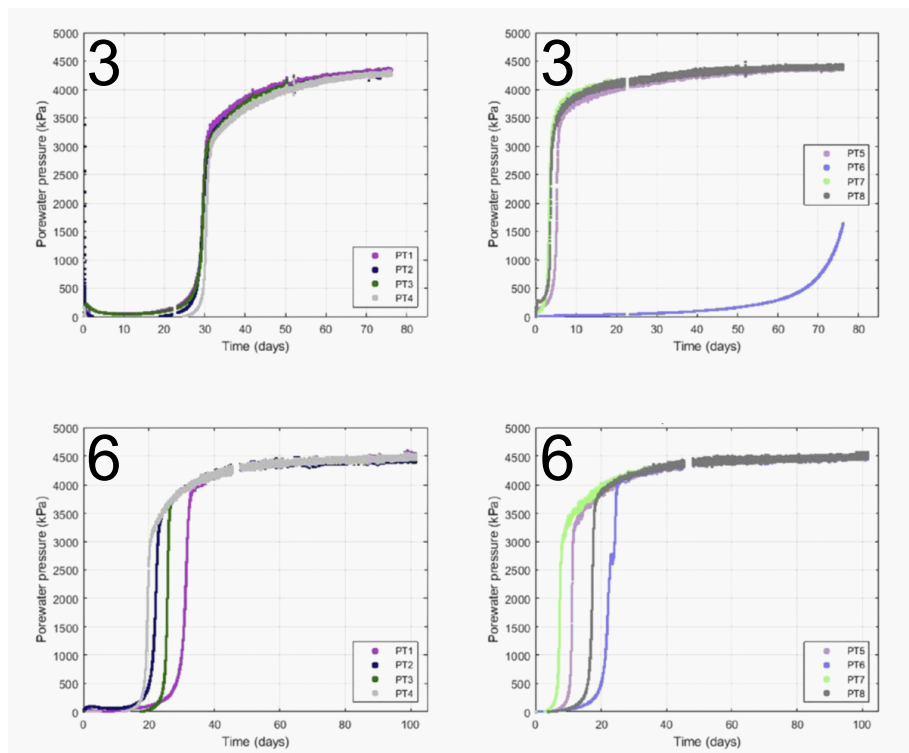


**Figure 4-7. Top row: Development of porewater pressure in Arrays (left) 1 (closest to the end of the vessel against which the samples were placed; transducers PT1, PT2, PT3, PT4) and (right) 2 (at the midplane of the vessel; transducers PT5, PT6, PT7, PT8), during the hydration in Test 3. Bottom row: (Left) and (right) shows the same responses but for Test 6. [BGS (C) UKRI]**

**Post-test analysis of the samples**

Following the completion of each test, each specimen was subsampled to provide spatial data on the geotechnical properties of the clay. This information provided insight into the swelling response of the clay and the degree of homogenisation that had occurred during each test. Given the low strength and density of the samples, it was not feasible to directly obtain volumetrically accurate sub-samples. Instead, each sample was carefully extruded in increments using a hydraulic ram and regular slices of core were taken with a sharp blade. The slices were immediately weighed, whilst the exposed end of the sample was covered with clingfilm to minimise moisture loss. Each segment was then dried at 105 °C, and the pre- and post-test weights were used to determine the moisture content (a parameter which is not dependent on sample volume). In this way, the error in the calculation of the moisture content was minimal.

A cross-plot of the moisture content data versus distance from the end of the vessel against which the samples were placed, is presented in Figure 4-8. Unsurprisingly, all samples show a pronounced increase in moisture content compared to their start value, and moisture contents were also seen to be higher for smaller initial sample starting length (i.e. larger axial strains). Significant swelling was also evident within the first 45–55 mm of each post-test sample, demonstrated by the three-fold increase in moisture contents in this region (Figure 4-8). Here, the values are unexpectedly uniform throughout these sections of each sample. The cause of this remains unclear. In Test 1 there is a small but measurable increase in moisture content nearest the base of the vessel (Figure 4-8). Whilst it is not possible to say for certain, it seems likely this increase was caused by an initial uplift of the sample as axial stress developed more rapidly than radial stress during the very early stages of the experiment (Harrington et al., 2020).

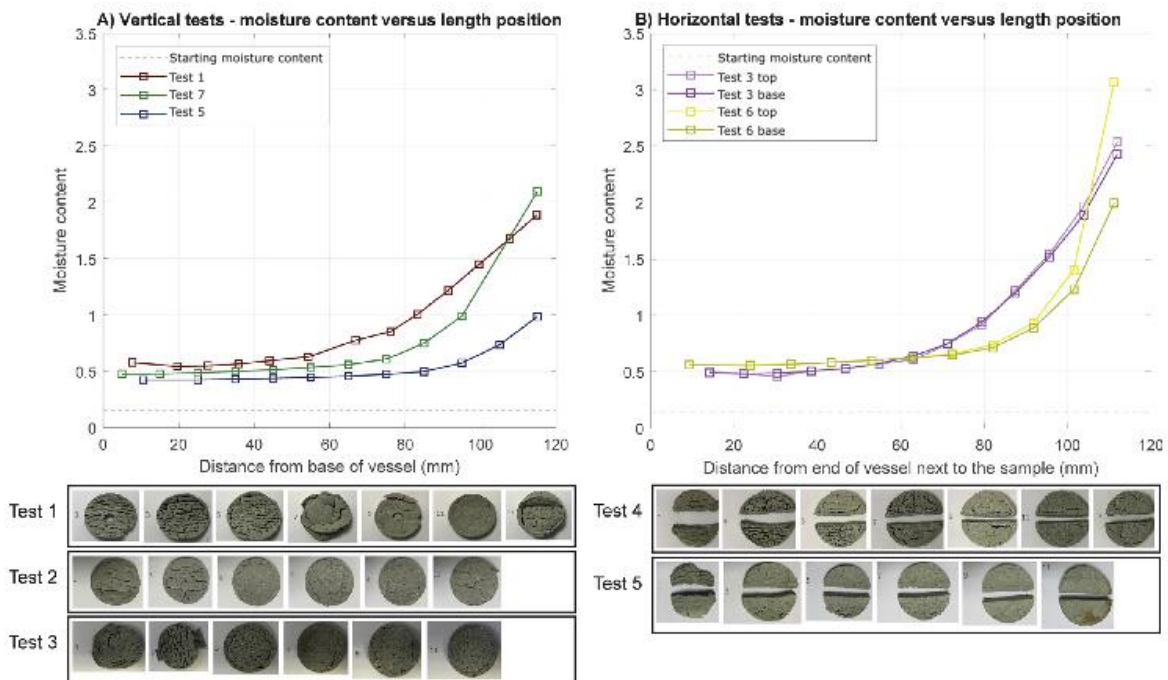


**Figure 4-8. Cross-plot of moisture content against distance from the base of the vessel for (left) Tests 1, 5 and 7, and (right) Tests 3 and 6. In the horizontal tests (Tests 3 and 6), the base is equivalent to the end of the vessel against which the clay was placed in prior to testing. [BGS (C) UKRI]**

Inspection of the data shows that large gradients in moisture content were only observed in the volume originally occupied by the void. This latter observation is to be expected as progressive unconfined swelling of the clay occurred into the void. This is also supported by the cumulative flow data collected which suggests that around 70%-80% of swelling occurred through water uptake from the top face of the clay (Harrington et al., 2020).

Figure 4-8 also shows moisture content data from the two horizontal experiments (Tests 3 and 6). From 0 to 100 mm, the data from Test 3 is very similar in form and magnitude to that of Test 1. However, from 100 to 116 mm the moisture content values for Test 3 increase rapidly compared to those of Test 1, though the reason for this behaviour, given the same composition and similar dimension of the samples, is unclear. To examine the possible effects of gravity on the swelling behaviour of the bentonite, the core from the horizontal tests, was also slabbed at its mid-plane to provide two estimates of moisture content, one in the upper half of the clay and the other in the lower half (Figure 4-8). Whilst the moisture content values are consistent in each half of the Test 3 sample through much of its length, as moisture contents increase above approximately 150% the data diverges providing clear evidence of gravity segregation present in these high moisture content sections of the clay. The longevity of these differences cannot be derived from the current data and further work is required to define the evolution of this long-term behaviour.

The Ca-bentonite sample (Test 6) exhibited similar moisture content values to Test 3 for the first half of the sample length (0–58 mm), and after this point in the sample, showed increasingly lower values (Figure 4-8). Such observations suggest that significantly less swelling and thus homogenisation of the clay, occurred in the upper half of the Ca-bentonite sample. However, above 100 mm the Ca-bentonite sample showed very large moisture content values, most especially at the top of the void and in the top half of the sample. This provides strong evidence for gravity segregation in this sample during swelling.

#### **4.1.4.3. Testing under elevated temperature conditions**

Tests 2, 4 and 8 were conducted at an elevated temperature of 90°C, using deionised water to enable resaturation and swelling. All 3 tests were carried out in apparatus 1 and were vertically orientated. The test samples were allowed to resaturate and swell under a constant applied water pressure of 4.5MPa. The test samples had differing lengths, so as to examine the influence of void size on the swelling behaviour of the clay at elevated temperatures. Test 13 was also conducted at an elevated temperature of 100°C and a sample length of 95mm.

#### ***Development of swelling pressure***

The swelling pressures measured during each test showed a similar and generalised pattern, though there was significant variance between the values present throughout all of the tests. The value recorded by each of the sensors except those closest to the top of the vessel peaked within the first 10 days of testing (Figure 4-9). The peak value was generally larger the lower down the vessel the sensor was located. Over the course of each test, the recorded pressures tended to converge, however, a significant differential in the observed spread of pressure values persisted when the tests were terminated, despite measured stresses and pore pressures reaching almost steady values. Larger peak swelling pressures were observed in the test where the sample-to-void ratio (and consequent swelling strain) was smaller.

As might be expected, the pressures measured at the base of the vessel (where the clay sample was initially located) were always higher and the values decreased towards the top of the vessel. This trend was not quite the case for every sensor in every test at all times and some overlap was occasionally seen. The swelling pressure was defined as the total stress minus the

pore pressure. It should be noted that the calculation of swelling pressure assumed that pore pressure was uniform along the length of the apparatus. This assumption is valid for parts of the sample that expanded into the void space in the vessel. During the early stages of the test, for sensors located next to the pre-compacted clay, it is likely that total stress rather than swelling pressure was recorded. However, the rapid increase in the radial stresses suggested that the clay had access to water within the first couple of days (Figure 4-9). The swelling pressure traces evolved in a smooth manner and there were no large inflections indicative of discontinuous frictional behaviour (stick-slip phenomena). However, continuous friction will still have occurred between the sample and the vessel wall and CT evidence relating to this is presented in Section 4.1.4.5. Based on the observations from the experiments presented in this study and those of (Dueck et al., 2016), the friction angle was likely to be relatively small (Harrington et al., 2020).

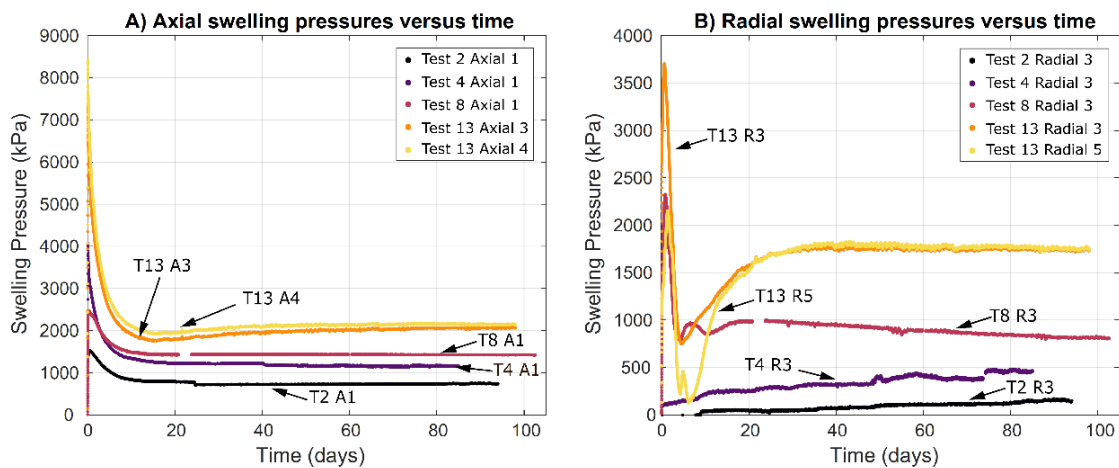


**Figure 4-9. Swelling pressure evolution for (left) axial and (right) radial sensors. [BGS (C) UKRI]**

It is important to note that during Tests 2 and 4 a number of technical issues were encountered with the pressure sensors, including long-term drift and failure. As a result, these 2 tests are less heavily instrumented than intended, meaning that the full range of swelling pressures within the clay could not be estimated. All 3 radial load cells and the axial A5 load cell at the top of the vessel were, therefore, replaced with the total pressure sensors used in Apparatus 3 (XP1147-200BS temperature-compensated custom sensors supplied by StrainSense Ltd). These sensors were then also utilised for Test 8.

All tests conducted at 90°C showed that the development of swelling pressure was spatially complicated and there was significant anisotropy in the response. This was especially highlighted by the data from Test 13 (Figure 4-10) where a substantial differential swelling pressures were observed for both axial and radial orientations, which did not equilibrate for some time. The large differences in orthogonal pressures observed at early test times are thought to have occurred because of very small differences in the starting sample dimensions, which may have caused the sample to contact differently on the individual sensors whilst also influencing both the initial fluid migration and the absolute values of peak stress in the early stages of testing.

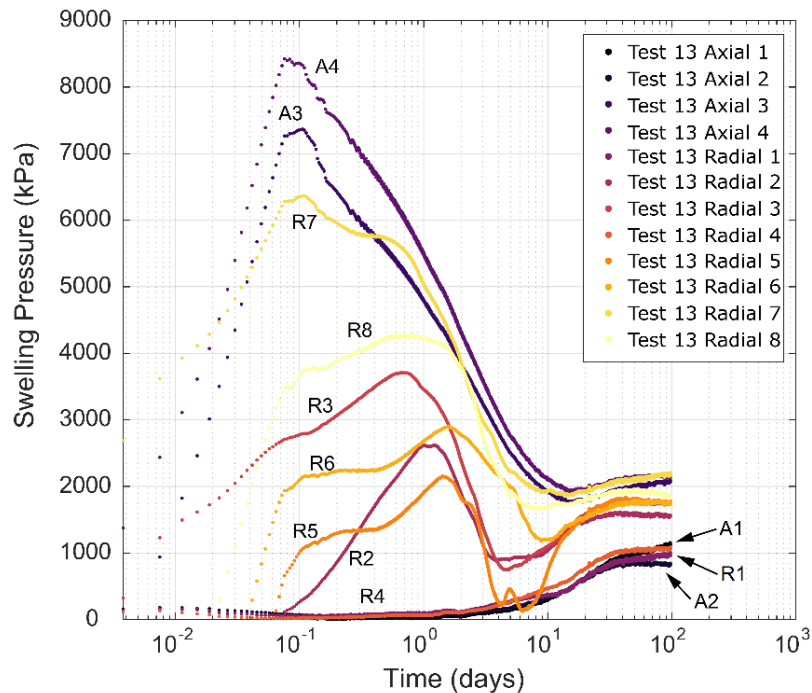


**Figure 4-10. Swelling pressures over the duration of Test 13, measured by the axial and radial swelling pressure sensors, highlighting the peak values at early times in the test history. [BGS (C) UKRI]**

There was still a significant difference between the maximum and minimum recorded swelling pressures in each test at the end of testing, and the rate of change of swelling pressure after about 20–30 days in each of the tests was small. This implies that the bentonite was able to use its internal shear strength (Gilbert et al., 1996; Stark and Eid, 1996; Fox et al., 1998; Fox and Stark, 2015) to maintain the differential stresses for long periods of time, which may have impacted rates of homogenisation. In addition, where information from axial load cell A5 (at the top of the apparatus) was available, the data showed either a peak (Test 8) or the data was approaching an asymptote (Test 13) by about 30 days of testing. Together this suggests that the sample had swelled to completely fill the initial void by this time in the test, and from this point onwards, internal reorganisation of the clay and fluid distribution within the sample was occurring up until the point that the test was terminated. It also indicated that if the samples had swelled to completely fill the start void within 30 days and significant anisotropy in the swelling pressure data was still extant at 100 days, homogenisation of the full length of the sample would take a substantial amount of time.

A correlation between the peak swelling pressure and the initial void length of each test was also apparent, although it should be noted that peak values of swelling pressure are sensitive to the initial conditions, as well as the availability and migration of water through the sample. For longer initial void lengths (equating to shorter starting samples), both the peak and the end-of-test swelling pressures were smaller. This result was expected because the test with the shortest starting sample had the least clay material within the test vessel and had the lowest average final dry density, thus the reduced quantity of clay would have been able to exert less of a force on the walls of the vessel compared with a starting test sample that had originally been longer.

The axial peak value in Test 8 was much lower than expected based on the data from the other three tests and previous observations (Harrington et al., 2020) and it is thought that this was the result of a slight shift in the sample positioning away from the base of the vessel at the

start of the test. For a sodium bentonite with a dry density of 1.7 g/cm<sup>3</sup> exposed to pure water, a swelling pressure in excess of 16 MPa is expected at 100% saturation and ambient temperature (Karlund et al., 2006); however, it should also be noted that the swelling pressure is both stress-path dependent and affected by the measurement method, with isovolumetric methods providing intermediate values (Sridharan et al., 1986). Whilst the starting sample in each test had a dry density of around 1.7 g/cm<sup>3</sup>, as the sample expanded the dry density of the material would have evolved to lower values. In addition to this, at elevated temperatures bentonite swelling pressures may be expected to be lower (e.g. Pusch, 1980; Villar and Lloret, 2004), although the reverse result has also been seen (e.g. Pusch et al., 1990). Every sample's peak swelling pressure was significantly lower than 16 Mpa, with the peak axial and radial swelling pressures for the longest tested sample (Test 13: 95 mm) being the highest. This is consistent with the expectation that the reduced peak values result from the decrease in dry density and increase in moisture content as the sample expanded into the void space.

**Water uptake**

The flow of distilled water into and out of the testing vessel was measured in each test (Figure 4-11) and a well-defined transient was recorded. The most significant rate of inflow to and outflow from the vessel in each of the tests occurred in the first 20 days of testing. The cumulative flow curves were adjusted to account for the thermal expansion of water entering the testing vessel at an elevated temperature from the syringe pumps at an ambient temperature, using a thermal expansion coefficient of  $2.1 \times 10^{-4} \text{ }^\circ\text{C}^{-1}$  (Tennent, 1971). The flow rate curves were nearly symmetrical and the magnitudes of the in- and outflows were approximately equal in Tests 2, 4 and 8, indicating that the overall change in volume in the vessel was very small in these tests. This is in contrast to Test 13 where the inflow was substantially larger than the outflow, and does not appear to have reached a steady state.

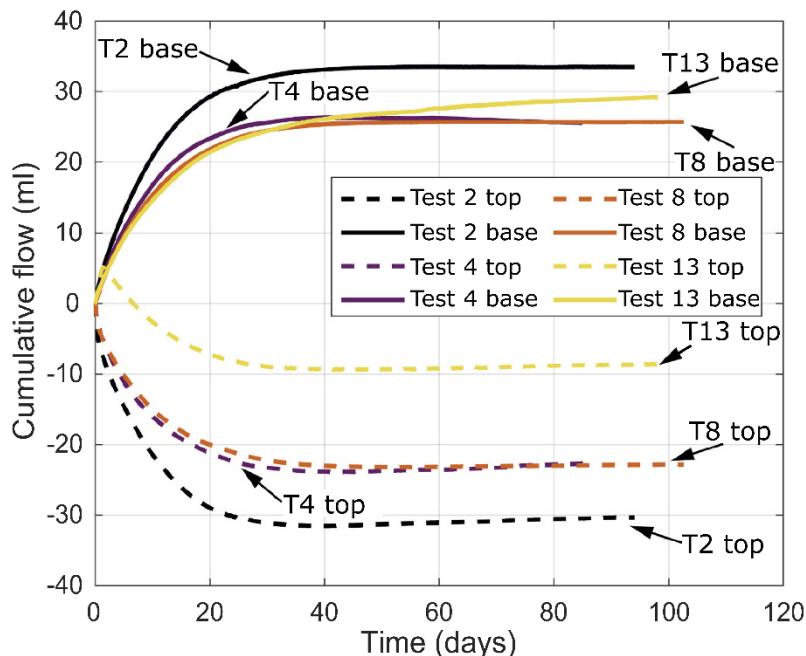


**Figure 4-11. Cumulative flow into the testing vessel from its base and out of the vessel at the top of the apparatus. [BGS (C) UKRI]**

In Test 13, the syringe pump connected to the top of the vessel initially recorded a volume decrease suggesting that fluid was flowing into the sample. At day 1.4, the observed inflow reversed, with the pump recording an outflow until approximately day 35. Between day 35 and day 45 the volume flux was near-constant. From day 45 for the remainder of the test, the pump recorded a very gradual inflow at a rate consistent with the observations made from the pump at the top of the vessel in Test 2. It is not clear what caused the reverse in the direction of flow at the pump connected to the top of the vessel in Test 13, although it is possible that a leak from the outflow pump was causing the volume recorded in the pump to be smaller than it should be.

**Development of pore pressure**

As with the swelling pressure data, pore pressure evolution was a gradual process for all high temperature experiments (Figure 4-12). For pore pressure arrays 1 and 2, the filters connected to these transducers were located next to the sample at the start of each test. Pore pressure array 3 was located closest to the top of the vessel and at the start of Tests 2 and 4 it was adjacent to the initial void space; thus pore pressure array 3 registered the pressurised test fluid immediately. In Test 8, where the starting sample was longer (85 mm), pore pressure array 3, like arrays 1 and 2 in all of the tests, was obstructed by the starting sample. As the test fluid moved into the clay and the clay expanded up into the initial void space, this sensor array began to register a pressure. For array 3 in Test 8 this happened between day 6 and 7 (Figure 4-12).

Once the pressure recorded by each sensor reached the applied pore pressure, the recorded value remained constant for the rest of the test. Pore pressures equilibrated with the applied water pressure soonest in Test 2, were most delayed in Test 8 and took an intermediary amount of time for Test 4. This observation is consistent with the expected reduction in dry density, as a result of sample swelling, which would result in an increase in permeability and more rapid redistribution of fluid within the sample.

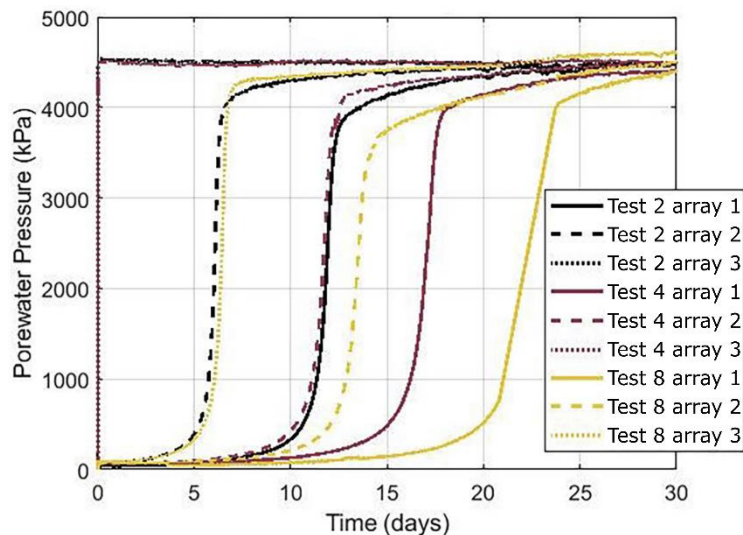


**Figure 4-12. Pore pressures measured by the three radial transducer arrays over the first 30 days of Tests 2, 4 and 8. [BGS (C) UKRI]**

### Post-test moisture content and dry density

As with the ambient test programme, at the end of the testing period (approximately 100 days) each sample was removed from the testing vessel and subsampled to give information on the moisture content as a function of the sample length.

During the testing period, each of the samples had swelled to completely fill the internal volume of the vessel, although there was a large difference in the consistency, water content and density of the material between the top and bottom of the sample. All of the samples experienced a large amount of swelling and they all produced post-test samples that were similar in that there was not much variation in the moisture content in the first half of the sample, from its base to approximately the midplane. In all of the tests, the moisture contents were significantly higher at the top of the sample, and showed large gradients in the region of the internal vessel volume that would have been void space at the start of each test. Figure 4-13 (left) shows that the post-test samples absorbed a minimum of 2–3 times the starting moisture content.

There is a correlation between the length of the starting sample and final moisture contents throughout the post-test sample; the samples that had a longer starting length had lower moisture contents at all points along the sample length. This is unsurprising because the increased volume of clay in the vessel at the start of the test would have needed to absorb a smaller amount of water at either end to induce enough swelling in the material to close the void space. These longer samples also show a trend for smaller moisture content increases in the part of the interior of the vessel that would have been void space at the start of the test.

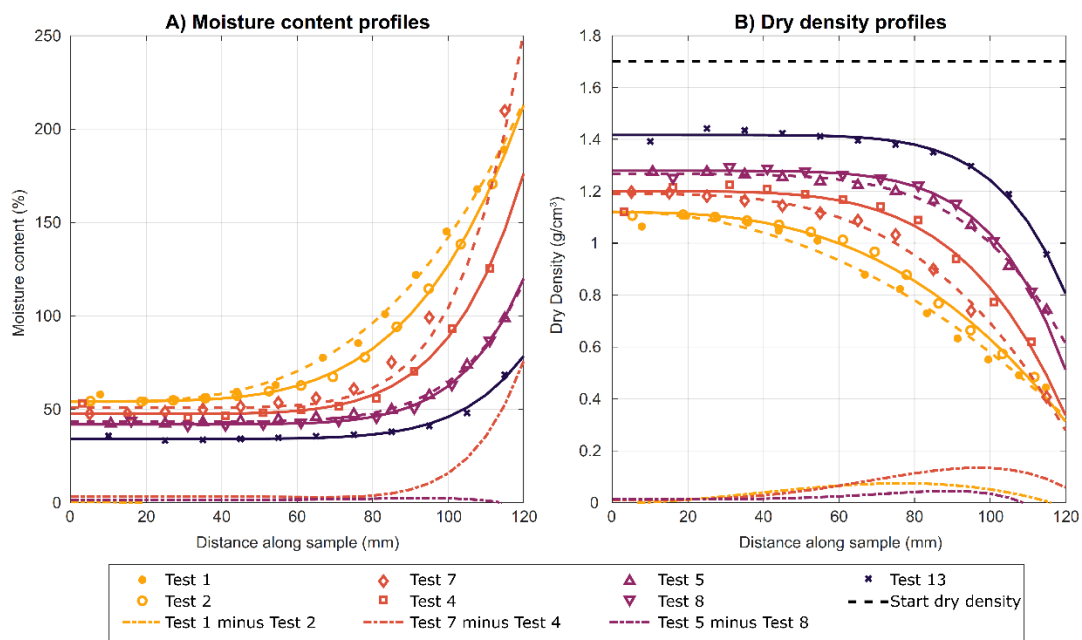


**Figure 4-13. Left: Moisture content and B) dry density profiles along sample lengths for ambient tests (1, 5 and 7) and equivalent elevated temperature tests (2, 4 and 8). Power law fits to the data are shown and the difference between the two power law fits for each test pair is indicated by the dot-dashed line. There was no equivalent 95 mm long ambient temperature test for comparison with Test 13. [BGS (C) UKRI]**

As expected, the same correlations in the moisture content data are observed in the dry densities (Figure 4-13, right); samples with longer starting lengths had higher final dry densities at all points along the length of the sample. Also, the increase in sample length correlates with an increase in dry density in the part of the interior of the vessel that was originally void space at the start of the test. The general trend of these moisture content profiles appears consistent with those measured at ambient conditions and indicate that the system is in a transient state and suggest that the timeframe necessary for homogenisation may be considerably longer.

#### 4.1.4.4. Testing under high salinity conditions

To examine the influence of salinity on the swelling pressure of bentonite in the presence of a void, a series of experiments were conducted using 1 Molar NaCl solution to enable saturation and swelling of the clay (Tests 10, 11 and 12). An additional experiment was also conducted with a 3 molar NaCl solution (Test 16). These hyper-saline experiments were all carried out using Mx80 bentonite samples with an initial dry density of 1.7 g/cm<sup>3</sup> and with varying sample lengths of 65, 85, 75 and 65mm (for Tests 10, 11, 12 and 16, respectively). Testing was conducted at an ambient temperature of ~20°C and, as with previous experiments, bentonite samples were allowed to rehydrate and swell under an applied water pressure of 4.5MPa, for a period of 100 days. It should be noted that there were number of sensor failures in these experiments, meaning that data could be collected at fewer locations than in other tests. Initial swelling pressures were calculated by subtracting the average applied water pressure (at the up- and down-stream pumps) from the recorded axial and radial stresses.

As with previous experiments using deionised water (Section 4.1.4.2), the initially-generated swelling pressures were seen to vary substantially at different measurement locations (Figure 4-14) in each test. Again, the lowest pressures were recorded at the void end of the vessel and the highest pressures were detected at the end where the clay sample was initially present. However, lower swelling pressures were not seen to increase significantly during the course of testing and remained at or below detectable limits throughout the duration of the test, resulting in some sensors reporting negative values. Higher stress value were seen to reduce with time, resulting in a degree of convergence, but a significant heterogeneity in the observed stress distribution persisted in the 1 Molar NaCl tests, even after 100 days (Figure 4-14). When an exceptionally high pore fluid of 3 Molar NaCl was used (Test 16), minimal swelling pressure was detected over the 100 day period. This observation is in line with the expected inhibition of swelling under these conditions and is backed up by observations during decommissioning, at which time the clay at the low density end of the test cell was found to still be in a fluid state (Figure 4-15).

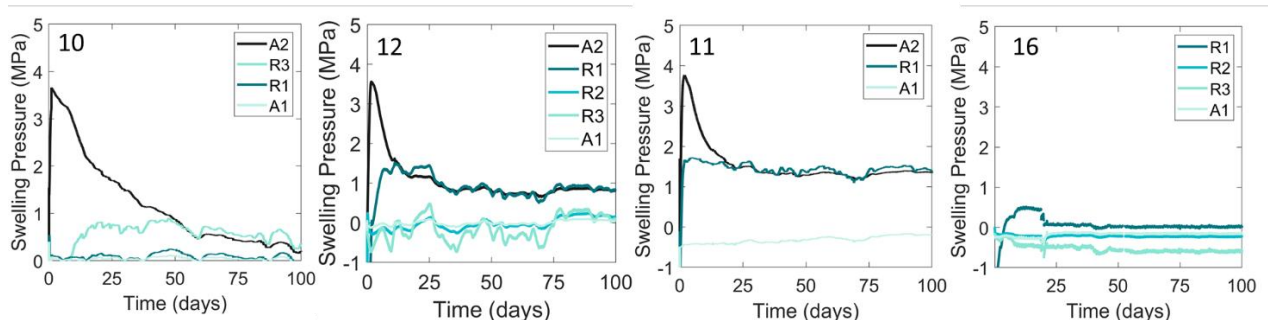


**Figure 4-14. Swelling pressure evolution for high salinity swelling experiments. A 1Molar NaCl solution was used for Tests 10, 12 and 11 and a 3 Molar NaCl solution for Test 16. Sample lengths were 65, 85, 75 and 65mm for Tests 10, 11, 12 and 16, respectively. [BGS (C) UKRI]**



**Figure 4-15.** During decommissioning of Test 16 (3M NaCl), the clay was found to still be in a fluid state at the end of the vessel which original contained only water. [BGS (C) UKRI]

Pore pressure evolution in multiple locations around the sample was also monitored during testing and a marked difference was apparent the equilibration time between experiments (Figure 4-16). The shorter the initial sample and the greater the degree of axial swelling permitted, the more rapidly pore pressures were able to equilibrate along the length of the sample. This observation is consistent with the expected reduction in dry density, as a result of sample swelling, which would result in a drop in permeability and a more rapid redistribution of water within the clay. Comparison of pore pressure evolution between Tests 10 and 16, in which the same degree of axial swelling was permitted, shows a substantially faster approach to hydraulic equilibrium at the higher salinity of 3 Molar NaCl. This can be explained by the low swelling pressures that occurred in this test, which will have resulted in a significantly higher permeability of the clay and more rapid redistribution of water within the sample.

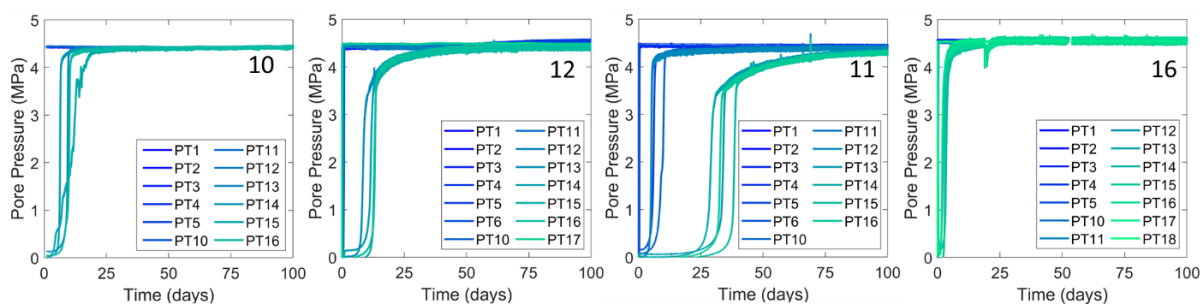


**Figure 4-16.** Swelling pressure evolution for high salinity swelling experiments. A 1Molar NaCl solution was used for Tests 10, 12 and 11 and a 3 Molar NaCl solution for Test 16. Sample lengths were 65, 85, 75 and 65mm for Tests 10, 11, 12 and 16, respectively. [BGS (C) UKRI]

As with previous experiments, moisture content measurements were also made after depressurisation of the samples. The resulting moisture content profiles further demonstrate the influence of salinity and axial strain on the resulting geotechnical properties of the clay after swelling (Figure 4-17). It should be noted that moisture contents for Test 16 could not be included, because the clay was fluid at the low density end after testing.

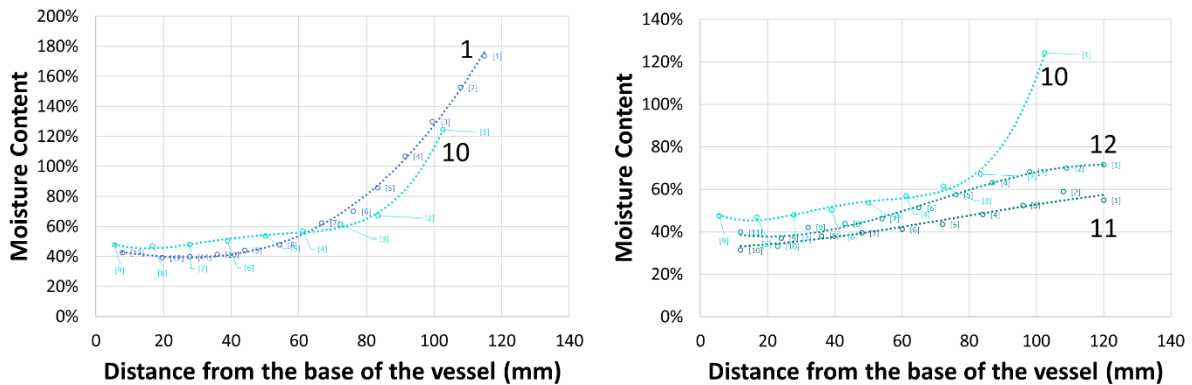


**Figure 4-17. Moisture content profiles along sample length, comparing (i) deionised and 1M NaCl test fluid (left, Tests 1 and 10, respectively) and (ii) differing sample lengths (Tests 10, 12 and 11) at 1M NaCl (right). [BGS (C) UKRI]**

#### 4.1.4.5. CT data

In some of the experiments, conducted in this study, the role of frictional effects along the side wall of the test vessel was investigated using pre and post-test Computed Tomography (CT). Samples were laced with small lead shots in a regular distribution, before compaction to the dry density specified for testing. They were then scanned with a Geotek Rotating X-ray CT scanner, before and after swelling. An example of the results acquired is given in Figure 4-18, which relates to Test 12 (ambient temperature, 1M NaCl, 75mm long sample). The difference in the size of the sample before and after testing reflects the volume change due to swelling. In the pre-test samples, a degree of concavity was noted in the lead shot layers, which is attributed to frictional effects during the initial compaction of the samples.

After swelling this concavity is more pronounced, indicating that friction on the sidewalls may have played a minor role in slowing the sample expansion at the edges. Such frictional effects are a necessary complication of real-world experimentation and will also occur in the GDF environment. Additional testing using the same lead shot arrangement will allow the degree and scaling of such effects to be quantified and used to validate the handling of frictional effects in numerical models.

Nevertheless, these observations do also demonstrate that lead shot within the centre of the clay was displaced substantially during testing, as a result of the swelling process. The CT slice thickness and the number of slices between the lead shot layers can be used to calculate the degree of swelling that occurred along the sample length (Table 4-4). The minimum scan thickness is 8.8  $\mu\text{m}$ , providing a resolution limit for this approach. The resulting strain distribution (Figure 4-19), whilst only for 3 layers, indicates that swelling occurred relatively linearly along the sample length, over the course of the 100 day experiment.

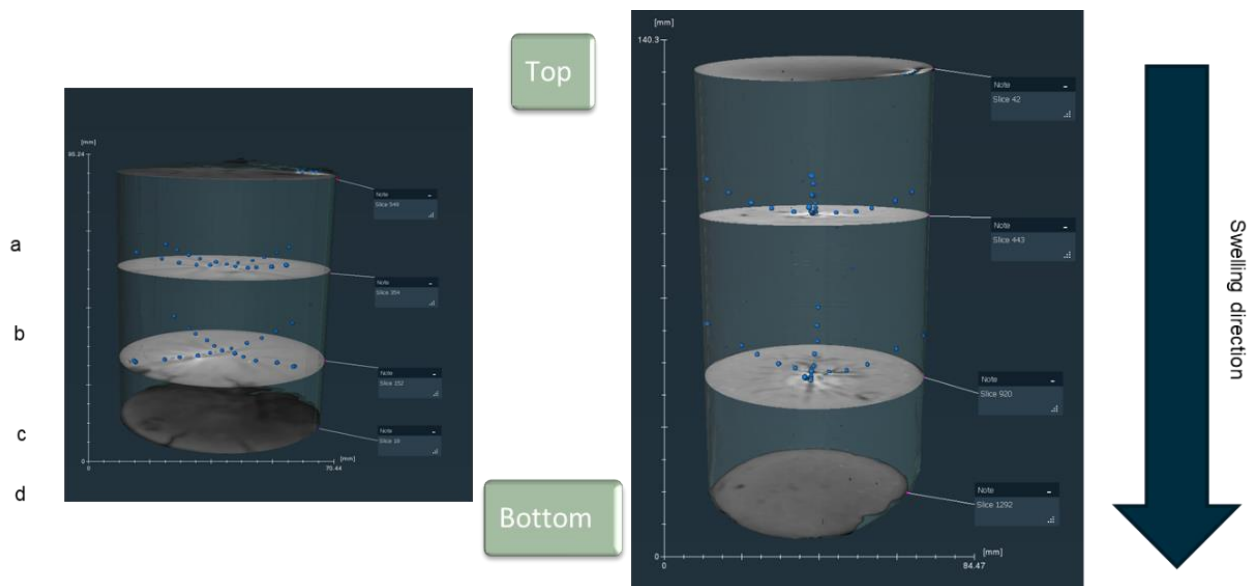
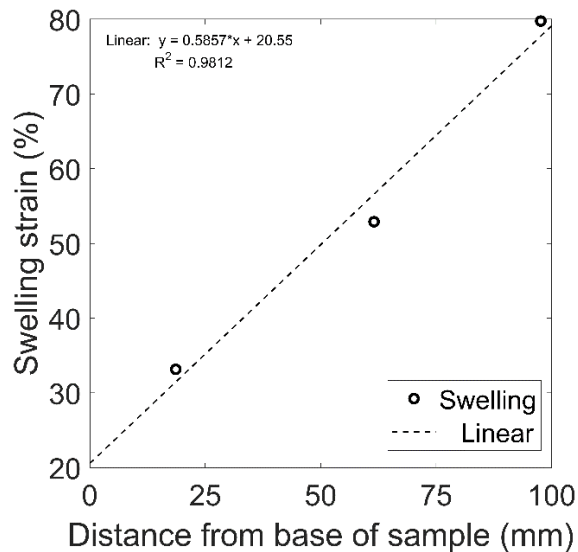


Figure 4-18. CT images showing lead shot distribution before (left) and (after) testing for Test 12, 1 Molar NaCl solution,  $L_0=75\text{mm}$ ,  $P_{dry}=1.7\text{g/cm}^3$ . [BGS (C) UKRI]

Table 4-4. Summary of swelling behaviour calculate from CT images of lead shot. [BGS (C) UKRI]

Layer	Pre-test			Post-test			Summary	
	Slice number	Slice thickness (cm)	Separation (cm)	Slice number	Slice thickness (cm)	Separation (cm)	Swelling between layers (cm)	% increase in layer thickness
a	549	0.0139		42	0.009			
			2.7105			3.609	0.899	33.149
b	354	0.0139		443	0.009			
			2.8078			4.293	1.485	52.896
c	152	0.0139		920	0.009			
			1.8626			3.348	1.485	79.749
d	18	0.0139		1292	0.009			



**Figure 4-19. Swelling strain profile along sample length, as calculated from the increase in CT layers between lead shot tracers. [BGS (C) UKRI]**

#### 4.1.4.6. Discussion

The primary factor under investigation during this test programme has been the impact of voidage present on the development of swelling pressure in bentonite. The size of the void selected in these experiments has been large in relation to the initial sample size, leading to a large axial swelling strain. For the largest voids the result is, therefore, a relatively extreme behaviour, but this provides us with an end member in order to delineate the form of the relationship under investigation. Before considering further the influence of strain on homogenisation of swelling pressure it is, perhaps, helpful to first highlight some of the commonalities observed for these tests despite the differing environmental conditions considered (ambient, elevated temperature and elevated salinity).

Figure 4-20 provides an overview of the swelling pressure curves collected during this test programme. All experiments were conducted at the same applied water pressure and the following behaviours were observed to occur as a result:

- After a 100 days of testing the clay had fully swelled into the void and differential swelling pressures had reduced substantially. This emphasises the enormous capacity of bentonite to fill a void, even in more extreme scenarios. The 3 Molar NaCl test (Test 16) was the one exception to this, in that minimal swelling pressures were generated and the void end was still liquid at the time of disassembly, but such high salinities represent an unlikely scenario for a geological disposal facility.
- A substantial differential in swelling pressures occurred in the early stages of testing, followed by a relatively rapid decline in measured values.
- As might be expected, the lowest pressures were always recorded at the void end of the vessel and the highest pressures were detected at the end where the clay sample was initially present.
- Differential pressures were still relatively significant by the end of day 100, despite the overall rate of pressure decline having reduced to low levels at this time.
- Pore pressure evolution in all tests was seen to occur in a staggered fashion along the length of the vessel, with hydraulic equilibrium being reached soonest at the higher density end, where the compacted clay sample was initially situated.

- The time period required for hydraulic equilibrium to be reached along the sample length was shortest for those samples which experienced the greatest degree of axial strain.

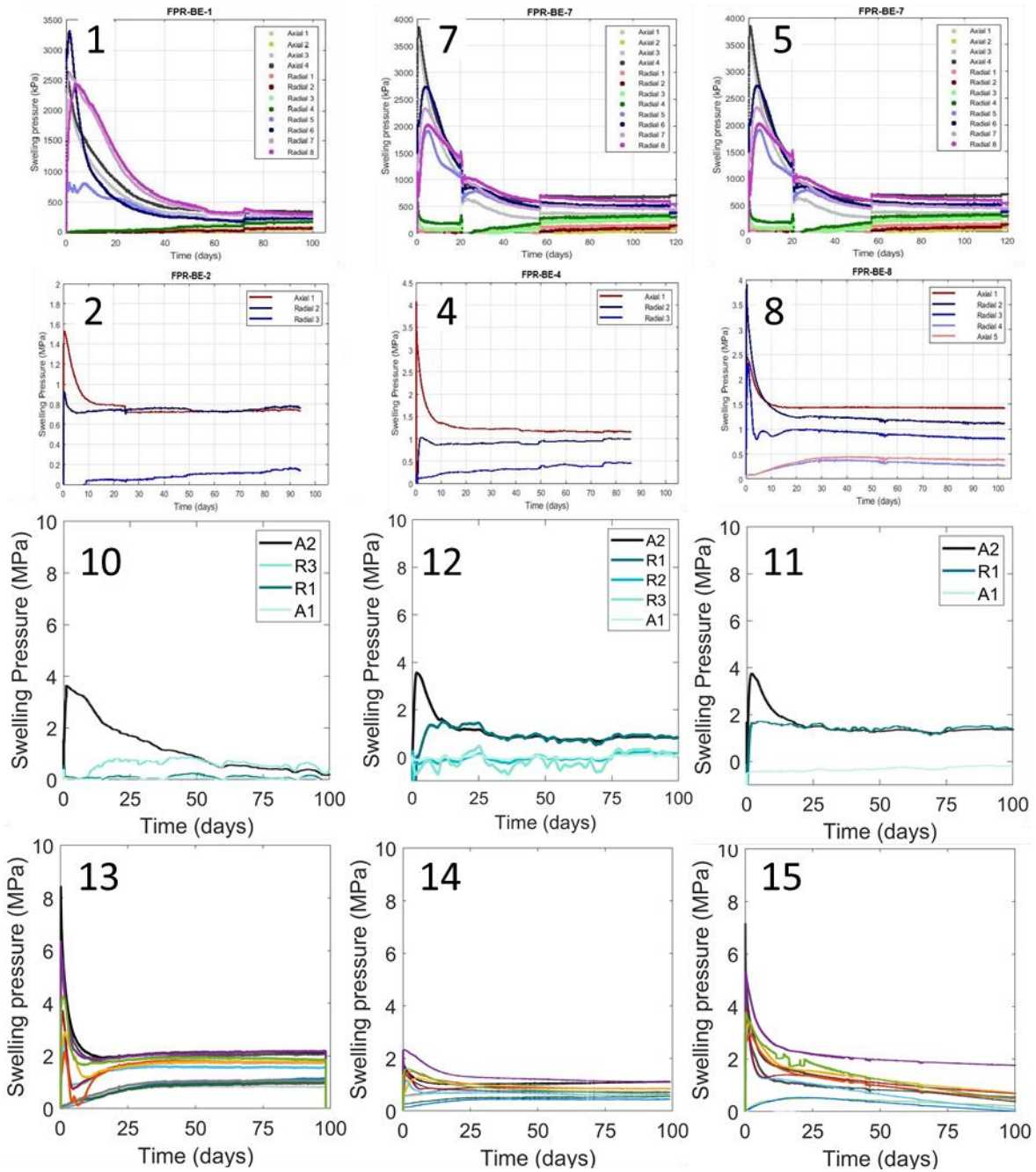


**Figure 4-20. Summary of swelling pressure evolution for sample lengths of 65, 75 and 85mm (left to right) at ambient temperature with deionised water (Tests 1, 7, 5), elevated temperature of 90C (Test 2, 4, 8) and elevated salinity conditions of 1 Molar NaCl (10, 12, 11). Elevated temperature tests from HITEC are also shown (Tests 13, 14, 15), all of which had a sample length of 95mm. Test 13: 100°C, 1.7g/cm<sup>3</sup>, Test 14: 100°C, 1.5g/cm<sup>3</sup>, Test 15: 150°C, 1.7g/cm<sup>3</sup>. [BGS (C) UKRI]**

To compare swelling pressure development between tests, average swelling pressures were calculated at day 100 of each experiment, over an interval of 30 data points. Given the ongoing differential pressures seen at this stage of testing, average pressures values were found to be substantially lower for those sensors closest to the initial void location than those closest to the initial compacted clay end of the pressure vessel interior. Figure 4-21 (left) shows these average axial pressures at both ends of the sample for comparison, as a function of axial strain due to swelling. The latest data from EURAD HITEC programme (Tests 13, 14 and 15) has also been included for comparison. Further information on these tests can be found in reporting for this project (HITEC, 2021).

For ambient conditions (20°C; Tests 1, 5 and 7) the difference in swelling pressures at the ends that were initially clay and void is clearly apparent, as would be expected due to the resulting density gradient, which persisted after 100 days. However, at both ends of the sample a general trend of decreasing swelling pressure at higher axial strains is also clear. This is intuitive behaviour and can be explained by the greater reduction in average sample density as a consequence of the swelling necessary to fill the void space.

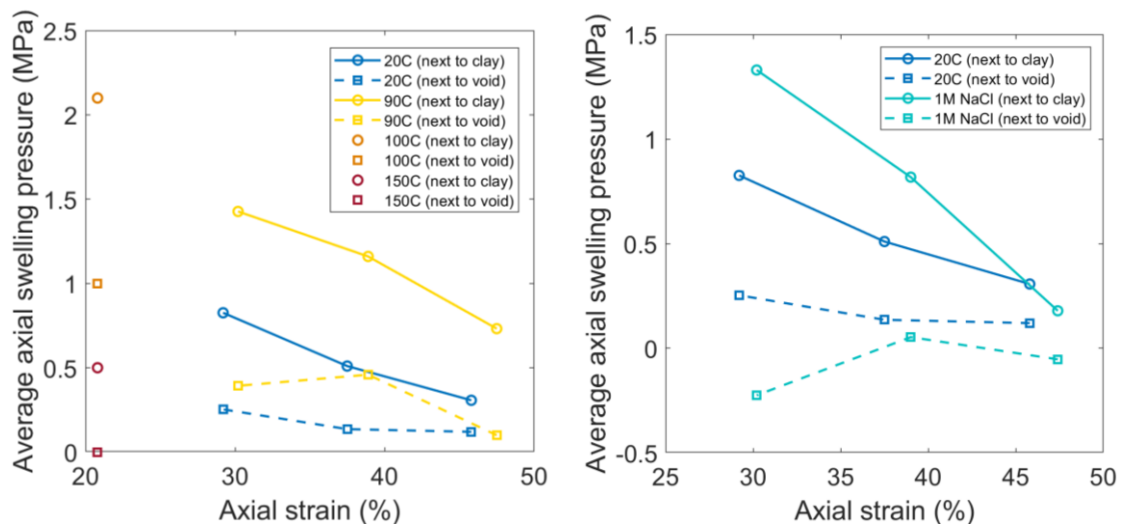


**Figure 4-21. Average axial swelling pressure after 100 days, as a function of axial strain resulting from swelling. Left: ambient and elevated temperature. Right: ambient and elevated salinity. [BGS (C) UKRI]**

In the case of the experiments at 90°C (Tests 2, 4 and 8), the same behaviour is apparent with two additional points to note. Firstly, sensor failures which occurred during the first 2 tests (at lower axial strains) mean that there is no reliable axial stress data at the low density (initially void) end of the sample. Instead, the highest value radial strain is plotted as a proxy, but these values should be considered with caution. Nevertheless, a similar trend to the ambient tests is observed at the opposite end of the sample, suggesting that a similar response occurred. Secondly, average axial swelling pressures in the 90°C tests are notably elevated in comparison to those run at ambient conditions. Given that this behaviour is present at both ends of the sample it seems reasonable to assume that this behaviour would occur even in the absence of a void, as opposed to being the result of redistribution of the clay due to the presence of the void. The cause of this behaviour is not yet clear, but may relate to: (i) the reduction in fluid viscosity at elevated temperatures, which would enhance the uptake of water through the sample or (ii) an increase in the intrinsic capacity of the clay to swell at high temperatures. Further work is needed to explain this behaviour more fully.

Elevated swelling pressures are also observed at both ends of the sample at 100°C, but a substantial drop in swelling pressure is apparent at 150°C. Further geochemical and petrological analysis ongoing to explain these results, but it may relate to the chemical degradation of the clay. Recent findings from the HITEC project indicate that changes in the Cation Exchange Capacity (CEC) of the clay at elevated temperatures may be responsible for a reduced swelling capacity (HITEC, 2021). At both 100 and 150°C, a significant difference in residual pressure is apparent. Measured swelling pressures are comparatively lower for those experiments conducted at or above 100°C, but because less swelling was allowed in these samples it is not yet clear what fraction of this observation is the result of the elevated temperatures, as opposed to the differences in axial strain between tests. Further testing at lower strains is necessary to delineate the form of the relationship between swelling pressure and axial stress more fully.

The same approach was applied to the 1M NaCl tests to produce Figure 4-21 (right). As with deionised water, even after 100 days, higher swelling pressures were measured at the high density end of the sample and lower pressures at the low density end. Under elevated salinity conditions, however, the differential between these values is elevated, with swelling pressure essentially absent at the low density end of the sample. In line with this, the pressures measured at the high density end of the sample are greater than those for testing with deionised fluid, indicating that higher dry density values have persisted longer in the original location of the clay sample under elevated salinity conditions. This finding suggests that suppression of clay swelling at these higher salinities is likely to impact the void-filling process.

Inspection of the swelling pressure curves for the entire test programme indicate that the degree of spread in swelling pressures differs notably between experiments. To quantify the degree of homogenisation that occurred, the residual swelling pressure differential was determined by finding the difference in pressure between the maximum and minimum values observed after 100 days of testing. Figure 4-22 shows this metric plotted across all tests, as a function of axial strain. A correlation is clearly apparent, indicating that a greater degree of homogenisation occurs over the test interval for higher axial strains (larger initial void size). This behaviour can be explained by a comparatively greater drop in dry density resulting from the greater degree of expansion of the clay. A larger increase in hydraulic permeability would be expected to occur at these higher strains, providing more rapid access to water along the sample length. This is also consistent with pore pressure observations, which indicate that hydraulic equilibrium is established more rapidly at higher axial swelling strains.

It should be noted that due to sensor failures, the pressure differential may have been higher for the 90°C tests, except the one conducted at the largest axial strain. Based on the current data set, however, it is not possible to infer a significant impact of heating on the degree of homogenisation over the timeframe of testing. Inspection of the data does hint that higher salinities result in an elevated trend, however, with a higher degree of heterogeneity for equivalent strains. Nevertheless, additional data is necessary to provide confidence in this statement.

What is clear is that the primary control on the swelling pressures observed is the degree of axial swelling permitted in each test. This finding implies that where the clay has minimal room for expansion, the homogenisation process is likely to take substantially longer to occur. It will, therefore, be important to understand the rate of homogenisation under these conditions and whether the remaining differential swelling pressures observed are small enough to be tolerated for as long as they persist. Additional testing at low strains will also help to confirm whether this relationship is truly linear and whether these environmental conditions play a more significant role for smaller voids.

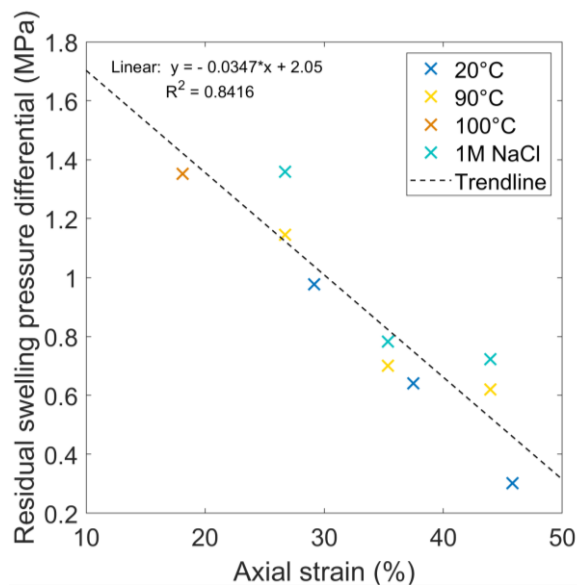


**Figure 4-22. Residual swelling pressure differential after 100 days of testing, as a function of axial strain. [BGS (C) UKRI]**

#### 4.1.5 Conclusions

A suite of experiments were conducted for this task, examining the evolution of swelling and pore pressures in bentonite clay, as a function of the degree of swelling permitted into a void space. This behaviour was examined under ambient conditions and also at elevated temperatures and salinities.

A few key observations from this test programme are summarised as follows:

- In almost all tests, after 100 days the clay had fully swelled into the void and differential swelling pressures had reduced substantially. This emphasises the enormous capacity of bentonite to fill a void, even in more extreme scenarios.
- The larger the degree of swelling into a void, the smaller the swelling pressures that were measured along the sample length, as might be expected by the consequent reduction in dry density reducing swelling capacity.
- Swelling pressures across the entire sample length were higher at elevated temperatures of 90 and 100°C, but a substantial reduction in values was apparent at 150°C. Additional XRD, petrological imaging and geotechnical analysis is underway that may provide additional insight into these observations.
- At elevated salinities, clay that swelled into the void never generated significant swelling pressures during the testing period.
- In almost all tests differential pressures were still relatively significant by day 100, despite the overall rate of pressure decline having reduced to low levels at this time.
- Pore pressure evolution in all tests was seen to occur in a staggered fashion along the length of the vessel, with hydraulic equilibrium being reached soonest at the higher density end, where the compacted clay sample was initially situated.
- The time period required for hydraulic equilibrium to be reached along the sample length was shortest for those samples that experienced the greatest degree of axial strain.
- This is consistent with the observations in relation to residual heterogeneity, which was found to be highest for those samples that experienced the smallest axial swelling strains.

As such the primary implication of this test programme is that the larger the void present, the greater the capacity for the clay to reach hydraulic equilibrium and the faster the homogenisation of swelling pressures. Additional testing at low strains will help to confirm whether this relationship is truly linear and the degree to which environmental conditions have an impact in the case of smaller voids. Further work using this data-set should help to assess the rate at which swelling pressure homogenisation occurs, as a function of strain, so as to provide a better understanding of likely swelling pressure ranges that may be expected at lower strains. Such information is key to assessing whether any residual heterogeneity is significant or can be tolerated. The data generated by these experiments also provide a suitable resource for parameterisation and validation of numerical models that can further assess the long-term homogenisation behaviour of bentonite in geological disposal facilities.

## **4.2 Swelling into a void under suction control or flow control (CIEMAT)**

In the framework of the project Beacon (Bentonite Mechanical Evolution), CIEMAT performed a series of tests to follow the density and water content changes in compacted bentonite samples saturated under limited axial swelling conditions and at the same time observe the closing of the initial gap. FEBEX bentonite initially compacted with its hygroscopic water content (~14%) at a nominal dry density of 1.7 g/cm<sup>3</sup> was used in all the tests. The hydration of the samples took place with water in the vapour phase through the sample surface closest to the gap (GAP-vapour tests), and with liquid water (GAP-liquid), either through the sample surface away from the gap or from the gap surface. The experimental procedures and detailed results are presented in Villar et al. (2021a).

### **4.2.1 Material**

The FEBEX bentonite is a 900-t batch of bentonite extracted from the Cortijo de Archidona quarry (Almería, Spain) and processed in 1996 for the FEBEX project. The processing consisted in homogenisation, air-drying and manual removing of volcanic pebbles on-site and, at the factory, crumbling, drying in a rotary oven at clay temperatures between 50 and 60°C and sieving through a 5-mm mesh. The physico-chemical properties of the FEBEX bentonite, as well as its most relevant thermo-hydro-mechanical and geochemical characteristics obtained during the FEBEX project were summarised in e.g. ENRESA (2006) and updated in e.g. Villar (2017).

The smectite content of the FEBEX bentonite is close to 90 wt.%. The smectitic phases are actually made up of a montmorillonite-illite mixed layer, with 10-15 wt.% of illite layers. Besides, the bentonite contains variable quantities of quartz (2±1 wt.%), plagioclase (3±1 wt.%), K-feldspar (traces), calcite (1 wt.%) and cristobalite–trydimite (2±1 wt.%). The cation exchange capacity is 98±2 meq/100 g, the main exchangeable cations being calcium (33±2 meq/100 g), magnesium (33±3 meq/100 g) and sodium (28±1 meq/100 g). The predominant soluble ions are chloride, sulphate, bicarbonate and sodium.

The liquid limit of the bentonite is 102±4 %, the plastic limit 53±3 %, the density of the solid particles 2.70±0.04 g/cm<sup>3</sup>, and 67±3 % of particles are smaller than 2 µm. The hygroscopic water content in equilibrium with the laboratory atmosphere (relative humidity 50±10 %, temperature 21±3 °C) is 13.7±1.3 %. The external specific surface area is 67 m<sup>2</sup>/g and the total specific surface area is about 725±47 m<sup>2</sup>/g.

The swelling pressure ( $P_s$ , MPa) of FEBEX samples flooded with deionised water up to saturation at room temperature and constant volume conditions can be related to dry density ( $\rho_d$ , g/cm<sup>3</sup>) through the following equation (Villar, 2002):

$$\ln P_s = 6.77\rho_d - 9.07 \quad [4.1]$$

The difference between experimental values and this fitting is, on average, 25 percent.

The hydraulic conductivity ( $k_w$ ) of the bentonite at room temperature is also exponentially related to its dry density, according to the following empirical expressions: for dry densities of less than 1.47 g/cm<sup>3</sup>:

$$\log k_w = -6.00 \rho_d - 4.09 \quad [4.2]$$

for dry densities in excess of 1.47 g/cm<sup>3</sup>:

$$\log k_w = -2.96 \rho_d - 8.57 \quad [4.3]$$

The variation in the experimental values with respect to these fittings is smaller for low densities than it is for higher values, with an average –in absolute values– of 30 percent.

Relationships between suction and water content obtained for different bentonite dry densities under isochoric conditions can be found in Villar (2007), Villar et al. (2012a, 2019). For a sample compacted at dry density 1.6 g/cm<sup>3</sup> with hygroscopic water content the initial suction value would be ~120 MPa.

## 4.2.2 Methodology

The objective of these tests was to follow the density and water content changes in a block sample saturated under limited axial swelling conditions and at the same time observe the closing of the initial gap. FEBEX bentonite samples were compacted inside stainless steel rings and a gap was left on top. In all cases the granulated bentonite was initially compacted with its hygroscopic water content (~14%) at a target dry density of 1.7 g/cm<sup>3</sup>. These samples were hydrated with water either in vapour (GAP-vapour) or liquid phase (GAP-liquid) and were dismantled after different periods of time. The final water content and dry density of the bentonite at different levels of the sample were measured, as well as the pore size distribution.

### 4.2.2.1. GAP-vapour tests

In the GAP-vapour tests the samples were compacted in a cell with perforated lids, and saturated from the top surface, where the gap was, using the vapour transfer technique (Figure 4-23), which consists in subjecting the sample to a certain relative humidity in a close container (vacuum desiccator). The diameter of the samples was 3.8 cm and the initial height was 2.5 cm. The bottom part of the cell was sealed, and on the top surface of the sample a porous stone was placed, so that water transfer took place through this porous medium. The initial gap thickness was of 0.5 cm. The evolution over time of the gap closing and the changes in bentonite overall water content and dry density were followed by periodically measuring the gap height and weighing the cylinder with the sample inside (Figure 4-24). A total of 26 cells were tested and dismantled at different periods of time between 15 days and 15.5 months. The samples were subjected to relative humidities corresponding to total suctions of 6 and 0.5 MPa keeping a constant temperature of 20°C. These suctions were obtained by placing in the desiccators a sulphuric acid solution of concentration 10% and a sodium chloride solution of concentration 0.6%, respectively.

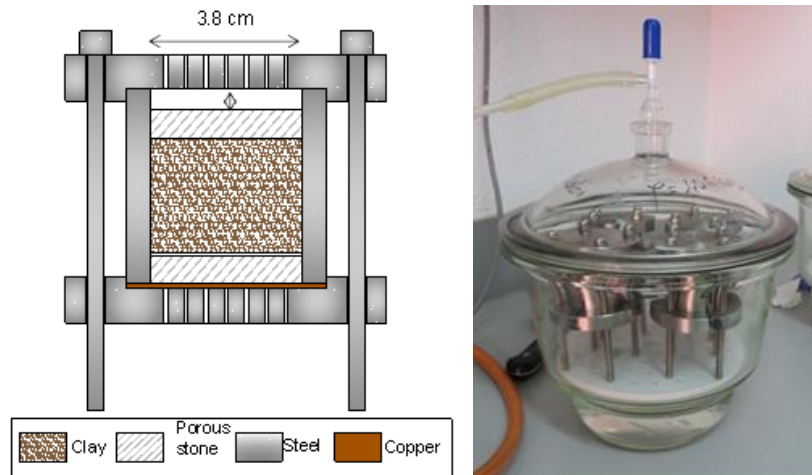


**Figure 4-23. Schematic representation of the GAP-vapour test cells and desiccator with cells inside**



**Figure 4-24. Intermediate measurement of gap height in GAP-vapour tests**

#### 4.2.2.2. GAP-liquid tests

In the GAP-liquid tests the bentonite was saturated with water in the liquid phase under a very low flow rate either from the bottom surface, opposite to the gap or from the gap surface (as in the GAP-vapour tests). The initial characteristics of the samples were the same in both cases for all the tests: the bentonite was compacted with its hygroscopic water content inside the cell ring applying a uniaxial pressure of  $\sim 29$  MPa, to reach a nominal dry density of  $1.7 \text{ g/cm}^3$ . The diameter of the resulting samples was 50 mm and the nominal initial height 25 mm, leaving a gap of  $\sim 0.8$  cm on top of them. The sample was sandwiched between porous stones (Figure 4-25).

Deionised water was injected either through the bottom or through the top with a pressure/volume controller at a rate of  $0.07 \text{ cm}^3/\text{h}$ , and the part of the cell opposite to the hydration surface was open to atmosphere (Figure 4-26 shows the configuration for the tests with water injection opposite to the gap). In the set of tests with saturation through the gap (except in the first one, GL6), the porous stone was saturated prior to the start of the test. Injection pressure was atmospheric at the beginning of the tests. Both injection pressure and water intake were measured online.

The tests were performed at laboratory temperature ( $22.9 \pm 1.6^\circ\text{C}$ ). The results of 12 dismantled tests are presented in this report.

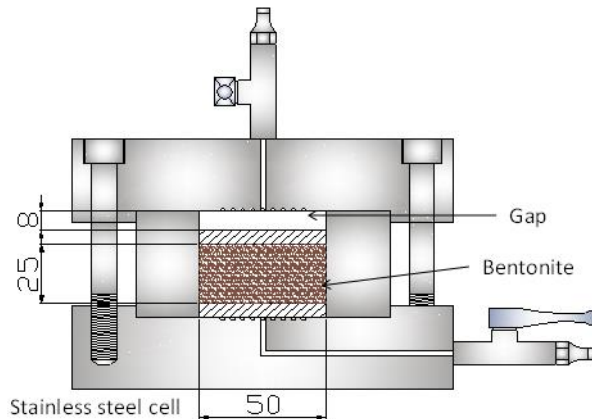


**Figure 4-25. Blueprint of the cell for the GAP-liquid tests with the sample inside**

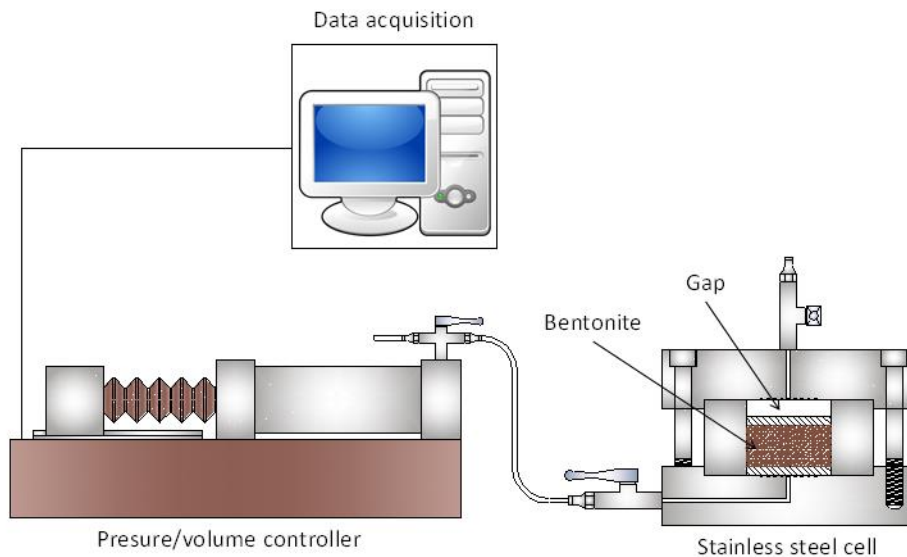


**Figure 4-26. Schematic representation of the assembly for GAP-liquid tests (injection opposite to gap)**

#### 4.2.2.3. Postmortem tests

At the end of the two kinds of tests the samples were measured, weighed, and cut in transversal sections (Figure 4-27). In each section subsamples were obtained to determine water content, dry density and pore size distribution (Figure 4-28). Three sections were usually defined, because a minimum section volume was necessary to obtain subsamples coherent enough to determine their dry density.

The mass of water was determined as the difference between the mass of the sample and its mass after oven drying at  $110^\circ\text{C}$  for 48 hours. Dry density ( $\rho_d$ ) is defined as the ratio between the mass of the dry sample and the volume occupied by it prior to drying. The volume of the specimens after extraction from the cell was determined by measuring their dimensions,

whereas the volume of the subsamples of each section was determined by immersing them in a recipient containing mercury and by weighing the mercury displaced, considering a density of mercury of 13.6 g/cm<sup>3</sup>. The water content was determined in the subsamples used for the dry density determination and also in an additional subsample of each section (Figure 4-28). The gravimetric water content ( $w$ ) is defined as the ratio between the mass of water and the mass of dry solid expressed as a percentage. The mass of water was determined as the difference between the mass of the sample and its mass after oven drying at 110°C for 48 hours.



**Figure 4-27. Final subsampling after extraction of samples from the GAP tests cells**

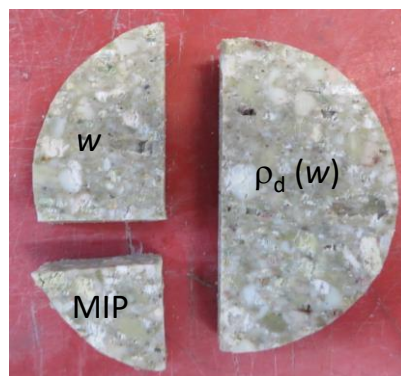


**Figure 4-28. Subsamples of a section for postmortem determinations**

The pore size distribution of the subsamples was determined by mercury intrusion porosimetry (MIP). The samples were put in the ice condenser of a Telstar LioQuest equipment at -30°C for 3 hours. Subsequently, they were lyophilised for 22 hours at a temperature of -50°C under a vacuum of 0.2 mbar, so that to eliminate the water in the pores by sublimation. Thereafter, they were heated at 25-30°C for 3 hours. The samples were later kept in a desiccator until the MIP analysis. The porosimeter used was a Micromeritics AutoPore Series IV 9500, which allowed the exploration of pore diameters between 0.006 and 600 μm. Prior to mercury injection the sample was outgassed by applying a vacuum of 50 μm-Hg. Afterwards the mercury injection pressure was increased from 2.7 kPa to 220 MPa in 109 steps. To determine the extrusion branch of the curve, the pressure was released in 56 steps down to a pressure of 68.6 kPa. A contact angle of mercury of 139° both on advancing and of receding on the clay surface was considered.

## 4.2.3 Results

### 4.2.3.1. GAP-vapour tests

#### Evolution over time

The GAP-vapour cells were checked every week. For that, the lids were unscrewed and the cell with the sample inside was weighed and the height of the gap measured (Figure 4-24). This way, the evolution over time of the overall bentonite water content and dry density was followed, as reported in the Tables included in Villar et al. (2021a). Since the bentonite was compacted with hygroscopic water content, the initial suction of the samples was very high, about 100 MPa. For this reason, all the samples took water under the two suctions applied (6 and 0.5 MPa), swelled and tended to close the gap. Figure 4-29 and Figure 4-30 show the evolution of the overall water content and dry density of the samples in the tests performed under suctions 6 and 0.5 MPa. All the tests were performed in duplicate, and in most cases the results of the two samples were coherent.

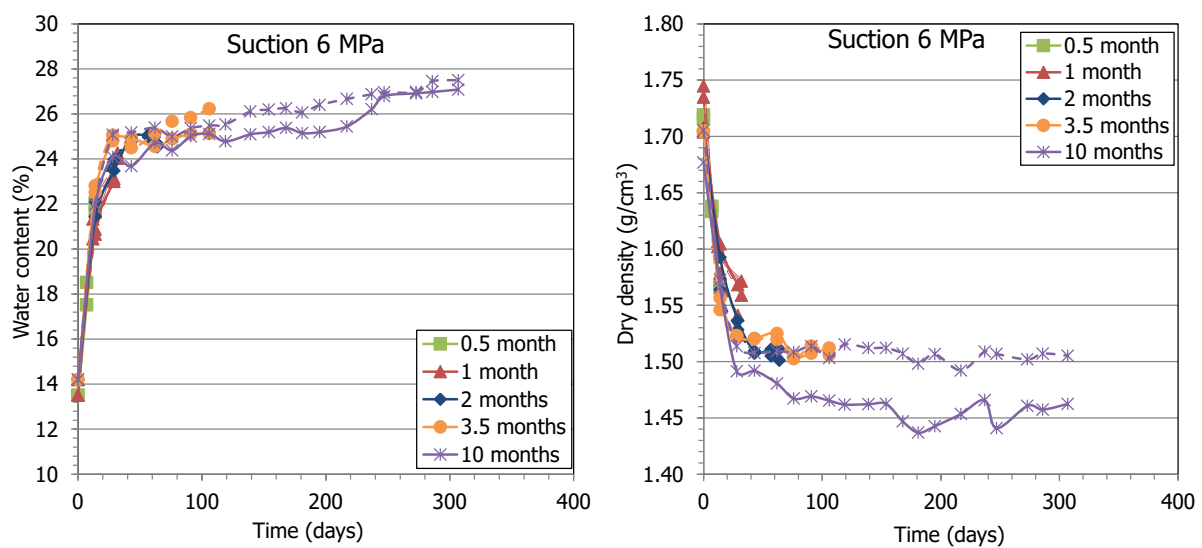


**Figure 4-29. Evolution of water content and dry density in GAP-vapour tests under suction 6 MPa**

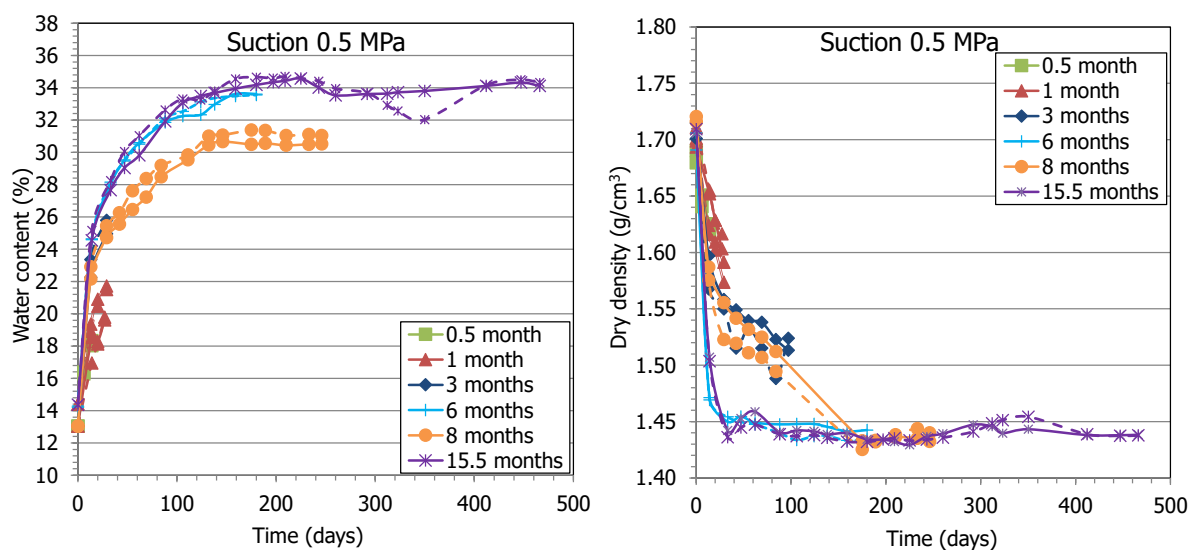


**Figure 4-30. Evolution of water content and dry density in GAP-vapour tests under suction 0.5 MPa**

The initial and final values of dry density and water content for each test performed under the two different suctions are shown in Table 4-5 and Table 4-6 and the final values are plotted in Figure 4-31. In the first stages, for times shorter than 40 days, the samples under 6 MPa took more water and swelled more. For longer equilibration times the trend inverted and consequently the final water contents of samples under 0.5 MPa were higher and their dry densities lower. After approximately 300 days the equilibrium water content for a suction of 6 MPa was reached (~27%), whereas for suction 0.5 MPa about 250 days were needed to reach the equilibrium water content (~34%). These equilibrium values are slightly above those expected for bentonite compacted to similar dry densities (1.44-1.51 g/cm<sup>3</sup>) and subjected to the same suctions under confined conditions (Figure 4-32).

**Table 4-5. Initial and final overall water content (w) and dry density (ρ<sub>d</sub>) of the GAP-vapour samples tested under 6 MPa**

Sample	Time (days)	Initial w (%)	Initial ρ <sub>d</sub> (g/cm <sup>3</sup> )	Initial gap (mm)	Final w (%)	Final ρ <sub>d</sub> (g/cm <sup>3</sup> )	Final gap (mm)	Final Δh/h <sub>0</sub> (%)
9	14	13.5	1.72	4.77	21.5	1.57	2.21	9.6
10		13.5	1.72	5.06	21.9	1.57	2.50	9.6
3	29	14.2	1.71	4.59	22.4	1.57	2.20	8.9
4		14.2	1.70	4.85	22.6	1.54	2.02	10.6
11	32	13.5	1.74	5.20	22.6	1.57	2.34	11.0
12		13.5	1.73	5.31	22.3	1.56	2.37	11.3
1	64	14.2	1.70	4.89	24.8	1.51	1.52	12.8
2		14.2	1.71	4.89	25.0	1.50	1.30	13.7
6	106	14.2	1.71	4.68	25.0	1.51	1.31	12.8
7		14.2	1.70	5.08	25.4	1.51	1.62	13.2
5	307	14.2	1.68	4.90	24.5	1.46	1.02	14.7
8		14.2	1.71	5.08	24.8	1.51	1.61	13.3

**Table 4-6. Initial and final overall water content (w) and dry density (ρ<sub>d</sub>) of the GAP-vapour samples tested under 0.5 MPa**

Sample	Time (days)	Initial w (%)	Initial ρ <sub>d</sub> (g/cm <sup>3</sup> )	Initial gap (mm)	Final w (%)	Final ρ <sub>d</sub> (g/cm <sup>3</sup> )	Final gap (mm)	Final Δh/h <sub>0</sub> (%)
19	14	13.1	1.69	4.39	17.5	1.63	3.23	4.0
20		13.1	1.68	4.51	16.9	1.62	3.37	3.9
17	27	13.1	1.69	4.37	19.5	1.60	2.80	5.6
18		13.1	1.71	5.04	19.3	1.62	3.42	5.8
21	29	14.4	1.70	4.60	20.4	1.57	2.40	8.1
22		14.4	1.70	4.77	19.7	1.59	2.92	6.8
15	97	13.1	1.71	4.91	27.9	1.51	1.44	13.3
16		13.1	1.70	5.07	29.7	1.52	1.99	11.6
23	180	14.4	1.69	4.45	32.9	1.44	0.00	17.2
24		14.4	1.71	4.82	32.8	1.43	0.00	19.0
13	246	13.1	1.72	5.14	32.2	1.43	0.07	19.8
14		13.1	1.72	5.08	32.8	1.44	0.10	19.5
25	466	14.4	1.71	4.82	32.6	1.44	0.02	18.6
26		14.4	1.71	4.92	32.7	1.44	0.05	18.9

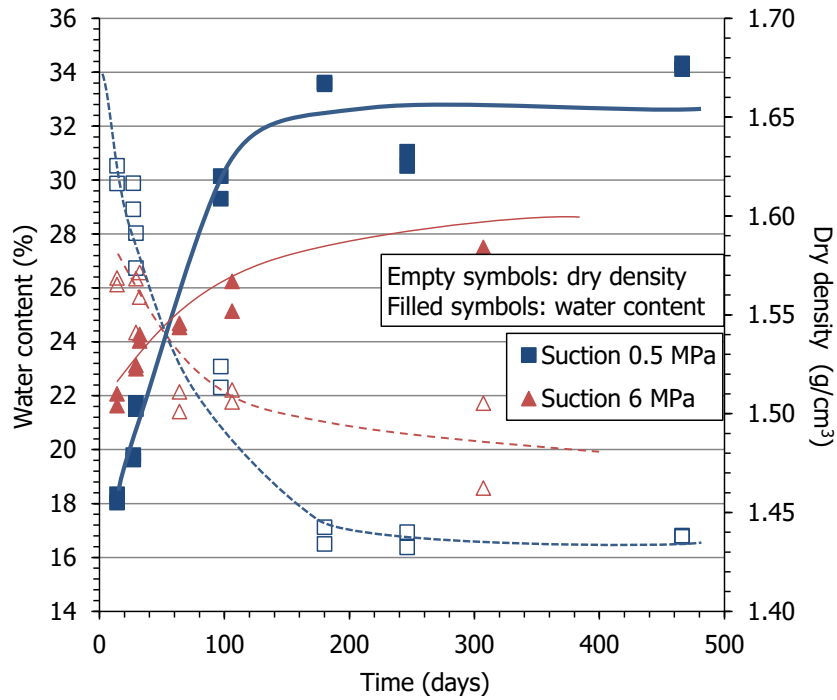


Figure 4-31. Final results of dry density and water content in GAP-vapour tests

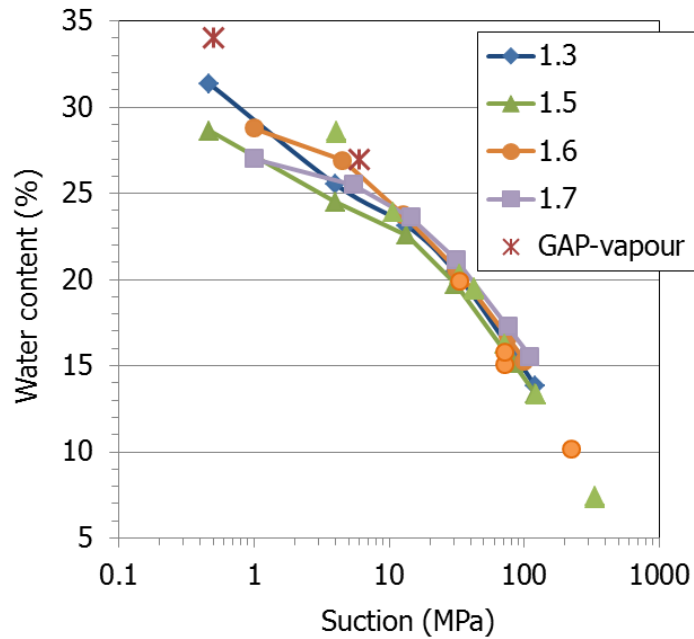


Figure 4-32. Equilibrium values reached in the GAP-vapour tests and water retention curves of FEBEX bentonite compacted to different dry densities (indicated in g/cm³) obtained under isochoric conditions. Results from Villar 2007, Villar et al. 2012 and unpublished

**Final physical state**

After different equilibration times the cells were dismantled, the bentonite weighed and measured and cut into sections for the postmortem determinations, as described above. Figure 4-33 shows the appearance of some of the samples at the end of the tests, with the top of the sample presenting a crumbled, uneven surface because of the free swelling. The results obtained for the different subsamples in terms of water content and dry density are detailed in Villar et al. (2021a) and plotted in Figure 4-34 and Figure 4-35. In the case of the samples tested under suction 6 MPa, the shorter tests showed a water content gradient from top to bottom. This gradient attenuated over time and was coupled to an inverse dry density gradient: towards the top of the sample, where the gap was, the water content was higher and the dry density lower. In fact, the upper surface of the sample crumbled easily, since it swelled into a void (see Figure 4-33). For this reason it was difficult in some cases to cut subsamples and determine their dry density. The water content gradients in the samples tested under suction 0.5 MPa were in all cases less steep and kept more or less constant as the overall water content increased. As well, the dry density gradients were softer for the samples tested under the lower suction. This could be explained by the slowness of the saturation process in the last case (Figure 4-31).



**Figure 4-33: Appearance of samples after extraction of the cells and subsampling for postmortem analyses**

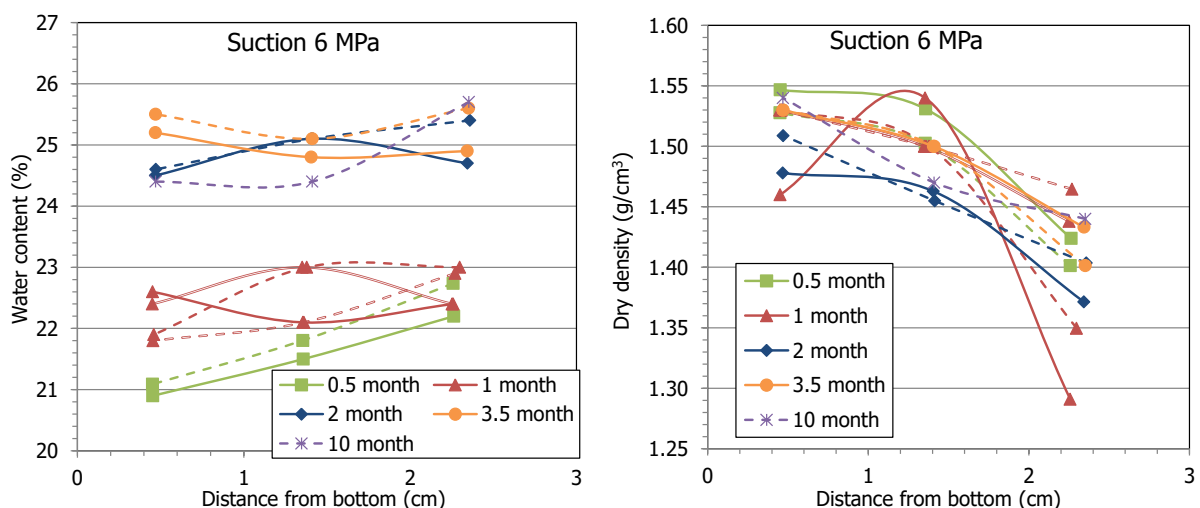


**Figure 4-34. Final water content and dry density of subsamples of the tests performed under suction 6 MPa**

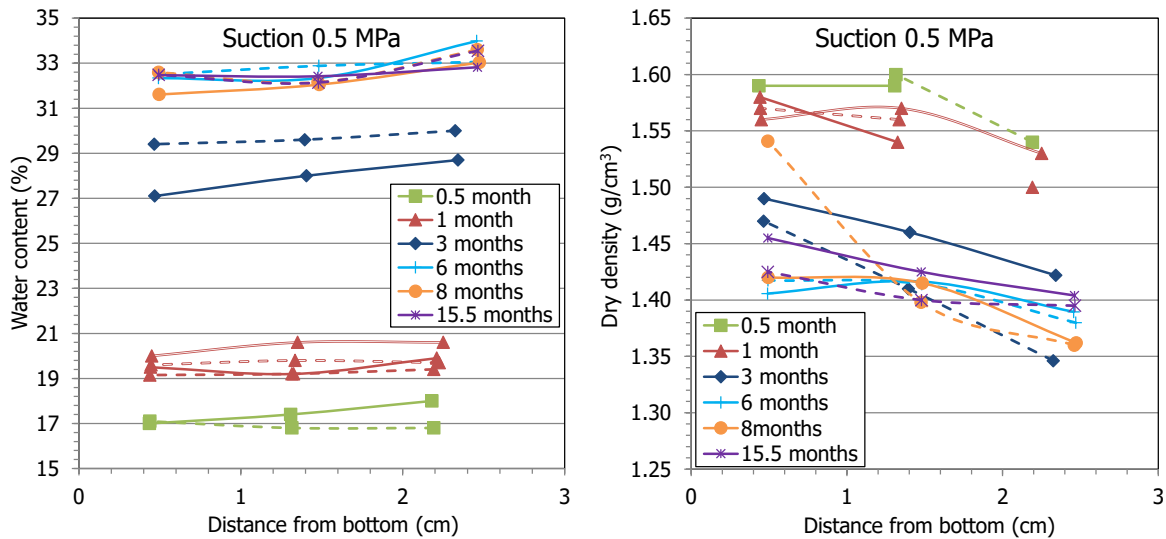


**Figure 4-35. Final water content and dry density of subsamples of the tests performed under suction 0.5 MPa**

**Pore size distribution**

From each cell three other subsamples taken at different distances from the gap were used to determine the pore size distribution by MIP. The determination was performed in the subsamples of all the cells, but only those corresponding to the shorter and longer tests performed under each suction are shown (the others are included in Villar et al. 2021a). Figure 4-36 and Figure 4-37 show the incremental curves of mercury intrusion as a function of the mean pore diameter of the diameter size intervals corresponding to each pressure increase step of the samples from these cells. The curve corresponding to a FEBEX sample compacted with approximately the same dry density and water content as the initial conditions used in the cells (1.69 g/cm<sup>3</sup>, 13.5%) is also included (labelled "Initial"). For all the samples there were two pore families corresponding approximately to pores larger and smaller than 200 nm. In several THM models, this pore size represents the limit separating inter-aggregate from intra-aggregate pores, the latter not affected by density changes (e.g. Sánchez et al. 2005). There is discussion on the criteria that can be followed to select this delimiting value (Yuan et al. 2020). The 'valley' criterion was chosen in this work, consisting of using the lowest point of the valley between the two peaks of a bimodal distribution. The figures show that the volume of pores larger than 200 nm increased during testing, particularly as the test was longer. The average size of the macropores also tended to increase.

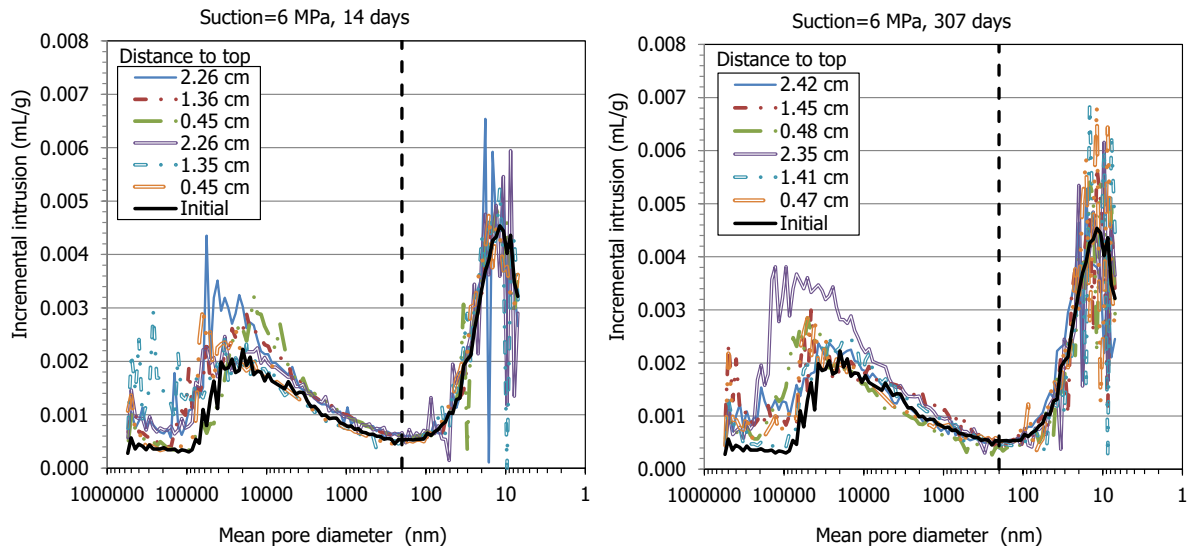


**Figure 4-36. Pore size distribution of subsamples tested in GAP-vapour cells under suction 6 MPa for two different times and for the initial block expressed as incremental mercury intrusion (duplicate samples for each duration)**

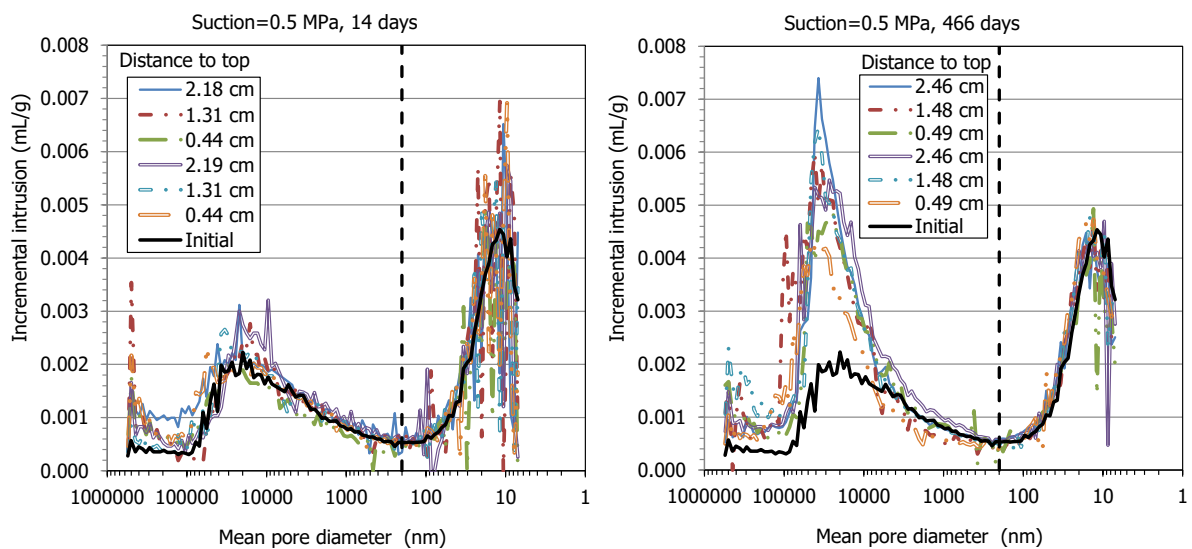


**Figure 4-37. Pore size distribution of subsamples tested in GAP-vapour cells under suction 0.5 MPa for two different times and for the initial block expressed as incremental mercury intrusion (duplicate samples for each duration)**

The mercury intrusion method allows access to be gained only to part of the macroporosity (pores of diameter smaller than  $\sim 550 \mu\text{m}$ ) and to part of the mesopores (those of diameters larger than 7 nm), since mercury does not intrude the microporosity (pores of a size of less than 2 nm, according to Sing et al. (1985)). An estimation of the percentage of pores actually intruded can be made by comparing the actual void ratio of the samples (computed from their dry density and density of solid particles) and the apparent void ratio calculated from mercury intrusion by the equipment software. Thus, the percentage of pores intruded by mercury in these subsamples was between 42 and 74%. The non-intruded porosity is usually associated in compacted clays to the pores of a size smaller than the limit of the apparatus

(7 nm). There is uncertainty in this approach, since it is possible that pores larger than 7 nm were not intruded because of the bottleneck effect. All of the volume of such pores will be allocated to the threshold radius class of the most restricted part of the entryway, which will result in an overestimation of the smaller pore sizes volume. Likewise, although in compacted clay materials pores larger than those that can be quantified by MIP are not expected, pores of this size could be present in the samples closest to the gap of the shorter tests, which were friable and crumbly. A visual inspection of the samples upon dismantling allowed to conclude that this was the case for the upper part of the samples shown in Figure 4-38, all of them corresponding to tests shorter than 32 days.



**Figure 4-38. Appearance upon dismantling of some of the shorter GAP-vapour tests**

Hence, to take into account the large pores observed in those upper subsamples, an estimation of the volume of pores larger than 550  $\mu\text{m}$  has been made following this approach (Villar et al. 2021b):

At the beginning of a MIP test the calibrated sample holder is filled with mercury under a low injection pressure. Considering the sample mass and the volumes of the sample holder and of mercury intruded, the dry density of the sample is computed by the equipment software. This initial mercury injection is considered by the equipment as the zero value for the rest of the MIP test, which actually starts when injection pressure is increased above this value. Thus, all the large porosity filled during this initial step is disregarded. The comparison between the dry density determined by the equipment at this step and the actual dry density of the sample allows computing the volume of pores larger than 550  $\mu\text{m}$ : when the sample contains a significant volume of large pores, the dry density determined by the porosimeter is considerably higher than the actual dry density of the sample, whereas if there are not large pores the two values tend to be similar.

Taking all the above into account, the void ratio corresponding to pores larger and smaller than 200 nm ( $e_M$  and  $e_m$ , macro and micro, respectively) was recalculated, assuming that the non-intruded porosity corresponds to pores smaller than the equipment injection capacity and, in some upper subsamples, also to pores larger than 550  $\mu\text{m}$ . The values are plotted in Figure 4-39 and Figure 4-40 for subsamples of the specimens tested under suctions 6 and 0.5 MPa, respectively. In all cases the largest proportion of void ratio corresponded to the pores of diameter smaller than 200 nm, the volume of which increased during testing with respect to the reference sample. Also, the percentage of void ratio corresponding to pores larger than 200 nm increased with respect to the reference sample, since the total void ratio increased because of the bentonite swelling into the gap. In fact, the highest increase in void ratio was experienced by the samples closest to the gap, which agrees with their lower dry density (Figure 4-34 and Figure 4-35). The overall void ratio increase took place very quickly in the samples tested under 6 MPa (it was already clear after 15 days) but took longer in the samples tested under suction 0.5 MPa. This agrees with the different hydration kinetics of the two sets of tests commented above and would indicate that hydration under free swelling conditions brought about an increase in the volume of all pore sizes. Furthermore, in all the tests performed under suction 6 MPa the macropore void ratio was higher in the subsample closest to the gap than in the other subsamples. In contrast, this difference among subsamples was less clear in the longer tests performed under suction 0.5 MPa.

The ratio between the void ratio corresponding to pores smaller ( $e_m$ ) and larger ( $e_M$ ) than 200 nm is plotted on the right-hand side of the Figures. This ratio was lower in the subsample closest to the gap for the tests shorter than 2 months performed under suction 6 MPa, whereas it remained similar to the initial one in the rest of subsamples. In the shorter tests ( $\leq 3$  months) performed under suction 0.5 MPa, this ratio increased at the bottom and tended to decrease towards the part of the samples closest to the hydration surface (gap), which would mean that the percentage of macropores increased in the most hydrated bentonite. Over time these differences inside a given sample were obliterated by the increase in void ratio corresponding to larger pores. As a result, all the subsamples from larger tests ( $\geq 6$  months), those in which the gap was closed, had  $e_m/e_M$  ratios lower than the initial one and similar among them, which would be an additional indication of equilibrium being reached.

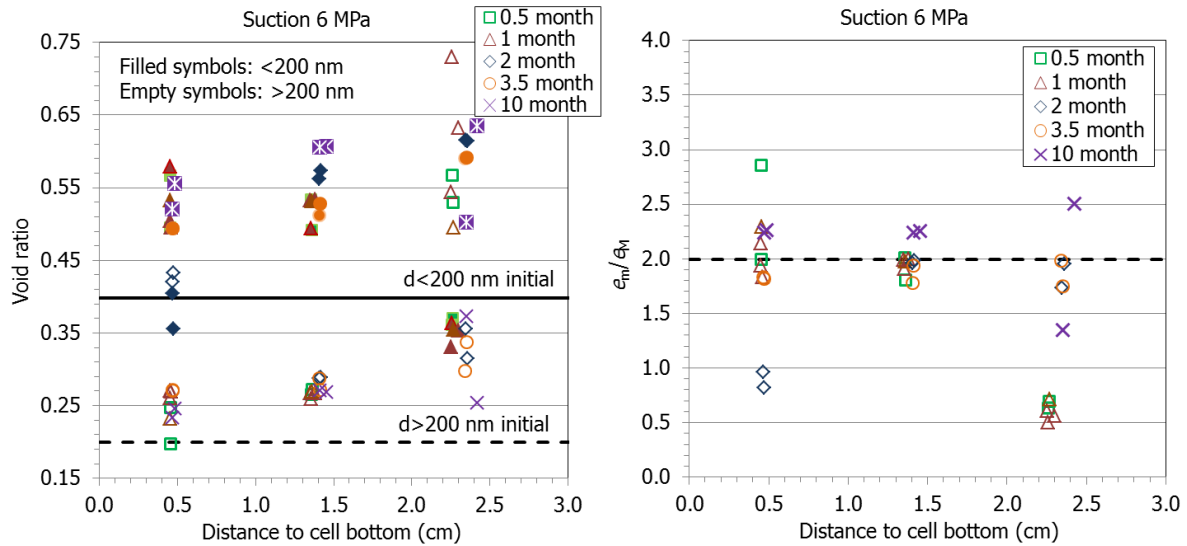


**Figure 4-39.** Void ratio corresponding to pores smaller ( $e_m$ ) and larger than 200 nm ( $e_M$ ) obtained by MIP in samples tested under suction 6 MPa (left) and ratio between both (right). The thick horizontal lines indicate the values for the reference sample

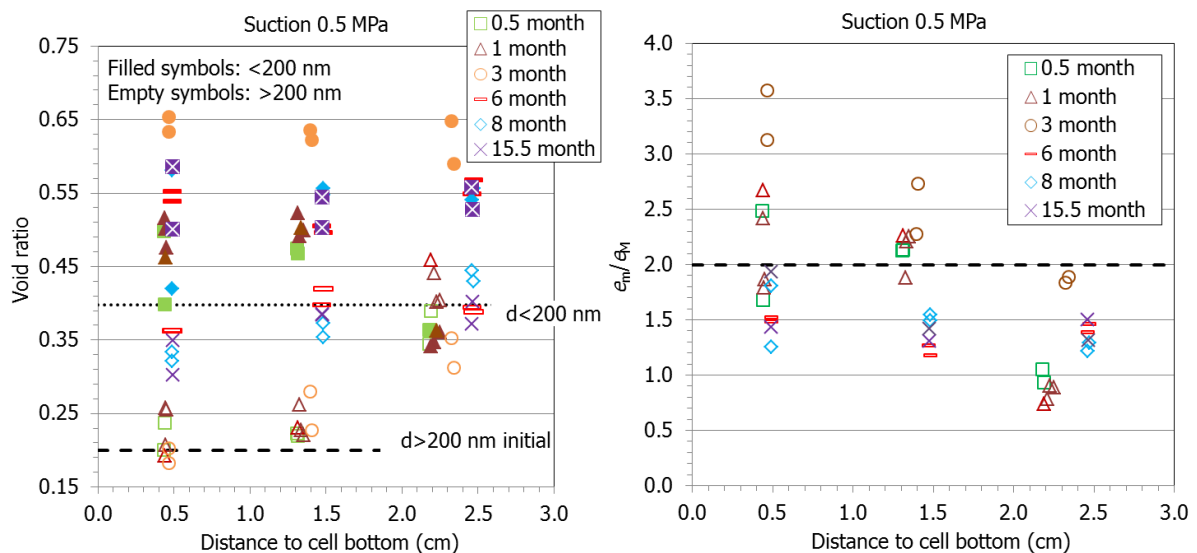


**Figure 4-40.** Void ratio corresponding to pores smaller ( $e_m$ ) and larger than 200 nm ( $e_M$ ) obtained by MIP in samples tested under suction 0.5 MPa (left) and ratio between both (right). The thick horizontal lines indicate the values for the reference block

The evolution of void ratio over time corresponding to pores larger and smaller than 200 nm can be seen in Figure 4-41 as a function of the position along the sample for the two suction values. In the tests under suction 0.5 MPa, close to the gap the macropore void ratio quickly increased, but then remained almost constant. In the middle part of the sample the increase in macropore void ratio was more gradual and reached a maximum after 180 days (when the gap was already closed), remaining constant afterwards. For the bottom part of the sample the increase in macropore void ratio took place only after 100 days. The increase in micropore void ratio was more uniform across a given sample, had a maximum after 97 days (once the gap was closed) and then remained approximately constant. In the tests under suction 6 MPa, there was a quick and huge increase in macropore void ratio close to the gap that was

reduced after two months and then did not change much. The middle and bottom parts of the samples behaved similarly over time, with the pores <200 nm accounting for most of the overall increase in void ratio.

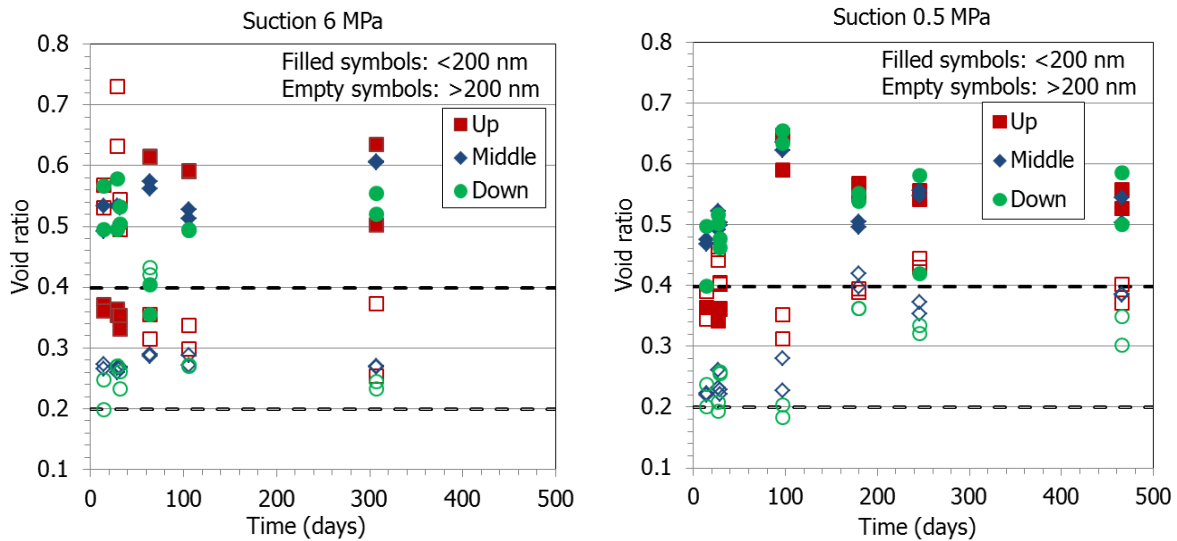


**Figure 4-41. Evolution of void ratio over time corresponding to pores larger and smaller than 200 nm for the two sets of GAP-vapour tests**

#### 4.2.3.2. GAP-liquid tests

The tests in which the bentonite was saturated with liquid water were performed either injecting the water from the surface of the block opposite to the gap, or from the gap surface. The results of these two sets of tests are described separately. The initial characteristics of the samples were the same in both cases for all the tests: hygroscopic water content, nominal dry density of 1.7 g/cm<sup>3</sup>, nominal height of 2.5 cm, a gap of 8 mm on top of them (Figure 4-25). For the GAP-liquid tests only the state of the sample at the end of each test is available, because their state could not be periodically checked without disturbing too much the state of the samples.

##### **Injection opposite to the gap**

Six tests of the same initial characteristics were performed and dismantled after different hydration times (Table 4-7). In contrast with the GAP-vapour tests, the gap in these GAP-liquid tests was in the opposite side to the hydration surface. It was observed that the injection pressure (Figure 4-42), which was null at the beginning of the experiments, started to increase after ~7 days from the beginning of water injection, which was necessary to keep the flow rate imposed (0.07 cm<sup>3</sup>/h). In all cases the upper outlet remained open to atmosphere during the whole duration of the test, except in the case of the longest one (GL1). In this test the injection pressure increased up to 2 MPa before a blackout made the injection pressure decrease. When the system was re-started the upper outlet was closed because water was flowing out. The tables with the numerical values of the pressure and water intake along the tests are included in Villar et al. (2021a).

**Table 4-7. Initial and final characteristics of the GAP-liquid tests**

Test	Duration (days)	Initial w (%)	Initial $\rho_d$ (g/cm <sup>3</sup> )	Initial $S_r$ (%)	Initial sample h (cm)	Initial gap h (cm)	Final w (%)	Final $\rho_d$ (g/cm <sup>3</sup> )	Final $S_r$ (%)	Final sample h (cm)	Final gap h (cm)
GL1	63	13.3	1.65	57	2.58	0.83	45.2	1.25	103	3.41	0.00
GL2	14	13.3	1.67	59	2.54	0.87	32.2	1.32	83	3.21	0.20
GL3	28	13.8	1.67	60	2.53	0.90	44.9	1.23	102	3.43	0.00
GL4	7	14.3	1.67	62	2.52	0.89	24.1	1.50	81	2.81	0.60
GL5	4	14.4	1.66	62	2.55	0.85	18.9	1.58	72	2.69	0.70
GL12	10	13.1	1.69	59	2.52	0.90	26.3	1.43	80	2.98	0.44

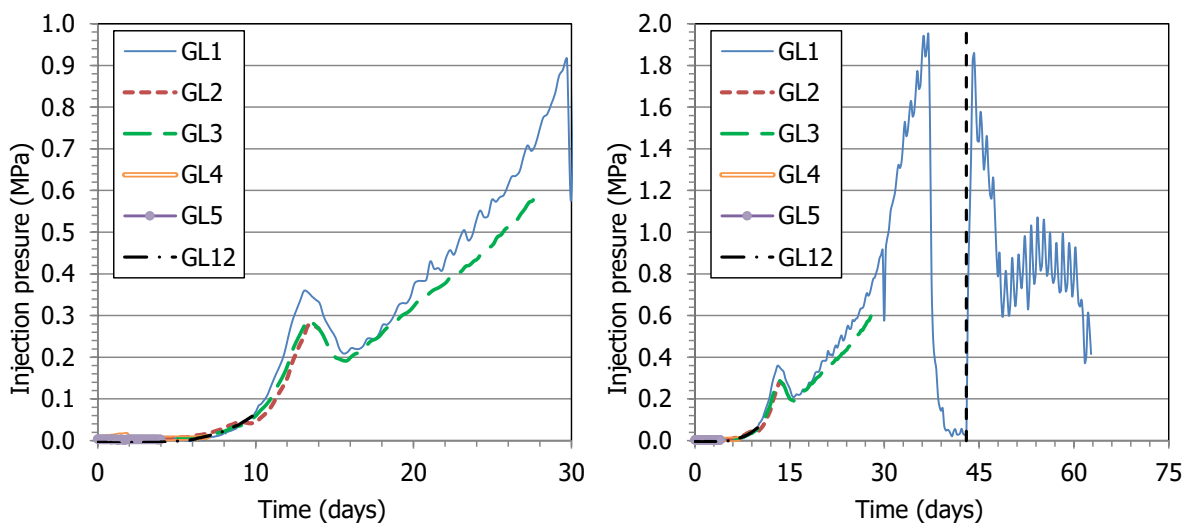


**Figure 4-42. Injection pressure evolution in the GAP-liquid tests (the dotted vertical line indicates the closing of the upper outlet in test GL1)**

The evolution of the gap height (which was initially 0.8 cm) and of the bentonite degree of saturation are shown in Figure 4-43. After about 30 days the gap was completely closed and the samples were fully saturated.

The water content and dry density at different levels of the samples measured at the end of the tests are plotted in Figure 4-44. The overall water content increased with time but was always higher towards the hydration surface. In the same way the dry density decreased as the gap was filled and was always lower towards the hydration surface. Although the gradients attenuated over time, they did not disappear, even when the sample was completely saturated: the water content near the hydration surface remained higher and the dry density lower (tests GL1 and GL3).

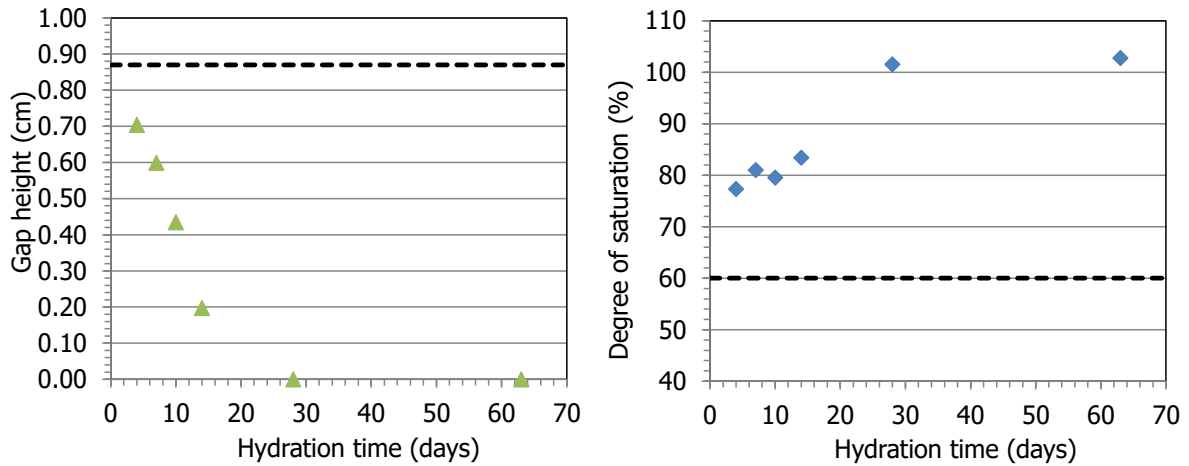


**Figure 4-43. Evolution of gap height and of bentonite degree of saturation in GAP-liquid tests (the dotted horizontal lines indicate the initial values)**

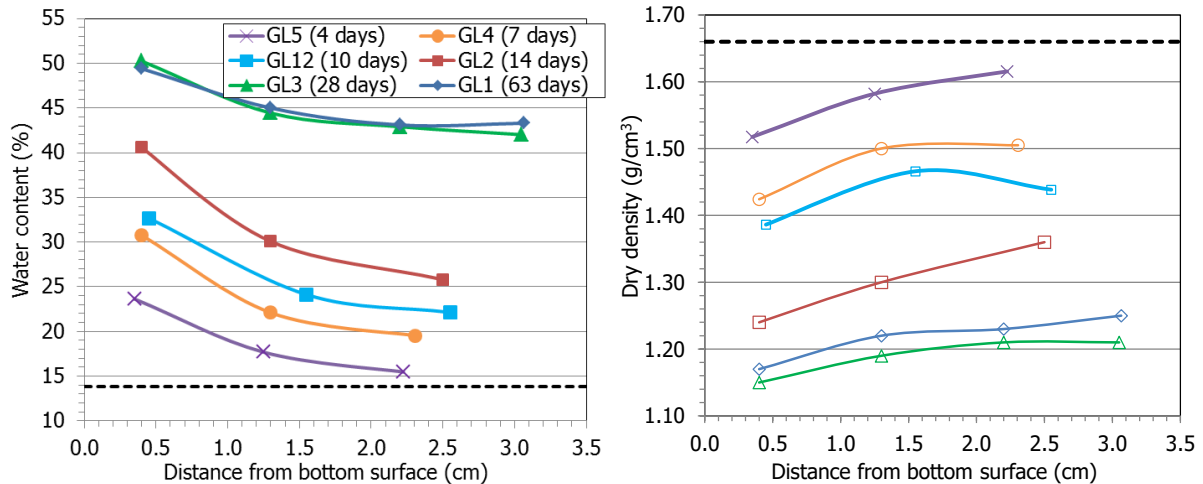


**Figure 4-44. Final water content and dry density of GAP-liquid tests at different levels of samples (the dotted horizontal lines indicate the initial values)**

### Injection from gap

Six tests in which the bentonite was saturated from the gap (as in the GAP-vapour tests) were performed and dismantled after different hydration times (Table 4-8). They all had the same nominal initial characteristics. In all cases the bottom outlet remained open to atmosphere during the whole duration of the test. At the beginning of the tests, a flow rate was prescribed and the gap on top of the cell became initially inundated. During the first test, GL6, it was realised that it was no possible to identify how much water had actually been taken by the bentonite, by the porous stone on top, or had gone between the porous stone and the cell wall. To partly solve this uncertainty, in the rest of the tests the upper porous stone was saturated prior to test initiation. In test GL10 a saturated porous stone was placed in contact with the bentonite sample inside the cell (in the same way as for tests GL7 to GL11), but no water injection took place. After 6 days, the cell was dismantled and the water content along the sample was determined, so that to estimate the water quantity taken by the sample from the porous stone. The average water content of the bentonite increased to 17.8% in one day just by adsorption of the water in the porous stone, and in two days to 18.6%, with a considerable gradient from top to bottom.

**Table 4-8. Initial and final characteristics of the GAP-liquid tests with hydration from gap**

Test	Duration (days)	Initial w (%)	Initial $\rho_d$ (g/cm <sup>3</sup> )	Initial $S_r$ (%)	Initial sample h (cm)	Initial gap h (cm)	Final w (%)	Final $\rho_d$ (g/cm <sup>3</sup> )	Final $S_r$ (%)	Final sample h (cm)	Final gap h (cm)
GL6	7	14.3	1.66	62	2.55	0.87	29.0	1.22	64	3.42	0.00
GL7 <sup>a</sup>	7	14.4	1.67	63	2.54	0.88	33.6	1.22	75	3.42	0.00
GL8 <sup>a</sup>	22	14.1	1.67	61	2.56	0.85	45.1	1.25	105	3.41	0.00
GL9 <sup>a</sup>	14	13.6	1.70	63	2.53	0.89	41.2	1.26	98	3.41	0.00
GL10 <sup>a</sup>	6	14.9	1.68	67	2.52	0.89	20.9	1.36	57	3.06	0.35
GL11 <sup>a</sup>	2	14.3	1.67	62	2.51	0.91	18.3	1.47	59	2.87	0.78

<sup>a</sup> upper porous stone saturated before starting water injection

In order to keep the flow rate prescribed (0.07 cm<sup>3</sup>/h), the injection pressure was null at the beginning of the experiments and started to increase after 11 days from the beginning of injection (Figure 4-45). The degree of saturation when this happened was between 75 and 87%. The tables with the numerical values of the pressure and water intake along the tests are included in Villar et al. (2021a).

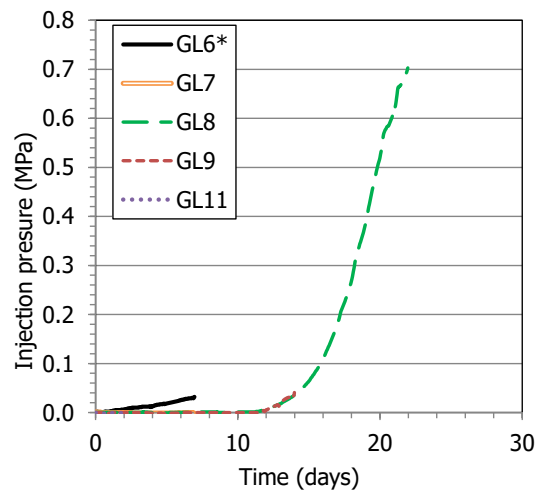


**Figure 4-45. Injection pressure evolution in the GAP-liquid tests with hydration through the gap**

The evolution of the gap height and of the bentonite degree of saturation are shown in Figure 4-46. The gap was closed after 7 days. After 22 days the sample seems to be fully saturated ( $S_r=105\%$ ), but this should have to be checked with a longer test.

The external and internal water content and dry density of the bentonite at different levels along the samples are plotted Figure 4-47. The swelling of the bentonite surface close to the gap was irregular in the shorter tests (GL6, GL7, GL11) and the water content of the central area was higher than in the periphery (Figure 4-48). In contrast, for the longer tests the water content along the whole sample was higher in the external part of each section than in the internal part. The comparison of the two longer tests (GL8 and GL9) shows that the water content close to the gap seems to have reached its higher value, but had not equilibrated in yet farther away from the gap.

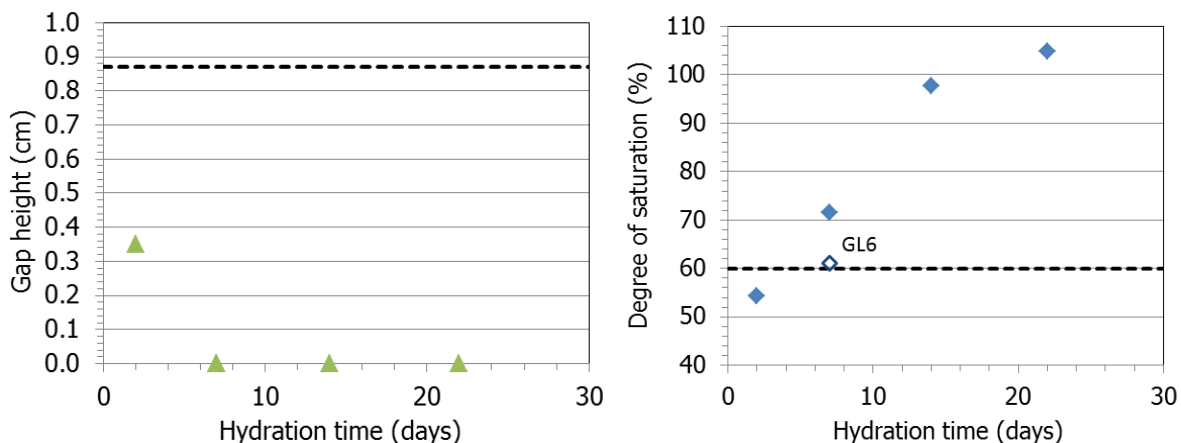


**Figure 4-46. Evolution of gap height and of bentonite degree of saturation in GAP-liquid tests with hydration from gap (the dotted horizontal lines indicate the initial values)**

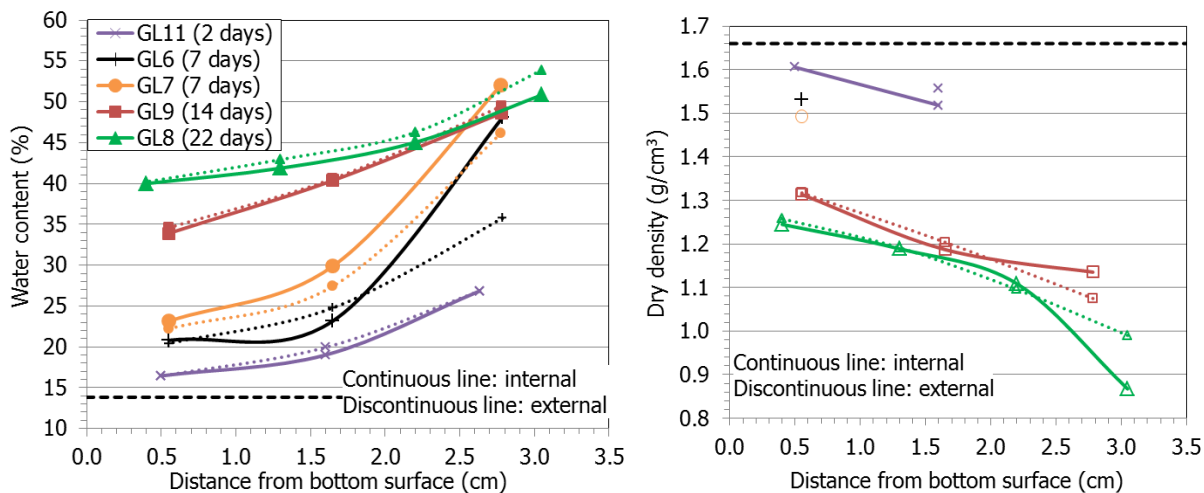


**Figure 4-47. Final water content and dry density of GAP-liquid tests with hydration from gap at different levels of samples**



**Figure 4-48: Final appearance (upper and lateral views) of sample GL7 (7 days)**

**Comparison**

In this section, the two different types of GAP-liquid test (hydration from bottom surface and from gap surface) are compared. When hydration took place from the gap, it was faster than the hydration from the opposite surface, as witnessed by the evolution of water content (Figure 4-49). Consequently, the dry density also decreased initially faster and reached earlier the lowest possible value when the bentonite was hydrated from the gap. As a result, the gap closed sooner when hydration occurred through the gap surface, 7 vs. 28 days. Figure 4-50 shows a comparison of the final water content and dry density distribution along the height of the samples from all the tests. In this case, the water content values for the tests performed with saturation through the gap, are the weighted average values of those measured in the external and internal parts of each section which were plotted in Figure 4-47. Both the water content and the dry density gradients for a given test duration tended to be higher in the samples saturated through the gap.

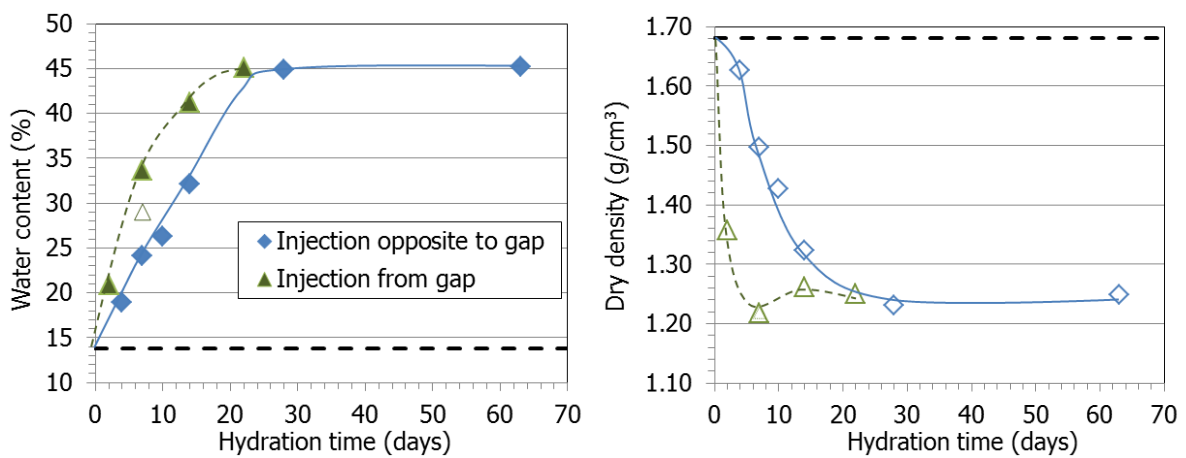


**Figure 4-49. Evolution of water content and dry density in GAP-liquid tests (the dotted horizontal lines indicate the initial values)**

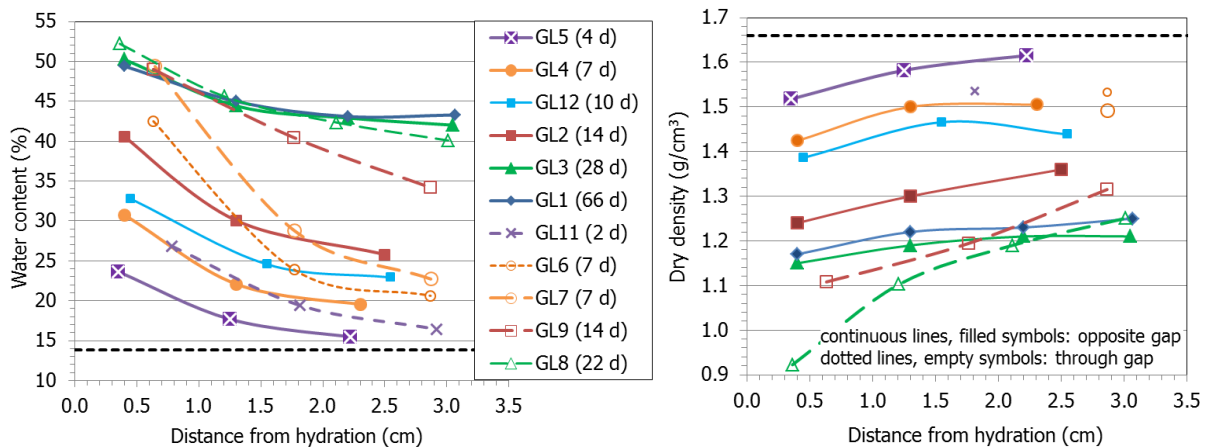


**Figure 4-50. Final water content and dry density along the samples used for GAP-liquid tests**

**Pore size distribution**

The same analysis of the final pore size distribution of the subsamples described for the GAP-vapour tests was performed with the subsamples of the GAP-liquid tests. The incremental mercury intrusion curves for all the samples are included in Villar et al. (2021a). As an example for the tests saturated from the bottom, Figure 4-51 shows the incremental curves of mercury intrusion for the subsamples of the tests lasting 14 and 66 days and for a FEBEX sample compacted with approximately the same dry density and water content as the initial conditions used in the cells (1.69 g/cm<sup>3</sup>, 13.5%). In some tests it was not possible to get material from the upper part of the specimens (the one swelling into the void) for the MIP tests because of its inconsistency. In fact, in the tests saturated from the gap the pore size distribution was only obtained for samples of tests GL9 and GL11 (Figure 4-52) for lack of enough material. Again, two pore families corresponding approximately to pores larger and smaller than 200 nm could be told apart. The volume of pores larger than 200 nm increased during testing, particularly as the test was longer.

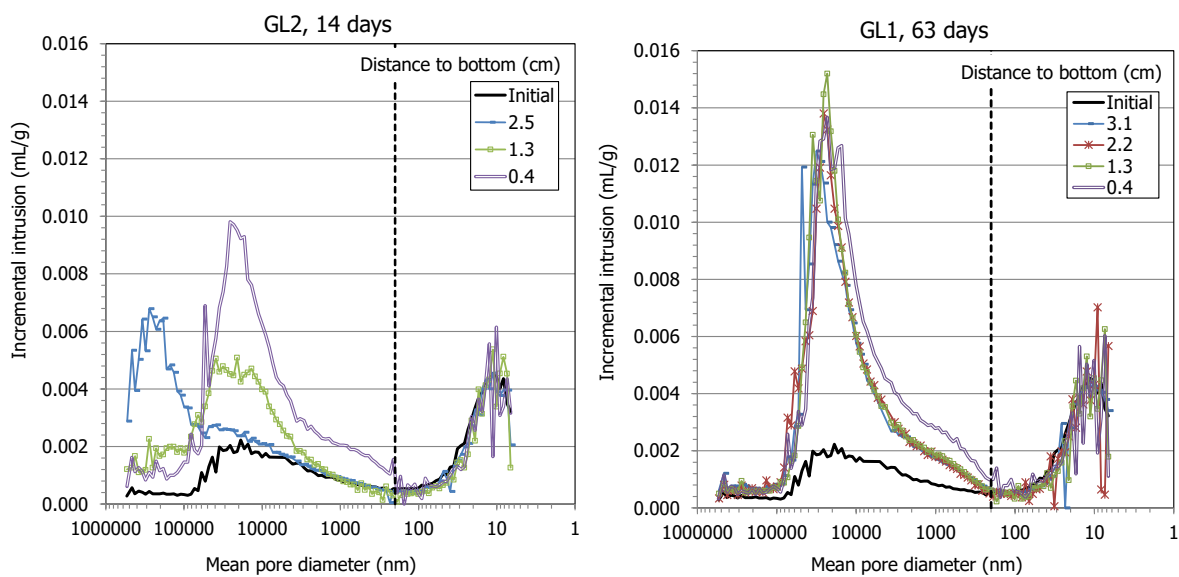


**Figure 4-51. Pore size distribution of samples tested in GAP-liquid cells for 14 days (GL2) and 66 days (GL1) and for the initial block expressed as incremental mercury intrusion**

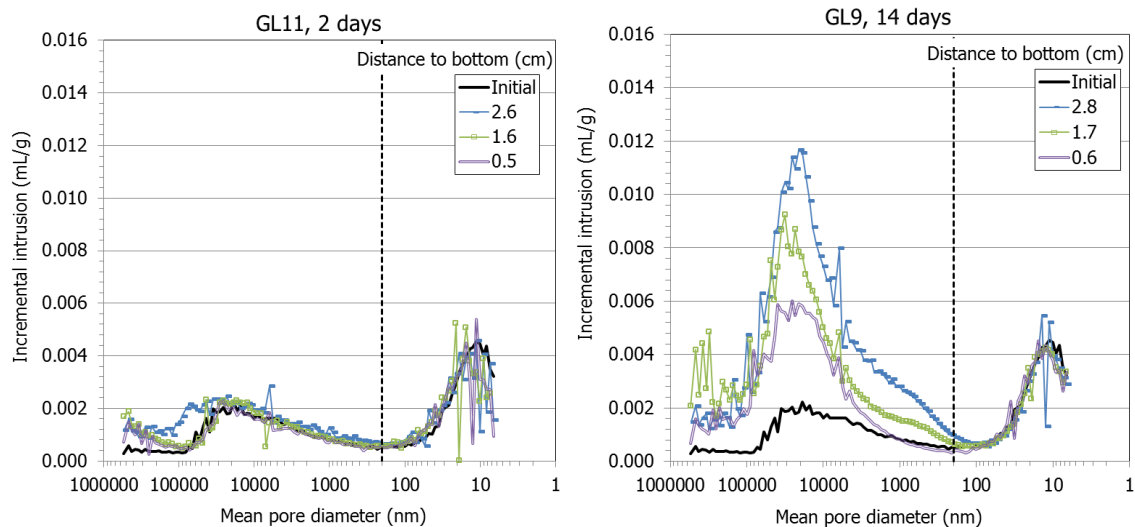


**Figure 4-52. Pore size distribution of samples tested in GAP-liquid cells for 2 days (GL11) and 14 days (GL9) and for the initial block expressed as incremental mercury intrusion**

The percentage of pores intruded by mercury in these subsamples was between 28 and 85%. As it was explained for the GAP-vapour tests, in some subsamples (those closest to the gap), part of the porosity not explored by the porosimeter may correspond to pores larger than 550  $\mu\text{m}$ . This would be the case of the upper subsamples of the tests shown in Figure 4-53, i.e. those shorter than 14 days in the samples saturated from the bottom and shorter than 7 days in the samples saturated from the gap. Taking this into account, the void ratio corresponding to pores larger and smaller than 200 nm was calculated and is plotted in Figure 4-54 for the tests saturated from the bottom and in Figure 4-55 for the tests saturated from the gap. Although the volume of pores smaller than 200 nm was initially higher, over time the volume of macropores increased more, and in fact the two longer tests had the highest void ratio corresponding to macropores. As a result, the ratio between the void ratios corresponding to pores smaller ( $e_m$ ) and larger ( $e_M$ ) than 200 nm significantly decreased during testing for the longer tests and was lower for the subsamples closer to the gap, where the bentonite could freely swell. It is remarkable that, in the tests with hydration through the bottom, this ratio was the same after 28 and 63 days, possibly indicating steady conditions, which were also shown by the water content and dry density distributions (Figure 4-44).

There are only available results for two tests with hydration from the gap (Figure 4-55). After 2 days only the subsample closest to the hydration surface experienced a huge increase in the size of the macropores. After 14 days the volume of macropores increased considerably with respect to the original sample in all subsamples, but more as the subsample was closer to the gap. This resulted in an overall decreased in  $e_m/e_M$  ratio.



**Figure 4-53. Appearance upon dismantling of some of the shorter GAP-liquid tests (hydration from bottom or gap)**

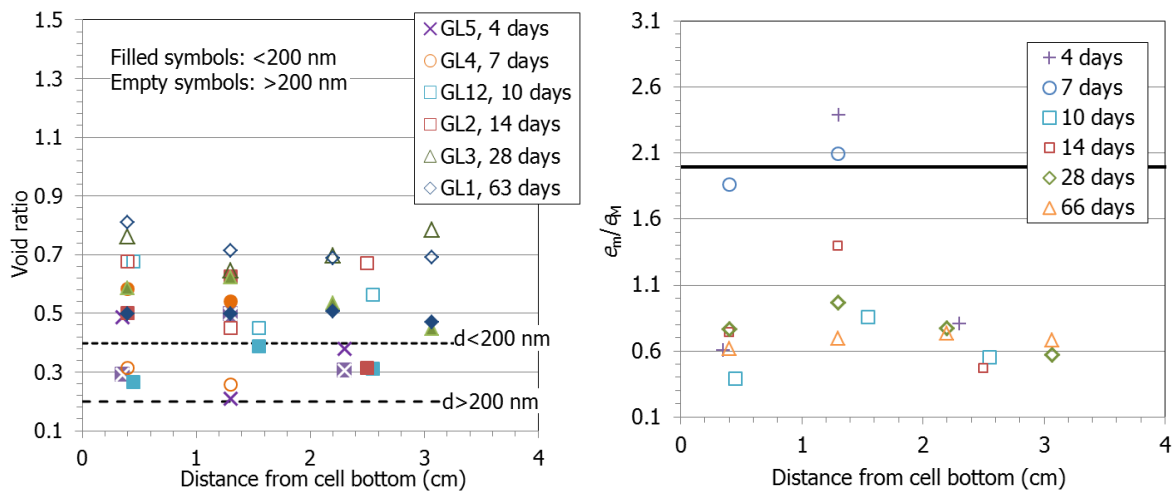


**Figure 4-54. Void ratio corresponding to pores smaller ( $e_m$ ) and larger than 200 nm ( $e_M$ ) obtained by MIP in samples tested in GAP-liquid cells saturated from the opposite surface to the gap for different times (left) and ratio between both (right). The thick horizontal lines indicate the values for the reference block**

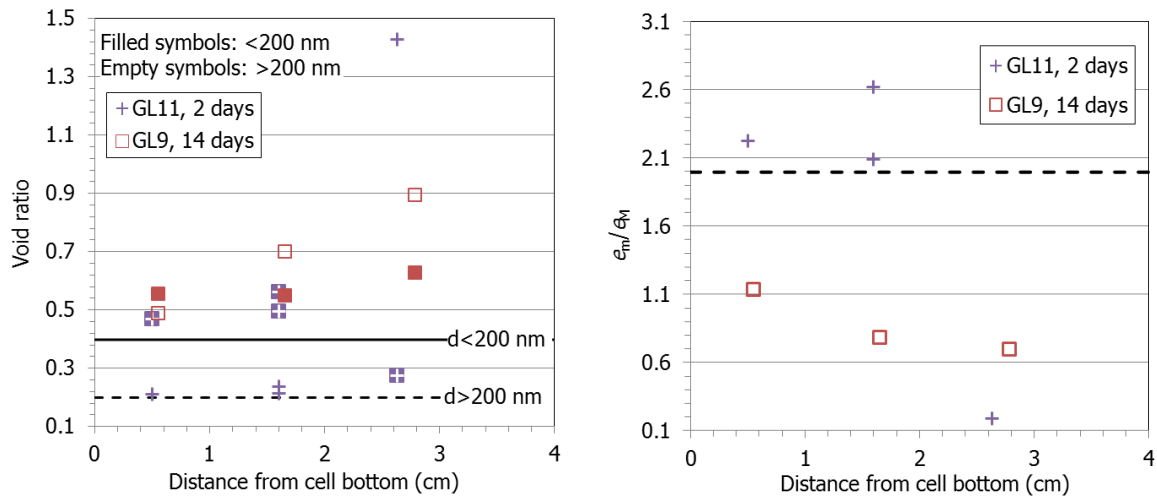


**Figure 4-55. Void ratio corresponding to pores smaller ( $e_m$ ) and larger than 200 nm ( $e_M$ ) obtained by MIP in samples tested in GAP-liquid cells saturated from the gap for different times (left) and ratio between both (right). The thick horizontal lines indicate the values for the reference block**

The evolution over time of the void ratio corresponding to different pore sizes is shown in Figure 4-56 for the different subsamples. This representation allows to see that the changes are quicker and more drastic when hydration takes place through the gap; that the samples saturated through the bottom experienced very soon an overall increase in macropore (and micropore) void ratio at all locations; and that a “steady microstructural state” was reached after 30 days (for the samples saturated through the bottom).

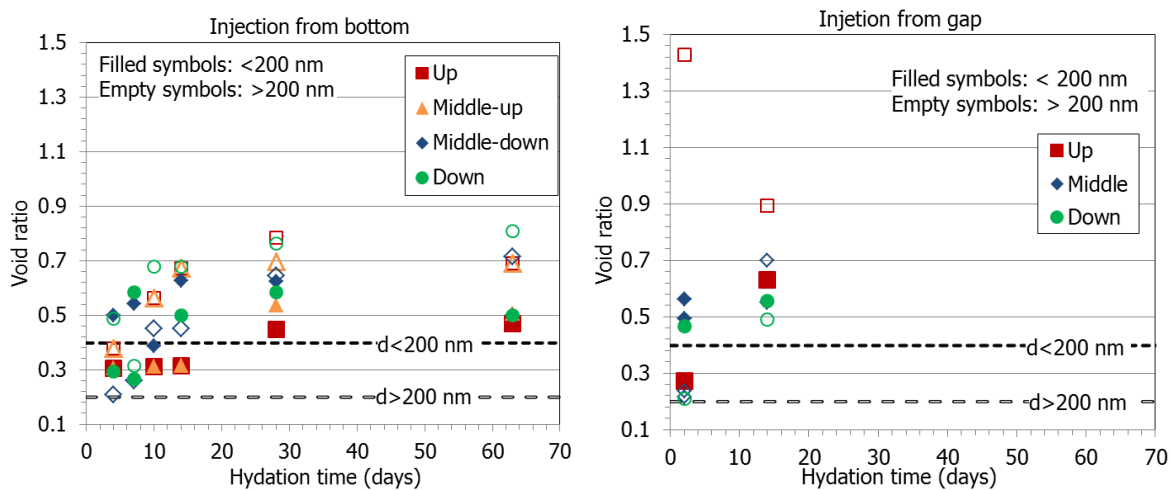


**Figure 4-56. Evolution of void ratio over time corresponding to pores larger and smaller than 200 nm for the two sets of GAP-liquid tests**

#### 4.2.4 Conclusions

The evaluation of the results obtained in the two kinds of cells indicates that hydration was slower via water vapour than liquid water and that the hydration kinetics was also affected by the actual suction and by the boundary conditions, i.e. if hydration took place through the gap or opposite to it. In turn, the persistence of water content and dry density gradients was linked

to the velocity of saturation: the quicker the hydration took place, the steeper and more persistent the gradients were. Hence the gradients were more remarkable and persistent when hydration took place in the water phase, then under “high” suction and finally under low suction. In tests sufficiently long steady gradients were reached, with no further changes in water content or dry density.

The samples under suction 6 MPa hydrated faster than those under 0.5 MPa and the strains that occurred under quick hydration were larger and irreversible. The final water content of the samples saturated via vapour transfer was approximately related to the water retention curve and thus, the final swelling of the samples under suction 6 MPa was not enough as to close the gap (which would have meant a 20% swelling). The samples saturated under the lowest suction (0.5 MPa) were able to swell enough as to close the gap before the equilibrium water content had been reached.

There was also a difference related to the velocity of saturation in the two kinds of tests performed with liquid water, even though the flow rate prescribed was the same in the two sets of tests. When water was supplied through the gap, the samples saturated more quickly because they were able to swell into the open void and take water very quickly (because of the lower permeability of the swollen, low-density bentonite), developing higher internal gradients. Saturation was slower when it took place from the opposite side to the gap, where no free swelling was readily allowed and the permeability of the bentonite was lower. Consequently, the dry density also decreased initially faster and reached earlier the lowest possible value when the bentonite was hydrated from the gap. As a result, the gap closed sooner when hydration occurred from the gap surface.

Hydration brought about an overall increase in the void ratio corresponding to all pore sizes (because of the swelling into the gap). Although the volume of pores smaller than 200 nm was initially higher, over time the volume of macropores increased more. The average size of the macropores also tended to increase. In agreement with the different hydration kinetics of the different kinds of tests, the overall void ratio increase took place very quickly in the samples saturated with liquid water through the gap and under suction 6 MPa but took longer in the samples tested under suction 0.5 MPa or hydrated with liquid water opposite to the gap. Initially, the increase in macropore void ratio took place mainly in the more hydrated samples, but over time the increase in this area was reduced and started to be also notable in the samples farther away from the hydration surfaces. As a result of these changes, the ratio between the void ratio corresponding to pores smaller ( $e_m$ ) and larger ( $e_M$ ) than 200 nm was lower in the subsamples closest to the gap in the shorter tests, but over time it would tend to be the same in all the bentonite block, and lower than the initial one, which would be an additional indication of equilibrium being reached. The closing of the gap might have played a role on the pore size distribution, but as a general observation the microstructural changes were quicker and more drastic when hydration was faster.

### 4.3 Swelling into a limited void (CTU)

A set of small-scale experiments has been performed in order to investigate swelling into void and homogenisation. The experiments used stainless steel cells (Figure 4-57) of internal diameter 120mm and height 120 mm which was fully or partially filled with investigated material (BCV bentonite). Both ends of the cells were fitted porous stone. The cell was submerged into water with water level kept at  $\frac{1}{2}$  of cell height (Figure 4-58). That ensured that the material was saturated only through the bottom porous stone.



**Figure 4-57. Small scale experiment vessels**

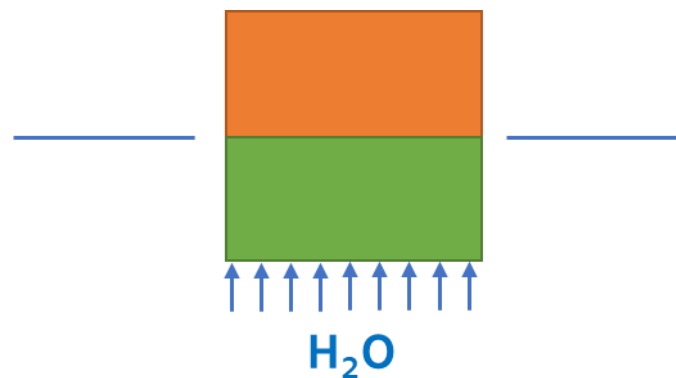


**Figure 4-58. Schema of scale experiment set-up**

Four sets of experiments were performed:

- Fully filled vessel with BCV bentonite
- ¾ filled vessel with BCV bentonite (void at the top)
- ½ filled vessel with BCV bentonite (void at the top)
- Fully filled vessel with BCV bentonite pellets & compacted blocks – bottom & top half filled with different material

Each set consisted of several identical tests each dismantled at different time. This allowed to observe temporal evolution of the processes.

Fully filled experiments (Figure 4-59) were designed as reference ones. They show the temporal evolution of saturation and the changes of density over time. The results show that there is slightly lower density at the bottom of the vessel and higher water content.

Figure 4-60 and Figure 4-61 show results of partly filled vessels. In 14 days the top part is not affected by water for ¾ filled vessel. The values of the water content curve are very similar to the curve of ½ filled vessel at 12 days. It indicates that there is quite sharp waterfront boundary.

It could be connected to the water level used to the saturation which is at the middle of the height of the vessel. In later stages the boundary is not present anymore.

Figure 4-62 shows the results of investigation with block & pellets infill. Both variants of configuration were investigated – e.g. pellets in top part with blocks at the bottom and reversed configuration with blocks at the top. This allowed to investigate influence of spatial density distribution and homogenisation. The results show similar trends for both configurations although the final densities differ. It indicates that the saturation direction (water progress inside the sample) plays very significant role. This leads to inhomogeneity regardless to initial configuration. That has been seen even in the initially “homogenous” tests.

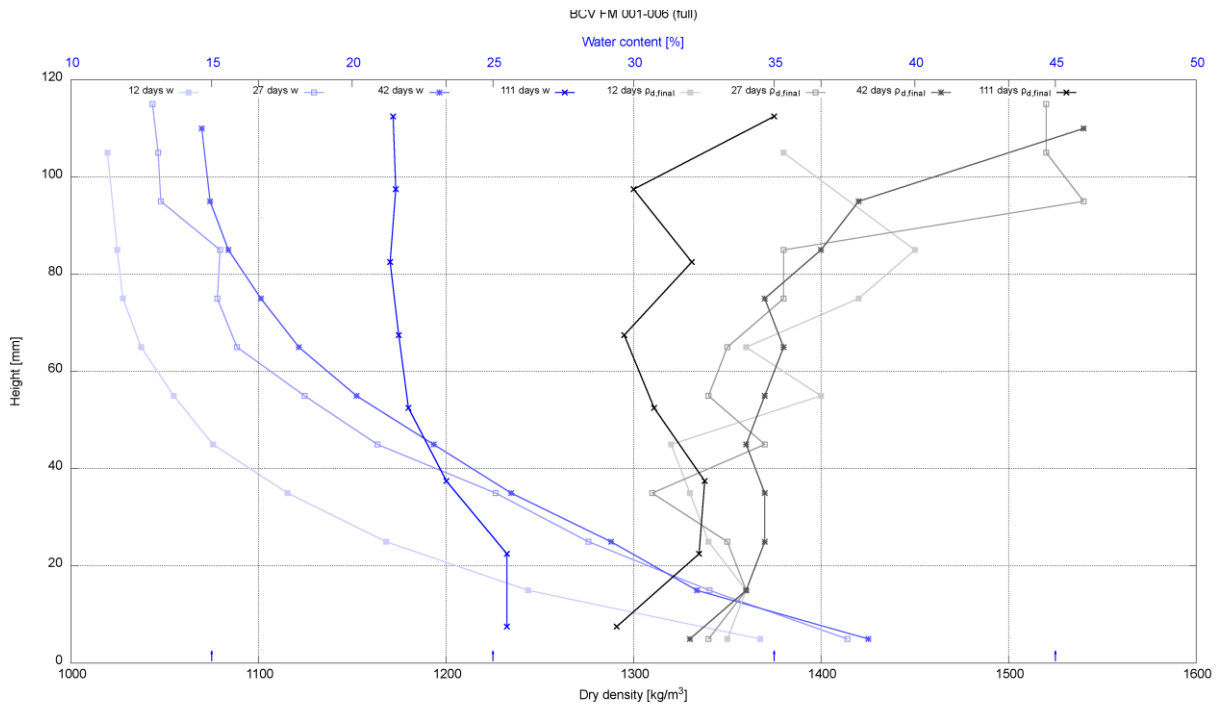


**Figure 4-59. Saturation and dry density evolution over time (fully filled vessels)**

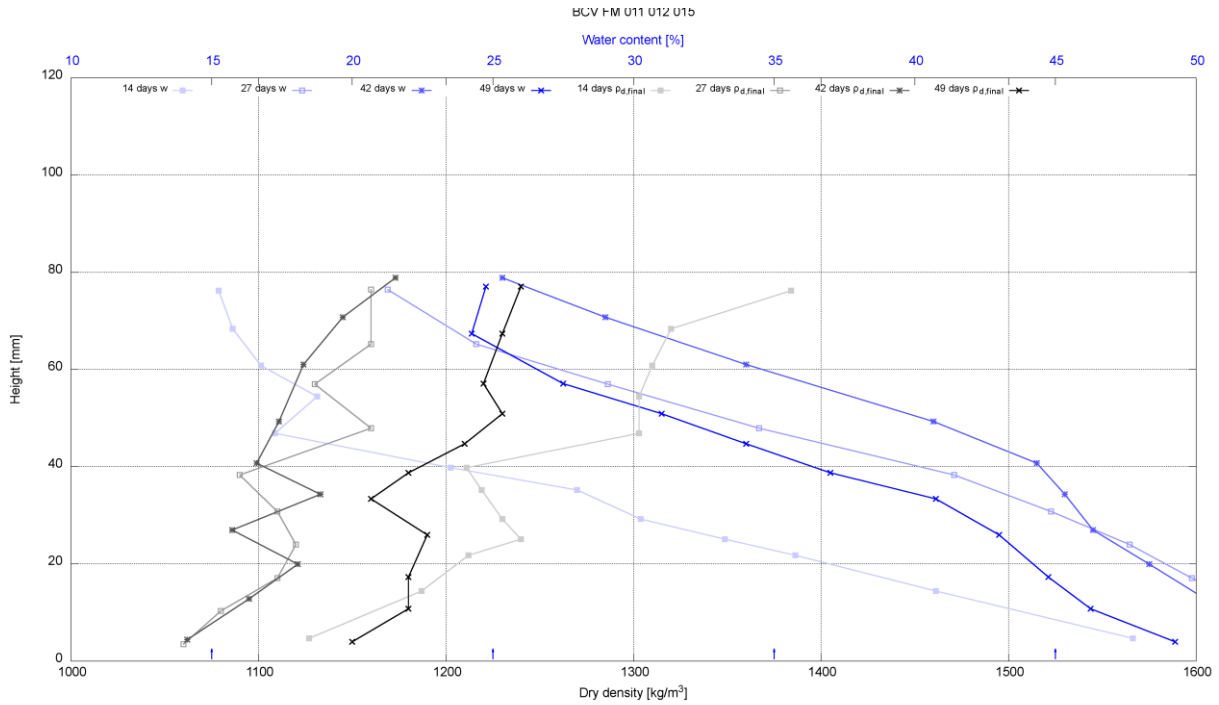


**Figure 4-60. Saturation and dry density evolution over time (3/4 filled vessels)**

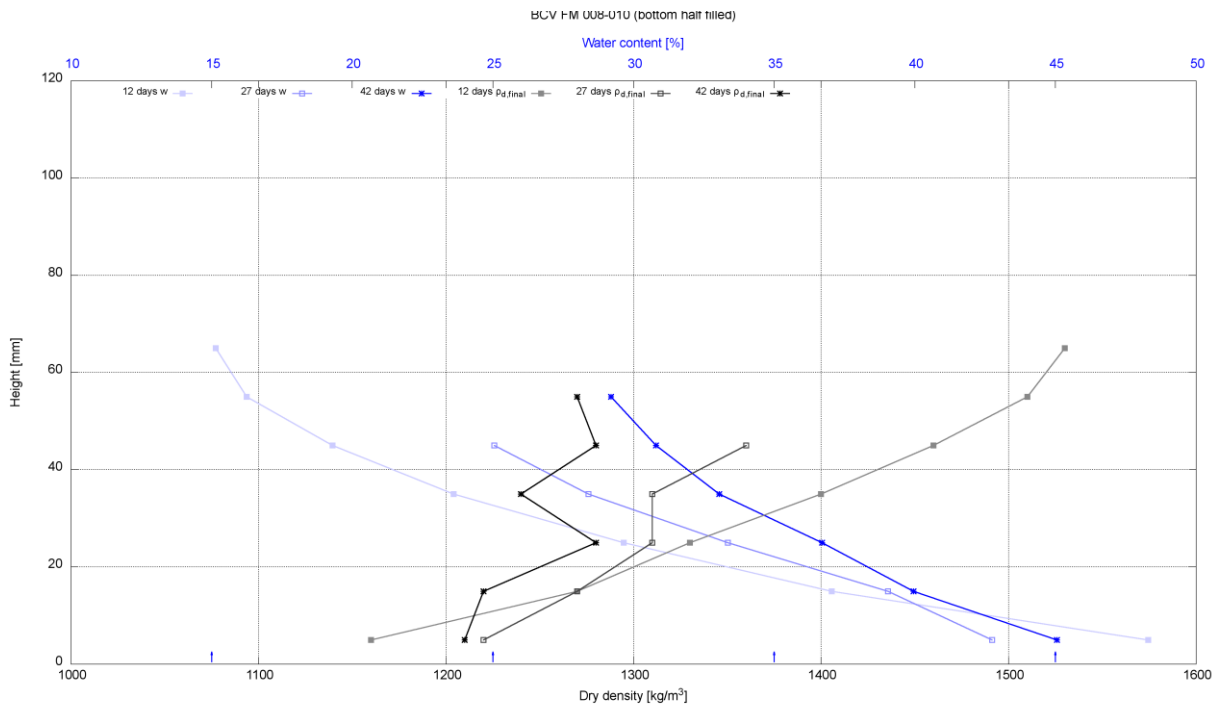


**Figure 4-61. Saturation and dry density evolution over time (1/2 filled vessels)**

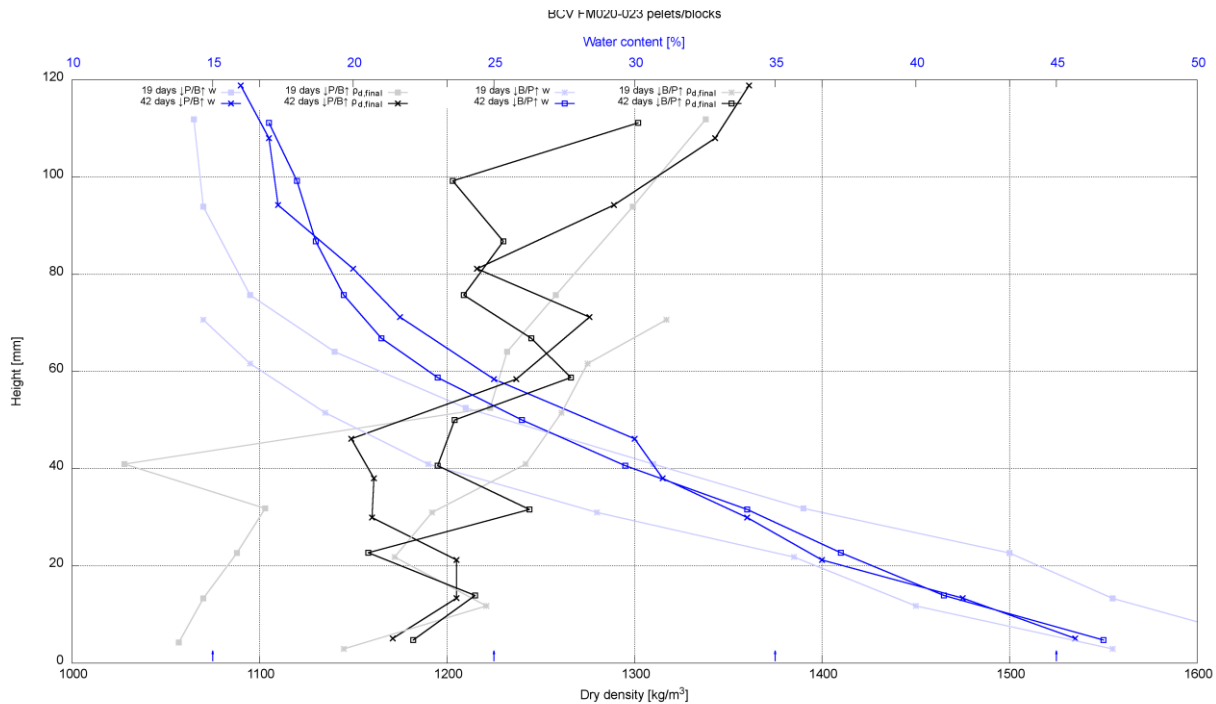


**Figure 4-62. Saturation and dry density evolution over time (compacted blocks & pellets)**

## 4.4 X-ray imaging and wetting of semi-free swelling bentonite in a sample chamber (JYU)

JYU has successfully developed non-intrusive experimental method for measuring simultaneous water transport and deformation in swelling clay materials. The method yields broad range of bentonite hydro-mechanical data which is aimed to help validate and develop material models.

### 4.4.1 Setup and methods

An extensive experimental measurement series of semi-free swelling of bentonite utilizing X-ray imaging and numerical image analysis has been completed. In the measurement setup, the compressed bentonite samples that initially partially fill the custom build sample chamber (Figure 4-63) are wetted and sample saturation process and semi-free swelling into the chamber void is monitored by X-ray imaging and axial pressure measurements. Sample chamber is built in a way that wetting and limited void expansion can be easily controlled and monitored and that the setup simulates for example a situation where buffer material swells into bedrock cracks. X-ray imaging was done with SkyScan 1172 scanner at operating voltage and current of 100 kV and 80  $\mu$ A respectively. Exposure time of each image was set to be 4130 ms and total of three images were averaged. Limited field of view of the equipment was enlarged by imaging the sample in three different vertical positions and stitching these images together. This made the final field of view 34 mm x 30 mm which is approximately 2000 px x 1767 px with pixel size value of 17.1  $\mu$ m used in the experiments. Lastly, 0.5 mm Al + 0.04 mm Cu filter was used in the imaging to filter lower energy part of the polychromatic X-ray radiation spectrum.

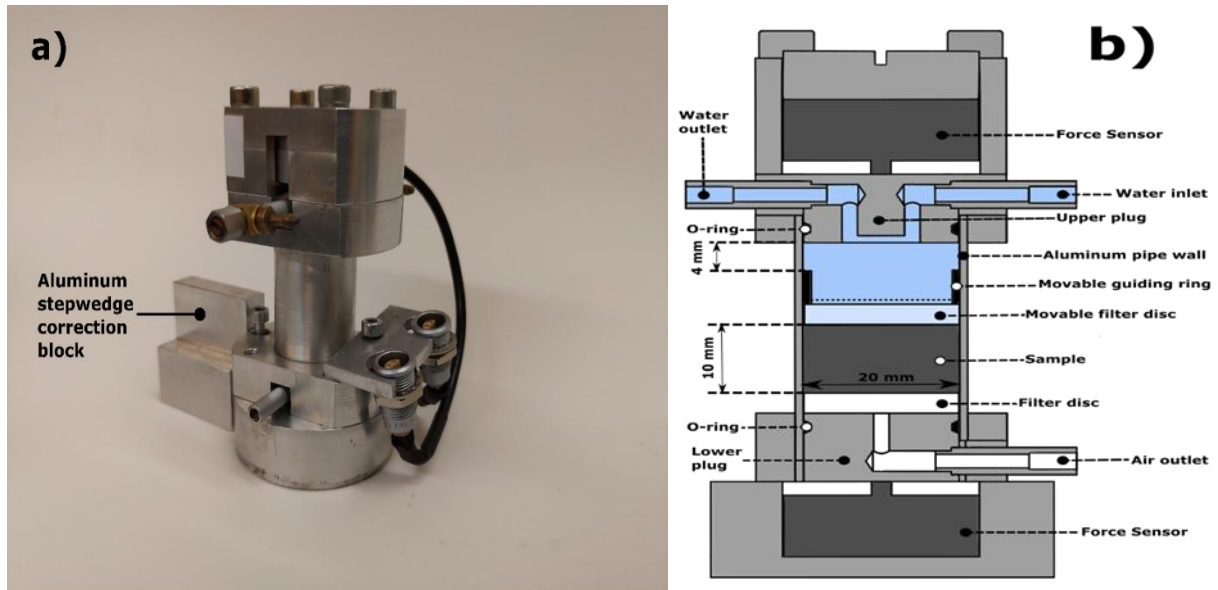


**Figure 4-63. a) Picture of the sample chamber and b) its more detailed schematic**

Numerical analysis of the method is based on comparing the X-ray images of sample reference state to the X-ray images of wet and deformed sample. Wetting process changes the pixel specific intensity values, i.e. local linear attenuation coefficient (LAC) of the X-ray images. Furthermore, samples are doped with ZrO<sub>2</sub> particles whose displacements are tracked with image block matching algorithm to obtain sample displacement field. With LAC and displacement development water and bentonite content time evolutions can be computed. Method includes various denoising steps which include X-ray local beam hardening correction, image processing methods and backward time integration of the swelling process from acquired X-ray images.

#### 4.4.2 Experiments

The now completed research plan consisted altogether 30 experiments in which sample material, initial material dry density and wetting water varied. Individual experiment spans approximately 16 days and covers 10 X-ray imaging sessions throughout the wetting cycle. Detailed experiment information is shown in Table 4-9.

**Table 4-9. Detailed experiment information. Every experiment has been repeated three times. NaMMT and CaMMT are purified clay materials consisting mainly bentonites main swelling component montmorillonite**

Material	Dry density (g/cm <sup>3</sup> )	Solution composition	Ionic strength (mmol/l)	Test ID
BaraKade	1.4	NaCl + CaCl <sub>2</sub>	3.5	T1
BaraKade	1.4	NaCl + CaCl <sub>2</sub>	489	T2
BaraKade	1.4	NaCl + CaCl <sub>2</sub>	975	T3
BaraKade	1.8	NaCl + CaCl <sub>2</sub>	3.5	T4
BaraKade	1.8	NaCl + CaCl <sub>2</sub>	489	T5
BaraKade	1.8	NaCl + CaCl <sub>2</sub>	975	T6
NaMMT	1.4	NaCl	975	T3.Na
NaMMT	1.8	NaCl	3.5	T4.Na
CaMMT	1.4	CaCl <sub>2</sub>	975	T3.Ca
CaMMT	1.8	CaCl <sub>2</sub>	3.5	T4.Ca

#### 4.4.3 Results and conclusions

Example of data produced by the method is shown in Figure 4-64 which includes both bentonite and water contents, saturation limit and corresponding X-ray images of the swelling process. In addition, figure of the end state at day 16 includes gravimetrically measured local water and bentonite contents from thin cut sample slices to validate the method. Figure 4-65 shows collection of all the pressure measurements of sample T1. Pressure value depends on initial bentonite dry density and ionic strength of the wetting solution. Combination of denser bentonite sample and low saline wetting water exhibit higher swelling pressures. There is also relatively noticeable amount of wall friction in some experiments although the absolute pressure values are on the low side mainly due to the energy loss to the initial void expansion. Additionally, the higher water salinity tests exhibit negligible swelling pressures.

Temporary repository web page for the data bank is now online (<http://users.jyu.fi/~joautant/BeaconDataBank.php>). Collected data has been made openly available in original .mat and in more condensed .csv file formats.

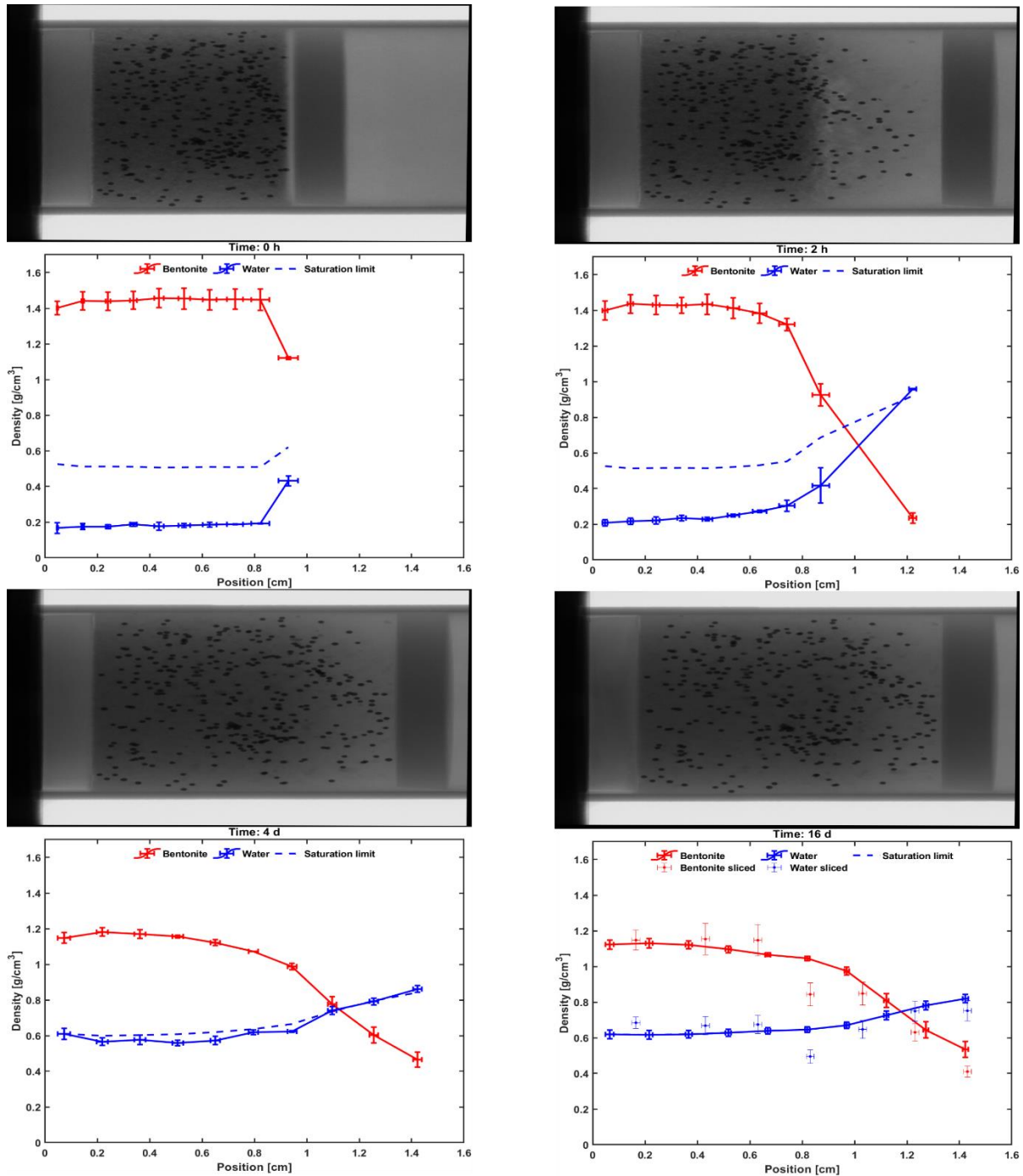


**Figure 4-64. Bentonite (solid red) and water (solid blue) content and saturation limit (dashed blue) as a function of sample layer position at different times. In addition, corresponding X-ray images of swelling process are included above the plots. Furthermore, local data from gravimetrical sample slicing method at end state is included as red dots for bentonite content and blue dots for water content**

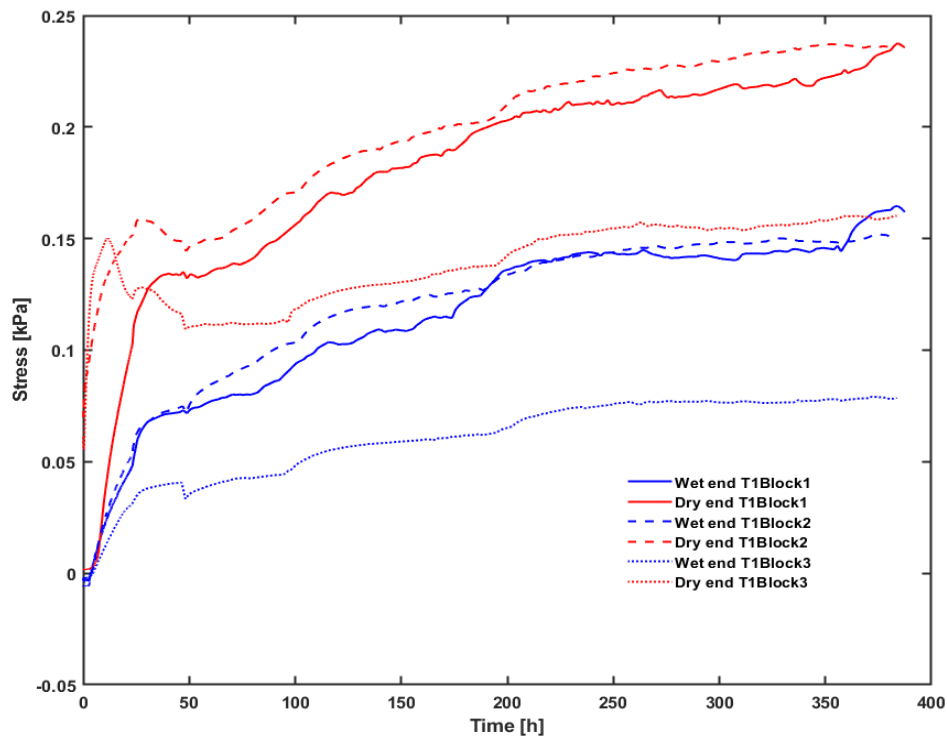


**Figure 4-65.** Collection of all the T1 sample axial pressure measurements. Blue curves indicate pressure at the wetting i.e. top end of the sample and red curves the pressure at the dry end i.e. bottom end of the sample

JYUs method based in numerical image analysis of X-ray images is useful in measuring water transport and swelling in bentonite. The method can effectively collect time dependent data on deformation and water content of clay materials without disturbing or damaging the sample itself.

As the method uses imaging as measurement mechanism, rather than just means of visualization, the image resolution is crucial for the accuracy of the method. Image pixel values change marginally as the water passes through the sample. Thus, the low signal-to-noise ratio between water and other materials seen in the X-ray image is one systematic error source. The local beam hardening correction of the images reduces X-ray beam hardening artefact that distorts the pixel values. Still, various X-ray scattering artefacts might affect the pixel values.

Another problem in the experiments has been the rapid swelling of bentonite which deteriorates the image resolution. Fortunately, the issue has been worked around by time integrating the swelling process backwards using saturated end state as reference. However, this kind of analysis assumes that sample is fully saturated which might not be the case for every experiment according to swelling pressure data.

Measurement setup used in current semi-free bentonite swelling studies has restricted field of view, thus vertical sample movement is required to fit the whole sample into the image. This sample movement lessens the temporal resolution of the method. However, in the current and future studies better equipment is utilized so that even larger samples fit to the field of view.

Finally, in the density analysis, results depend on the clay materials grain density. For BaraKade bentonite well established value of 2.75 g/cm<sup>3</sup> was used. However, this value is unknown for the purified montmorillonite samples used in these experiments and should be investigated.

## 4.5 Pellet-scale investigations (KIT/GRS)

The idea of the pellet-scale investigations was to look at a single bentonite pellet with its immediate surrounding during hydration, and to relate the single pellet behaviour to the overall behaviour of a pellet buffer. In order to do this, two types of tests were performed: Single-pellet tests (SPT) with a cell accommodating one pellet and several fragments, representing neighbouring pellets, and pellet-cluster tests (PCT) with a constant volume cell containing several tens of pellets. The SPT allowed a spatially resolved swelling pressure measurement USING a Tekscan pressure sensor foil.

### 4.5.1 Material

In all tests, pillow-shaped pellets of MX-80 bentonite (Figure 4-66) from the Hard Rock Laboratory Äspö, Sweden have been used. Five pellets have been weighed and the related volume was determined by means of 3D-scanning. From these data, a mean air-dry density of 2.064 g/cm<sup>3</sup> with a standard deviation of 0.043 g/cm<sup>3</sup> was determined.



**Figure 4-66. MX-80 pellet used in the tests**

The five pellets were then dried at 105 °C over 24 hours and weighed again. From these measurements the water content could be calculated amounting to 12.3 %. The resulting mean dry density of the pellets came to 1.838 g/cm<sup>3</sup>. This value compares rather well with information from the Canister Retrieval Test at the HRL Äspö in Sweden (Kristensson and Börgesson 2015). Here, the same type of pellets had been used and the dry density was given as 1.800 g/cm<sup>3</sup>.

#### 4.5.2 Pre-tests with a preliminary cell design

Several preliminary tests were performed with a first cell layout (Figure 4-67). In these tests, different filling degrees and two solutions (Pearson water type A and Grimsel groundwater) were used in order to get acquainted with the new film pressure sensors (described further down) and to perform calibrations. These cells had the drawback that a continuous hydration was not possible – the cell was filled with bentonite material and solution and closed afterwards. As a consequence, the bentonite never got close to full saturation. Therefore, a different cell design was used for the subsequent tests. The pre-tests are described in more detail in Deliverable 4.1 of the Beacon project (Baryla et al. 2019).



**Figure 4-67. Preliminary test cell array with bentonite pellet samples. The cells are still open and the pressure sensors can be found above the sample cells**

#### 4.5.3 Single-pellet tests

##### 4.5.3.1. Test setup and components

The two-piece single-pellet test cells (Figure 4-68) are made from transparent acrylic glass and have a swelling chamber with a total height of 20 mm, a diameter of 25 mm and a total volume of 9817.19 mm<sup>3</sup>. The inlet and outlet have an access drilling with a diameter of 1 mm, which is connected to an UNF ¼ "28G screw thread. The two cell caps are sealed with a rubber notch ring and four metal screws. Sinter plates (Robu® 15er Series) with a diameter of 25 mm and a total height of 3 mm are placed in front of the inlet and outlet to ensure an even water distribution. The plates have an average pore diameter of 40-100 µm and reduce the available sample volume within the cell to a total of 6.8720 cm<sup>3</sup>.

Between the bentonite material and the upper sinter plate, a Tekscan pressure sensor foil (Type 6900 – 1100 psi, Figure 4-69) is fit in, facing towards the swelling material. The pressure sensor foil is applied to investigate temporally and spatially resolved swelling pressure evolution. The foil spans an area of 14x14 mm (196 mm<sup>2</sup>) with a total of 121 sensels (pressure sensor points), providing a high resolution of 62 dots/cm<sup>2</sup>. Calibrating the Tekscan system to the default (S:21) or a higher sensitivity (S:33), the necessary detection pressure per sensel thereby has a minimum value of 50 kPa for the default and 10 kPa for the more sensitive calibration. Enabling an in-situ pressure mapping, data like the total force within the cell, the contact or mean pressure, as well as peak pressure values can be acquired.

- The total force describes the overall force that is measured within the cell, using the Tekscan pressure foil

- The contact pressure is the total force divided by the active area of the sensor foil
- In contrast, the mean pressure is the total force divided by the total sensor area
- The peak pressure is the pressure maximum, measured for a given time at one sensel

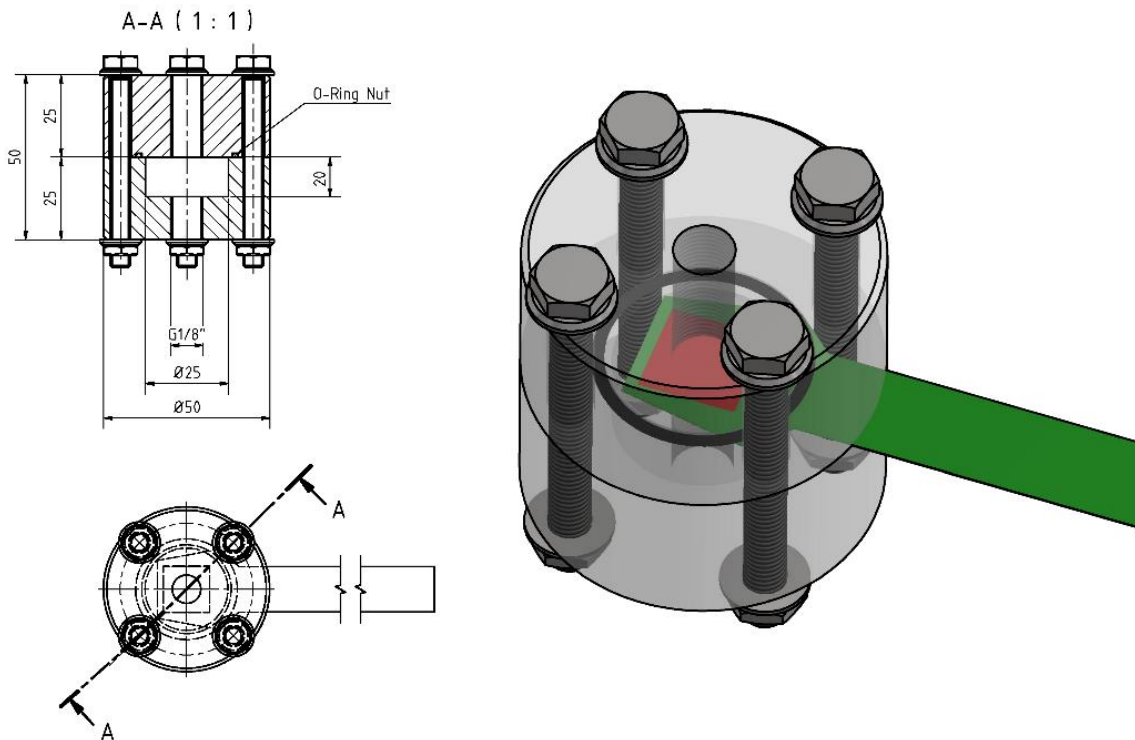


**Figure 4-68. Technical drawing of the cell on the left and a 3D-view, including the pressure sensor foil, on the right**



**Figure 4-69. Single pellet emplaced in the cell, bedded on pellet fragments (left). Faced down, the pressure sensitive foil is placed onto the bentonite material (right)**

A 50 ml syringe filled with Pearson water is attached to a syringe pump and a HPLC tubing with an inner diameter of 0.8 mm and a total length of 10 cm. The tubing thereby is connected to the bottom inlet of the cell. The cell itself is placed onto a holder, which in turn is placed onto an electronic balance. The outlet on top of the cell is connected to an open-end glass tube, which is mounted vertically at the side of the holder. The complete setup is shown in Figure 4-69.

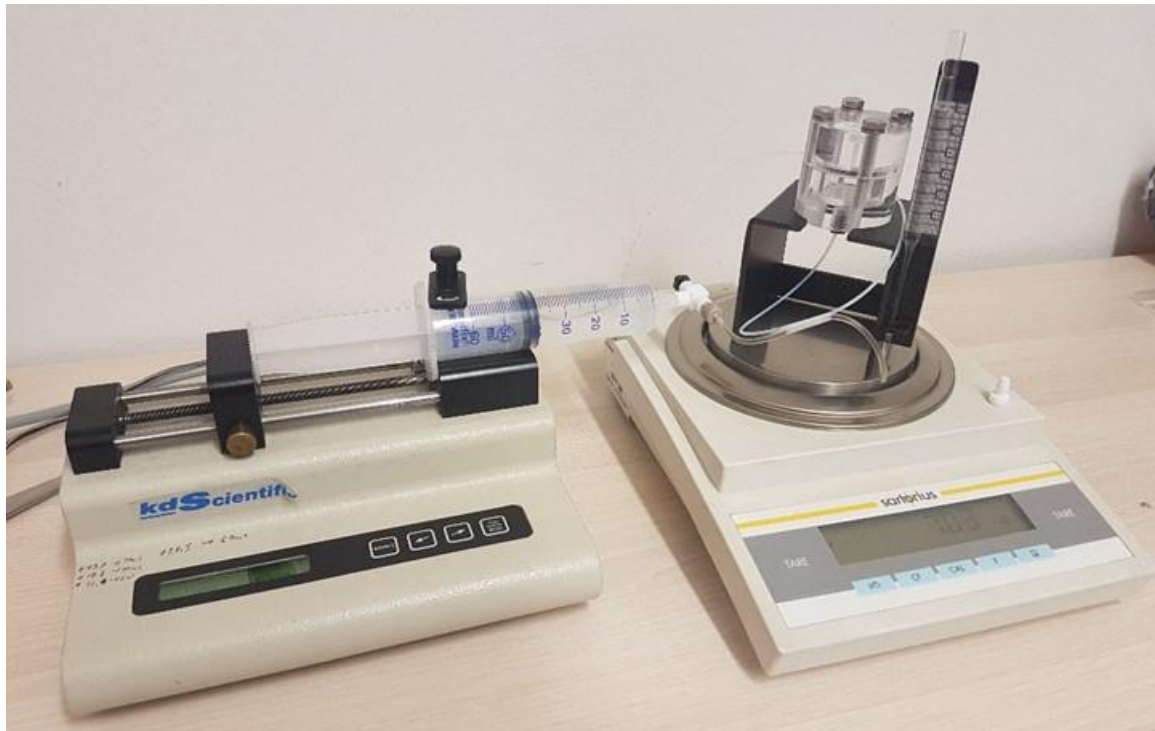


**Figure 4-69. Test setup: Syringe pump with a 50 ml Pearson water filled syringe on the left. On the right, the cell mounted on a plastic holder placed on a balance. Inlet is at the bottom of the cell, outlet at the top. Water leaving by the outlet is caught in a glass tube vertically mounted to the holder**

#### 4.5.3.2. Test procedure

For each test the total amount of ca. 2.5 bentonite pellets (one pellet plus fragments) was placed in the cell in order to reach the target dry density of 1.0 g/cm<sup>3</sup> which represents the density of a pellet bulk or cluster (see section 4.5.4). One intact pellet was placed within the middle of the cell, surrounded by fragments of the same material. Afterwards, a Tekscan pressure sensor foil was fit between the bentonite material and the upper sinter plate, with the sensor area facing towards the bentonite sample.

After closing the cell, the system was flushed with a constant flow rate of ca. 2 ml/min, inhibiting the formation of major air enclosures within the cell, as well as providing an even water distribution between the pellet and the fragments. After a period of ca. three minutes, the cell was completely filled (see Figure 4-70). After the initial flooding, fresh water was regularly injected into the cell over a period of seven days, in order to provide the swelling bentonite with additional water. As the pressure within the cell increased, it became increasingly difficult to provide the system with Pearson water. The transparent acrylic glass cell design made a continuous observation of the interior possible, and major changes within the system could be observed during the initial flooding and swelling phase (see Figure 4-70). The continuous

weighing of the sample allowed estimating of the total water content within the cell. A continuous quantitative mapping of the pressure progression was possible with the Tekscan pressure foil (see next section). After finishing each test, the wet bentonite was collected and dried for a period of 24 h with a temperature of 105 °C to determine the total water uptake of the material.

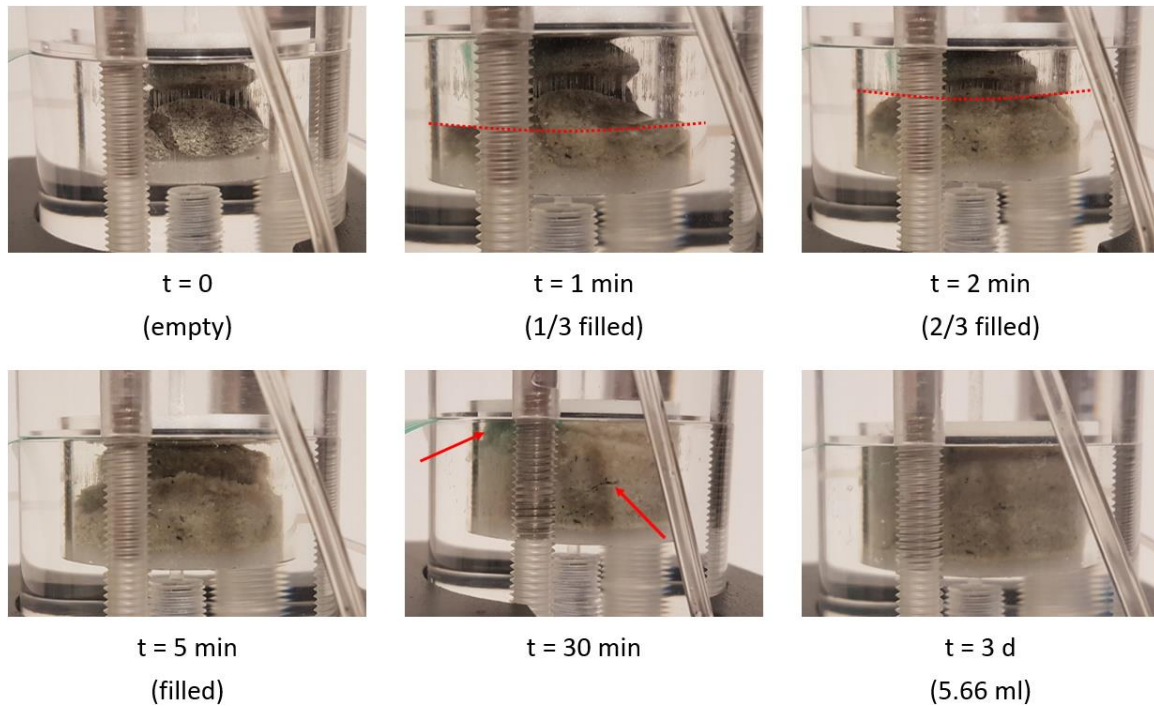


**Figure 4-70. Dynamics of the swelling bentonite material over a period of three days. Red lines indicate a rising water level within the cell, red arrows highlight trapped air for  $t = 30$  min**

#### 4.5.3.3. Test results

##### Test 1

The first test was performed with a lower dry density of ca. 0.88%. Using the default sensitivity of the Tekscan system, the initial phase of the test showed a rapid pressure increase of the swelling bentonite, reaching a total force of up to 245 kPa after ca. 1 hour. Simultaneously, the mean pressure within the cell reached its maximum value of 125 kPa within the same period of time (see Figure 4-71). Unfortunately, as the single pellet was packed too closely and in direct contact with the pressure foil, the values for the contact and peak pressure were highly influenced and exceeded a reasonable value for the initial phase. Over time, the pressure values declined, reaching a general low shortly after, until the seventh day. A slight increase can be observed afterwards, though. After the testing time of 17 days, the bentonite was weighed with a wet mass of 11.11 g, which corresponds to a water uptake of 46.85%

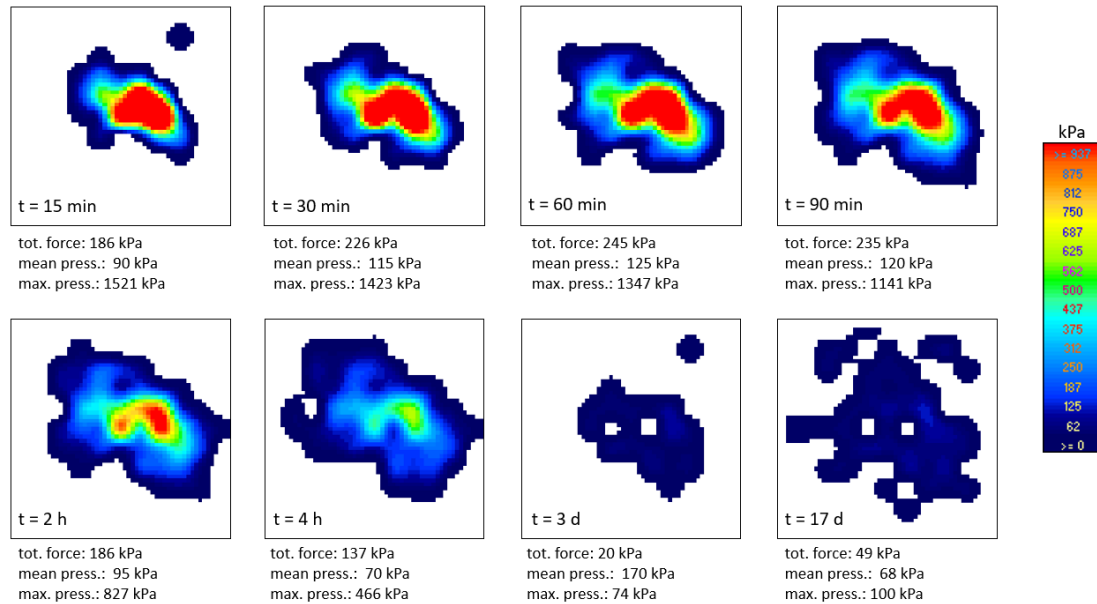


**Figure 4-71. Spatially resolved pressure evolution in the first test**

## Test 2

The second test was performed with the target dry density of  $1.0 \text{ g/cm}^3$ . Lasting for 22 days, the test showed similar results to the first one. In order to acquire a better resolution of the lower pressure areas within the cell, the Tekscan system was set to a higher sensitivity.

Having a higher mass to volume ratio than the first test, the total force and the mean pressure within the cell were also measured with slightly higher values of 265 kPa and 135 kPa, respectively, after a period of ca. three to four hours (see Figure 4-72). Since the bentonite material was better distributed in the cell, more realistic values were measured for the contact and maximum pressure, both peaking within the first hour. As before, the pressure evolution within the cell shows a rapid growth during its initial phase, with declining values immediately afterwards and an overall low pressure until the tenth day. Afterwards, a slight but steady increase of the pressure can be observed. Interestingly, the boundaries of the intact pellet can already be conjectured shortly after the start of the test, when a ring of higher pressures forms within the center of the investigated area (see Figure 4-72). As the swelling of the bentonite obviously starts at the water/material interface, these areas show a higher swelling pressure from the beginning. However, as higher local pressures fade over time, the visibly distinct ring-structure was obtained for the whole test. Due to the increased sensitivity of the pressure sensor, it was further possible to detect the low-pressure propagation within the cell, especially towards the border regions, revealing an almost complete pressure occupation of the investigated area.

Regarding the total water uptake, the bentonite was weighed with a total wet mass of 11.42 g and dried afterwards. The total amount of water was measured with 4.74 g or 41.56%, respectively.

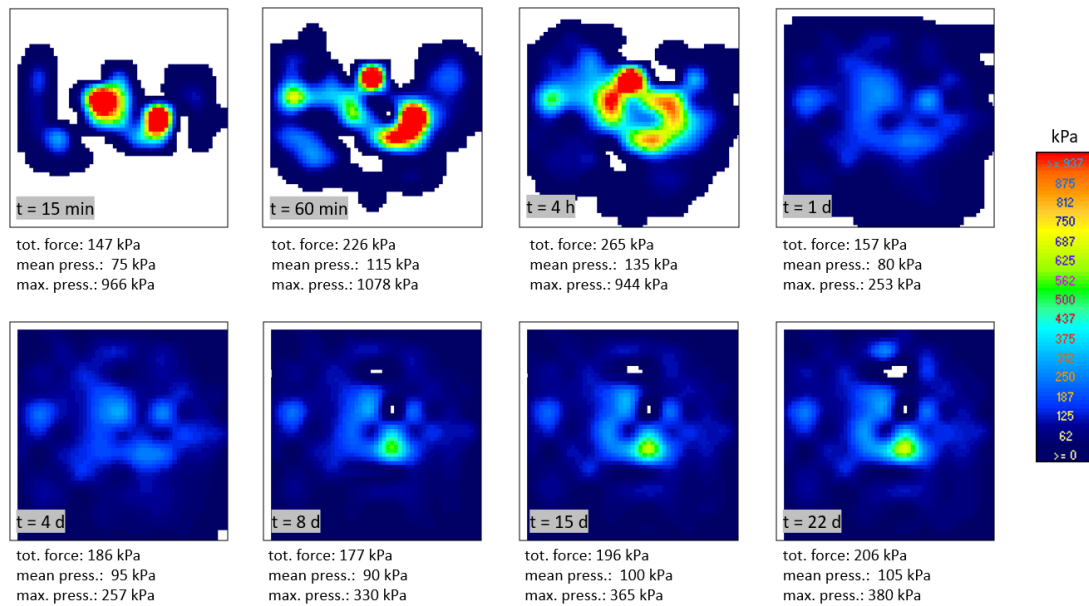


**Figure 4-72. Spatially resolved pressure evolution in the second test**

### Test 3

In order to observe the long-term pressure evolution of the bentonite material, a third test was set up with the same boundary conditions as the previous one, lasting for 127 days.

In the initial phase of the test, similar pressure peaks for the total force (206 kPa), the mean pressure (105 kPa), the contact pressure (255 kPa) and the maximum pressure (1142 kPa) were reached, followed by a fast decline of the values until the end of the second day. As before, this transient phase of an overall low-pressure state was followed by a rebound of pressure within the cell, after ten to fifteen days. As the long-term propagation shows, the measured values even exceeded the initial peak values in the long run (see Figure 4-73) and show a steady rise over time at decreasing rate. Like the previous test, ring structures of locally higher pressure develop within the area observed, indicating the position of the bentonite single-pellet and its surrounding fragments. The data again revealed an almost complete pressure occupation, with the exception of a small area towards the upper right corner, which is likely due to a local air bubble.

The cell was not opened after finishing the test, because a  $\mu$ -CT scan of the single-pellet cell was conducted, in order to study the internal structures of the wet bentonite material. As the images revealed, the wet bentonite material did not show a continuous or homogeneous water distribution within the cell, as distinct density boundaries can be seen between the original bentonite fragments and the surrounding areas (Figure 4-74). This is especially conspicuous for the interfaces of the intact single-pellet and its surrounding fragments. Being especially prone to occur towards the fringes of the cell, many air enclosures of varying sizes were found surrounding the original material. However, these air bubbles only make up a total volume of less than 1%.

Since it was not possible to determine the total water uptake of the sample directly, an empty but identical test setup was weighed, in order to determine the weight differences and thus indirectly come up with the water uptake value. Considering a minor error due to material dependent weight variations, the total water uptake was estimated to be around 46-47%.

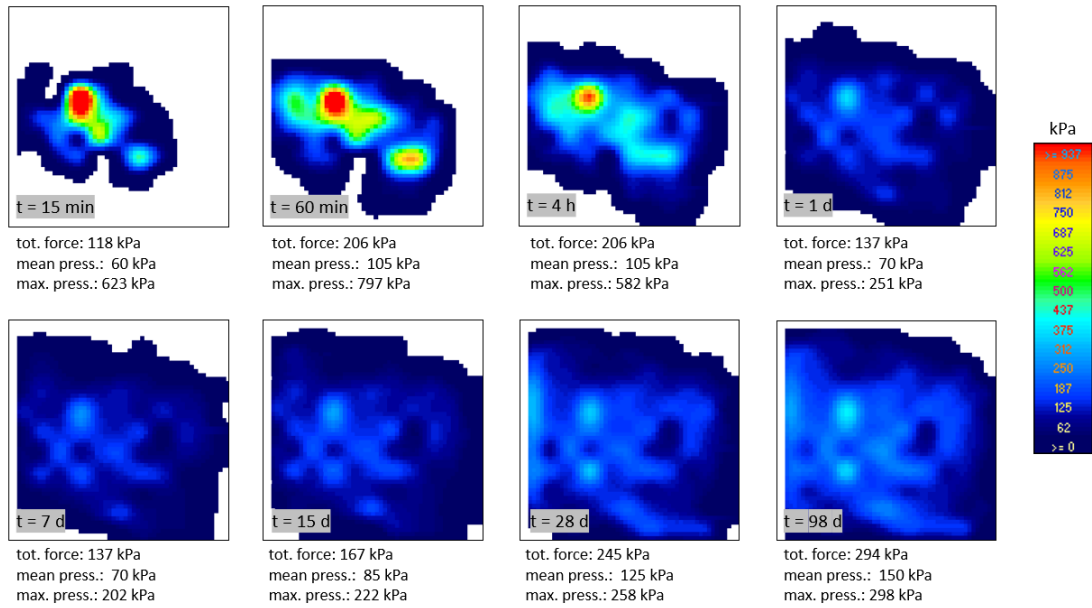


**Figure 4-73. Spatially resolved pressure evolution in the third test**

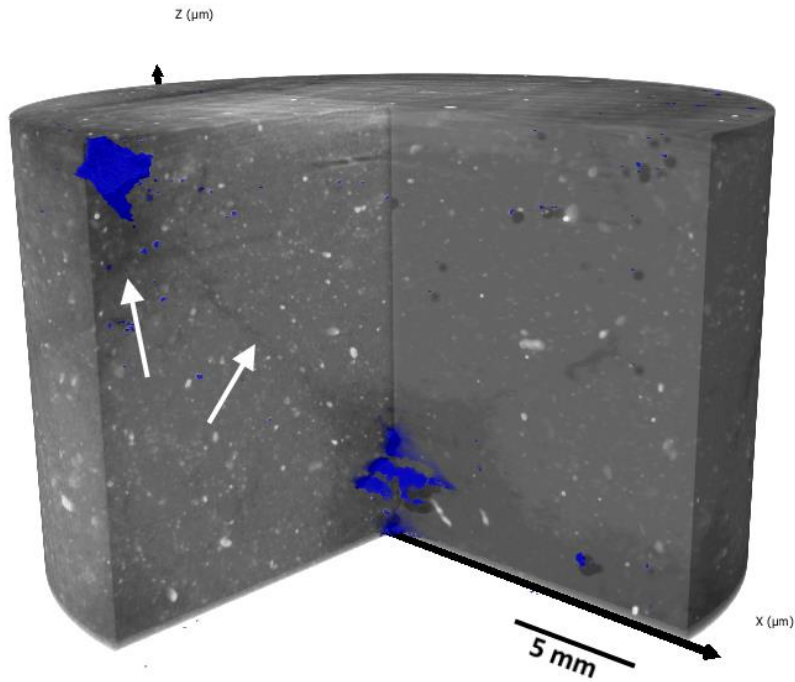


**Figure 4-74. 3D  $\mu$ -CT image projection of the single-pellet cell with a high resolution of 26.8  $\mu$ m. White arrows mark distinct fragment boundaries with a lower density (darkish gray), trapped air is highlighted in blue**

#### 4.5.3.4. Discussion of results

In all three single-pellet tests comparable results could be observed. Generally, high pressure values (total, mean, contact and max. pressure) have been measured during the initial phase, peaking at ca. 30-60 minutes after start of hydration. Additionally, a following rapid decline of these values could be observed for all tests, leading to generally low-stagnant pressure values within the first 24 hours. This drop is likely due to the relocation and homogenization process of the swelling bentonite during this transient phase of the test, as the wet material starts to expand and fills out the swelling chamber. Following this rearrangement, a period of fast pressure growth could be observed within the cells between the ca. tenth and twenty-first day, due to an increasing water uptake and hence a rising pressure of the swelling bentonite. As much of the bentonites swelling potential was reached after ca. 21 days in the cell, a slow but steady pressure propagation was still detected afterwards in Test 3. Hence it cannot be assumed that a steady state has been reached for the third test, even after a period of over 120 days.

Indicated by the  $\mu$ -CT images, this ongoing pressure augmentation is likely due to a still lasting reallocation process within the cell, as the original grain boundaries were still recognizable. As the wet bentonite material seems to have swollen into most of the chamber, distinct density variations can be observed between the centers of the original single-pellet and its surrounding fragments (higher values) and the surrounding areas of swollen material (lower values). Even though the flooding of the cells has been conducted with very low flow rates, multiple air bubbles of varying sizes were discovered within the cell of the third test. Although these bubbles only sum up to a total volume of less than 1%, they still indicate a further swelling space or potential, respectively.

It has to be noted that the pellet material was still not fully saturated even in the long-lasting Test 3, because the total water uptake of 45% is considerably lower than the theoretical value of 65%.

#### 4.5.4 Pellet-cluster test

The water uptake test on a pellet cluster has been included to provide a basis for a comparison with the tests on a single pellet. To that end, the number of pellets has been chosen to achieve the same ratio of dry bentonite mass and cell volume as in the single-pellet tests. Also, Pearson-solution was used for saturating the cluster.

Due to the different scales of the single-pellet and the pellet-cluster test, the means for comparison are limited. Basic quantities like sample weight, inflow rates etc. compare badly even if at least the trends may show useful similarities. However, properties that are related to size or mass like pressure or water content can be directly checked against each other.

The comparison in the present work was aimed at the water uptake dynamics, the evolution of the axial swelling pressure and axial swelling pressure as well as hydraulic permeability at steady state.

##### 4.5.4.1. Test setup and preparations

The pellet-cluster test was performed with a cylindrical cell (see Figure 4-75) that had already been used earlier for other swelling tests. The diameter of the sample space – also called test chamber further on – amounts to 50 mm, the sample height has also been set to 50 mm resulting in a test volume of 98.17 cm<sup>3</sup>.

The bottom part of the cell provides two inlets for the saturating solution that lead to an inflow distribution section (left out in Figure 4-75 for clarity). This section contains boreholes for the inflowing solution and has a system of grooves on top for distribution of solution over the surface of the adjacent sinter plate. The sinter plate prevents the sample from swelling out of the test chamber. A similar arrangement can be found on top of the sample. Two small tubes lead the solution out of the cell. The top head end contains a force transducer, whose readings have been stored by a data acquisition system and eventually transformed into the swelling pressure data. The free volumes between the ball valves and the test chamber have been measured to amount to about 5 ml at the bottom as well as at the top of the cell. To ensure confinement and at the same time a reading from the force transducer right from start, the pellet cluster has been put under slight pressure when closing the test cell.

Two differently sized burettes have been linked to the cell via ball valves at the two inlets, allowing for connecting each one individually to the distribution section. The big one with a large volume has been used for the initial flooding and the thinner, more precise one for reading the volume of water that was taken up later on during the test. The water uptake data have been recorded in a written log.

The whole setup installed in the laboratory is depicted in Figure 4-76. The room was climatized to a temperature of 20 °C.

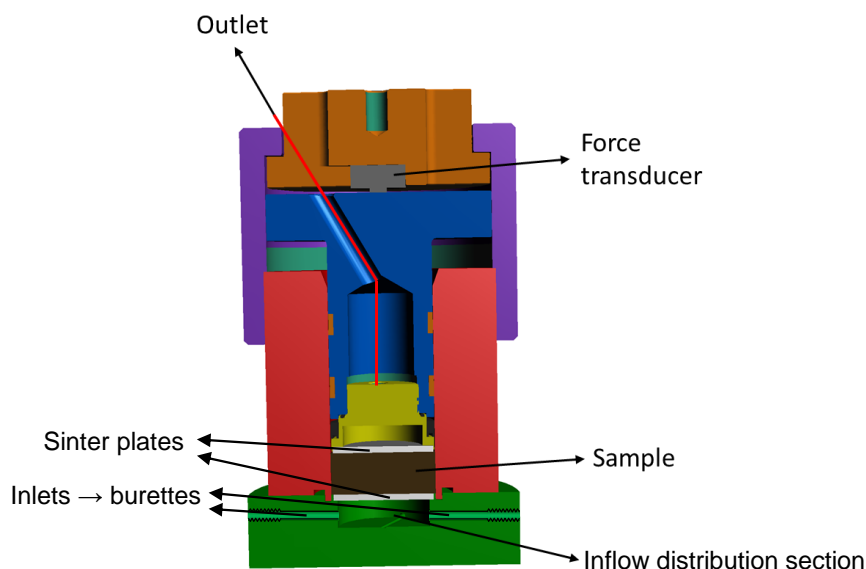


**Figure 4-75. Sketch of the test cell for the cluster-test**

Ensuring the bulk dry density is easily done by notionally distributing the pellet material homogeneously over the test chamber. Calculating the amount of water to fill the free space between the pellets in the cluster requires a bit more finesse, though.

The initial configuration of pellets in a confined space is conceived as a triple continuum that is illustrated in Figure 4-77. It consists of the interlamellar space, which is filled with hydrated water, the air-filled interpellet space and an also air-filled pore space within the pellet between the clay particles. Each of these three spaces occupies its own volume which are often related to as micro-, macro- and meso-porosity, respectively.

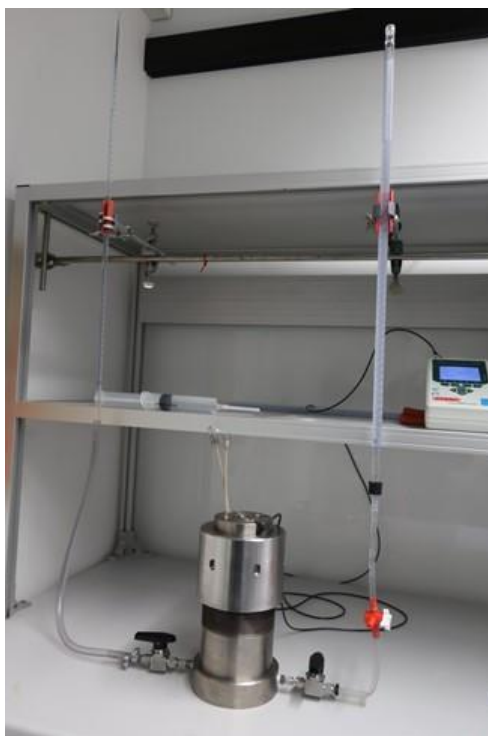


**Figure 4-76. Set-up for the test with pellet clusters**

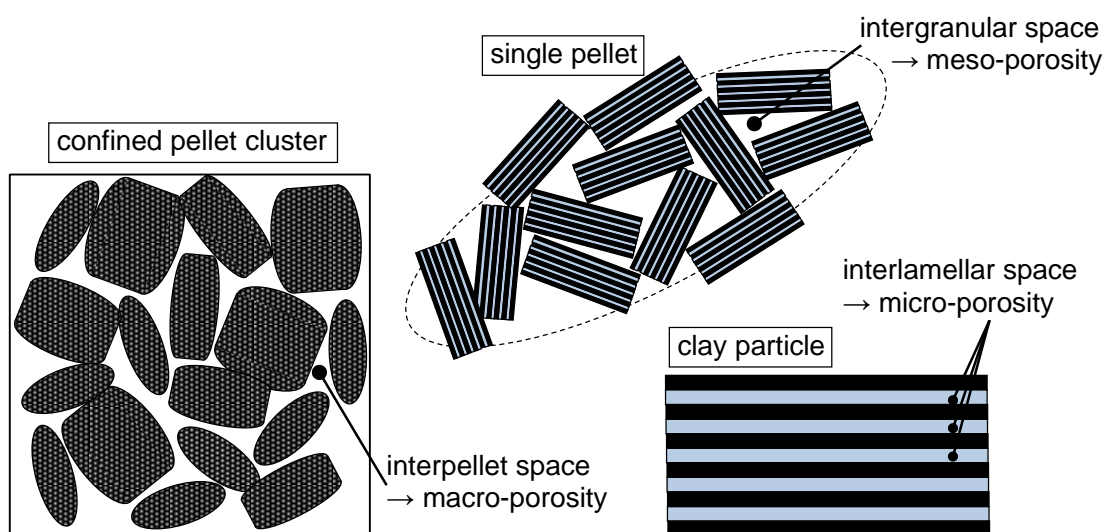


**Figure 4-77. Concept for the initial pellet configuration in a confined space**

Flooding of the test chamber with solution is expected to fill up the interpellet space quickly which should therefore enclose the air in the meso pores to a large extent. Further water uptake filling also the meso pore space should therefore take much more time. The final fate of the entrapped air remains to be unclear, though, and basically depends on the concept for water transport in compacted bentonite that is expanding into a limited space. For evaluating the tests, the volume occupied by the air is neglected.

The air-dry density  $\rho_{h_0}$  of the total pellet mass that is equally distributed over the known volume of the test chamber  $V_T$  can be calculated as the ratio of weight and volume:

$$\rho_{h_0} = \frac{m_p}{V_T} \quad [4.4]$$

- $m_p$  - air-dry total pellet mass [kg]
- $V_T$  - volume of the test chamber [m<sup>3</sup>]
- $\rho_{h_0}$  - air-dry density of the ideally distributed pellet material [kg]

With the help of the water content, the dry density  $\rho_{h_d}$  of the distributed pellet material can then easily be calculated. In order to achieve a bulk dry density of 1 g/cm<sup>3</sup>, 109.97 g pellet material with a water content of 12.3 % has been installed. The resulting bulk dry density deviated from the target value by 0.003 g/cm<sup>3</sup>.

The total volume of the pellets  $V_p$  would ideally have to be measured pellet by pellet. Since this would have been an excessively tedious task, the mean pellet density (see section 4.5.1) is approximately been used instead:

$$V_p = \frac{m_p}{\rho_p} \quad [4.5]$$

- $V_p$  - total volume of the pellets [m<sup>3</sup>]
- $\rho_p$  - mean air-dry density of the pellets [kg]

The interpellet volume  $V_a$  is then the difference between total and the pellet volume

$$V_a = V_T - V_p \quad [4.6]$$

- $V_a$  - total volume of the air-filled interpellet space [m<sup>3</sup>]

which can be calculated as a fraction of 45.7 % of the total test volume.

#### 4.5.4.2. Simple pre-tests

Flooding the cell in the single-pellet test could be achieved reasonably quick. This ensured simple initial conditions for the test and the subsequent modelling, i.e., a fully water-filled space outside a basically yet unaltered pellet (plus pieces). However, bentonite takes up water at contact with water instantaneously and a much larger test chamber was to be filled with water in the pellet-cluster test taking more time to do so. It was therefore apprehended that swelling of the pellets at the inflow side could impede flooding of the test cell. Since the envisaged test cell was non-transparent, there was no way to allow for a visual inspection of the flooding dynamics during the test.

The actual test was therefore preceded by two simple pre-tests in an acrylic glass tube, called pre-test 1 and pre-test 2. The tube with an inner diameter of 50 mm was cut to a length that left room for an equivalent of the test chamber in the steel cell and a coarse bronze sinter plate plus some extra space at the top end. Steel rings were emplaced in the extra space to allow for filling in the test solution and to keep the sample in place at the same time (see Figure 4-78). The other end has been sealed by gluing an acrylic glass plate to the tube. The whole set-up was kept together with the help of a vice. Since the conditions in the actual test cell were

to be mimicked, a target bulk dry density of  $1 \text{ g/cm}^3$  in the acrylic glass tube has been aimed at. The cluster was then flooded with Pearson-solution and afterwards, a photo has been taken every 30 s.



**Figure 4-78. Pellet cluster installed in the acrylic glass tube for pre-test 1, dry at  $t = 0$**

The conditions in the cluster column of pre-tests 1 and 2 at  $t = 0$ , 1 and 10 minutes after flooding are depicted as a series of photographs in Figure 4-79. A comparison of the initial pellet configurations ( $t=0$ ) in the two pre-tests reveals that while the pellet clusters had the same bulk dry, the resulting orientation of the pellets has been entirely different. In pre-test 1, the pellets were quite horizontally oriented and in pre-test 2 rather vertically. This was recognized only later after the tests.

Visible swelling can be observed within a minute. Also, a slight reorganisation of the pellets is recognisable. Air bubbles can be seen at the top of the cluster. They disappear, though, over some ten minutes.

It appears that the pellets have taken up a significant amount of water in the outer regions already during the first minute of immersion which has led to a certain swelling. Also within a minute, some light grey features appear on the area where pellets are in contact with the transparent wall. This effect is particularly pronounced at the two pellets in the second lowest layer in pre-test 2 (lower row in Figure 4-79). It can also be found in pre-test 1 (upper row in Figure 4-79) in the top left corner but to a much lesser extent. The effect is interpreted as bentonite material being softened in the wetted outer pellet regions while preserving a dry core. As the pellets next to the tube wall were swelling and at the same time experiencing the outward directed swelling pressure from inside the cluster column, they were consequently pressed against the transparent wall. The soft outer material of these pellets was thereby squeezed aside giving way to the still harder and dryer core which would show in a brighter shade of grey than the wetted part.



**Figure 4-79. Pellet cluster in the acrylic glass tube; pre-tests 1 & 2 after 0, 1, and 10 min**

After several minutes, the comparatively dry core in light grey is surrounded by a thin dark grey zone. Why the darker zone emerges remains to be explained.

The pictures of the second series depicted in Figure 4-80 show the situation at 20, 80 and 320 minutes after flooding. Even after 20 minutes the water-filled interpellet space appears to be still well connected even if the remaining free interpellet space is much narrower. Impediment of inflow in the pellet-cluster test by swelling of the pellets can therefore not be concluded from these pictures.

Out of curiosity, the first and later the second test have been prolonged. The effect of exposing the dry pellet core at the transparent walls appears to reach its maximum after an hour or two. Concurrently, the dark zones surrounding the bright grey areas appear to intensify but do not grow after about 20 minutes. However, when the bright grey zones disappear again, they are replaced by the dark zones that are persistent over the rest of the observation time of about 3 days (see Figure 4-81). Homogenisation is thus far from being completed at that time.

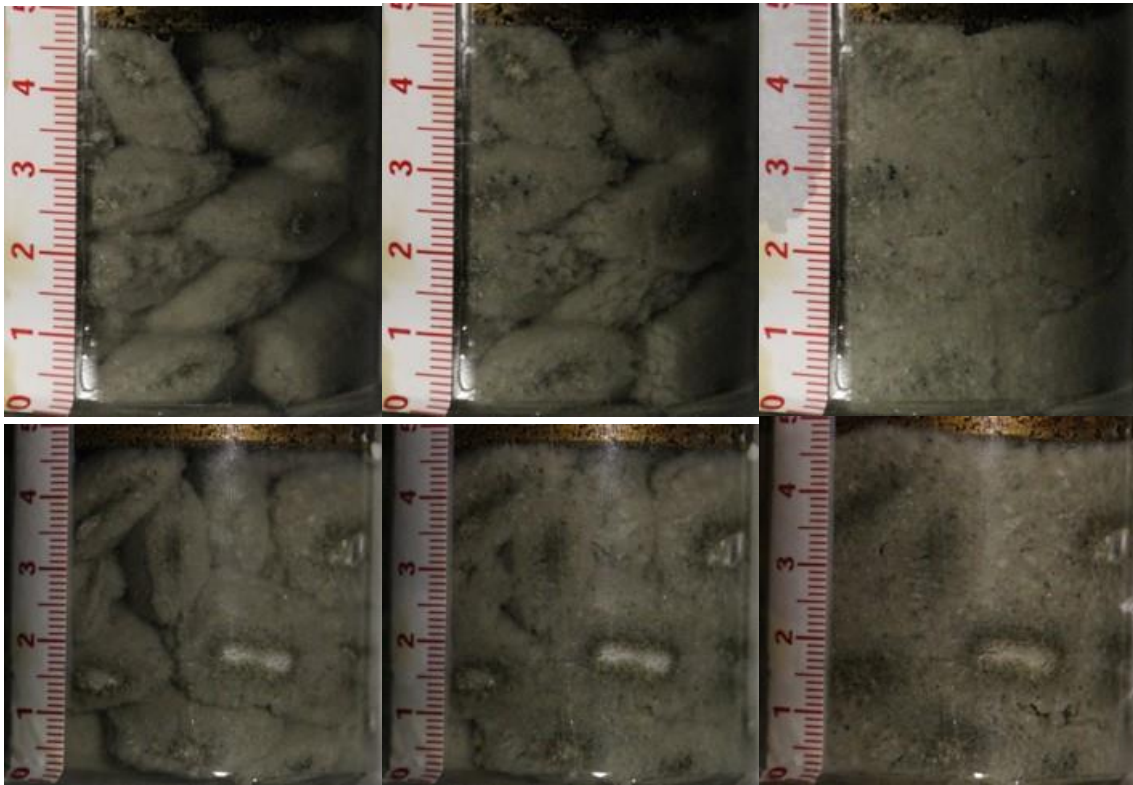


**Figure 4-80. Pellet cluster in the acrylic glass tube; pre-tests; after 20, 80 and 320 min**

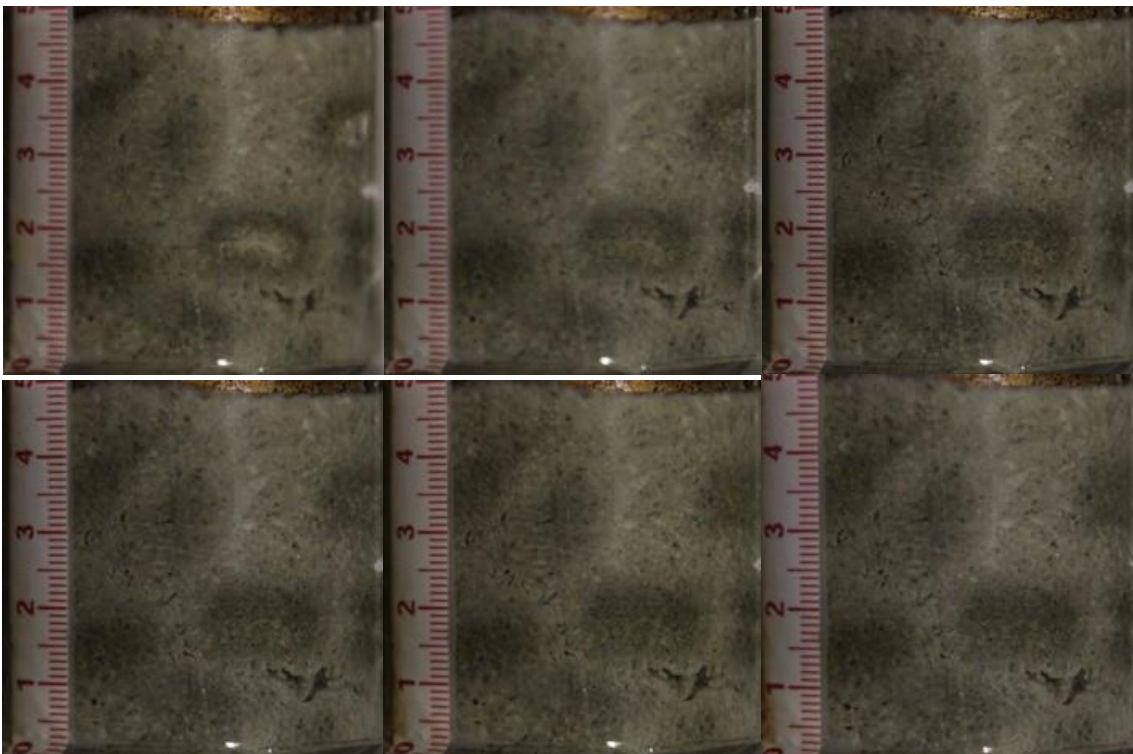


**Fig 4-81. Pellet cluster in the acrylic glass tube; pre-test 2; after 540, 950, and 1315 min (~22h), and after 24, 45, and 74 h**

#### 4.5.4.3. Test procedure

##### *General outline*

The main water uptake test with a pellet cluster comprised three phases: (1) flooding, (2) saturation and (3) the permeability test at steady-state conditions. Since the primary target has been the permeability test in phase 3, the nature of the water uptake test required a criterion for reaching steady-state conditions that could only be based on observations on the transient behaviour during phase 2. Basis of such a decision had been envisaged to be either the water uptake rate or the swelling pressure. The dynamics of cluster saturation were therefore followed by gathering data on the swelling pressure and to the water uptake. As sort of a bonus, the transient data could also be compared to the related data from the single-pellet test.

Formulating a criterion for reaching steady state from transient data is a tricky task, though. The deceptively easy definition of steady-state conditions as the absence of changes of properties with time at any considered point in space has a catch. Water uptake of bentonite appears to be a convergent process like solute transport by diffusion which mathematically never reaches steady-state conditions. What is really sought in these cases is “absence of changes of properties with time at any considered point for all practical purposes”.

Such a criterion should therefore be based on the purpose for which steady-state conditions are required and the related tolerance to deviations from the ideal steady-state. What should not happen then, is that this tolerance is uncritically related to the accuracy of the measurements which depend somewhat arbitrarily on the accuracy of the measuring equipment. If a converging curve – may it be a breakthrough curve or a spatial distribution – gets scanned by a measurement device with a finite degree of accuracy, the long tail towards later times or larger distances gets lost in the noise of measurement errors sooner or later. When the measured signal gets in or below the range of the detection limits there are no means of determining the further course of the true curve (e.g., Kröhn, 2020). A discussion about the closeness to steady-state conditions must therefore include the trends in the curves that can be determined with reasonable accuracy before the actual curve gets lost in the noise.

##### *Phase 1: Flooding*

After installation of the pellets in the test cell, the two burettes were filled with Pearson-solution up to the 0 cm<sup>3</sup> mark. Then the ball valve at the bigger burette was opened, filling the test cell including the dead volumes at the top and the bottom of the cell with the solution under hydrostatic pressure. At the top end of the cell a small tube was left open to allow the gas in the test chamber to escape. The small tube was closed when the first droplets appeared at the outflow end. This happened about 11 minutes after opening the ball valve to the bigger burette.

Due to a subsequent procedural confusion, the ball valve to the finer burette was opened then, too. This phase lasted approximately for the following 6 minutes. There are two readings for the two burettes during this period of time showing that the water surfaces in the two burettes have basically been levelling out. Then, the bigger burette was shut off.

##### *Phase 2: Saturation*

While the swelling pressure has constantly been monitored, the water level in the burette was read and protocolled at intervals. For evaluation purposes, the water levels were transformed into a cumulative volume of water being taken up. Implying a constant flow rate between two

readings, these flow rates could be calculated as the quotient of increase of water in the cell and the related time interval.

Furthermore, it has been tried to derive the increasing water content of the pellets from water uptake and the pellet dry mass. This would have been correct only, though, if all the water flowing into the cell had been taken up by the pellets on arrival. But the pre-test shows clearly a significant interpellet space for at least one to two days (see Figure 4-81). The initially large interpellet space apparently required days to be fully filled with expanding pellet material. Furthermore, the inhomogeneities inside a formerly single pellet are persistent over even more time. The water content values are therefore considered to be reliable after 4 days earliest and at that only in terms of a mean water content over the whole cell volume. They have reached then almost 63 % which is equivalent to a degree of saturation of roughly 97 %. A comprehensive graphical summary of the results is given in Figure 4-82.

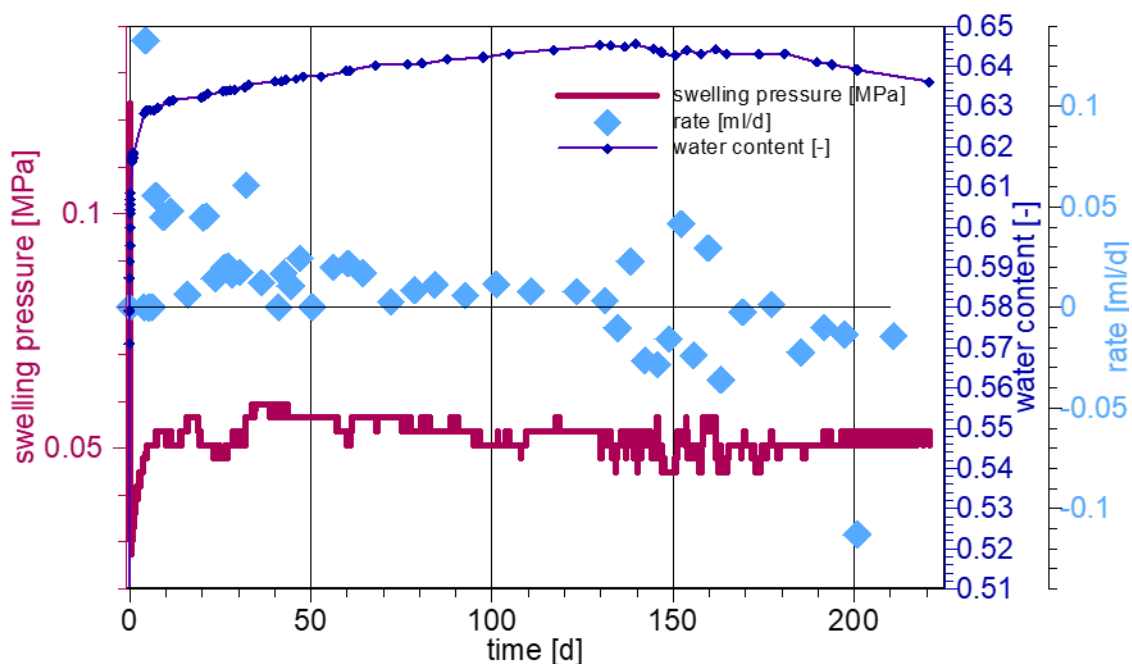


**Figure 4-82. Swelling pressure, water content and water uptake rate in the cluster test**

The initial mechanical pressure on the pellets that had been applied to the pellet cluster for technical reasons (see section 4.5.4.1) proved to be a bit high, amounting to 0.118 MPa. After flooding of the cluster, it increases within 10 minutes to 0.123 MPa but then starts to collapse, reaching a minimum value of 0.03 MPa after about 4 hours, remaining at that value for another 17 hours and rising back again to almost 0.06 MPa at 35 days after flooding. Between 35 and about 170 days, the swelling pressure decreases slowly to 0.0508 MPa. For the final 50 days, it appears to increase so slightly that the swelling pressure cannot be clearly resolved with the accuracy of the force transducer. While the overall trend is rather clear, it has to be conceded that there are quite some irregularities in the curve. It rather strongly deviates from this trend between 12 and 34 days. There are also somewhat strange oscillations between 130 and 175 days.

The most astonishing feature in the results, however, is the apparent loss of water from the cell after 130 days. The water level in the small burette starts rising again, slowly and somewhat oscillating in the beginning but more pronounced after 160 days. This has been entirely unexpected. Note that the beginning of the decrease in water content coincides with the

beginning of oscillations in the swelling pressure indicating a triggering event of unknown nature in the cluster. However, it can also be imagined that the calculated water uptake rates follow an earlier commencing trend towards the negative region thereby rather indicating a continuous development in the cluster. Which explanation is the better one, remains to be decided. In any case, while observing the squeezing out of water from the cell it has already been speculated that the driving process could be gas generation in the bentonite. This speculation has been corroborated much later by discovering a large gas bubble in the transparent tube that connects the burette with the cells.

Note that presently neither the water content nor the swelling pressure appeared to have reached steady state yet.

### *Phase 3: Steady state*

One major goal of the experiment has been the comparison of the saturated hydraulic permeability in the single-pellet and the pellet-cluster test. It has therefore been decided to perform the permeability tests in parallel at the GRS geotechnical laboratory in order to provide maximum comparability in terms of test conditions. This proved to be even more important when it was been realised that a safely applicable inflow pressure should be somewhat less than the swelling pressure to avoid mechanical damage on the samples. In turn, very low flow rates have been expected, too, so that quite low hydraulic pressures would have been involved over longer times than initially expected. All in all, this would have called for an unexpected high effort for performing the test in terms of equipment and test procedure.

A sample from the single-pellet test still installed in the test cell was sent to GRS for that purpose. However, it arrived not fully saturated (compare section 4.5.3.4). A meaningful comparison of permeabilities was therefore not possible and the permeability tests had to be cancelled.

#### **4.5.4.4. Discussion of the results**

The evolution of the swelling pressure in the pellet-cluster test is a rather complex one. For later reference, it will be divided into phases whose definition and period along the timeline of the test will be described in the following.

The pellet-cluster test started at a confining pressure of 0.118 MPa which nevertheless increased slightly up to 0.123 MPa over the first 10 minutes (phase 1; see Figure 4-83). During the following 10 minutes, the swelling pressure dropped quickly to almost half, namely 0.068 MPa (phase 2) with a subsequent period of slower further decrease (phase 3).

The slower decrease in phase 3 reveals to be of convergent nature as shown in Figure 4-84. After about 10 hours it reaches a minimum at 0.027 MPa. Afterwards, an even slower increase of the swelling pressure can be observed (phase 4) that continues with some serious interruptions until day 37 (see Figure 4-85) converging towards 0.059 MPa. Even slower is the decrease in the swelling pressure during subsequent phase 5 again as shown in Figure 4-86. Interpretation becomes a bit hampered by the changes being small in comparison to the accuracy of the measuring equipment. This results in a seemingly erroneous up and down along the measured curve. However, a certain trend down to 0.051 MPa at 175 days can still be recognised. Note that there is a particular period between 130 and 165 days where the swelling pressure oscillates apparently quite strongly, namely more than can be explained by the limited measurement accuracy.

In the latest observed phase, phase 6, depicted also in Figure 4-86, the swelling pressure appears to increase ever so slowly again.

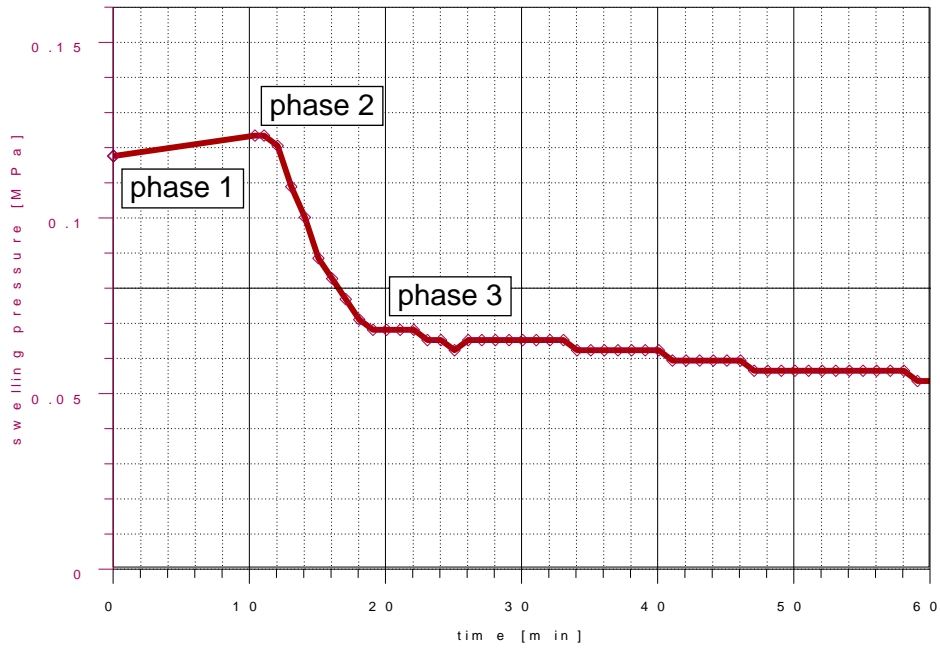


**Figure 4-83. Swelling pressure in the pellet-cluster test; close-up over 60 minutes**

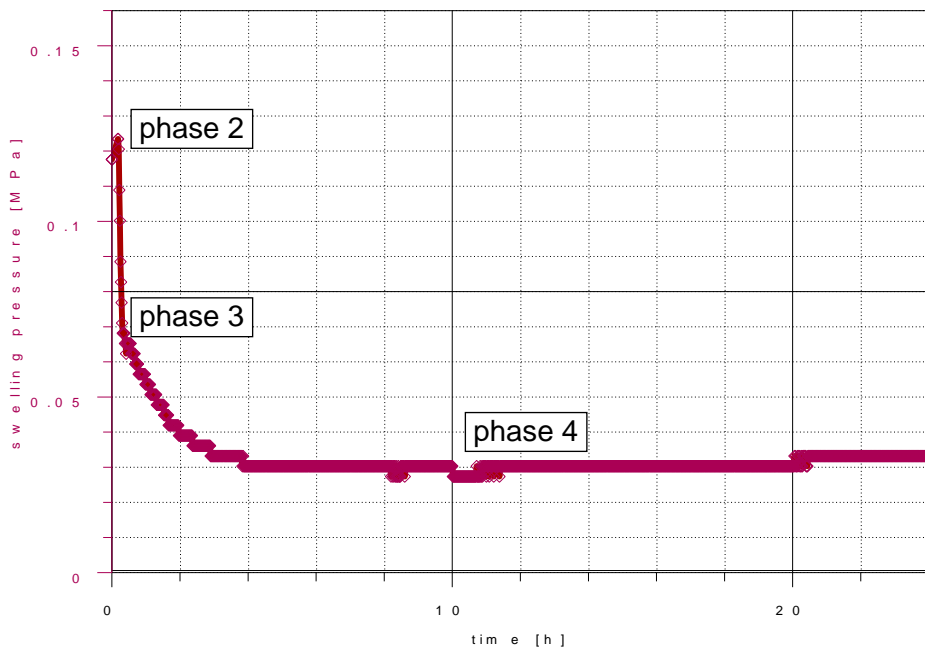


**Figure 4-84. Swelling pressure in the pellet-cluster test; close-up over 24 hours**

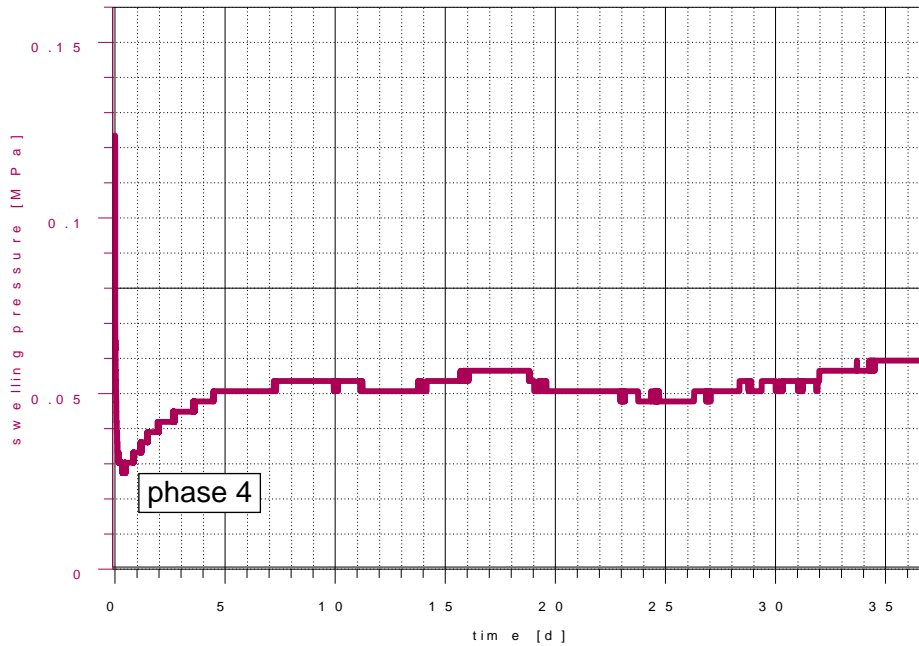


**Figure 4-85. Swelling pressure in the pellet-cluster test; close-up over 37 days**

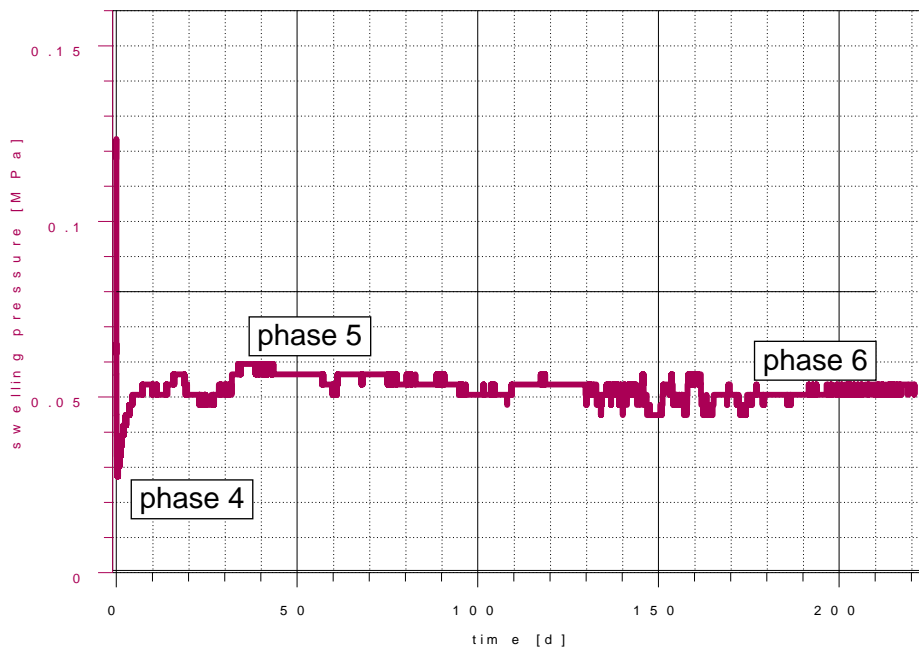


**Figure 4-86. Swelling pressure in the pellet-cluster test; whole test**

The pre-tests in the acrylic glass tube cover only the first period of up to 3 days after flooding and may differ from the actual pellet configuration in the test cell. Nevertheless, cross-referencing the photographs from the longer running pre-test 2 and the measurements on swelling pressure from the main test allows for some interesting observations. The same photos as in Figure 4-79 to Figure 4-81 are depicted also in Figure 4-87 to Figure 4-89 but complemented with plots of the swelling pressure showing the related points in time on the swelling pressure curves.

Figure 4-87 shows pictures covering the very first period of testing until 10 minutes after start, which marks the end of the increasing swelling pressure in phase 1. The relation to the swelling pressure curve corroborates the conclusion drawn in section 4.5.4.2 that (1) the initial increase in swelling pressure during phase 1 is an immediate response of the pellets to the solution and (2) that the softening of the outer pellet regions in combination with an increasing swelling pressure squeezes the soft part at contact points away which shows at the transparent wall as exposure of the dryer inner part. In the cluster, the pellets try to expand under the influence of wetting but are mechanically impeded by their neighbours. A swelling pressure builds up in each individual pellet between the contact points and gets conveyed through the cluster to the force transducer.



**Figure 4-87. Pellet cluster in the pre-test, after 0, 1, and 10 min and swelling pressure**

This pressure build-up is in principle not unlike water uptake in compacted and confined bentonite where the bentonite also takes up water almost immediately. And since in this case, the bentonite cannot expand due to the confinement, it exerts concurrently a swelling pressure on the adjacent still dry part thereby compacting the dry part to a certain extent. This is believed to happen in a matter of minutes (e.g., Kröhn, 2011).

However, in case of the clustered pellets this effect can hold only between contact points. Laterally, the pellet can – at least initially – freely expand thus counteracting the initial pressure build-up. Since the contact areas are small in comparison to the freely expanding surface, the net effect is an overall pressure decrease. This apparently takes some time, though, delaying the related beginning of phase 2 for a few minutes.

At the onset of phase 2 (third picture in Figure 4-87) the pellets are by and large still surrounded by water and thus experience a quick and efficient water supply which gives reason to the subsequent fast decrease of the swelling pressure. However, at the same time the outer pellet material continues to swell into the interpellet space building up an increasingly effective obstacle for further water flow.

The transition from phase 2 to phase 3 occurs at about 20 minutes after flooding. The related photograph in Figure 4-88 indicates that parts of the interpellet space are about to get fully filled with bentonite. While the explanation for the decrease of swelling pressure during phase 2 holds in principle also true for the further decrease in phase 3, the increasing impediment of water flow in the interpellet space appears to slow down the process considerably and explains the convergent progress of the swelling pressure.

After 320 minutes, the interpellet space has apparently vanished as a whole. At this point the decrease of swelling pressure has not quite come to a temporary end but goes down in velocity again. For reference, this point in time is also marked in the swelling pressure plot in Figure 4-89.

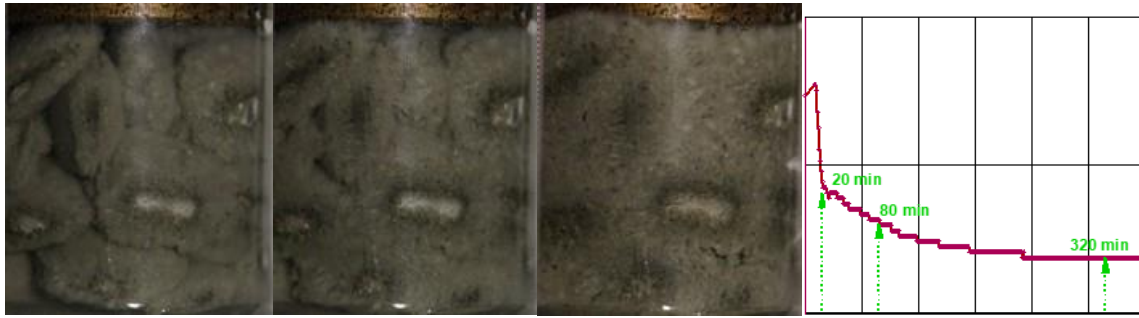


**Figure 4-88. Pellet cluster in the pre-test, after 20, 80 and 320 min and swelling pressure**

The final series of photographs in Figure 4-89 comprises six pictures from pre-test 2 for 540, 950 and 1315 minutes and for 1, 2, and 3 days after flooding. After 540 minutes, phase 3 is basically done and the temporary minimum swelling pressure is reached. Comparison of the pictures from 320 minutes (Figure 4-88) and 540 minutes (Figure 4-89) does not really show any structural differences in the bentonite material. This applies also for the rest of the pre-test 2. Only observable is the vanishing of the bright grey areas that are basically gone after about a day and are replaced by the dark shades that have formerly only formed the rings.

Further evolution, however, lies beyond a possible correlation of visual inspection with the data on swelling pressure from the pellet-cluster test. Looking deeper into explanations for the observed complex behaviour, in particular the seemingly oscillating sequence of increasing and decreasing swelling pressure that increases in oscillation period and decreases in amplitude, lies outside the scope of this work and requires further investigations.

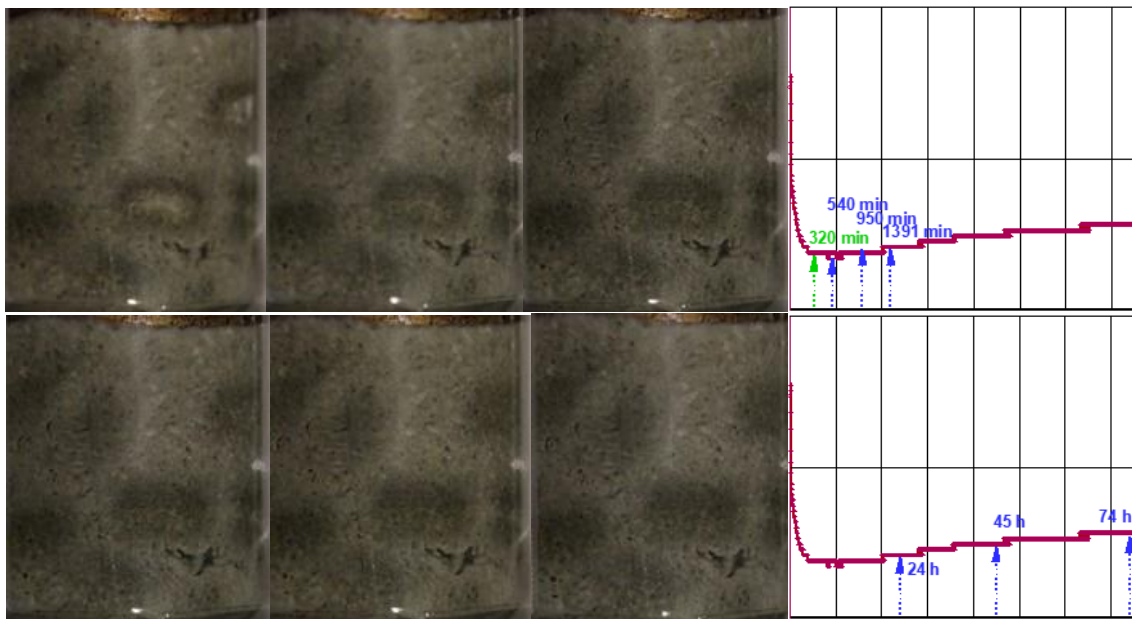


**Figure 4-89. Pellet cluster in the pre-test and swelling pressure; after 540, 950, and 1315 min (~22h), and after 24, 45, and 74 h**

#### 4.5.5 Data comparison

##### 4.5.5.1. Test conditions

###### *Cell*

The test chambers for the single-pellet and the pellet-cluster tests have both been cylindrical. Due to the purpose of the experiment, the sizes differed of course. The test chamber for the pellet-cluster test has been 10 times larger than the one for the single-pellet test. The geometry data are compiled in Table 4-10.

**Table 4-10. Geometry of the test cells**

Test	Length [mm]	Diameter [mm]	Volume [cm <sup>3</sup> ]
Single-pellet	20	25	9.82
Pellet-cluster	50	50	98.2

In order to allow for visual inspection of the evolution of the swelling dynamics, the single-pellet test cell has been manufactured from acrylic glass. Since an existing steel cell had to be used for the pellet-cluster test, direct observation was not an option. Instead, a supplementary pre-test with an acrylic glass tube has been performed.

###### *Wetting procedure*

For the wetting, Pearson solution has been used for the single-pellet as well as for the pellet-cluster tests. However, the associated procedures have been quite different. In case of the single-pellet test, the solution has been injected with the help of a syringe pump until initial flooding was complete. This took about 3 minutes. Later, it has been tried to add solution manually with a syringe but not enough pressure could be mustered.

In case of the pellet-cluster test, the solution was simply driven by the slight hydrostatic pressure caused by the connected burettes. It took about 11 minutes until the first droplets appeared at the outlet. After closing the outlet, the sample remained permanently connected to the solution reservoir provided by the burettes until the end of the test. No air bubbles have been created by the injection procedure, neither in the single-pellet test nor the pre-test with a pellet cluster in an acrylic glass tube.

##### 4.5.5.2. Test results

As has been hoped for, there are quite some similarities in the evolution of the swelling pressure. The data are discussed in the course of events. First, the results for the swelling pressure in the three single-pellet tests (SPT1 to SPT3) as well as the pellet-cluster test (PCT) are shown in Figure 4-90 for the period of 1 day.

All three single-pellet tests show a fast increase in swelling pressure from 0 to values between about 0.105 to 0.135 MPa. In that they look quite similar. The pellet-cluster test by comparison, had initially been under a confining pressure of 0.118 MPa but also still increases slightly up to 0.123 MPa.

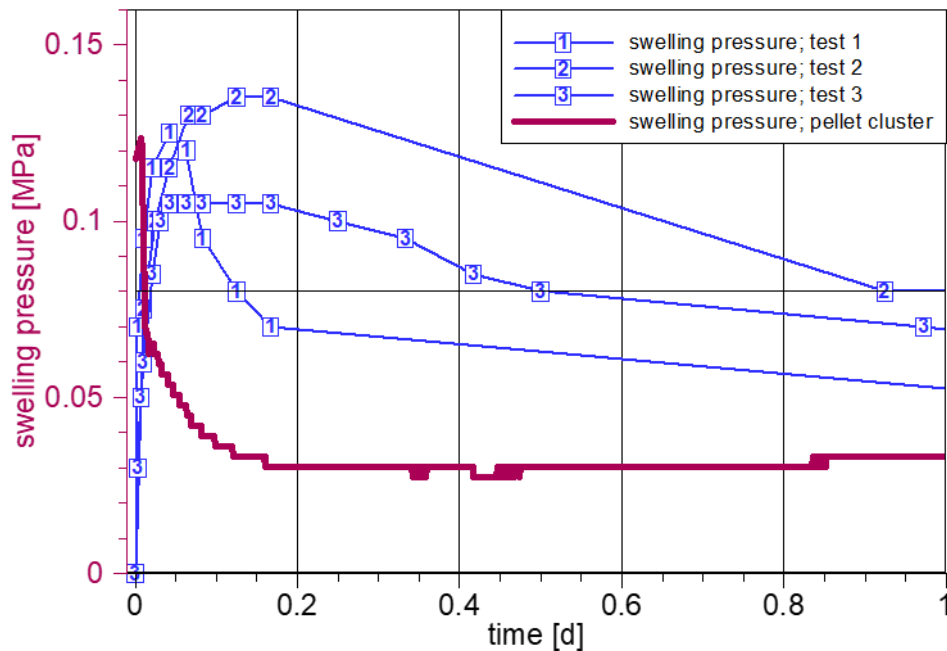


**Figure 4-90. Swelling pressure in the three single-pellet tests and the pellet-cluster test for the first day**

Subsequently, the swelling pressure decreases, however, at rather different dynamics. Fastest is the PCT, then SPT1 to SPT3, in that order. What appears as sort of a peak in SPT1 and the PCT, is quite stretched out in SPT2 and SPT3. Already within one day, the swelling pressure increases again in the PCT, even if comparatively slowly, while this cannot be seen, yet, in SPT1 to SPT3. However, it has to be conceded that there is a gap in the data from SPT1 between about 4 hours and 3 days as can be seen in Figure 4-91. A quite similar gap between 4 and 22 hours can be found in the data from SPT2. The rising of the swelling pressure could therefore have begun anytime during these gaps.

The curves in Figure 4.91 put the observations from Figure 4-90 concerning the shape of the peaks into perspective. Equally prominent as the peaks is the slow increase of the swelling pressure during the first 10 days that can be seen in all curves, if not in absolute values then at least in the trend. Note that the swelling pressure in the PCT lies in between the curves for SPT1 to SPT3 but noticeably closer to the later tests.

While this trend lasts in SPT1 and SPT2 until end-of-test at 17 and 21 days, respectively, there is a strong increase in SPT3 that does not appear to be in line with the other tests. Between day 10 and day 22, it almost doubles from 0.065 to 0.125 MPa (see Figure 4-92). From that point on, it increases basically monotonously at a slightly decreasing slope until end-of-test at 127 days. This evolution is contradictory to the more even but also more complex sequence of events in the PCT as discussed in section 4.5.4.3.

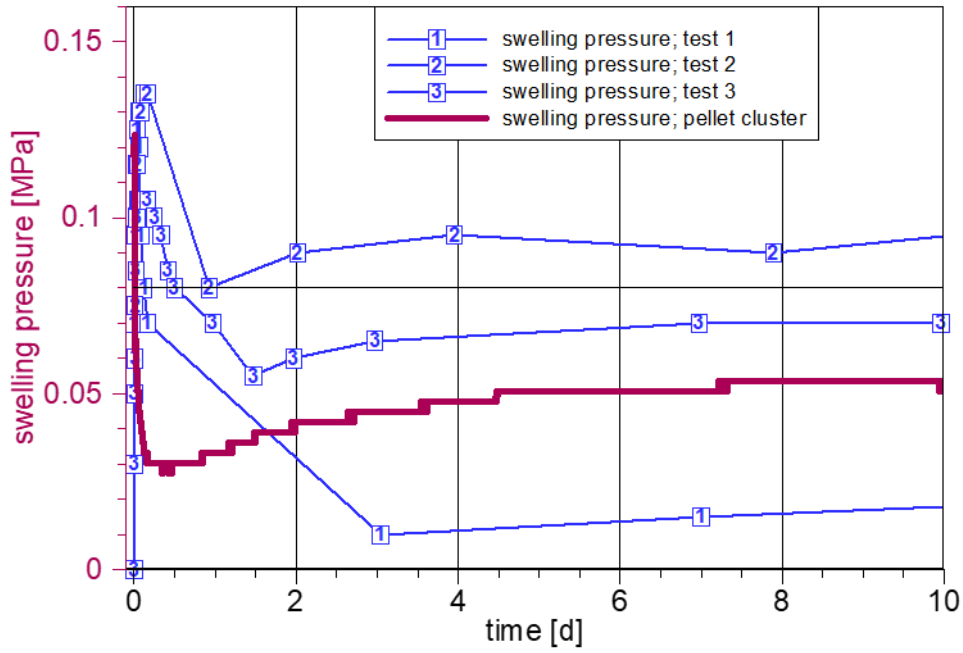


Figure 4-91. Swelling pressure for the first 10 days

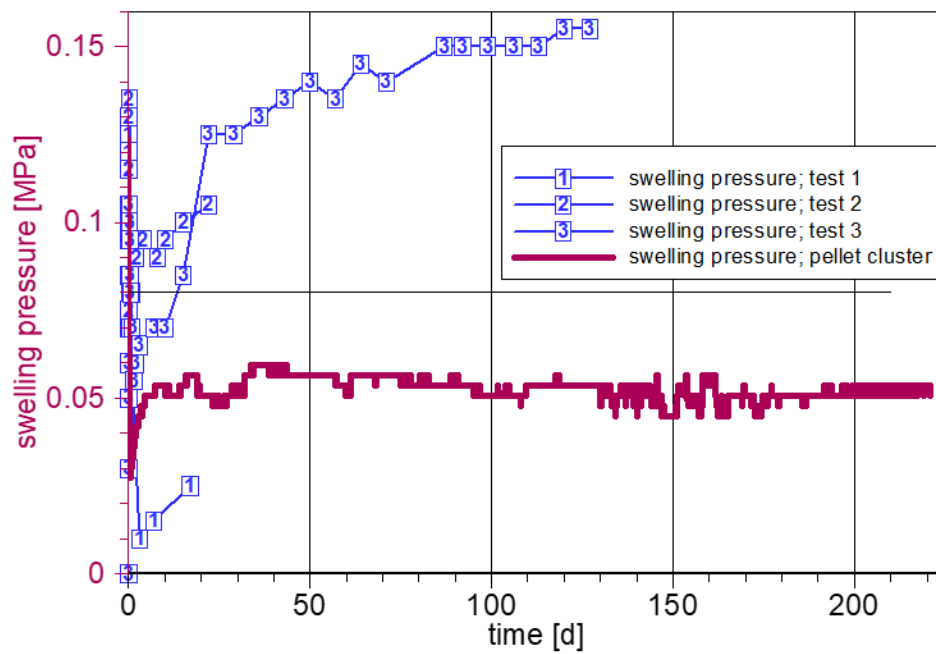


Figure 4-92. Swelling pressure over the whole experiment

## 4.5.6 Summary, conclusions and recommendations

### 4.5.6.1. Summary

An experiment concerning scalability of properties of bentonite pellets has been performed. It consists of a series of tests at different test scales. Small cells that are slightly larger than a single pellet have been deployed as well as a larger cell for accommodating a cluster of pellets. The tests are thus called here “Single-pellet tests” (SPT) and “Pellet-cluster test” (PCT). Since the PCT has been performed in a steel cell, a pre-test as a mock-up of the PCT using acrylic glass for visual inspection of wetting and swelling has been performed additionally. In all tests, the slightly salty Pearson-solution has been used for wetting.

The following results from the PCT appear to be noteworthy:

- For all practical purposes, swelling of a pellet fully immersed in Pearson solution starts immediately with the first contact with water.
- At the same time, the outer regions of a pellet become very soft. If the pellet cluster is emplaced in a confined space, the swelling pressure squeezes the soft part of a pellet away, thereby exposing the still dry part and providing a spatial framework of beam-like pressure conveying structures.
- The subsequent decrease of the swelling pressure over a quick strong and a following slower convergent phase appears to be related to the filling of the interpellet space with swelling bentonite material.
- Swelling of the pellets in the PCT could not have impeded the inflow of the solution.

It appears that several observations from the PCT need to be explained yet:

- Entirely unexpected is the significant continuous flow of solution out of the test cell beginning at about 130 days. The reason for this phenomenon is still unclear but it appears to be systematic as it has been observed in comparable tests elsewhere as well.
- The evolution of the swelling pressure follows a series of consecutive phases of increase and decrease. It increases in oscillation period but decreases in amplitude. When the test has been terminated, changes in swelling pressure have come down to the range of the measurement accuracy. It is nevertheless quite possible that the end of this evolution has not been reached yet.
- The phases of swelling pressure evolution do not follow a continuous curve but are sometimes overlain by comparatively strong oscillations with a comparatively high frequency.

The comparison of the cells for SPTs and the PCT shows that the volume in the PCT is ten times larger than in the SPTs ensuring a considerable difference in scale. This is, however, not reflected in the time used for complete flooding of the respective test cells which has been 3 minutes in the SPTs and 11 minutes in the PCT.

Independently of the size of the tests, the swelling pressure evolution follows the same pattern of initial short increase, subsequent slower decrease and after that an even slower increase in all tests. The shape of the initial peak is somewhat different, but this can probably be attributed to the different configuration of pellet material in the single-pellet cells. However, the long-term SPT 3 does not show signs of ending phase 4 (increase in swelling pressure) even after 127 days while this can already be observed after 37 days in the PCT.

#### 4.5.6.2. Conclusions

Wetting-induced swelling of a confined pellet(-cluster) is much more complex than the wetting processes applying to compacted and confined bentonite. The first reaction of a pellet(-cluster) to water (phase 1 in the PCT) has some similarities to the wetting of confined bentonite in that basically instantaneously an overall mechanical pressure develops. However, as the bentonite is not homogeneously distributed in a pellet cluster, the pressure can only build up between contact points of each pellet to neighbouring pellets or the cell walls. The swelling pressure in a pellet cluster is therefore not homogeneously distributed like in the compacted and confined bentonite but can rather be imagined as being restricted to a three-dimensional framework of pressure conveying beams.

After the initial pressure build-up, however, the subsequent swelling of pellet material into the initially free interpellet space has its own dynamics and an opposing effect on the swelling pressure (phase 2 and phase 3 in the PCT). Since the surface area of a pellet that can be attributed to free swelling is much larger than the contact area to neighbouring pellets or the cell walls, the effect from free swelling quickly begins to dominate the overall swelling pressure evolution for the first few hours. The total swelling pressure does not drop down to zero, though, which suggests that the swelling pressure bearing framework of pellet material is still stiff enough to carry a certain mechanical load.

At this stage, the previously free interpellet space in the PCT has already been filled with bentonite of probably rather low density. But it took about 10 hours until the water reached the centre of a pellet. Wetting of the comparatively dry pellet cores explains the subsequent increase of the swelling pressure (phase 4 in the PCT) even more so as it is a much slower process than the preceding decrease.

Up to this point, the swelling pressure measured in the SPT3 and the PCT agree, not in absolute values but in the trends in general. The equivalent of phase 4 in SPT3 takes much longer, though, and there is no sign of phase 5 or 6 like in the PCT. The difference can possibly be explained by the different degree of homogeneity. While the pellet material forms a highly irregular structure in the SPTs, there is a more structured pattern of pellets present in the PCT even if the two pre-tests show that there is more than one way of installing the pellets. What gives rise to the occurrence of phases 5 and 6, is not totally clear, though. Even more mysterious is the cause for expelling the water from the test cell in the PCT during phase 5. Complex structural reorganisation in the pellet cluster has to be suspected, therefore. However, also gas generation in the pellet cluster appears to be conceivable at this point.

A final interesting observation on a confined pellet(-cluster) concerns the time required for equilibration. The PCT shows that the pellet cluster has still not been at steady state after 220 days despite being nearly instantaneously immersed in the solution. Had the individual pellets been confined, they would have shown the wetting characteristics of a compacted bentonite body. Tentative model calculations indicate that in this case, a rather small single pellet would have been fully saturated already in a matter of a few days.

In principle, there are two regions that are different concerning the arrangement of the pellets. Within a pellet cluster, there is a certain overlap of pellets. It is therefore impossible to imagine a virtual subvolume with regular boundaries without cutting through some of the pellets. This is different at the cell walls where the walls prevent from such an overlap. It is thus that a certain difference is introduced in the pellet configuration if the test volume is smaller than the envisaged assembly in-situ. The error increases with decreasing cell size. In order to minimise this effect in the SPTs, the single pellets have been supplemented by pellet fragments. This is necessary for realism but of course somewhat arbitrary and may have led to the difference in the swelling pressure curves from the SPTs.

The swelling pressure curves from the SPTs and the PCT show a reasonable match up to a certain point. While a SPT may therefore have a similar predictive capacity for the early swelling pressure evolution as a PCT, this appears to be lost at longer testing times. If this observation is, as suspected, the consequence of a different degree of homogeneity, it would be preferable to use PCTs instead of SPTs, at least for longer testing periods.

#### **4.5.6.3. Recommendations**

The experiment described in this section leaves several questions open. Further tests appear therefore to be highly advisable to complement the present understanding of the wetting of a pellet buffer. They should be addressing the following questions:

- What is the time required to reach steady-state in the water-uptake? Supplemental questions:
- What degree of homogeneity will the buffer show at steady state?
- How can reaching steady state be defined?
- Are the six phases in the evolution of the swelling pressure real or a measurement artefact? If they are real, are there more than 6 phases? This presents challenges to the accuracy of the measuring equipment.
- Why is water expelled from the test cell during phase 5?

Concerning air in the test cell:

- Where do the air bubbles go that are involuntary trapped in the interpellet space during flooding?
- What is the fate of the intrapellet air that is enclosed by flooding of the cell?
- How do the results of the PCT compare to measurements at a technical scale?
- How do the results of the PCT compare to tests with more realistic inflow scenarios, i.e., lower inflow rates?

A final recommendation concerns the cell material. As optical monitoring of the swelling process has proved to be highly valuable, there should be supplementary tests with transparent cells. These should be combined with an automated picture taking equipment.

## 5 Binary mixtures or artificial inhomogeneities

### 5.1 Saturation of pellet/block systems under isochoric conditions (CIEMAT)

CIEMAT carried out a series of hydration tests in isochoric cells to qualitative and quantitative evaluate one of the possible sources of bentonite heterogeneity: the combination in the same barrier of pellets and blocks of compacted bentonite, whose initial dry densities and structures noticeably differ. The tests performed with FEBEX bentonite in the large-scale oedometer and the transparent cell were described and jointly analysed in an open published paper (Villar et al., 2021b) and with more detail in the report Villar et al. (2001c), whose contents are approximately reproduced in the following subsections. Once the project had started a new large cell was fine-tuned and a similar test using MX-80 bentonite was mounted and is currently running.

#### 5.1.1 Material

##### 5.1.1.1. FEBEX bentonite

The material used in the laboratory tests performed in the large-scale oedometer and the transparent cell was a bentonite extracted from the Cortijo de Archidona quarry (Almería, Spain) in two different phases. The first batch, known as FEBEX bentonite, was extracted in 1995 and is a granulate used to obtain the compacted blocks. The second batch was extracted in 2001 and was used to manufacture in a factory the pellets used in some tests.

The FEBEX bentonite was a 900-t batch of bentonite processed in 1996 for the FEBEX project. The processing consisted in homogenisation, air-drying and manual removing of volcanic pebbles on site and, at the factory, crumbling, drying in a rotary oven at temperatures between 50 and 60°C to a water content of around 13%, and sieving through a 5-mm mesh. The physico-chemical properties of the FEBEX bentonite, as well as its most relevant thermo-hydro-mechanical and geochemical characteristics were reported in ENRESA (2006) and updated in e.g. Villar (2017).

The smectite content of the FEBEX bentonite is close to 90 wt.%. The smectitic phases are actually made up of a montmorillonite-illite mixed layer, with 10-15 wt.% of illite layers. Besides, the bentonite contains variable quantities of quartz, plagioclase, K-felspar, calcite, and cristobalite-trydimite. The cation exchange capacity is  $98 \pm 2$  meq/100 g, the main exchangeable cations being calcium ( $35 \pm 2$  meq/100 g), magnesium ( $31 \pm 3$  meq/100 g) and sodium ( $27 \pm 1$  meq/100 g). The predominant soluble ions are chloride, sulphate, bicarbonate and sodium.

The liquid limit of the bentonite is  $102 \pm 4\%$ , the plastic limit  $53 \pm 3\%$ , the density of the solid particles  $2.70 \pm 0.04$  g/cm<sup>3</sup>, and  $67 \pm 3\%$  of particles are smaller than 2 µm. The hygroscopic water content in equilibrium with the laboratory atmosphere (relative humidity  $50 \pm 10\%$ , temperature  $21 \pm 3^\circ\text{C}$ ) is  $13.7 \pm 1.3\%$ . The external specific surface area is 67 m<sup>2</sup>/g and the total specific surface area is about  $725 \pm 47$  m<sup>2</sup>/g.

The saturated hydraulic conductivity of compacted samples of the FEBEX reference bentonite is exponentially related to their dry density. Two empirical relationships relating hydraulic conductivity ( $k_w$ , m/s) to dry density ( $\rho_d$ , g/cm<sup>3</sup>) were obtained for samples permeated with deionised water at room temperature, valid each for a different dry density range (Villar 2002):

$$\text{For } \rho_d > 1.47 \text{ g/cm}^3: \log k_w = -2.96 \rho_d - 8.58 \quad [5.1]$$

$$\text{For } \rho_d < 1.47 \text{ g/cm}^3: \log k_w = -6.00 \rho_d - 4.09 \quad [5.2]$$

The swelling pressure ( $P_s$ , MPa) of compacted samples is also exponentially related to the bentonite dry density, according to the empirical expression in Eq. 3 (Villar 2002):

$$\ln P_s = 6.77 \rho_d - 9.07 \quad [5.3]$$

Relationships between suction and water content obtained for different bentonite dry densities under isochoric conditions can be found in e.g. Villar et al. (2019). For a sample compacted at dry density  $1.6 \text{ g/cm}^3$  with hygroscopic water content the initial suction value would be  $\sim 120 \text{ MPa}$ .

The pellets were prepared for the EB project (ENRESA 2005) using a 100-t batch of bentonite extracted in 2001 from the Cortijo de Archidona deposit. To manufacture the pellets the bentonite was dried and milled in a multi-step process to produce a fine grade powder with a water content of between 3.0 and 4.5%. Later, a commercial plant with an in-line highly automated briquetting process produced coarse (7-15 mm) and fine (0.05-2 mm) grained materials with dry densities of  $2.11$  and  $2.13 \text{ g/cm}^3$ , respectively (Kennedy et al. 2004). The different grain sizes were kept separated in the laboratory and mixed in the right proportion just before every test, trying to keep a Fuller's curve similar to that used for the EB project, with a maximum diameter of 12.7 mm and a minimum diameter of 0.425 mm, in order to reduce segregation. The mineralogical analyses performed in samples of test MGR25 (see below) suggest that the content of smectite of this batch could be lower than in the 1995-batch, whereas the quartz, calcite and dolomite contents would be higher. The cationic exchange capacity was checked to be lower (e.g. Villar and Gómez-Espina 2012a). The external specific surface area is  $60 \text{ m}^2/\text{g}$ . A detailed hydro-mechanical characterisation of this mixture was performed by Hoffmann (2005).

#### 5.1.1.2. MX-80 bentonite

The test performed in the setup described in 5.1.2.2 was performed with a combination of an MX-80 bentonite block and a mixture of MX-80 bentonite pellets and powder in a ratio 70/30. The block was obtained by powder compaction. The initial water content of the bentonite powder was 8.9% and of the pellets 6.2%. The pellets have a regular shape with a diameter of 7 mm and a dry density of  $2.0 \text{ g/cm}^3$ . They were supplied by AITEMIN in 2013 in the framework of the in-situ test NSC, performed at the Bure URL in France.

The MX-80 bentonite is a brand name used by the American Colloid Company for sodium bentonite from Wyoming (USA), milled to millimetre-sized grains. The content of montmorillonite is between 65 and 90% ( $\sim 70\%$  for the batch used), with quartz, plagioclase and K-feldspars (contents between 4 and 15%), and minor quantities of cristobalite, tridymite, calcite, gypsum, pyrite, illite.  $\text{Na}^+$  is the main exchangeable cation (50-74 meq/100 g), with also  $\text{Ca}^{2+}$  (10-30 meq/100 g) and  $\text{Mg}^{2+}$  (3-8 meq/100g). The main soluble ions are sodium and sulphate.

The swelling pressure of small samples (3.8 or 5.0 cm in diameter, 1.2 cm in height) of MX-80 bentonite powder compacted with its hygroscopic water content was determined at CIEMAT at room temperature using deionised water as saturation fluid. The swelling pressure ( $P_s$ , MPa) could be related to final dry density ( $\rho_d$ ,  $\text{g/cm}^3$ ) through the following equation:

$$\ln P_s = 5.44 \rho_d - 6.94 \quad [5.4]$$

The hydraulic conductivity ( $k_w$ , m/s) of samples of powdered MX-80 bentonite (grain size <1 mm), compacted at different dry densities ( $\rho_d$ , g/cm<sup>3</sup>) and kept in stainless steel cells which hindered the swelling of the material upon saturation, was measured in a constant head permeameter (Villar 2005). Deionised water was used as permeant. The following exponential relation between dry density ( $\rho_d$ , g/cm<sup>3</sup>) and hydraulic conductivity ( $k_w$ , m/s) was found:

$$\log k_w = -2.94 \rho_d - 8.17 \quad [5.5]$$

## 5.1.2 Methodology

### 5.1.2.1. Tests with FEBEX bentonite

Isochoric infiltration tests were performed in two-part samples, half of them consisting of a bentonite compacted block and the other half of a pellet mixture. Two types of cells were used: a large-scale oedometer (MGR) and a transparent cell (CW). In most tests the lower half of the cell was filled with bentonite pellets with an average dry density close to 1.30 g/cm<sup>3</sup> and the upper part by a bentonite block of dry density 1.60 g/cm<sup>3</sup> (in two kinds of test: CW2 and MGR27 the placement was in reverse). In all cases hydration with deionised water took place through the bottom. These kinds of tests were complementary: whereas MGR tests provided quantitative data, the information provided by the CW test was mostly visual and qualitative.

The materials used in all the tests were the FEBEX bentonite for blocks and the EB pellets (see section 5.1.1). The block part of the sample was compacted from the granulate material with its hygroscopic water content, ~14%, resulting in an initial suction of ~116 MPa. The different grain sizes of the pellets were kept separated in the laboratory and mixed in the right proportion just before every test. The lab run out of pellets larger than 9.5 mm, and the granulometric distribution of tests MGR23 to MGR27, and CW1 and CW2 was modified to keep the Fuller's curve (Table 5-1). Also, in tests MGR23 to MGR27 the pellets were softly dried to a water content closer to the fabrication one (3.5%), because the water content of the pellets increased during storage (10.6%). These resulted in a significant different initial suction between the pellets that were dried and those that were not, 380 vs. 114 MPa (measured with a capacitive sensor).

**Table 5-1. Granulometric curve of the pellets of bentonite used in the tests**

Sieve sizes (mm)	Percentage retained (%)	
	MGR21, MGR22	Rest of tests
9.5	17	0
4.75	31	37
2.0	26	31
1.18	11	13
0.59	10	12
0.425	5	6

### Large-scale oedometer

The large-scale oedometer (MGR test) consists of a cylindrical body with base and an upper piston that may move in the cylinder (Figure 5-1). The body has an inner diameter of 10.0 cm and the length of the sample inside was 10.0 cm. The top and bottom of the sample were in contact with filter papers and ceramic porous discs connected to outlets. The cell was placed in a rigid frame that guaranteed the constant volume of the sample by hindering the displacement of the piston. An external LVDT measured the potential axial displacements, whereas a 10-t load cell in the upper part of the frame measured the force developed by the specimen.

The bentonite block was directly compacted inside the cell and the pellets were poured on it and carefully shaken as necessary to get the target density. Then the cell was overturned and mounted in the oedometric frame. The water intake took place through the bottom surface, either under a low injection pressure (a 1.5 m water column, 15 kPa, simulating reduced water intake conditions, e.g. Opalinus clay in Mont Terri) or under a constant low flow (0.05 cm<sup>3</sup>/h), simulating a continuous contribution of water, e.g. Grimsel granite). In the first case the water intake was measured with an automatic volume change apparatus and in the second case with a pressure/volume controller. During hydration the top outlet remained open to atmosphere and the pressure exerted by the material, the sample deformation and the water intake were measured and automatically recorded. The tests were performed at laboratory temperature.

A summary of the tests performed and of their characteristics is given in Table 5-2.

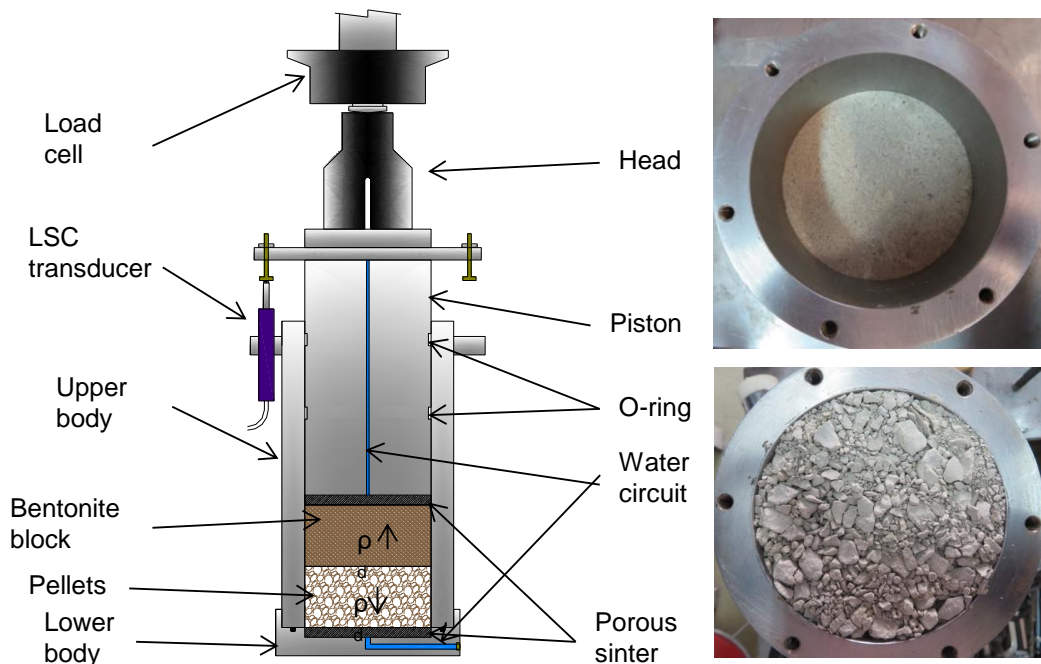


**Figure 5-1. Schematic representation of the MGR cell (left) and images of the block (upper right) and pellets (lower right)**

**Table 5-2. Characteristics of the MGR tests**

Test	Hydration	Duration (days)	Dates	T (°C)
MGR21	Constant pressure: 15 kPa (Pellets)	34	Aug – Sept 2017	23.1±0.6
MGR22	Constant flow: 0.05 cm <sup>3</sup> /h (Pellets)	266	Oct2017 – Jul 2018	22.5±1.3
MGR23	Constant pressure: 15 kPa (Pellets)	210	Aug 2018 – Mar 2019	22.6±1.5
MGR24	Constant pressure: 15 kPa (Pellets)	14	Mar – Apr 2019	22.5±0.6
MGR25	Constant pressure: 15 kPa (Pellets)	76	May – July 2019	22.7±1.1
MGR26	Constant flow: 0.05 cm <sup>3</sup> /h (Pellets)	132	Sep 2019 – Jan 2020	23.6±1.2
MGR27	Constant pressure: 15 kPa (Block)	278	Feb – Nov 2020	23.0±1.2
MGR28	Constant pressure: 15 kPa (Block)	>180	Feb 2021 - running	23.1±1.3

**Transparent cell**

The transparent cell or window cell (CW) is a custom-built square cell consisting of two transparent methacrylate faces reinforced with steel frames (Figure 5-2). The inner dimensions of the central steel frame are 121x118x20 mm. A square block of the same dimensions was compacted in a bespoke mould and half sectioned. One of the halves was placed in the cell and the rest of the cell was homogeneously filled with the pellets while the cell was horizontally laid. During assembly the fine fractions moved towards the bottom. This side of the cell, which was at the bottom during assembly, was called B-face. As a result, the two faces, A and B, of the cell presented different appearance (Figure 5-3).

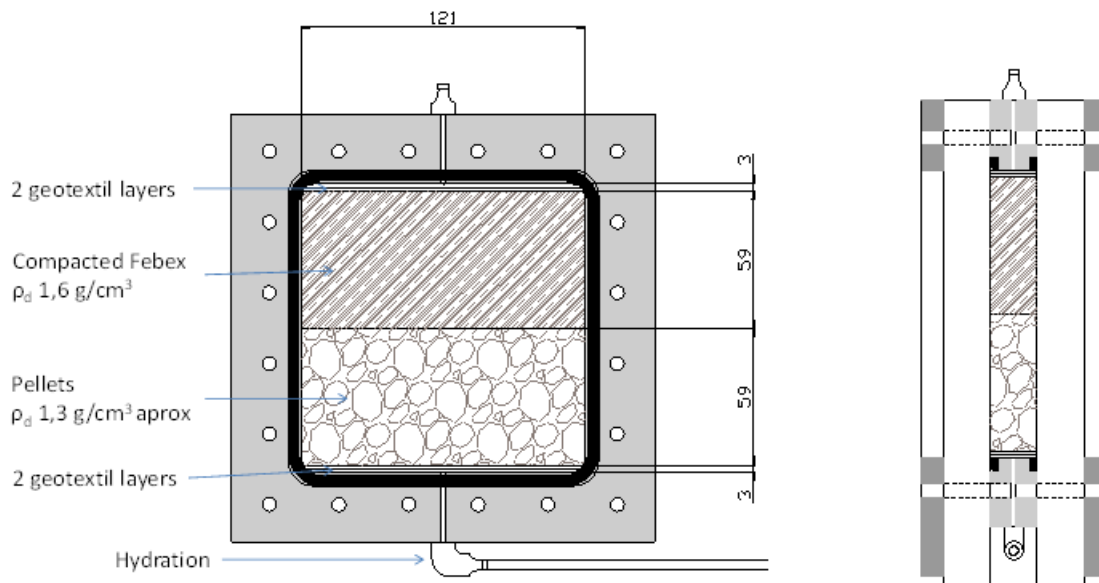


**Figure 5-2 Schematic front and lateral views of the transparent cell (CW1 with pellets at the bottom, as shown in the Figure, and CW2 with pellets on top)**

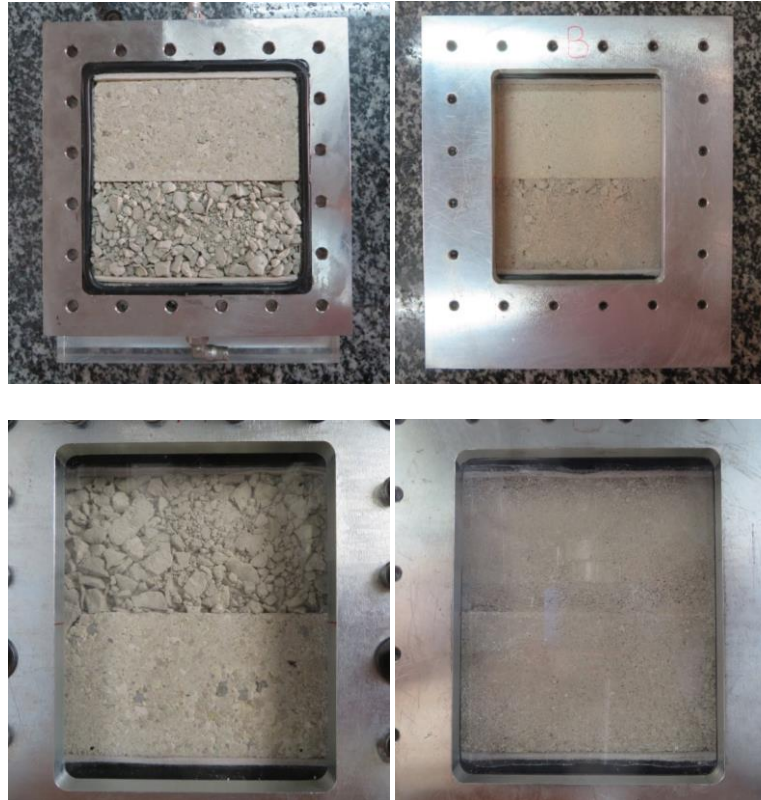


**Figure 5-3. Initial appearance of face A (left) and B (right) of test CW1 (up) and CW2 (down)**

Two geotextile layers were placed at the upper and bottom sides of the cell. Hydration took place through the bottom with a 30 cm (3 kPa) water column, and the water intake was measured with an automatic volume change apparatus. The CW1 test had the pellets placed at the bottom, and inversely, in the CW2 test, the block was the first part hydrated. Photographs of both sides were periodically taken.

The characteristics of the tests are summarised in Table 5-3.

**Table 5-3. Characteristics of the CW tests**

Test	Hydration	Duration (days)	Dates	T (°C)
CW1	Constant pressure: 3 kPa (Pellets)	379	Feb 2018 – Mar 2019	22.6±1.4
CW2	Constant pressure: 3 kPa (Block)	420	May 2019 – Jul 2020	23.5±1.2

**Postmortem tests: physical state and microstructure**

At the end of the tests the bentonite samples were extracted from the cell (by pushing with a piston in the case of cell MGR), measured, weighed, and cut in regular horizontal sections. Each section was subsampled to determine water content, dry density and pore size distribution. The cylindrical blocks from MGR tests were sliced in 6 horizontal levels (3 for pellets and 3 for block). The CW samples were cut into 15 parts (5 rows and 3 columns). The subsamples were numbered from top to bottom, i.e. sample #1 was the one farther away from the hydration surface.

The specific surface area of the bentonite samples from all the tests (except MGR21 and MGR22) was determined using the BET method (Brunauer et al. 1938) to analyse the adsorption isotherms of nitrogen gas in the solid at the temperature of liquid nitrogen (77 K, -196°C). This parameter represents the external surface area ( $a_s$ ), i.e. the surface of the intra-aggregate and inter-aggregate voids but not that of the interlayer space. The sorption isotherms were determined in an ASAP 2020 of Micromeritics. The unaltered samples were lyophilised prior to degassing and then finely ground. Samples of between 0.6 and 2.1 g were degassed at 90°C for the time necessary to reach a vacuum of 50  $\mu$ m Hg, which was kept for 10 min. Afterwards the samples were kept at 90°C under vacuum for 8 h, to eliminate moisture and impurities retained in the pores. The isotherms obtained had 55 point, 32 in the range of relative pressures between 0.01 and 0.995 and 23 points in the range 0.995 and 0.14. The BET method was applied in the range of  $P/P_0$  0.06-0.2 to compute the specific surface area.

The (001) reflection or basal reflection gives the distance along the crystallographic c-axis between clay lamellae, and for a given clay mineral, it depends on the exchangeable cations present in the interlayer and their degree of hydration. The samples of some of the tests were preserved in paraffined foil and the X-ray profile of a plane surface of them was registered at laboratory temperature after removing the foil and without any further treatment. For the samples of tests MGR23, MGR24, MGR25 and CW1, an anode of Cu (CuK $\alpha$ ) radiation was used with a Bruker D8 Advance diffractometer at 40 mA and 40 kV operating conditions. XRD experimental profiles were obtained with a 1-mm entrance slit, 0.05°2 $\theta$  step size and a counting time of 3 s per step. Data were collected between 2 and 30°2 $\theta$ . The divergence slit and diffracted beam slit of the goniometer were fixed at 1 mm. The Pearson VII profile function was fitted to the observed intensities in order to obtain better reflection parameters and to deconvolute overlapped reflections. For the samples of tests MGR27 and CW2, an anode of Cu (CuK $\alpha$ ) radiation was used with a Philips model X'Pert-MPD diffractometer at 40 mA, 45 kV operating condition. X-ray diffraction (XRD) experimental profiles were obtained with a 0.1-mm entrance slit and a scanning rate of 0.025°2 $\theta$ /s. Data were collected between 2 and 10°2 $\theta$ . The goniometer settings were: automatic divergence slit and diffracted beam slit 2 mm. The position of the diffraction peaks was adjusted by using the quartz in the samples as an internal standard. The complete mathematical description of the scan pattern was obtained by combination of a polynomial function that describes the background and a profile function that fits the experimental reflections. The pseudo-Voigt profile function was used to fit the diffraction peaks as well as to deconvolute overlapped reflections.

## Gas testing

Additionally, in tests CW cylindrical subsamples were obtained by drilling across the block/pellet interface to measure the gas breakthrough pressure as an indicator of the sealing quality of the interface. This subsample was vertically crossed by the interface (Figure 5-4). The core diameter was fit to 3.8 cm by using a cutting ring and knife. Filter paper and porous stones were placed on top and bottom of the sample and it was laterally wrapped in double latex membranes. Vacuum grease was applied between membranes in order to prevent the loss of gas. The wrapped sample was placed in a triaxial cell which was filled with de-aired water and pressurized to ensure perfect adherence of the membranes to the surface of the sample and avoid gas transport along it. The cell inlet at the upper part of the sample was connected to a nitrogen gas cylinder applying the gas injection. The outlet of the cell connected to the bottom of the sample was open to atmosphere, with a series of different range gas mass flowmeters measuring the gas outflow. More experimental details about the equipment and the equations used to compute permeability are given in Villar et al. (2018, 2021d). Gas was applied through face A (that of coarser granulometry (Figure 5-3)). The particular test procedure was adapted to the characteristics of the samples. In test CW1 the injection pressure was increased until outflow occurred and in test CW2 the confining pressure was increased until flow stopped.

The pore size distribution of subsamples obtained after gas testing was also determined.



**Figure 5-4. Appearance of the cylindrical sample obtained for gas testing in test CW1**

#### **5.1.2.2. Tests with MX-80 bentonite**

The test using binary mixtures of MX-80 pellets and block were performed in a setup mounted specifically for BEACON once the project had started. The experimental setup consists of an instrumented thermo-hydraulic cell, hydration system and control and data acquisition systems.

A stainless steel cell was used to contain the bentonite. The internal dimensions are 15 cm of diameter and 14.5 cm of height.

Figure 5-5 shows a blueprint of the cell, in which the location of RH/T sensors, pressure sensors and pore pressure sensor is indicated. The sample was hydrated through a porous stone at the bottom. The cell is instrumented with capacitive-type sensors placed inside the clay at three different levels (13, 78 and 128 mm from the bottom porous stone). The transmitters used are VAISALA HMT337, which include a humidity sensor (HUMICAP®) that changes its dielectrical characteristics with extremely small variations in humidity (capacitive-type RH sensor). They also include a temperature sensing element (Pt 100). The accuracy of the humidity sensor is  $\pm 1\%$  over the range 0-90 percent RH and  $\pm 2\%$  over the range 90-100 percent RH. The sensors are protected by cylindrical stainless steel filters (HM47280SP, length 41.5 mm). Radial pressures at the lateral bentonite cylinder interface are measured at the same distances from the bottom plate as those for the RH/T transmitters (i.e. 13, 78 and 128 mm). The pressure sensors used are XPM10 with a range of 0-100 bar. The pore pressure is measured on top of the cell with a PMP 4070 Druck Amplified Output Pressure Transducer. Its operating absolute pressure range is 700 mbar up to 7 bar.

The hydration system consists of a GDS volume/pressure controller connected to a control PC. Hydration took place with deionized water injected at a constant pressure of 0.014 MPa through a porous plate placed at the bottom of the cell.

The test was performed with the bentonite compacted block in the upper part and the pellets/powder mixture at the bottom part of the cell (Figure 5-5).

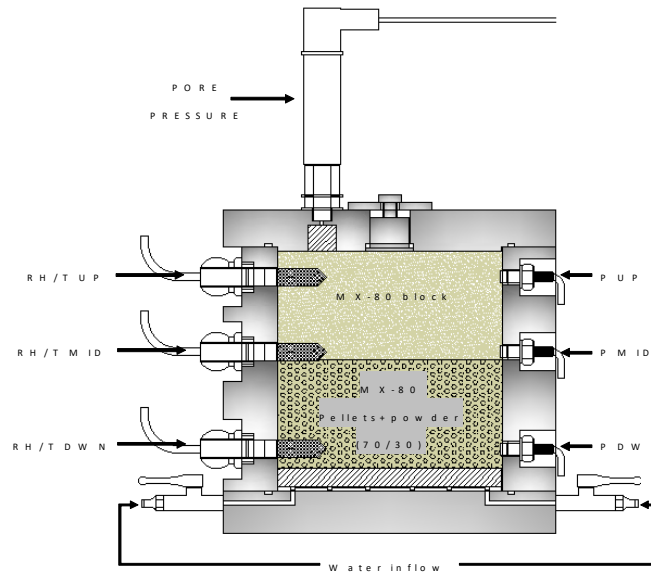


**Figure 5-5. Longitudinal cross-section of the cell with the sensors installed according to the configuration for test CT31**

The block was compacted at a dry density of 1.5 g/cm<sup>3</sup> inside of the cell body placed upside down using a uniaxial pressure of 11.4 MPa. Then the other half of the cell was filled with the mixture of pellets and MX-80 powder. This mixture was arranged in different layers in such a way that the powder filled the gaps between the pellets. Each layer consisted of a first level with 1/3 of powder, a second level with the pellets, and a third level with the remaining 2/3 of powder. During the process, light blows were given to the cell wall to readjust the particles so that the mass necessary to reach the target dry density of 1.50 g/cm<sup>3</sup> could fit inside.

The initial characteristics of the material inside the cell, including water content (*w*), dry density ( $\rho_d$ ), degree of saturation (*S<sub>r</sub>*) and height (*h*) can be seen in Table 5-4.

**Table 5-4: Initial characteristics of the materials of test CT31**

	<i>w</i> (%)	<i>h</i> (cm)	$\rho_d$ (g/cm <sup>3</sup> )	<i>S<sub>r</sub></i> (%)	Volume (cm <sup>3</sup> )	Dry mass (g)
Pellets/Powder mixture	7.0	7.20	1.50	23	1281.3	1927.2
Block	8.9	7.25	1.49	29	1286.7	19.34.0
Average / (Total)	8.0	(14.45)	1.50	26	(2568.0)	(3861.1)

After filling the cell, the sensors were installed. To insert the RH/T sensors, the bentonite was drilled with a bit of the same diameter as the sensor (12 mm). The material expelled during drilling was recovered and weighed. Afterwards, the sensors were very quickly inserted. The pore pressure sensor was fixed to the upper lid of the cell. The pressure sensors were fixed to the cell body in contact with the external surface of the bentonite cylinder. Hydration started six days after the cell was assembled. During this time the RH inside the block slightly decreased, whereas that of the mixture (bottom) slightly increased. This effect was triggered by the initial difference in water content of both materials (8.9 vs. 7.0%). The RH values measured just before hydration were between 41% close to the bottom to 43% on top.

### 5.1.3 Results

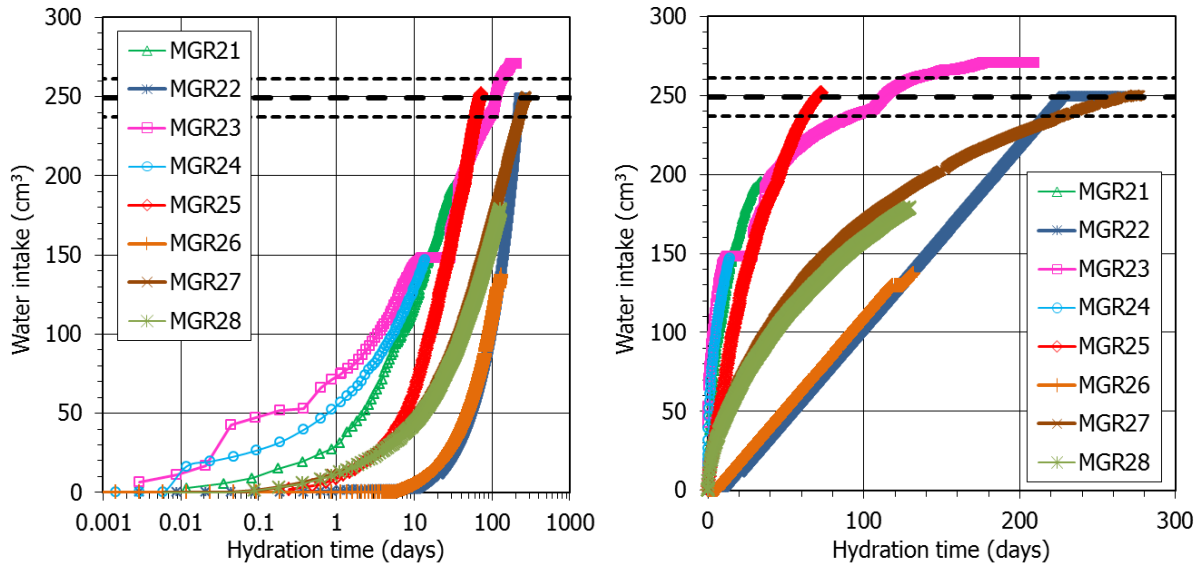
#### 5.1.3.1. Large-scale oedometer (FEBEX)

##### *Hydration process: online results*

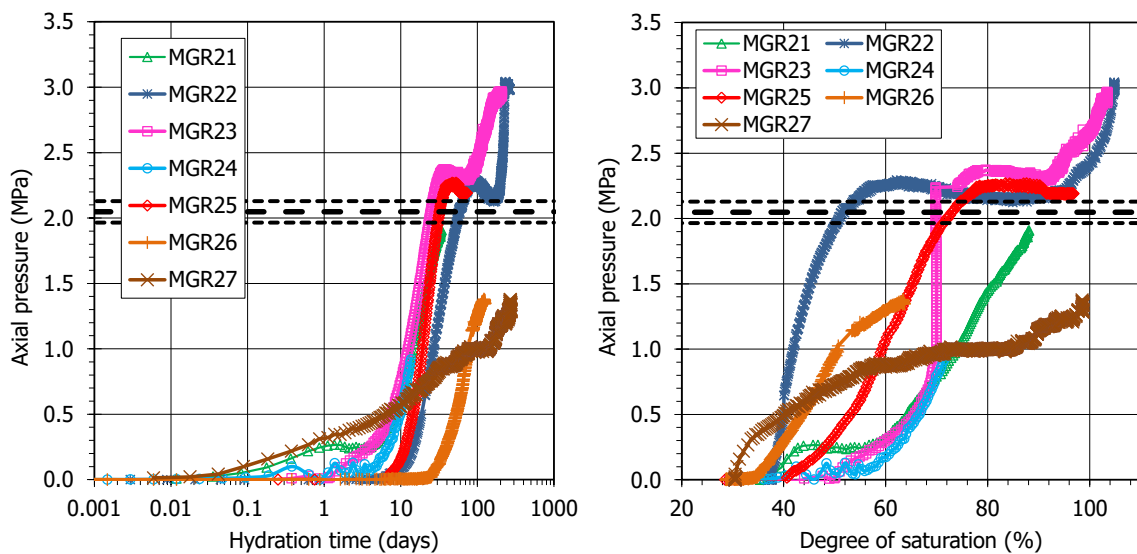
Water intake, axial pressure and vertical deformation were continuously measured during hydration. Vertical deformation was minimal, since the movement of the piston was blocked by the oedometer framework. In fact the changes in overall dry density occurred as a result of the small vertical deformation allowed were in all cases below  $0.005 \text{ g/cm}^3$ . The tests were stopped and dismantled after different periods of time to get the temporal evolution of the post-mortem information. Tests MGR22 and MGR23 continued until a pressure plateau was reached.

Figure 5-6 shows the evolution of water intake for the seven MGR tests along with the water weight necessary to reach full saturation ( $250 \pm 12 \text{ g}$ ), which was not the same in all the tests because of the slight differences among them in initial dry density and water content. Some of the tests reached full saturation. There was a significantly different behaviour between the tests performed under constant injection pressure (MGR21, MGR23, MGR24 and MGR25) and the tests performed under constant water inflow rate (MGR22 and MGR26). In the constant-pressure tests the water intake was very quick and more than half of the water volume necessary for full saturation was taken in about 20 days, which was probably caused by the high permeability of the pellets part. In contrast, the water intake was much slower in the two tests in which constant flow was prescribed, and it took more than 100 days to reach degrees of saturation close to 50%. The water intake rate in tests MGR27 and MGR28, in which hydration took place through the block part of the column (which was placed at the bottom), was initially intermediate between that of tests performed under constant pressure and those performed under constant inflow. However, they showed the slowest water intake rate in the long run, attesting the lower permeability of the higher density block. Some of the differences among the tests, particular concerning the initial water intake, were likely caused by experimental artefacts. In test MGR23 there was a short period ( $\sim 14$  days) during which no water was supplied to the cell because air entered the hydration line. As shown in Figure 5-7, this did not affect the swelling pressure evolution.

Figure 5-7 shows the axial pressure development over time and as a function of the overall degree of saturation. The degree of saturation shown in the Figure is an overall value for the two-component samples but, at any given time, the actual degrees of saturation at different points along the sample height were very different, as the postmortem determinations presented further down showed. In terms of temporal evolution, the axial pressure build up was generally steep at the beginning. In the longer tests, after the initial peak there was a soft decrease in axial pressure that eventually recovered and continued increasing after final stabilisation. The initial pressure peak occurred for degrees of saturation close to 80% in tests MGR23 and MGR25. In test MGR23 the period of time during which the axial pressure significantly increased with no change in the degree of saturation corresponds to the  $\sim 14$  days period during which inadvertently no water was supplied to the cell. The fact that pressure continued to build up would indicate that water redistribution inside the bentonite can cause pressure increase. In contrast, in test MGR22, performed under controlled flow conditions, the peak in axial pressure was reached for a degree of saturation of only  $\sim 60\%$ . This would mean that slow saturation was more efficient, in the sense that it allowed a better water redistribution inside the microstructure.



**Figure 5-6. Water intake evolution in the large-scale oedometer tests (constant flow was prescribed in tests MGR22 and MGR26). The thick horizontal lines indicate the water intake necessary to reach full saturation (average and standard deviation). In tests MGR22 and MGR26 the water intake includes partly the intake of the bottom porous stone (6-14 cm<sup>3</sup>)**



**Figure 5-7. Axial pressure evolution over time (left) and as a function of the degree of saturation (right) in the large-scale oedometer tests (constant flow was prescribed in tests MGR22 and MGR26). The thick horizontal lines indicate the expected swelling pressure according to Eq. 2 (average and standard deviation)**

After the sharp initial increase (the peak was reached after 30-40 days), in the longest test (MGR23) there was an intermediate stage of slight pressure decrease, and when the average degree of saturation was ~90% the axial pressure steadily increased again until full saturation was reached, with a stable pressure value of 3 MPa. Test MGR22 went also on until full saturation was reached. Since in this test the inflow was very low and controlled, the pressure development kinetics was very different to the other tests. Axial pressure started to develop slightly later than in the other tests (after 10 days), and when the degree of saturation was much

lower than in the other tests (37%). The first peak was reached after 80 days and the intermediate stage lasted until 200 days had elapsed. During this time the degree of saturation increased from 58% to 96%. In the final stage, the water injection pressure started to increase because the P/V controller was not able to keep a constant low injection flow into a quasi-saturated sample without increasing the injection pressure (Figure 5-8). As a result, there was a new steep increase in axial pressure until the final value of 3 MPa. When the water injection pressure had increased to 1.5 MPa, water injection was stopped and the pressure was allowed to dissipate for 38 days. This explains the odd final shape of the curves for test MGR22. During this period of water injection pressure decline, the axial pressure did not change.

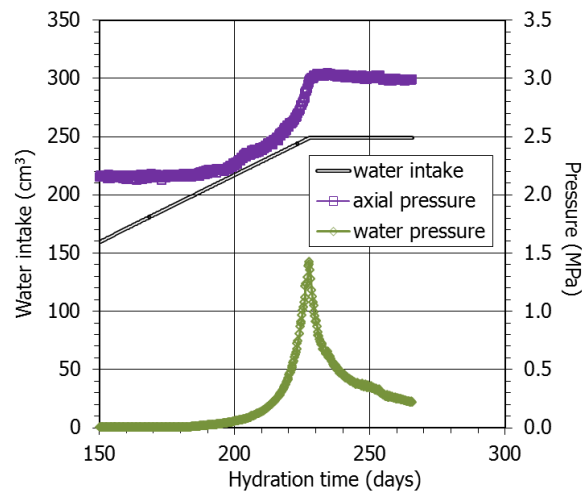


**Figure 5-8. Final stage of test MGR22**

**Final physical state**

The tests were dismantled after different running times. Once the test was finished, the sample was extracted, measured, weighed and photographed before proceeding to its separation into two halves (the part corresponding to the pellets, and the block part). The final appearance of the samples once extracted from the cell is shown in Figure 5-9 for the tests performed under constant pressure hydration through the pellets and in Figure 5-10 for the others. The sample from the shorter test (MGR24) shows a quite saturated bottom in which the pellets cannot be told apart, but the upper part of the pellets half still showed open voids. The two halves of this sample (pellets and block) could easily be detached. In the other cases the two halves were sealed and had to be separated with a knife. Already after 76 days the pellets half looked homogeneous. In contrast, in the tests performed under constant inflow rate, after 132 days (test MGR26) some pellets could still be told apart. In test MGR27 (saturated through the block), although the block looked saturated, the pellets' upper part still presented voids from the initial fabric.

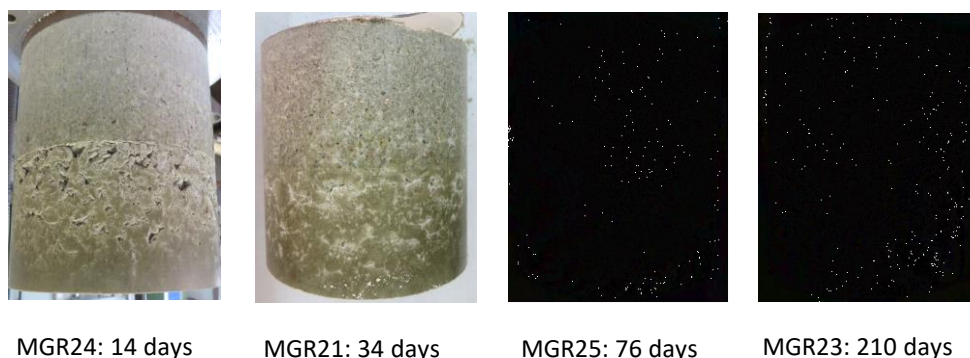


**Figure 5-9. Appearance of the MGR samples at the end of the tests performed under constant water injection pressure**

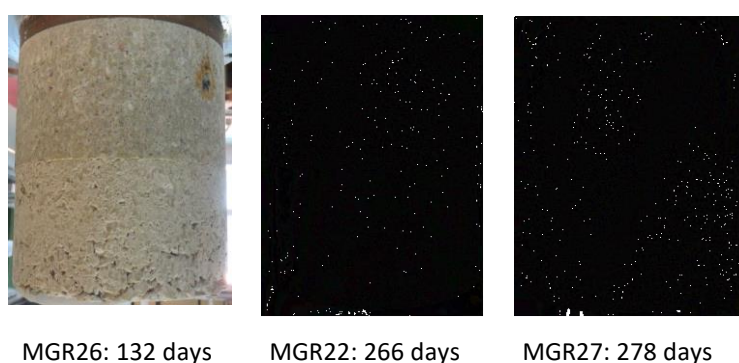


**Figure 5-10. Appearance of the MGR samples at the end of the tests performed under constant water inflow rate (MGR22, MGR26) and with saturation through the block (MGR27)**

Before carrying out the analyses and determinations of its characteristics (dry density, humidity, porosity, etc.), each of the halves indicated above was divided into 3 subsections numbered from 1 (upper part) to 6 (bottom part, closest to hydration), including a B for the sections belonging to the block part (1 to 3, except in MGR27), and a P for those belonging to the pellets part (4 to 6, except in MGR27). These six subsections were subsampled for the different determinations indicated in 5.1.2.1. Table 5-5 shows a summary of the final characteristics of the samples, along with the initial values. The original height of the halves changed during the tests: the height of the bottom, pellets half decreased whereas the height of the upper, block half increased, indicating the increase in the overall dry density of the pellets and decrease in the dry density of the block. These changes are illustrated in Figure 5-11 and were confirmed by the postmortem determination of dry density in the six horizontal sections. The water content of the bottom part (pellets) increased very quickly, but over time tended to decrease. In contrast, the dry density of the pellets half increased in a more continuous way. The behaviour of test MGR26 performed under constant flow (lasting 132 days) did not follow the overall trend, since the increase in water content was moderate and similar for both halves, attesting the more homogeneous water redistribution allowed by slow hydration. The two longest tests, which were performed under constant water inflow (MGR22) or with the block at the bottom (MGR27) should be separately considered. When hydration took place through the block, the final water content and dry density of both halves were more homogeneous.

**Table 5-5. Initial and final characteristics of MGR tests**

	Initial				Final			
	w (%)	h (cm)	$\rho_d$ (g/cm <sup>3</sup> )	$S_r$ (%)	w (%)	$\rho_d$ (g/cm <sup>3</sup> )	h (cm)	$S_r$ (%)
Test	MGR21, 34 days							
Pellets	9.5	4.97	1.26	23	35.9	1.31	4.80	91
Block	13.3	5.01	1.60	52	22.9	1.50	5.33	78
Total <sup>a</sup>	11.6	9.98	1.43	35	29.0	1.43	10.00	88
Test	MGR22, 266 days							
Pellets	9.9	5.04	1.28	24	35.3	1.35	4.79	95
Block	13.6	4.94	1.61	55	30.7	1.51	5.27	106
Total <sup>a</sup>	11.9	9.98	1.45	37	32.7	1.44	10.01	101
Test	MGR23, 210 days							
Pellets	3.5	5.00	1.30	9	35.7	1.34	4.84	95
Block	14.2	4.98	1.60	56	31.1	1.51	5.29	107
Total <sup>a</sup>	9.4	9.98	1.45	29	33.2	1.45	10.01	103
Test	MGR24, 14 days							
Pellets	5.7	5.02	1.28	14	31.0	1.30	4.93	78
Block	13.7	4.97	1.62	55	16.2	1.57	5.13	61
Total <sup>a</sup>	10.1	9.99	1.45	32	23.0	1.45	10.00	72
Test	MGR25, 76 days							
Pellets	3.2	4.99	1.30	8	37.0	1.33	4.88	97
Block	14.1	5.00	1.59	54	26.7	1.51	5.24	92
Total <sup>a</sup>	9.2	9.99	1.44	29	31.4	1.44	10.02	97
Test	MGR26, 132 days							
Pellets	3.5	5.01	1.30	9	21.0	1.32	4.92	54
Block	13.9	4.99	1.60	55	20.6	1.49	5.35	69
Total <sup>a</sup>	9.2	10.00	1.45	29	20.8	1.44	10.07	64
Test	MGR27, 278 days							
Pellets	3.0	5.00	1.31	8	32.3	1.43	4.55	99
Block	15.3	5.00	1.59	59	30.0	1.45	5.47	94
Total <sup>a</sup>	9.8	10.00	1.45	30	31.7	1.45	10.02	99

<sup>a</sup> the initial values are the averages of block and pellets, the final values correspond to online measurements (except in test MGR22)

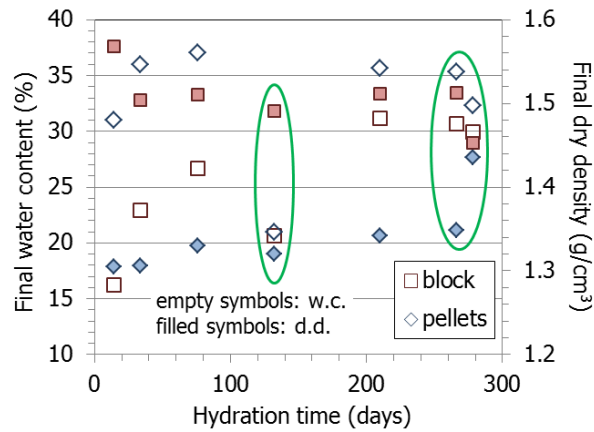


**Figure 5-11. Final average water content and dry density of the block and pellet halves of the samples (the values circled correspond to tests performed under constant inflow rate (MGR22, MGR26) or with the block at the bottom (MGR27))**

The water content, dry density and degree of saturation values measured in subsamples are plotted in Figure 5-12 to Figure 5-14 as a function of the distance to the hydration surface. The initial values are indicated by thick horizontal lines. The differences in the initial water content of the pellets were caused because in tests MGR23 to MGR27, prior to mounting, the pellets were dried to the values they had after they were manufactured. During the tests the water content and degree of saturation decreased from the hydration surface (sample bottom) upwards whereas the dry density increased. These gradients attenuated over time, hence they were smoother as the test duration was longer. The pellets/block interface did not seem to have any effect on the continuous gradients.

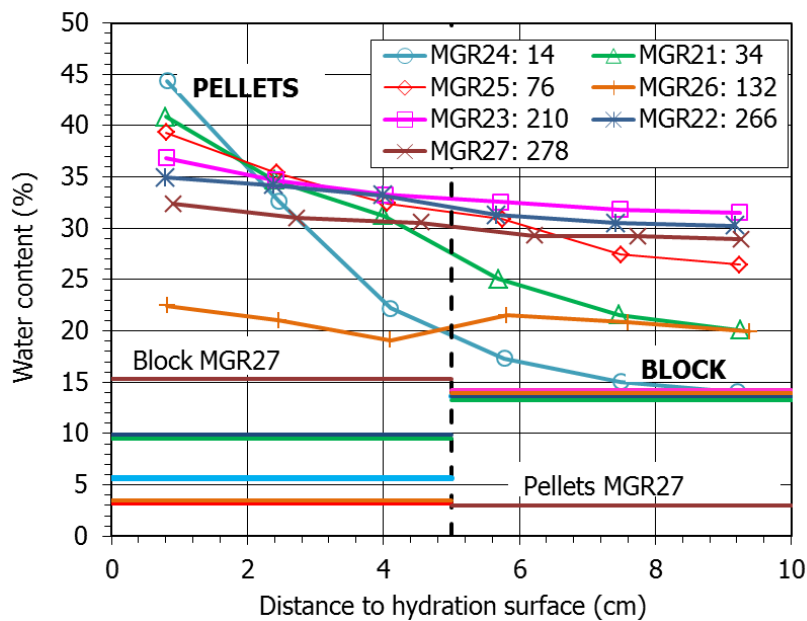


**Figure 5-12. Final water content along the samples of MGR tests. The duration of the tests is given in days in the legend. The thick horizontal lines mark the initial value**

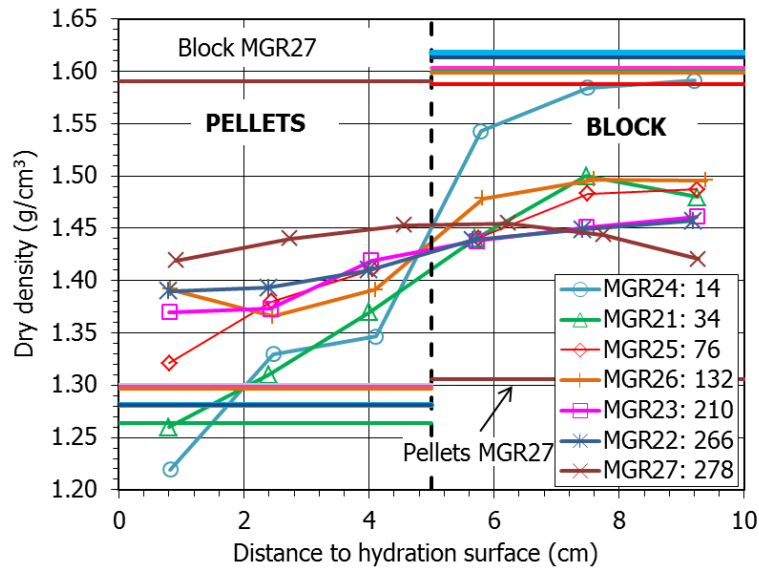


**Figure 5-13. Final dry density along the samples of MGR tests. The duration of the tests is given in days. The thick horizontal lines mark the initial value**

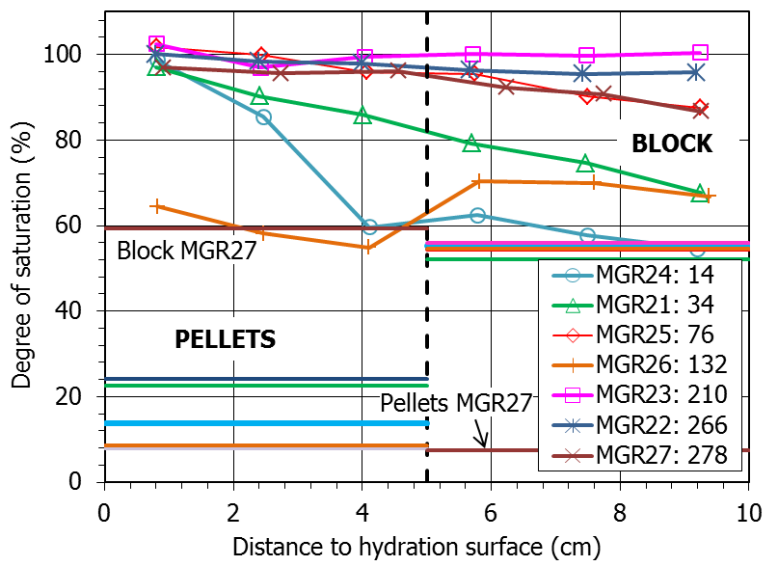


**Figure 5-14. Final degree of saturation along the samples of MGR tests. The duration of the tests is given in days in the legend. The thick horizontal lines mark the initial value**

The final dry density and water content values were similar in tests MGR22 and MGR23, despite the different hydration conditions (constant flow or pressure). Although the bentonite was finally fully saturated, the dry density and water content along the samples did not completely equalise. In contrast, test MGR26, which was far from full saturation, showed a quite homogeneous water content distribution, whereas the difference between the dry density of pellets and block was still significant.

### **Microstructural changes**

The pore size distribution of the samples was determined by mercury intrusion porosimetry (MIP). In some subsamples duplicates were tested. In the sections below, the intrusion curves obtained in some of the samples are shown. In all of them the usual two pore families of compacted FEBEX bentonite corresponding approximately to pores larger and smaller than 200 nm could be told apart. This limit is not the same as that between macropores and mesopores, which according to the classification of Sing et al. (1985) would be at 50 nm. There is also discussion on the criteria that can be followed to select this delimiting value (Yuan et al. 2020). The 'valley' criterion was chosen in this work, consisting of using the lowest point of the valley between the two peaks of a bimodal distribution. In several THM models, this pore size represents the limit separating inter-aggregate from intra-aggregate pores, the latter not affected by density changes.

The mercury intrusion method allows access to be gained only to part of the macroporosity (pores of diameter smaller than  $\sim 550 \mu\text{m}$ ) and to part of the mesopores (those of diameters larger than 7 nm), since mercury does not intrude the microporosity (pores of a size of less than 2 nm, according to the same classification mentioned above). Actually, the percentage of pores intruded by mercury in the samples analysed in this work was between 30% and 76%. Considering that most of the non-intruded porosity corresponds to the pores of a size smaller than the limit of the apparatus (7 nm), an estimation of the percentage of pores actually intruded can be made by comparing the actual void ratio of the samples ( $e$ , computed from their dry density and density of solid particles) and the apparent void ratio calculated from mercury intrusion ( $e^*$ ). There is uncertainty in this approach, since it is possible that pores larger than 7 nm were not intruded because of the bottleneck effect: the pores connected to the external surface by narrow openings will not be intruded until sufficient pressure is applied to intrude the entryways. All of the volume of such pores will be allocated to the threshold radius class of the most restricted part of the entryway, which will result in an overestimation of the smaller pore sizes volume. Likewise, although in compacted clay materials pores larger than those that can be quantified by MIP are not expected, pores of this size could be present in some of the driest pellets samples.

The intrusion curves of the subsamples are presented below along with the curves for FEBEX samples of the same characteristics as the initial conditions used in the cells. For the block part, the curve corresponding to a sample compacted at dry density  $1.59 \text{ g/cm}^3$  with a water content of 14% was used as representative of the initial state. For the pellets, mixtures of pellets having approximately a Fuller's curve grain size distribution, with a resulting dry density of  $1.29 \text{ g/cm}^3$  and water contents of 10% and 3% were used. The initial pellets curves showed a predominant pore size around  $300 \mu\text{m}$ . Despite the low density of the pellets mixtures, the percentage of non-intruded porosity in them was very high ( $\sim 70\%$ ). In this case not all the non-intruded porosity can be ascribed to pores smaller than 7 nm, because in the dry, low-density pellets mixture large pores are also to be expected. Hence, an estimation of the volume of pores larger than  $550 \mu\text{m}$  has been made following this approach:

At the beginning of a MIP test the calibrated sample holder is filled with mercury under a low injection pressure. Considering the sample mass and the volumes of the sample holder and of mercury intruded, the dry density of the sample is computed by the equipment software. This initial mercury injection is considered by the equipment as the zero value for the rest of the MIP test, which actually starts when injection pressure is increased above this value. Thus, all the large porosity filled during this initial step is disregarded. The comparison between the dry density determined by the equipment at this step and the actual dry density of the sample allows computing the volume of pores larger than  $550 \mu\text{m}$ : when the sample contains a significant volume of large pores, the dry density determined by the porosimeter is considerably higher than the actual dry density of the sample, whereas if there are not large pores the two

values tend to be similar. Hence, in the dry pellets samples this difference was quite large, whereas in the saturated and high-density samples the differences found were not significant. This correction was done to the initial GBM and to those samples whose visual inspection clearly showed that contained large pores, namely samples MGR24-4, MGR24-5, MGR21-4 (Figure 5-9) and all the pellets samples from tests MGR26 (Figure 5-10) and CW2. The subsamples were numbered from top to bottom, i.e. sample #1 was the one farther away from the hydration surface.

Taking all the above into account, the void ratio corresponding to pores larger and smaller than 200 nm ( $e_M$  and  $e_m$ , macro and micro, respectively) was recalculated, assuming that the non-intruded porosity corresponded to pores smaller than the equipment injection capacity and, in some pellets samples, also to pores larger than 550  $\mu\text{m}$ .

The curves obtained for all the tests are presented in Villar et al. (2021c). As an example, Figure 5-15 and Figure 5-16 show the incremental curves of mercury intrusion for the subsamples of the tests lasting 14 (MGR24) and 210 days (MGR23). In the shorter test the pore size distribution of the subsamples taken from the block half was similar to that of the initial block. Indeed, no relevant changes in the dry density and water content of the block samples took place during the oedometer test (only noticeable for the sample closest to the interface, 3b), because it was too short. This similarity proves the reliability of the technique. In contrast, the pore size distribution of the pellet half significantly changed. The size of pores larger than 200 nm and their volume decreased with respect to the initial pellets mixture. A similar pattern was found in test MGR21 (34 days). Overall, for the pellets subsamples of all the tests, the volume of pores larger than 200 nm significantly decreased, and the mean size of these macropores decreased from the initial  $\sim 300 \mu\text{m}$  to values mostly between 10 and 100  $\mu\text{m}$ . This can also be observed in Figure 5-16 for the subsamples from the pellets half of the longer test (MGR23). In contrast, the mean size of the pores smaller than 200 nm increased with respect to the original values for all the pellets subsamples, as well as for the block subsamples (Figure 5-17). Furthermore, in the block subsamples the volume and size of the macropores also increased, except in the shorter, less saturated tests. This overall increase in the pore volume of all the size ranges for the block subsamples is related to the decrease in the global dry density of the block parts during the tests (Figure 5-13).

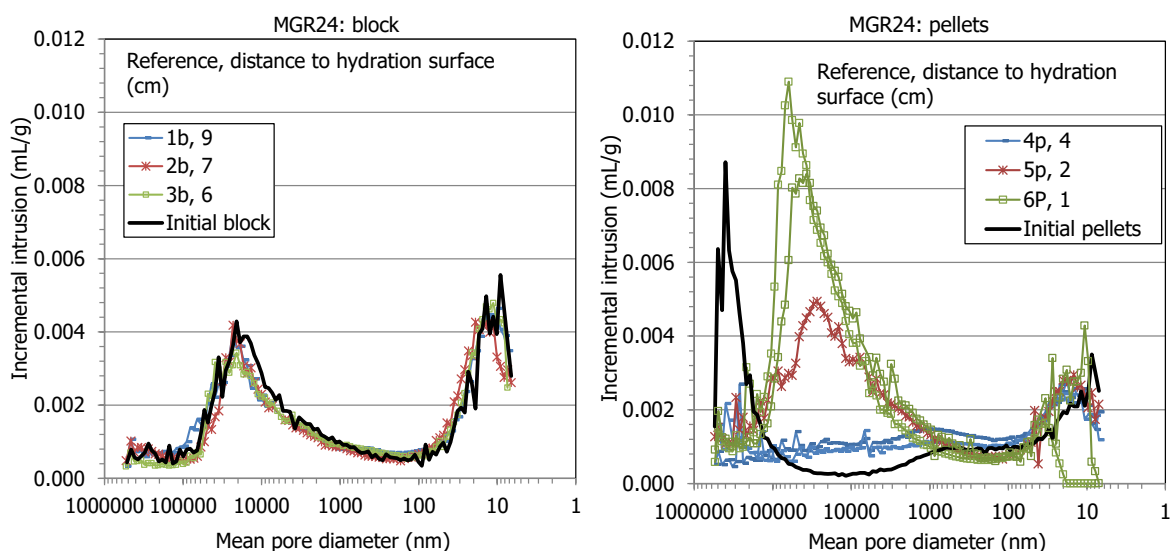


**Figure 5-15. Pore size distribution expressed as incremental mercury intrusion of samples from test MGR24 (lasting 14 days), corresponding to the block (left) and pellets (right) halves. The curves for the initial materials (blocks and pellets) are included**

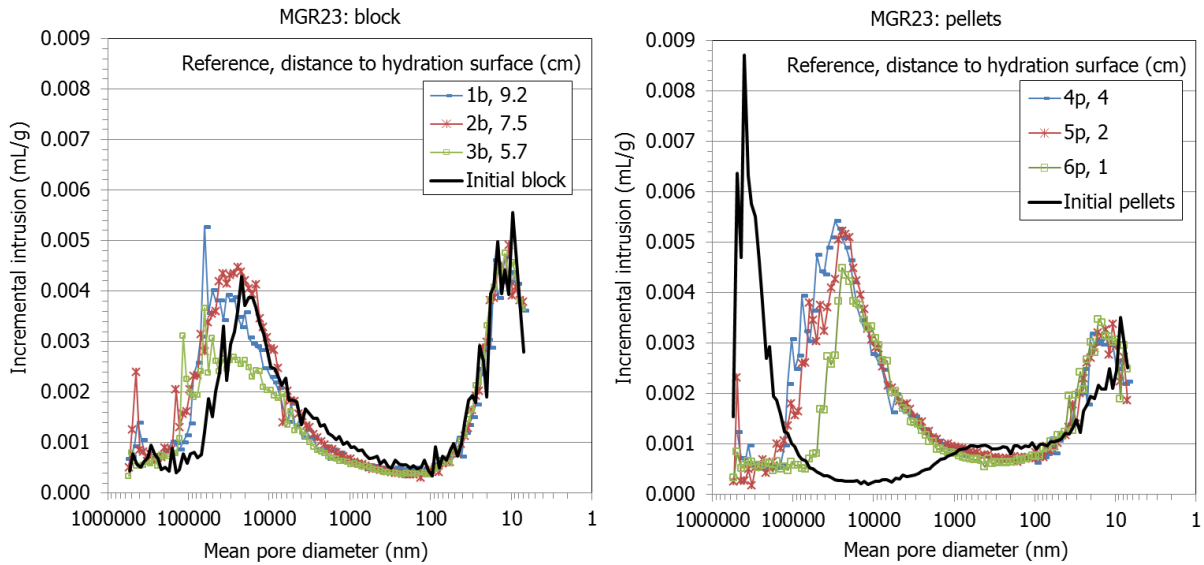


**Figure 5-16. Pore size distribution expressed as incremental mercury intrusion of samples from test MGR23 (lasting 210 days), corresponding to the block (left) and pellets (right) halves. The curves for the initial materials (blocks and pellets) are included**

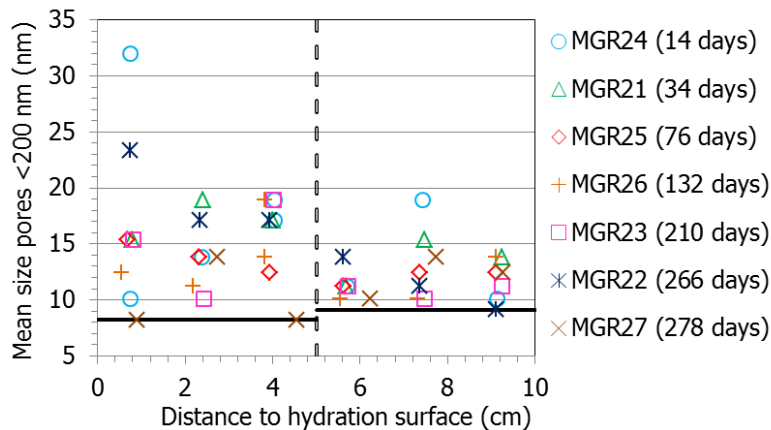


**Figure 5-17. Mean size of pores smaller than 200 nm as determined by MIP (except in test MGR27, the pellets samples were at 0-5 cm from the hydration surface, and the block samples were at 5-10 cm from the hydration surface)**

The void ratio corresponding to pores larger and smaller than 200 nm was recalculated as explained in by Villar et al. (2021b). The ratio between the void ratio corresponding to pores smaller ( $e_m$ ) and larger ( $e_M$ ) than 200 nm increased in all samples with respect to the reference values, which reflects the increase in the volume of micropores as a result of hydration (Figure 5-18). This increase was much more significant for the pellets subsamples, except in the driest ones. In the block samples the largest proportion of void ratio corresponded to the pores of diameter smaller than 200 nm, and in fact for each test the largest  $e_m/e_M$  values tended to be in the block samples. The highest homogeneity in terms of  $e_m/e_M$  was reached in test MGR27, saturated through the block, which also had the most homogeneous dry density.

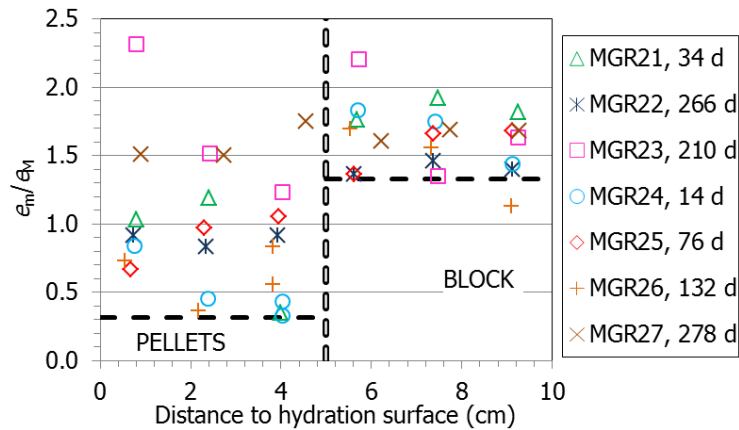


**Figure 5-18. Ratio between void ratio corresponding to pores smaller and larger than 200 nm ( $e_m$  and  $e_M$ ) obtained by MIP in subsamples from the MGR tests (the thick horizontal lines indicate the initial conditions for all the tests except MGR27, in which the position of pellets and block was inverted)**

The BET specific surface area values measured in the samples from the tests were higher than the reference value in the half closest to hydration (pellets in all tests, except MGR27), and lower in the half farthest from this one (block in all tests, except MGR27). A general decreasing trend towards the less hydrated areas was noticed (Figure 5-19).

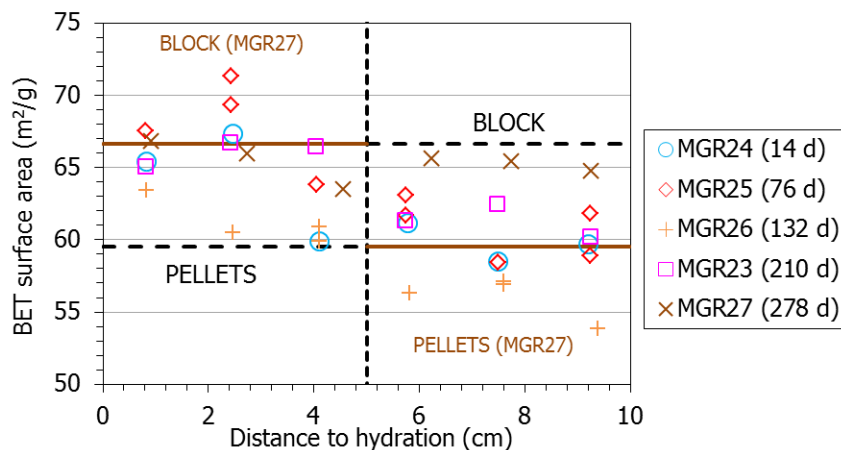


**Figure 5-19. BET specific surface area as a function of the distance to the hydration surface. Horizontal lines indicate the reference values (MGR27 hydrated through the block)**

Although the BET surface area depends on non-intrinsic factors such as the degree of grinding of the sample, previous researches have shown that it is closely related to water content (e.g. Villar 2017, for the FEBEX bentonite). Figure 5-20 shows the values measured in the different subsamples against their water contents, the increasing trend is clear. In contrast, as the previous figures showed, there is no correlation with the duration of the tests.

The basal reflection of the subsamples after some MGR tests was determined by XRD. Fragments of the samples were X-rayed the same day in which the cells were dismantled, trying to keep the final water content unchanged by avoiding any accidental drying. The results obtained showed that the (001)-reflection was a double one that could be decomposed into two diffraction peaks by profile fitting of the XRD patterns. In the case of the block samples the

main diffraction peak corresponded to the full development of the 2-layer hydrate (~1.5-1.7 nm) and the secondary one to the 3-layer hydrate (~1.8-1.9 nm), whereas in the pellets samples the main diffraction peak corresponded to the full development of the 3-layer hydrate and the secondary peak was higher (2.0-2.1 nm). However, the samples from test MGR24, the shortest one, showed a single diffraction peak for the (001)-reflection at much lower values.

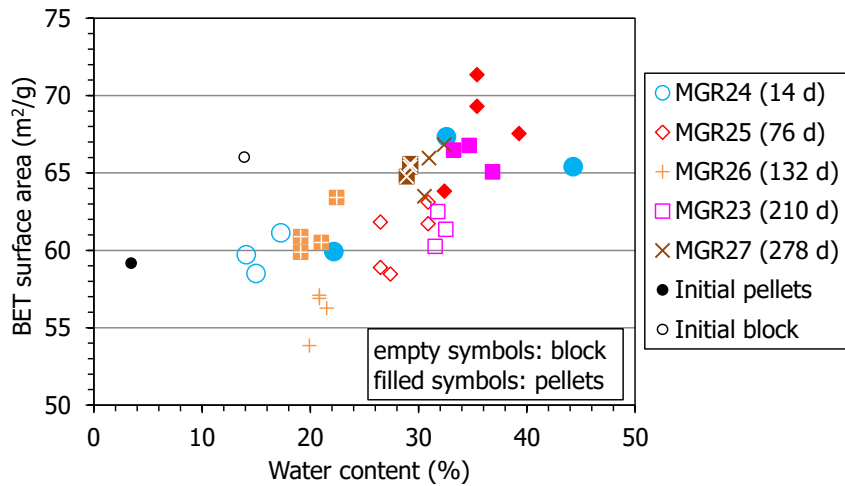


**Figure 5-20. BET specific surface area as a function of water content of the samples. The duration of the tests is indicated in days**

Figure 5-21 shows the values corresponding to the main reflections. The initial basal reflection for the pellets samples would be ~1.3 nm, and for the compacted block ~1.5 nm. For a given test, no matter its duration, the final values were higher in the pellets part. For the pellets samples with water content higher than 30% the values were all above 1.8 nm, practically corresponding to the 3 water layer hydration state of the smectite. In contrast, block samples of similar water content had lower basal spacings.

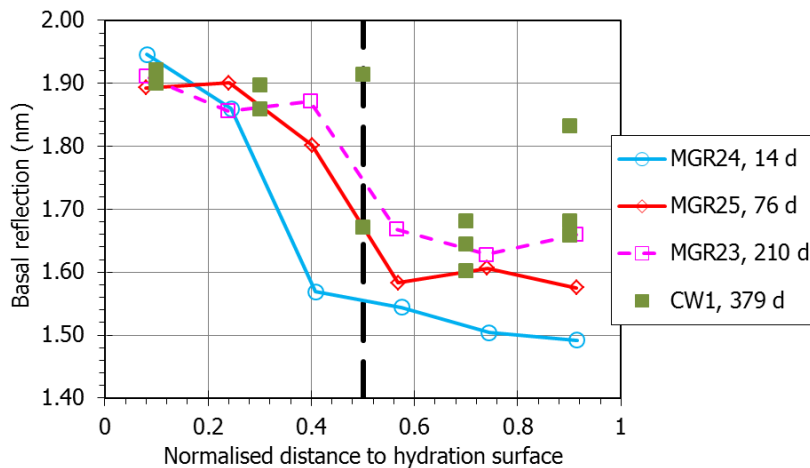


**Figure 5-21. Main diffraction peak of the basal reflection of subsamples of MGR and CW tests (total length of 10 cm in tests MGR and 12 cm in CW). Hydration took place through the pellets except in tests MGR27 and CW2. The duration of the tests is indicated in days**

### 5.1.3.2. Transparent cell (FEBEX)

#### Hydration process

Unfortunately, the online measuring system of the transparent cells did not work properly, and no consistent information was gotten from it (Villar et al. 2021c). Nevertheless, since cells CW1 and CW2 were photographed on both sides (A and B faces) periodically during hydration, some information on the temporal evolution of the system could be obtained. Figure 5-22 shows a comparison of the appearance of face A of the two tests at the same testing times. Variations in the coloration of the grains, changes in texture and shape, and displacement of the block-pellets interface were observed. As the pellets were hydrated, the grains increased in size, without displacement, and the whole of them lose sharpness. The appearance of the saturated pellets was gel-like. The evolution of hydration was slower in face B, where fine particles predominated. The reason could be the absence of large voids where water could quickly and easily penetrate. A downwards movement of the pellets/block interface in cell CW1 was observed, whereas this interface moved upwards in cell CW2.

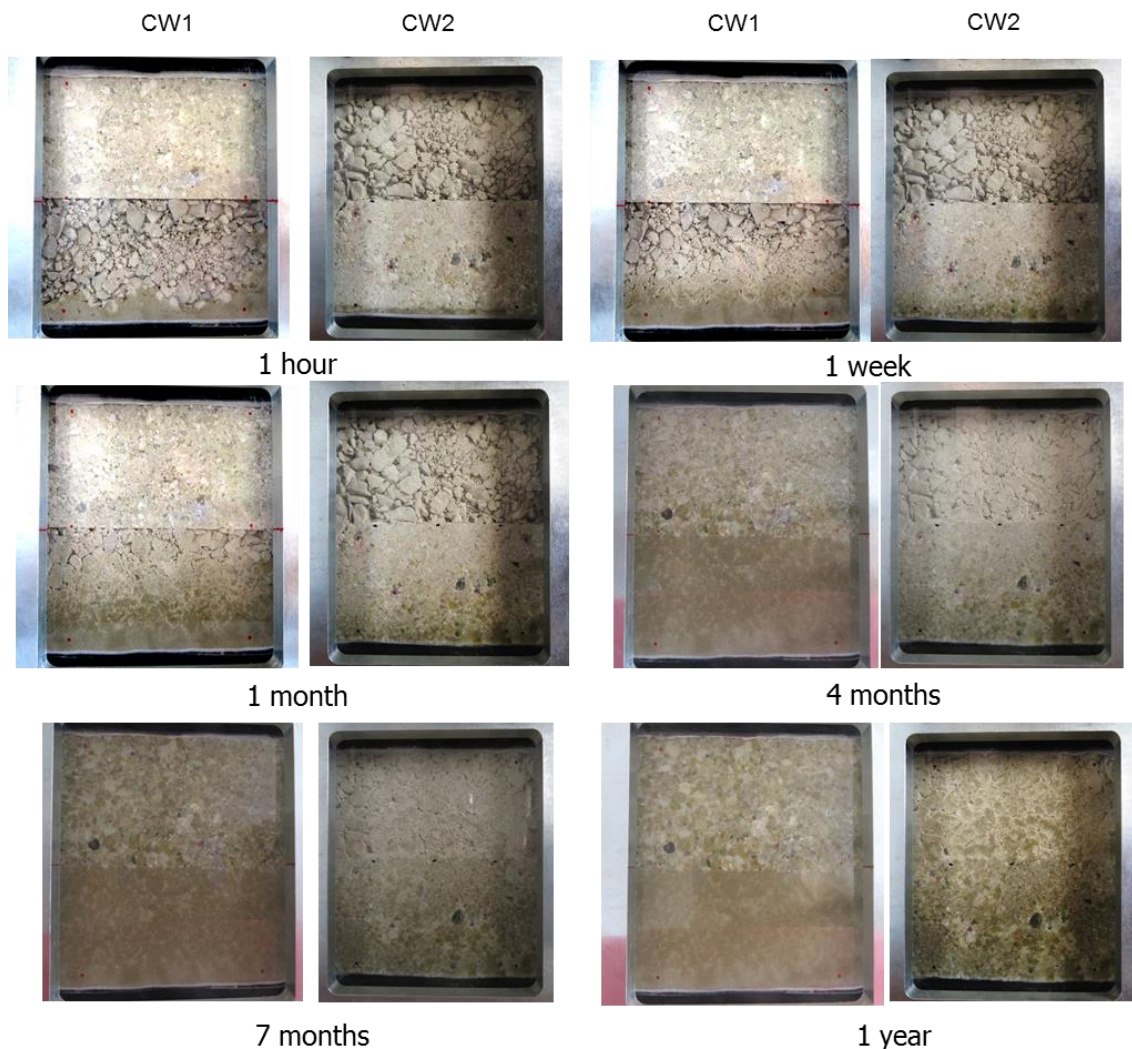


**Figure 5-22. Comparison, in face A, of the evolution of the hydration fronts in both cells (CW1: first and third column, and CW2: second and fourth column) for six different moments**

The face-A images for the three first months of hydration in CW1 were analysed and the evolution of some distinct pellets and of the block/pellets interface were followed. In Figure 5-23 the interface between blocks and pellets in CW1 is shown in more detail along with the indication of the position of the interface and of the contour of some pellets at different stages. As the pellets were hydrated, the grains increased in size, without displacement, and they lose sharpness. The downwards movement of the pellets/block interface was also observed, which indicates the compression (or collapse) of the pellets part.

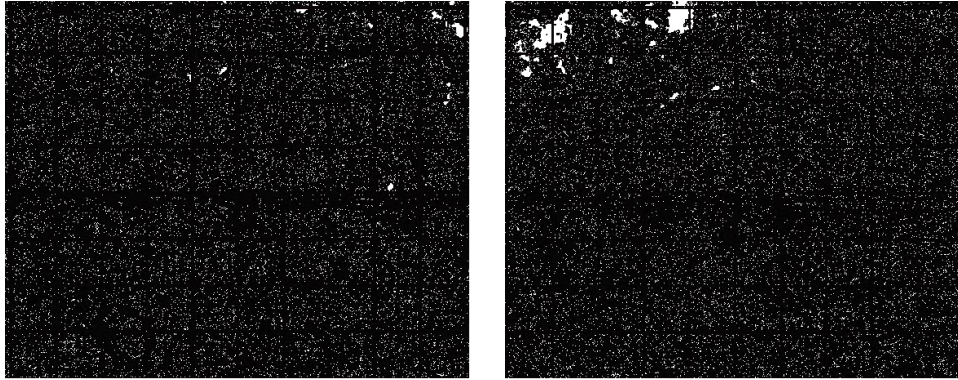


**Figure 5-23** Detail of texture evolution of the interface since the beginning of the CW1 test (yellow), after a month (red), after two months (green) and after three months of hydration (blue). A 5x5 mm mesh has been represented

### **Final physical state**

Cell CW1, saturated through the pellets, was dismantled after 379 days and cell CW2, saturated through the block, after 420 days of hydration. A detailed characterisation of the final state of the bentonite was carried out in subsamples taken according to the schema shown in Figure 5-24. It was not possible to distinctly separate the block and pellet parts. Table 5-6 summarises the initial and final characteristics of the tests. For the global values, the initial and final dimensions and weight of the pellets/block assemblage were considered. Because bentonite swelling caused the compression of the geotextiles placed on top and bottom of the cell, the total height of the sample increased and hence there was an overall decrease in dry density. Cell CW1 had reached full saturation, but not cell CW2, despite its longer duration. The values shown in the Table for the block and pellets parts are the average of the determinations in subsamples. These may be affected by trimming and slight drying during manipulation.

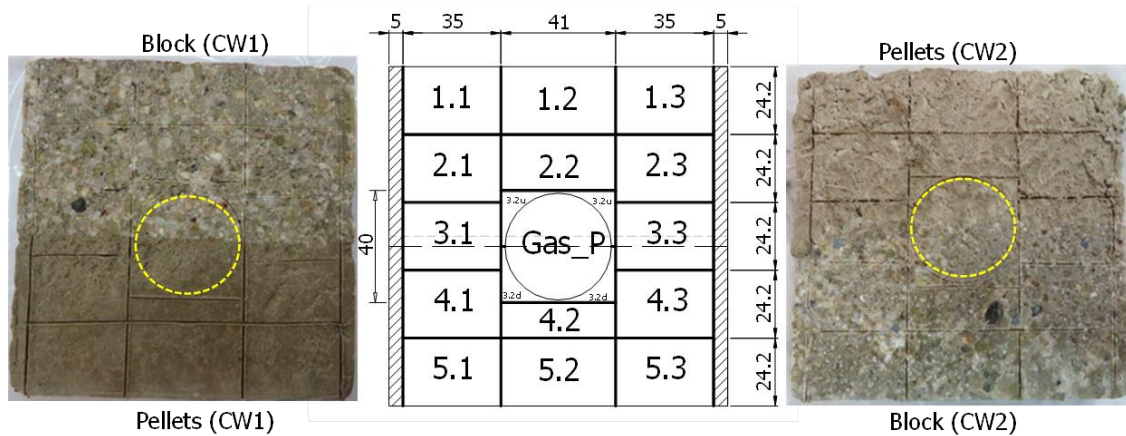


**Figure 5-24. Final subsampling of tests CW and location of samples for gas permeability (circle)**

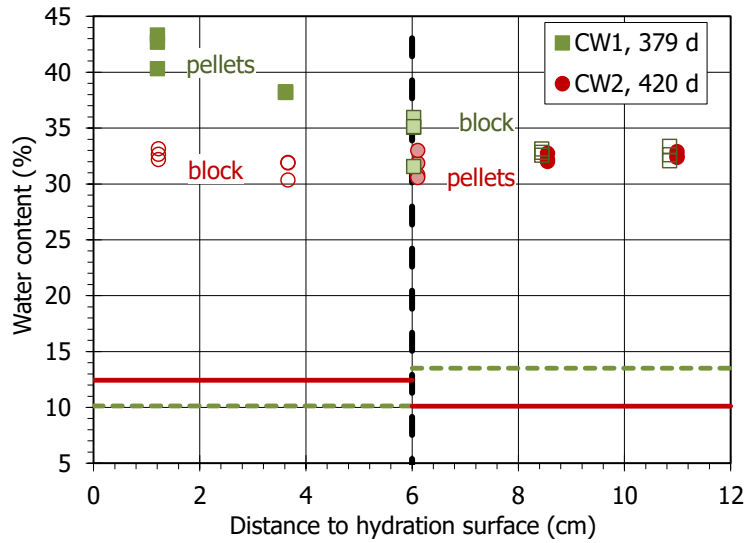
**Table 5-6. Initial and final characteristics of test CW1 and CW2**

Test		Initial				Final			
		$h$ (cm)	$w$ (%)	$\rho_d$ (g/cm <sup>3</sup> )	$S_r$ (%)	$h$ (cm)	$w$ (%)	$\rho_d$ (g/cm <sup>3</sup> )	$S_r$ (%)
CW1	Pellets <sup>a</sup>	5.75	10.1	1.30	25	5.69	40.5	1.28	99
	Block <sup>a</sup>	6.03	14.0	1.59	54	6.37	32.8	1.47	105
	Total <sup>b</sup>	11.79	11.9	1.45	37	12.06	35.9	1.38	102
CW2	Pellets <sup>a</sup>	5.60	10.1	1.30	25	5.58	32.4	1.31	82
	Block <sup>a</sup>	5.98	12.4	1.61	50	6.64	32.1	1.45	101
	Total <sup>b</sup>	11.58	11.2	1.46	36	12.22	32.1	1.39	92

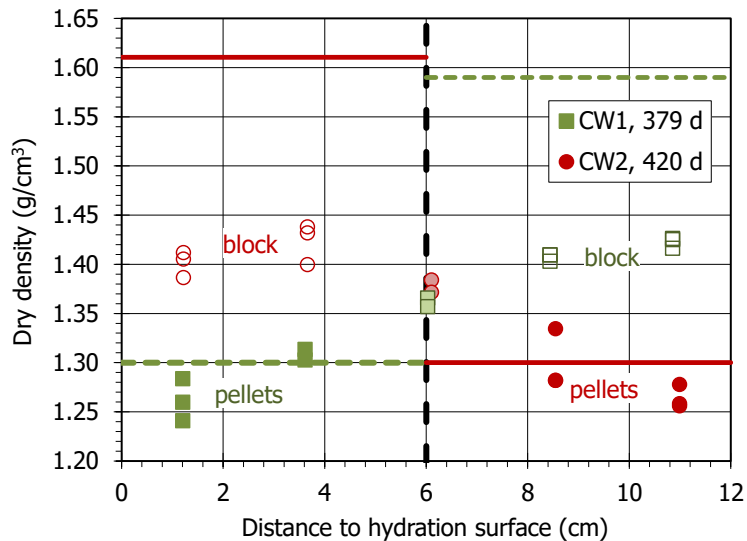
<sup>a</sup> final dry density and degree of saturation affected by subsampling and trimming, <sup>b</sup> final values affected by compression of geotextile during test

Figure 5-25 to Figure 5-27 show the final water content, dry density and degree of saturation determined in the subsamples of the two tests, along with the initial values. Hydration resulted in an overall water content increase both in the pellets and the block parts, considerably higher for the pellets part of test CW1. As a result of the water content increase, the bentonite swelled and the dry density of the assemblage decreased because of the slight deformation allowed by the geotextile compression (the overall dry density of cell CW decreased from 1.45 to 1.38 g/cm<sup>3</sup> and that of cell CW2 from 1.46 to 1.39 g/cm<sup>3</sup>). In both tests the swelling was higher in the block part, whose dry density significantly decreased. Despite the fact that the sample CW1 was fully saturated at the end of the test (Table 5-6

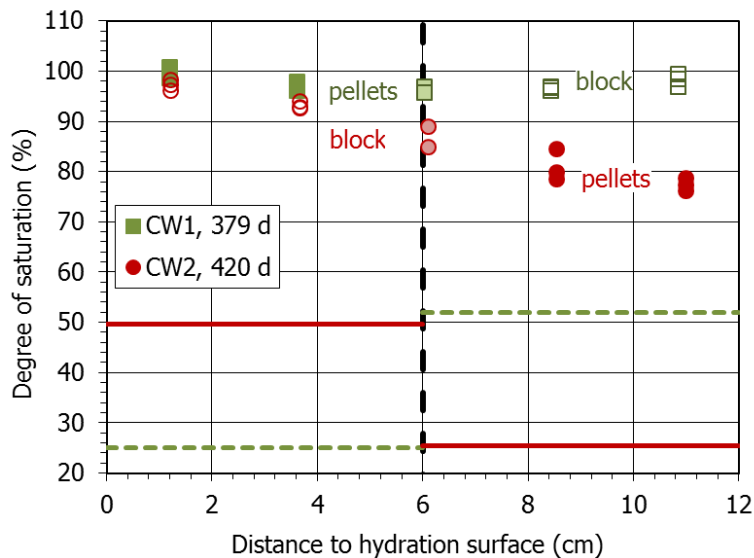
Table 5-6), there were still clear water content and dry density gradients, with higher water contents and lower dry densities in the pellets part, which was earlier saturated. In contrast, cell CW2, which was not completely saturated ( $S_r=92\%$ ), showed homogeneous water content, but still considerably higher dry densities and degrees of saturation in the block part. In fact, the average degree of saturation of the pellets part was only of 82%. The interface between pellets and block did not seem to play any role in the general trend of these variables.



**Figure 5-25.** Final water content along the samples of CW tests. The duration of the tests is given in days. The thick horizontal lines mark the initial values

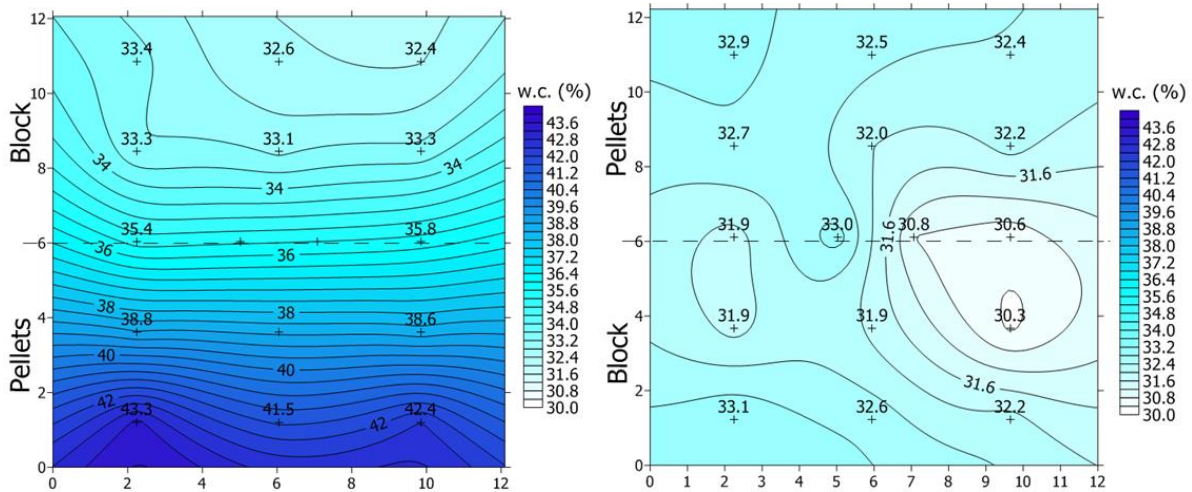


**Figure 5-26.** Dry density along the samples of CW tests. The duration of the tests is given in days. The thick horizontal lines mark the initial values

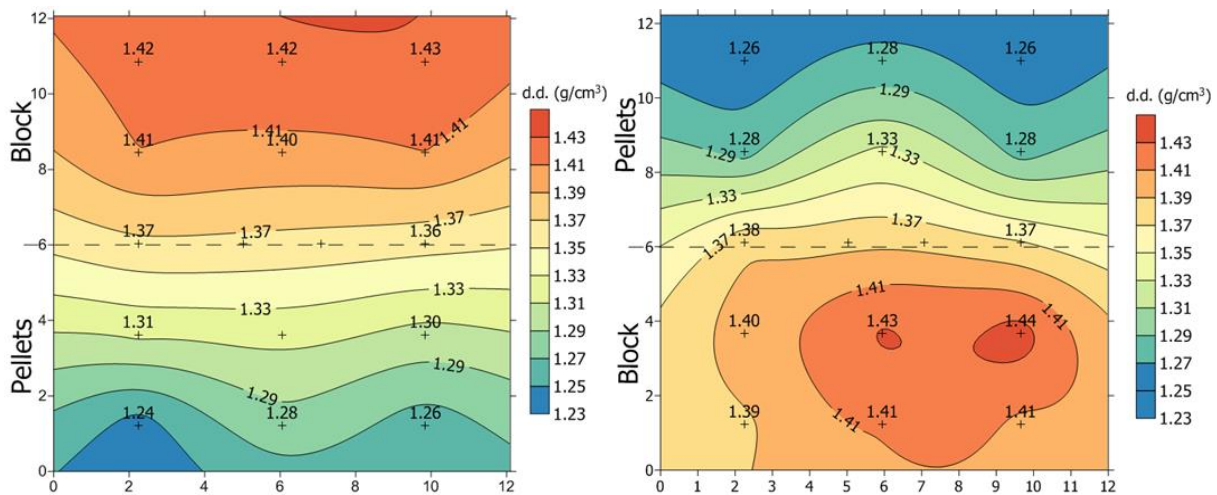


**Figure 5-27. Degree of saturation along the samples of CW tests. The duration of the tests is given in days. The thick horizontal lines mark the initial values**

However, a small border effect was observed at the bottom of the cell: the water content of the subsamples close to the border (5.1 and 5.3 in Figure 5-24) was slightly higher than that of the middle subsample (5.2), whereas the dry density was lower, especially in cell CW1. The cell border effect persisted, although weakened, until the upper part (e.g. samples 1.1 and 1.3 had slightly higher water content and lower dry density than sample 1.2). The border effect can be better noticed in the 2-D plots for water content and dry density, which were obtained with the contour mapping software Surfer® using the Kriging gridding method (Figure 5-28 and Figure 5-29). The same colour code was used to draw the contour plots for each parameter. The concentric isolines around a particular sampling point are probably plotting artefacts caused by the small range of values. The final distribution of water content was completely different in both samples. In the case of CW1, the highest water content occurred close to the hydration zone (pellets), whereas in CW2 the distribution was quite homogeneous all over the sample. In contrast, in both cases the dry density distributions show maximum values in the area of the block, decreasing towards the opposite end. The loss of dry density in the CW2 block compared to the CW1 block was greater, since it was precisely in that area where it began to hydrate, and therefore expanded.



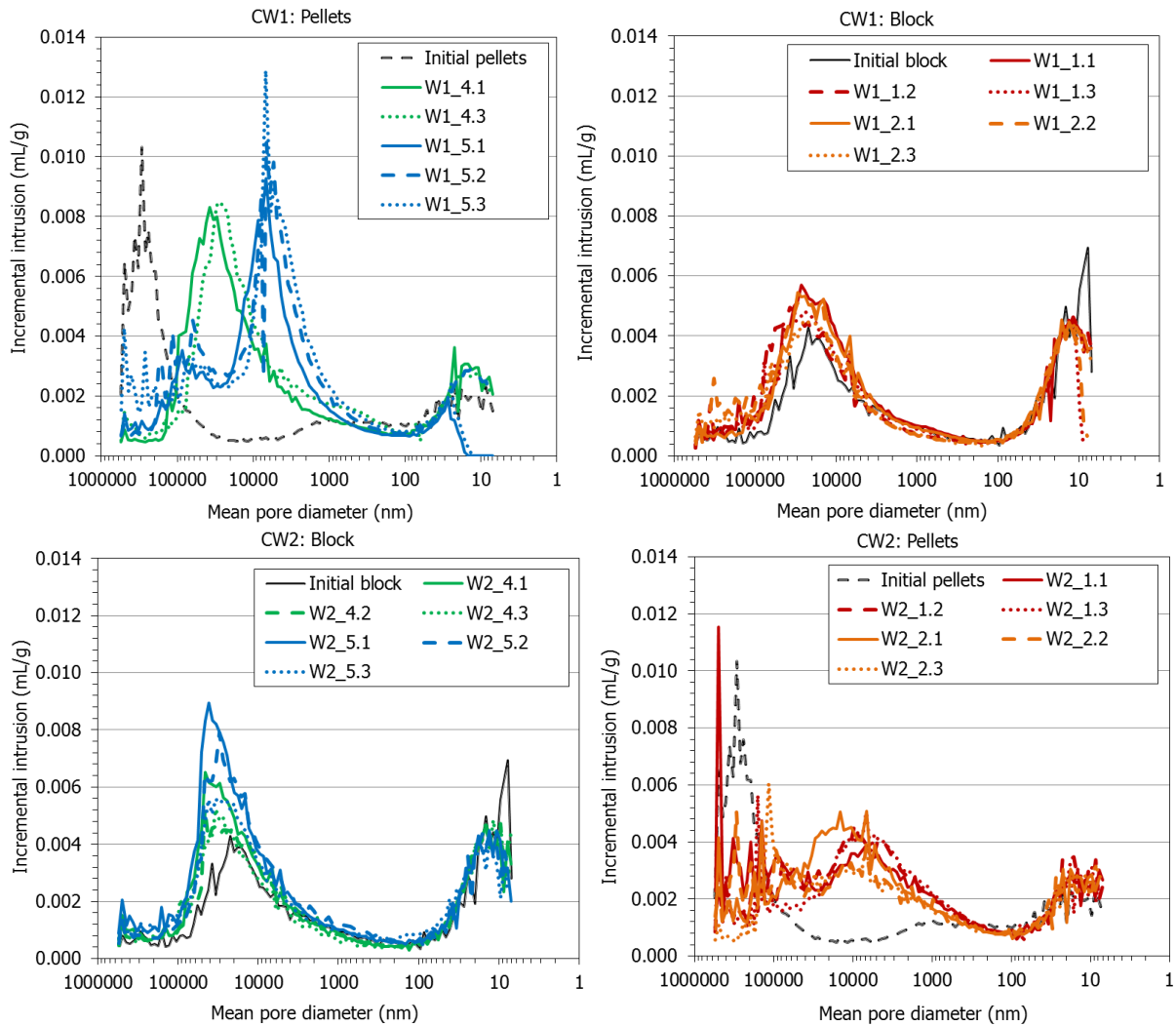
**Figure 5-28. Contour plot for final water content in CW1 (left) and CW2 (right). Distances in cm**



**Figure 5-29. Contour plot for final dry density in CW1 (left) and CW2 (right). Distances in cm**

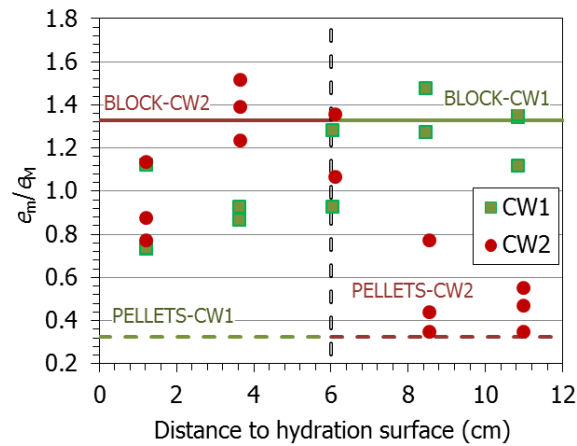
**Microstructural changes**

Figure 5-30 shows the incremental curves of mercury intrusion as a function of the mean pore diameter of the diameter size intervals corresponding to each pressure increase step. In both tests the macroporosity of the pellets shifted to smaller pore sizes, more as the water content was higher. In particular, for the pellets part in test CW1 the mean size of the macropores considerably decreased, from ~300  $\mu\text{m}$  to values between 6 and 40  $\mu\text{m}$ . However, in some cases, pores larger than ~70  $\mu\text{m}$  remained, particularly in CW2, where the pellets part was not completely saturated. The pore size distribution of the block parts did not change much as a result of hydration, particularly in test CW1. In the block part of test CW2 the size and volume of the macropores increased. All the samples had mean pore diameters for the pores smaller than 200 nm in a narrow range between 6 and 26 nm, and in test CW1 tended to decrease away from the hydration surface. In general the mean size of this pore family was higher than that for the initial block.



**Figure 5-30. Incremental mercury intrusion in CW1 and CW2 (the curves corresponding to the initial conditions are also included)**

The ratio  $e_m/e_M$  obtained by MIP for the different subsamples is shown in Figure 5-31 as a function of the distance to the hydration surface. For the pellets part in test CW1 the void ratio corresponding to pores larger than 200 nm considerably decreased, particularly away from the hydration surface. As a result, the  $e_m/e_M$  ratio increased in the same direction. In the pellets part of test CW2, the volume of large pores decreased only in some samples (except close to the pellets/block interface, where it significantly decreased), but the volume of pores smaller than 200 nm tended to increase, resulting in an increase of the  $e_m/e_M$  ratio in this area. In the block samples of both tests the largest proportion of void ratio corresponded to the pores of diameter smaller than 200 nm ( $e_m/e_M > 1$ ), but both  $e_m$  and  $e_M$  increased with respect to the initial values, reflecting the overall decrease in dry density allowed by the compression of the geotextiles as a result of bentonite swelling (Table 5-6). Hence the  $e_m/e_M$  ratio did not change much in the block parts of any of the tests, except for the samples closest to the hydration surface of test CW2, where it decreased.



**Figure 5-31. Void ratio corresponding to different pore sizes obtained by MIP in samples from tests CW (the thick horizontal lines indicate the distribution for the reference block and pellets)**

The mode sizes of each pore size interval are plotted in Figure 5-32. All the samples had mean pore diameters for the pores smaller than 200 nm in a narrow range between 7 and 26 nm. Overall the size of this pore family was higher than that for the initial block and lower than for the pellets, but in test CW1 tended to decrease away from the hydration surface. In contrast, the size of the macropores for the pellets part of CW1 was lower than the initial one.

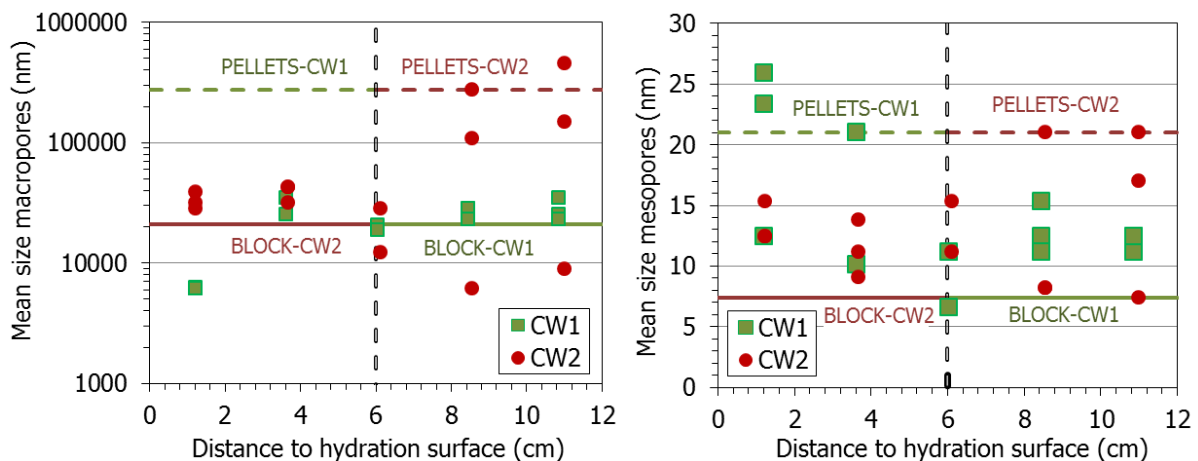


**Figure 5-32. Void ratio corresponding to pores larger and smaller than 200 nm (left and right, respectively) as a function of the distance to the hydration surface**

The BET specific surface area calculated from the sorption is shown in Figure 5-33. A reduction in the BET surface in the area of the block, and an increase for the pellets, compared to those for the reference bentonite were observed. In the case of CW1, the increase in the BET specific surface area of the pellets was higher than in test CW2, where the pellets had lower water content. In fact, the usual increase of specific surface area with water content is evinced in Figure 5-34.

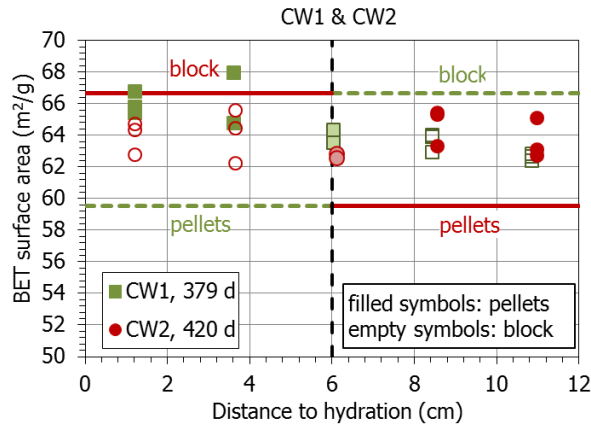


**Figure 5-33. BET specific surface area of samples from tests CW and in the reference bentonite (thick horizontal lines)**

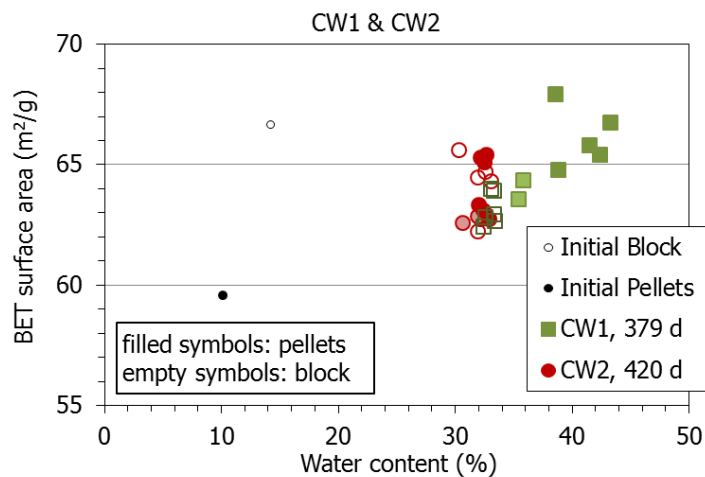


**Figure 5-34. BET specific surface area of samples from tests CW as a function of their water content**

### Healing of block/pellets interface: gas testing

At the end of the tests in transparent cell, a cylindrical subsample was obtained by drilling across the pellets/block interface to measure the gas breakthrough pressure as an indicator of the healing of the interface. These subsamples were vertically crossed by the interface (Figure 5-4

Figure 5-4, Figure 5-24) and had a nominal diameter of 3.8 cm. The initial and final characteristics of the samples as well as those of the tests are shown in Table 5-7.

In test CW1-gas a confining pressure of 3 MPa was applied, corresponding to the swelling pressure of the bentonite with a dry density of 1.45 g/cm<sup>3</sup> (the global value for test CW1) according to Equation 5.3. This value was selected to keep approximately the same stress state as the bentonite likely had at the end of the test, when almost full saturation was reached, and prevent the interface from mechanically splitting. The injection pressure was increased 0.1 MPa every two hours, from 0.2 to 2.95 MPa. The pressure and flow evolution during the test are shown in Figure 5-35. There was no flow until the injection pressure reached 2.00 MPa. For injection pressures from 2.00 to 2.20 MPa there were barely measurable flow pulses. There was again no

flow from 2.20 to 2.85 MPa of injection pressure. For gas injection pressure of 2.90 MPa unsteady flow pulses close to the turndown value of the flowmeters were detected. At the end of the test the sample had consolidated as a result of the confining and gas pressure applied and its water content had slightly decreased, which would indicate that some water movement took place during the test.

**Table 5-7. initial and final characteristics of the samples used for gas testing and characteristics of the tests**

Test	CW1		CW2	
	Initial	Final	Initial	Final
$\rho_d$ (g/cm <sup>3</sup> )	1.33	1.43	1.36	1.40
$h$ (cm)	2.16	2.13	2.15	2.15
$\phi$ (cm)	3.78	3.68	3.79	3.73
$w$ (%)	34.8	32.2	30.3	29.3
$S_r$ (%)	92	99	83	85
Confining P (MPa)	3.0		1.1-2.3	
Injection P (MPa)	0.2-2.9		0.2-0.3	
Duration (days)	32		4	

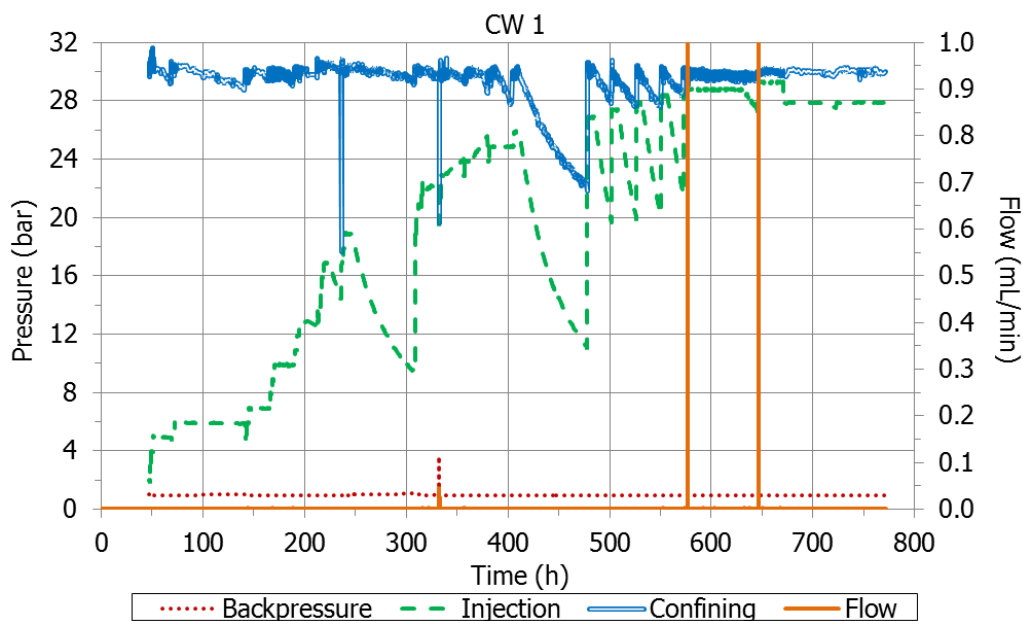


**Figure 5-35. Confining pressure, gas pressure in the upstream cylinder, downstream pressure and outflow in test CW1**

It can be considered that the gas breakthrough pressure was ~2.2 MPa, although no steady, correctly measurable flow was measured at any moment. This breakthrough pressure would be in the order of the values expected for FEBEX samples compacted to dry densities between 1.35 and 1.45 g/cm<sup>3</sup>, which would be between 1.5 and 3.5 MPa (Gutiérrez-Rodrigo 2018, Gutiérrez-Rodrigo et al. 2021).

Because the sample from test CW2 was not saturated, the confining pressure applied during gas testing was initially lower, 1.1 MPa. In this case the outflow was high from the first step of injection pressure (0.2 MPa), and the confining pressure had to be increased to reduce it. Outflow continued until the confining pressure was 2.3 MPa, for which no flow occurred. Then the injection pressure was increased to 0.3 MPa, flow resume and the test was dismantled. The permeability values obtained for each pressure step are shown in Figure 5-36. They are expressed as  $k_{rg} \cdot k_{ig}$ , where  $k_{rg}$  is the relative gas permeability and  $k_{ig}$  is the intrinsic permeability measured with gas flow. The duration of the steps had some influence on the values obtained, because the sample consolidated as a result of the confining pressure application, which resulted in a decrease of gas permeability. This would explain the significantly lower value obtained in the last step, which was obtained after the sample had been submitted to a confining pressure of 2.3 MPa for one day. Indeed the sample dry density increased during the test, even though the total duration of the test was of only 4 days. These permeability values are lower than those expected for the FEBEX bentonite compacted with similar accessible void ratio (0.165). In particular, the value obtained for a confining pressure of 0.1 MPa was  $8 \cdot 10^{-17}$  m<sup>2</sup>. According to the correlation presented in Villar et al. (2013), for a sample of FEBEX bentonite compacted at the same accessible void ratio, with no interface in it and tested under the same confining pressure, the intrinsic permeability should be  $\sim 2 \cdot 10^{-15}$  m<sup>2</sup>, i.e. considerably higher. This would indicate that the pellets/block interface was not a preferential gas pathway and flow took place through the bentonite whole porosity. Hence, the interface was perfectly healed and sealed, even though full saturation had not been reached in this area.

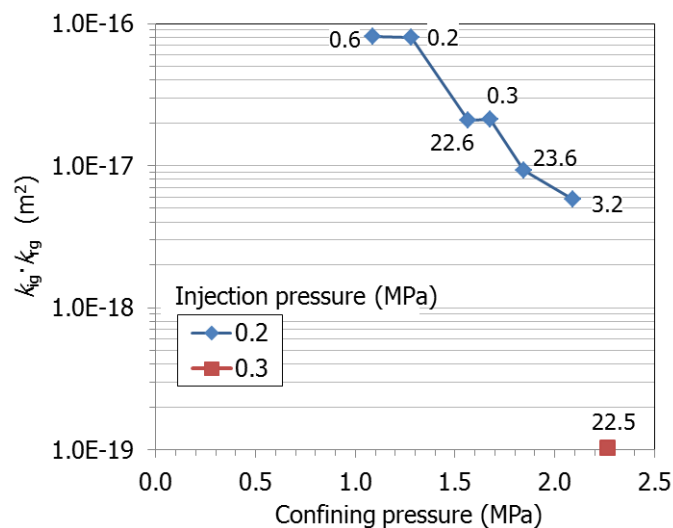


**Figure 5-36. Gas permeability measured in a sample from test CW2 including the interface between block and pellets. The duration of some of the steps is indicated in hours**

Figure 5-37 shows the pore size distribution of subsamples taken from the bentonite cores after the gas permeability tests along with the pore size distribution of samples taken at the same distance from the hydration surface as that of the samples used for gas testing (i.e. samples 3.1 and 3.3 in Figure 5-24). These curves were also shown in Figure 5-30. In all cases the subsamples used for MIP testing included the interface. In the sample from test CW1, the consolidation occurred during gas testing drastically reduced the volume of macropores. In contrast, in the sample from test CW2, which had been submitted to lower confining pressures and for shorter time during gas testing, the decrease in macroporosity was not so notable.

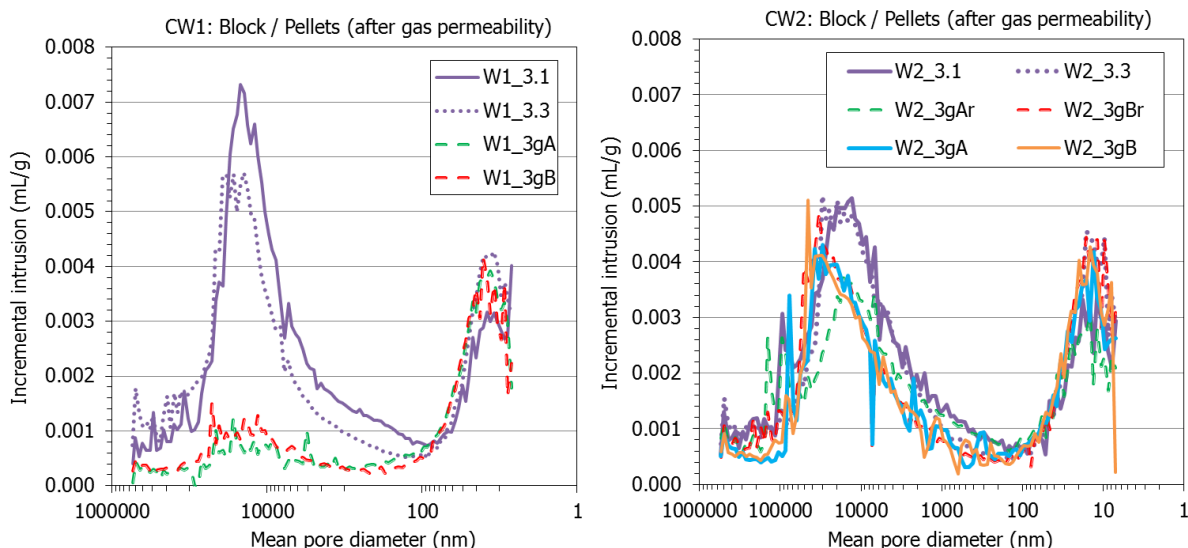


**Figure 5-37. Pore size distribution obtained by MIP of samples of tests CW1 and CW2 before and after gas testing**

### 5.1.3.3. Thermo-hydraulic cell (MX-80)

Deionised water was injected at a pressure of 14 kPa using a GDS volume/pressure controller. The water intake was faster at the beginning because the volume of water necessary to saturate the porous stone and the high porosity of the pellets mixture (Figure 5-38). After approximately 600 days the water intake stabilised at a value of ~930 cm<sup>3</sup>, which would correspond to an average water content of 32.2% and an average degree of saturation of 104%.

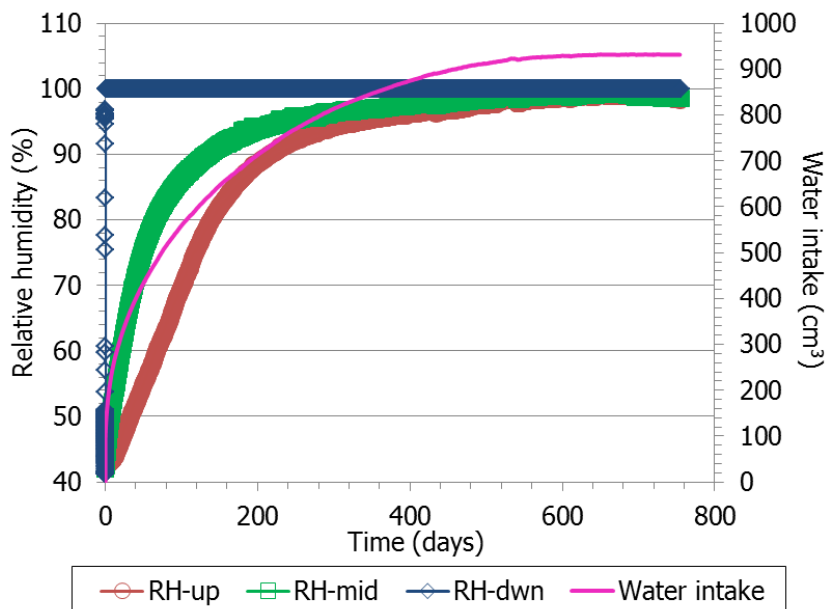


**Figure 5-38: Relative humidity and temperature evolution during hydration in test CT31**

The RH/T sensors' recordings during the whole test duration are shown in Figure 5-38. The sensor at the bottom was quickly flooded because of the high permeability of the low-density mixture. Hence, the relative humidity at 13 mm from the hydration surface was 100% almost from the beginning of hydration. After 2 years of hydration, the RH at all positions inside the bentonite is around 100%.

The pressure sensors operated correctly since hydration started (Figure 5-39). The bottom sensor recorded a quick and steady pressure increase. The middle sensor recorded initially a soft decrease, probably reflecting the collapse of the pellets part on saturation. Afterwards the middle sensor recorded a considerable increase in a relatively short period of time (from 0 to 4.3 MPa in 60 days) followed by a soft decrease and a new constant increase. It took longer for the upper sensor to start recording any pressure (~200 days), but then it continuously increased. After 700 days of hydration the three radial pressure sensors record constant values, with the middle sensor recording the highest one (6.4 MPa) and the bottom sensor the lowest one (4.5 MPa). This probably reflects the dry density gradient in the bentonite, where the lower part, which was first saturated, could swell more. According to Equation 4, the axial swelling pressure corresponding to an MX-80 bentonite compacted in a standard oedometer and saturated with deionised water would be 3.4 MPa.

As well, the pore pressure sensor on top of the cell did not record any change until 500 days had elapsed, and afterwards it steeply increased, reaching a value of 180 kPa.

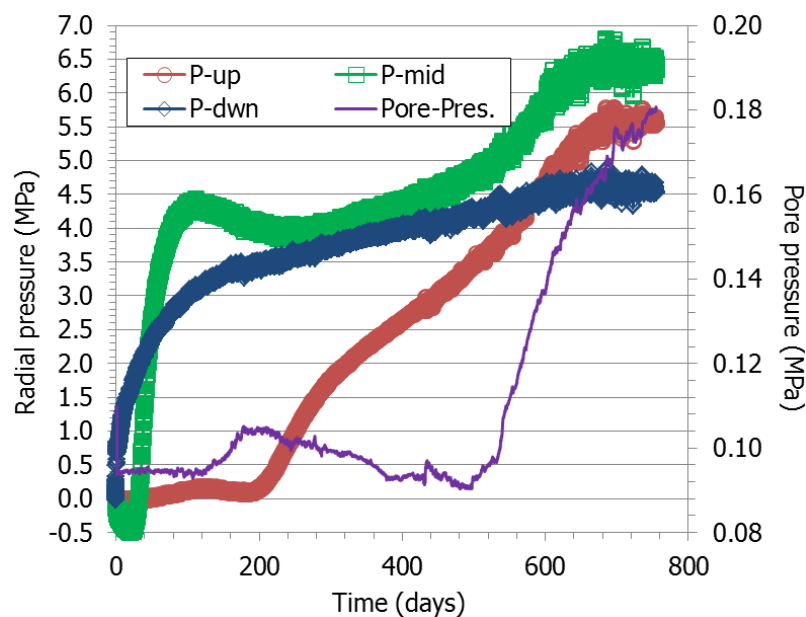


**Figure 5-39: Lateral pressure and pore pressure evolution during the hydration phase of test CT31**

#### 5.1.4 Discussion

The tests presented allowed to follow the hydro-mechanical evolution of a two-component buffer material upon hydration under isochoric conditions at ambient temperature. The dimensions of the testing cells were between 10 and 15 cm in height. In the case of the tests with FEBEX bentonite, the two components (bentonite pellets –GBM– and bentonite block) had different initial water contents and dry densities. The only test with MX-80 bentonite, CT31, is still ongoing, and in this case the initial dry density of the two components is the same and the

water contents are not too different. Except in tests MGR27 and CW2, hydration took place through the pellets part, which in the case of the FEBEX tests, had a higher intrinsic permeability than the block because of its lower dry density, higher macroporosity and lower water content (Villar and Lloret 2001, Romero 2013). During the MGR tests the axial pressure was measured on the sample surface opposite to hydration, whereas in test CT31 the radial pressure was measured at different levels. The discussion below is mainly based on the results obtained with the FEBEX bentonite and mostly taken from Villar et al. (2021b).

The pressure development was not mainly related to the quantity of water taken (i.e. to the overall degree of saturation), but to the water intake rate. Thus, when hydration took place under very low water inflow rate (MGR22, MGR26), the axial pressure for a given overall degree of saturation was much higher than for the tests in which hydration took place more quickly (Figure 5-7, right). Similarly, in test MGR27, in which hydration under constant injection pressure was slower because it took place through the higher-density block part, the pressure reached for a given overall degree of saturation was initially (namely until the overall degree of saturation reached ~60%) higher than for the tests in which saturation took place through the pellets. This suggests that it was the redistribution of water in the microstructure the mechanism that triggered most of the swelling. This is supported by the fact that in test MGR23 the axial pressure considerably increased during the 14-day period during which inadvertently no water was supplied to the cell, showing that water redistribution inside the bentonite can cause pressure increase. In the EB in situ test performed at the Mont Terri URL, where a large-scale two-component barrier (FEBEX GBM and blocks) was tested for 10.5 years, most of the sensors installed in the bentonite recorded relative humidity values of 100% only one year after the beginning of the test, whereas it took four years for the total pressure sensors to record stable values that kept approximately constant until the end of the test (García-Siñeriz et al. 2015). The comparison of Figure 5-38 and Figure 5-39 show that, except for the sensor closest to the hydration surface, which became quickly flooded, the middle and top pressure sensors recorded the largest pressure increases when the overall degree of saturation was higher than 90%. In particular the middle sensor, located in the block part at 8 cm from the hydration surface, recorded an increase in pressure from 4 to 7 MPa for a relative humidity increase of only 4 % (from 96 to 100%). This can be better observed in Figure 5-40.

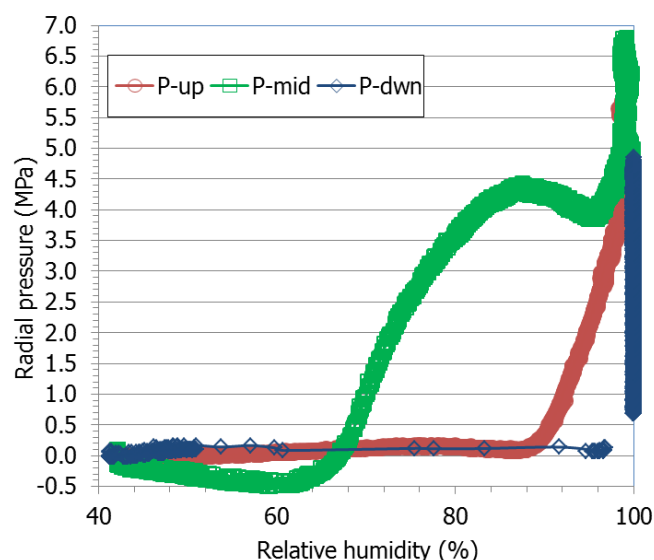


**Figure 5-40. Radial pressure measured at different heights in test CT31 against the relative humidity in the same locations (MX-80 bentonite, see Figure 5-5 for location of sensors)**

The different strength of the materials involved also played a role on the axial pressure development kinetics at the first stages of saturation. When the water intake was very slow, the block part was able to swell relatively quickly (see the dry density and water content distribution at the end of test MGR26 in Figure 5-12 and Figure 5-13), and because the pellet part was comparatively dry (drier than at the end of any other test) and consequently rigid, the stress was more effectively transmitted towards the top and hence recorded by the load cell. In contrast, when hydration was quicker, the pellet part soon collapsed and was easily compressed by the downwards swelling of the block, resulting in a lower axial load measured on top. In fact, a downwards movement of the pellets/block interface in cell CW1 was observed, indicating the compression (or collapse) of the pellets part. In contrast, this interface moved upwards in cell CW2, saturated through the block.

The final axial pressure measured in the tests is plotted against the final degree of saturation in Figure 5-41. Overall, the pressure consistently increased with the average degree of saturation, but in test MGR26, saturated under low water inflow, a pressure higher than expected according to the trend marked by the other tests was reached, consistent with the description of the initial stages of saturation given in the previous paragraph. Once full saturation was reached, the swelling pressure was the same irrespective of the way of saturation, and thus tests MGR22 and MGR23 showed the same final pressure (3 MPa). This value is higher than the swelling pressure expected for a FEBEX bentonite sample compacted to the average dry density value of the MGR tests ( $1.45 \text{ g/cm}^3$ ). The theoretical value would be  $2.0 \pm 0.5 \text{ MPa}$ , according to the empirical correlation between dry density and swelling pressure obtained in small standard oedometers (Eq. 5.3). Previous research suggested that there is a scale effect on the swelling pressure measured in the laboratory, which tends to be higher as the testing cell is larger (Imbert & Villar 2006).

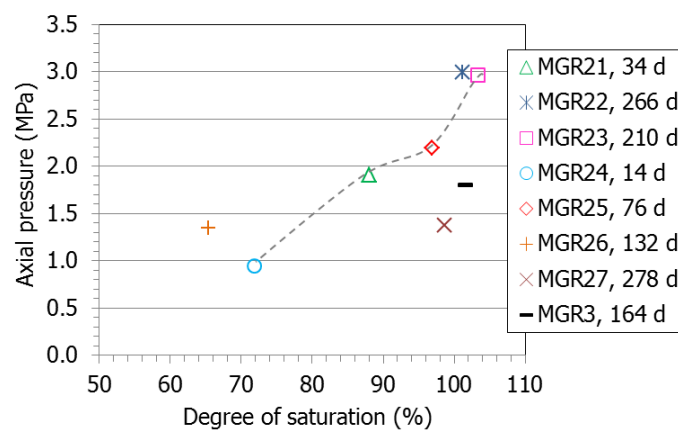


**Figure 5-41. Final axial pressures measured as a function of the final degree of saturation of MGR tests (average  $\rho_d=1.45 \text{ g/cm}^3$ )**

Even though full saturation had not been reached in test MGR27 (final  $S_r=99\%$ ), the final pressure measured in this test was much lower than could be expected according to the general trend for tests in which saturation took place through the pellets shown in Figure 5-41. Hydration tests performed in large-scale cells where radial and axial pressures were measured at different heights along the sample length showed that during saturation, the transient pressure values were related to the local dry density (Dueck et al. 2016, Baryla et al. 2019, Bian et al. 2019, Bernachy-Barbe et al. 2020, Harrington et al. 2020), as it has also been shown in test CT31 with MX-80 bentonite (section 5.1.3.3). In the case of test MGR27, the pellets part, on top of the sample, had the final lowest dry density (Figure 5-13) and lower degree of saturation (Figure 5-14). It is likely that the axial load measured reflected mainly the local pressure at the

upper part of the sample, which would be lower than the pressure that would have been measured at the bottom (in the block part) if there had been a pressure sensor in the area. In other words, the axial pressure measured on top would not be fully representative of the average pressure developed by the sample, because it would also be affected by the local conditions on top of the sample (lower density and degree of saturation). Similarly, the axial top pressure measured in the rest of the tests would also be conditioned by the higher dry densities in this area, where the block was placed (Figure 5-13). Also, in test CT31, which seems to be fully saturated, the axial pressure measured on top is higher than that measured at the bottom, where the pellets are placed (Figure 5-39). Hence, in addition to the scale effect commented in the previous paragraph, a further reason for the pressures observed higher than expected would be the influence of the higher density close to the measuring area on top.

As a further corroboration of that hypothesis, the final swelling pressure reached in a test performed in the same oedometer with a mixture of regular-shaped FEBEX bentonite pellets and powder in a 70/30 ratio has also been included in the figure (test MGR3). The average dry density of this mixture was  $1.45 \text{ g/cm}^3$  (as in the MGR tests presented here) and the initial water content 13.6% (Villar 1999). In this case the swelling pressure of the saturated sample had an intermediate value between the trend for tests having the pellets on top and the test with the block on top (MGR27). This would reflect the intermediate value of dry density on the top part of the sample, which was  $1.43 \text{ g/cm}^3$  at the end of test MG3,  $1.46 \text{ g/cm}^3$  at the end of tests MGR22 and MGR23 and  $1.42 \text{ g/cm}^3$  at the end of test MGR27, which in addition was less saturated.

The tests performed by Martikainen et al. 2018 (reported in Talandier, 2019) were very similar in design and dimensions to the tests presented here, with hydration under an injection pressure of 10 kPa taking place through the pellets (hence comparable to tests MGR21, MGR23 to MGR25 and CT31). Hydration took place through the top surface, where the pellets were placed. In these tests MX-80 bentonite was used, and the radial pressure developed by the block and the pellets parts were measured in addition to the axial ones. The axial and radial pressure development in the areas farther away from hydration (i.e. around the block part) displayed the initial peak followed by a decrease and a smooth eventual increase observed in some MGR tests (Figure 5-7) and in the middle part of test CT31 (Figure 5-39). These measurements also showed significantly lower pressures in the pellets than in the block part. The modelling groups involved in a benchmark where these tests were analysed, concluded that this difference was due to the initial contrast of density between the top and bottom of the sample but also to the friction between the bentonite and the steel cell wall (Talandier, 2019).

Indeed, none of the finished tests reached a final complete homogeneity in terms of dry density or water content: the water content decreased from the hydration surface upwards whereas the dry density increased (Figure 5-12 and Figure 5-13). These heterogeneities resulted from the initial swelling and ensuing density decrease of the bentonite that became first saturated (those parts closest to the bottom hydration surface), and the consequent compression of the bentonite located upwards. In contrast, a final homogeneous degree of saturation close to 100% was reached in the longer tests saturated through the pellets, i.e. MGR22, MGR23 and CW1 (Figure 5-42). Once overall full saturation was reached, no further water content or dry density changes are to be expected, which would mean that part of the initial volume changes were irreversible. Also, in the large-scale EB test mentioned above, no spatial trends were found for the degree of saturation, despite the fact that density and water content gradients remained (García-Siñeriz et al. 2015). In all cases the pellets/block interface did not seem to have any effect on the continuous gradients observed, i.e. there were no sudden changes across the interface.

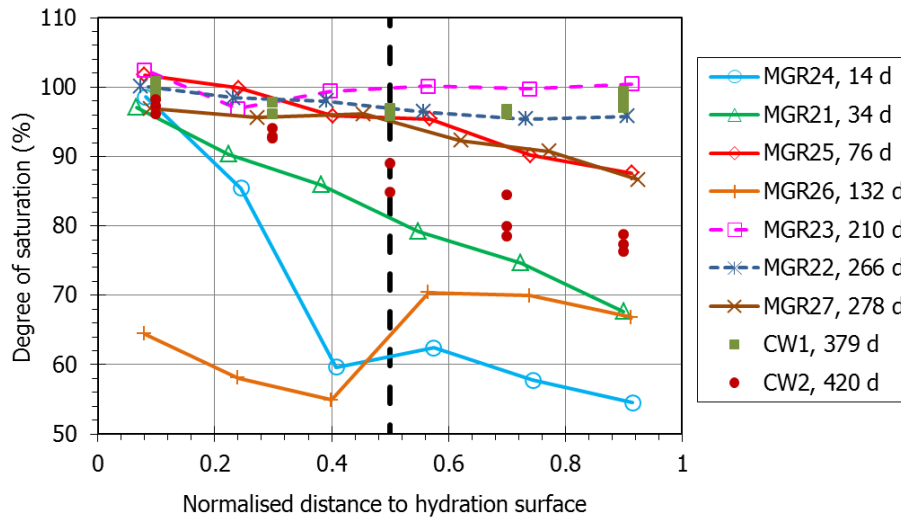


**Figure 5-42. Final degree of saturation along the samples of MGR and CW tests (total length of 10 cm in tests MGR and 12 cm in CW). Hydration took place through the pellets except in tests MGR27 and CW2. The duration of the tests is indicated in days**

The two tests in which hydration took place through the block (MGR27 and CW2) were far from full saturation, despite the fact that they were the longest ones performed in each kind of cell. It is remarkable that in all the tests the area closest to the hydration surface was fully saturated, except in test MGR26. This test, performed under constant flow and lasting 132 days, did not follow the overall trend, since the increase in water content was moderate and similar for both halves, attesting the more homogeneous water redistribution allowed by slow hydration. Vapour diffusion in the pore spaces would be the water transfer mechanism away from the hydration surface, as postulated by Kröhn (2005), who described the time-dependent water content distribution during the saturation of compacted bentonite under laboratory conditions by Fick's second law. Eventually, when full saturation was reached, the differences in the physical state of samples saturated under constant pressure or flow obliterated, resulting in the similar water content and dry density distribution patterns of tests MGR22 and MGR23.

Concerning the microstructural modifications during hydration, the GBM and the block parts behaved quite differently and in fact most parameters inferred by MIP (volume and size of each pore range, ratio between them), were different for the two components of the samples. Unlike the physical variables discussed in the previous paragraphs, in most tests there was not a smooth change between the microstructural parameters of pellets and block. The most notable change in the pellets parts was the disappearance of the pores larger than 550  $\mu\text{m}$  and the overall drastic decrease in size and volume of macropores. In contrast, the mean size of the pores smaller than 200 nm increased with respect to the original values for all the pellets subsamples. This was also the case for the block samples. Furthermore, in the block subsamples the volume and size of the macropores tended to increase, except in the shorter, less saturated tests. The increase of both  $e_m$  and  $e_M$  in the blocks subsamples resulted from the overall decrease in dry density experienced by the block upon hydration. Nevertheless, the  $e_m/e_M$  ratio increased from the initial  $\sim 0.3$  to values higher than 0.7 in all samples, but much more significantly in the pellets samples. Only the driest pellets samples (corresponding to the shorter tests, test MGR26 performed under constant flow, and test CW2 saturated through the block) had  $e_m/e_M$  ratios close to the initial one. These samples kept also pores larger than 550  $\mu\text{m}$  that cannot be detected by MIP (because of the technique limitations) but were inferred as explained in section 5.1.3.1. Pores larger than  $\sim 70 \mu\text{m}$  were actually observed by MIP in some pellets samples of test CW2 (Figure 5-30), where the pellets part was not completely saturated.

The only sample that kept quite homogeneous values across the pellets/block interface, in terms of  $e_m$ ,  $e_M$  and mean pore sizes, was that from test MGR27. This was also the test reaching the highest homogeneity concerning dry density and water content, which suggests that the microstructural changes were related to the changes in dry density and water content and thus to temporal evolution.

Hence, as a result of hydration the volume of micropores increased in all the bentonite with respect to the initial one, particularly in the case of the pellets. The increase in the volume of micropores was likely related to the increase in the smectite basal spacing as a result of the hydration of the interlayer cations (Figure 5-21), which is the driving mechanism for crystalline swelling, predominant in compacted bentonite saturated under isochoric conditions (e.g. Pusch et al. 1990, Devineau et al. 2006). As it happened with the pore size distribution obtained by MIP, the basal spacings were clearly distinct for pellets and block samples. In contrast, the basal spacings determined in wet samples from the in situ EB experiments (using the same procedure and methodology as in this work) did not show clear differences between block and pellets (Villar et al. 2014). Since the samples from the in-situ test were matured for 10.5 years, it could be expected that in the long term, also the microstructure of the two components of the much shorter MGR tests would become homogenised. In samples from the in-situ test –which were fully saturated– the basal spacings indicated that 3 water layers were completely developed in the interlayer (values around 1.85 nm). For water contents below ~38%, the basal spacing increased with the water content, but for higher values the basal spacing was quite constant, irrespective of the water content, which was also observed in the samples from the MGR tests.

### 5.1.5 Conclusions

The hydro-mechanical evolution of a two-component bentonite buffer material – low density pellets mixtures and higher density compacted blocks – was studied by CIEMAT by means of a series of laboratory hydration tests performed under isochoric conditions. The tests were performed in a large-scale oedometer (10x10 cm) and in a transparent cell (12x12x2 cm) with FEBEX bentonite, and in a thermo-hydraulic cell (15x15 cm) with MX-80 bentonite. In the first case the axial pressure was measured on the sample surface opposite to hydration, whereas in the test with MX-80 bentonite, radial pressures and relative humidity were measured at different locations. In most tests hydration took place through the pellets part, but the effect of hydrating through the block was also checked. As well, tests were performed either under a low water injection pressure or under a low water inflow rate.

The analysis of the results obtained allowed to draw the following conclusions:

- Because of their low density and large macroporosity, hydration through the pellets was initially quick, even though the water injection pressure was very low.
- The way of hydration conditioned the water intake and the pressure development kinetics. Slow hydration (e.g. under a controlled low flow of through the block) delayed the start of pressure development, but allowed higher pressures to be reached for lower overall degrees of saturation. The reason could be the longer time available for water redistribution from the macropores to the microstructure (particularly the montmorillonite interlayer), which would be the responsible for swelling. The interplay between the different strengths of the two components may also be a relevant factor on the axial load measured at the first stages of saturation.
- Irrespective of the way of saturation (constant flow or pressure), the pressure development (both axial and radial, away from the hydration surface) was not continuous. After a first sharp increase (which was quicker under constant pressure), there was an intermediate period of pressure stabilisation. Only when the overall degree of saturation was very high, the pressure increased again until its final equilibrium

value. This pressure development pattern had been previously observed also in samples of compacted bentonite and of pellets.

- The stress measuring devices reflect local stresses which are conditioned by the local dry density. Hence, when the block part was on top, the final pressure value of the saturated sample was higher than the value expected for smaller samples of bentonite compacted at the same average dry density. When the pellet part was on top, the contrary happened. Friction between the bentonite and the cell steel wall could also contribute to these differences. This research has put forward the necessity of using testing devices in which pressure can be measured at different locations to correctly assess the stress state of inhomogeneous samples.
- Bentonite water content and dry density gradients were observed at the end of the tests. For a given hydration rate they were dependent on the hydration time and, although they attenuated over time, they persisted even after full saturation was reached. Saturation under very low water inflow rate (either imposed or resulting from the low permeability of the block part when saturation took place through it) resulted in more uniform water contents and smoother gradients, also in terms of pore sizes.
- In contrast, the microstructure of the bentonite in the two components was very different even after full saturation. Despite of the drastic reduction in the volume and size of macropores in the pellets parts, they continued to be higher than in the block part and consequently the  $e_m/e_M$  was lower in the pellets part. The basal spacing of the smectite, which is an indication of the number of water layers in the interlayer, was higher in pellets samples than in block samples. However, an overall trend to pore size homogenisation towards smaller sizes over time was observed.
- The water content and dry density gradients were not affected by the pellets/block interface. After full saturation the pellets/block interface was impervious to gas.

The evidence provided by these experimental results along with the outcomes of the large-scale EB test, in which a similar two-component barrier was tested for 10.5 years, suggests that, although the initial heterogeneity of the barrier system and the deformations induced in the first stages of saturation tend to attenuate over time, residual inhomogeneities will persist and remain even after full saturation. The kind and extent of these heterogeneities will depend on the initial and boundary conditions of the barrier.

## **5.2 Stress field evolution and final state of heterogeneous samples saturated under isochoric conditions (CEA)**

### **5.2.1 Objectives and methods**

The objective of this series of tests is to investigate the resaturation in isochoric conditions of initially heterogeneous samples of MX-80 bentonite in controlled conditions. Although the heterogeneities in terms of dry density and water content are characterized only in a post-mortem way (in the final state of the experiment), the swelling pressure field development upon saturation (and heterogeneities) is assessed using an array of sensors at various spatial locations. The test cases are chosen so that a simple geometry and boundary conditions are ensured as well as, for example, comparable average dry density, so that effects of the type of heterogeneity can be more readily assessed.

A multi-sensor cell was designed for this purpose (Figure 5-43). The device is essentially an oedometric cell of diameter 57 mm equipped with 9 pressure sensors (total pressure or interstitial pressure) at 3 vertical positions (6.6 mm, 23.3 mm and 40 mm) and angular positions (0°, 90° and 180°). These sensitive elements are 9 mm in diameter. Moreover, 3 thermo-hygrometers are positioned at 270° and the same vertical positions. The cell is also equipped with continuous measurement of the axial pressure and displacement (top lid only) and injected water mass. Water is injected with a very small hydraulic head of 60-70 cm through porous plates on the bottom side (and/or the upper side) of the chamber, blocked at approximately zero displacement. In the case of unilateral hydration the other side is placed at laboratory conditions (atmospheric pressure, relative humidity of the room) to ensure evacuation of entrapped air.

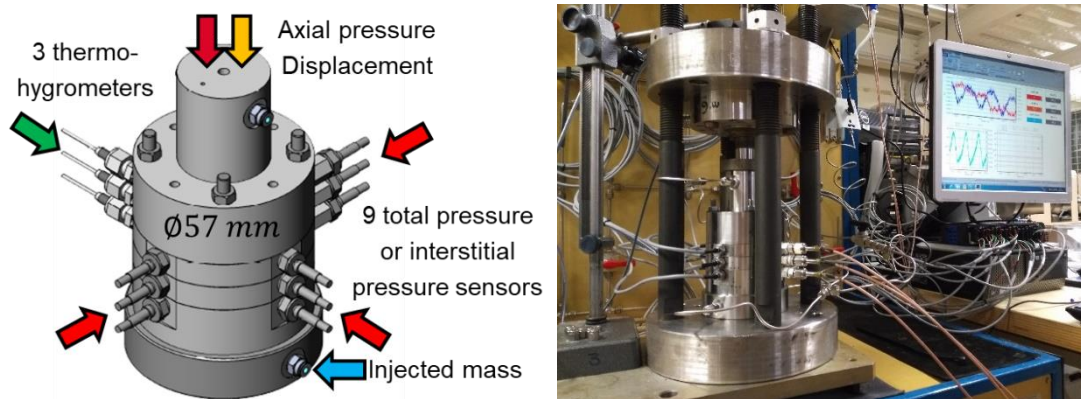


**Figure 5-43. Schematic of the multi-sensor cell and photograph of the experimental apparatus**

### 5.2.2 Investigated test cases and global measurements

The investigated test cases are summarized in the schematics below. Tests 1 and 2 are carried out on pellet/powder mixes arranged to minimize macroscopic gradients by building layer by layer dense arrangements of pellets with a fraction of powder (obtained from crushed pellets) filling the inter-pellet gaps. Tests 3 to 6 are obtained by stacking blocks (for high density) or powder (for low densities). Table 5-8 and Figure 5-44 give the main features of the different tests. All the sample were wetted using site water (excepted TOMO\_3 wetted with distilled water) injected through the bottom face (excepted C\_2 wetted through bottom face and top face).

C\_1 and C\_2 tests implying a mix of pellets and powder are similar. They differ by their hydration mode (one or two-sided). C\_3 test is based on the assembly of two different components: one high-density block and a filling with powder. C\_4 and C\_5 tests were made of two stacked blocks (one with low dry density, the other with high dry density). Considering C\_4 the water is introduced in front of low-density region. For the C\_5 test the order was reversed and above the low-density region the axial heterogeneity is increased by an axial small gap at the top of the sample. Comparing these two experiments will enable us to evaluate the influence of the density of the backfill place in front of the water source. The C\_6 sample was made of a compacted block placed in the cell with a radial gap but hydrated axially by one face. A very small quantity of powder was introduced in the gap to avoid fast intrusion of water into the void.

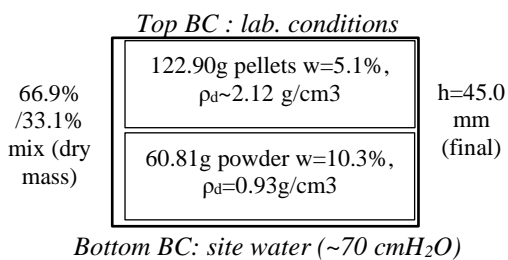
The goal of the experimental plan is to examine the separate effects of the initial heterogeneity types (pellet/powder or pellet only assemblage, compacted blocks, compacted blocks combined with granular material). The effects of the average dry density and density gradient are investigated. Test 3 with a very large density gradient was saturated in a discontinuous manner by injecting small amounts of water until a local pressure sensor reaches the value near 10 MPa (in order not to damage the sensors). Its interpretation is then mostly qualitative since the hydration history is not well known.

Global measurements (total injected water mass and axial (top lid) swelling pressure are presented below (Figure 5-45). Relative humidity at three different heights and temperature are shown further down in Figure 5-47. The final swelling pressure values do not show a simple correlation with the sample properties; indicating that this parameter largely depends on the hydromechanical history for these different assemblages.

**Table 5-8. Main features of the samples tested in a steel multi-sensor cell or in a PEEK cell for X-CT measurements**

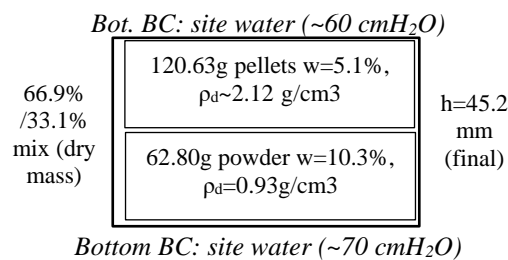
Test	H_initial	H_final	$\rho_d$ initial average	W pellets	W block/powder	Composition Bottom/Top	Densities Bottom/Top
	(mm)	(mm)	(g/cm <sup>3</sup> )	(%)	(%)		(g/cm <sup>3</sup> )
C_1	44.93	45.02	1.501	5.1	10.3	Mix pellets/powder	1.501
C_2	45.13	45.23	1.491	5.1	10.3	Mix pellets/powder	1.491
C_3		44.20	1.511	No	10.3	High density block / Powder	1.990 / 0.975
C_4	50.12	50.24	1.480	No	10.3	Low density block / high density block	1.397 / 1.561
C_5	53.37	53.48	1.408	No	10.3	High density block / low density block /axial gap	1.570 / 1.406 / 0.0
C_6	45.68	45.82	1.527	No	7.44	Block with radial gap	1.750
TOMO_1	33.2		1.500	5.1	5.35	One pellet-D32/powder	1.500
TOMO_2	28.2		1.519	5.1	10.3	Mix pellets/powder	1.519
TOMO_3	27.15	28.15	1.365	No	5.80	Powder	1.365

BEACON\_C 1



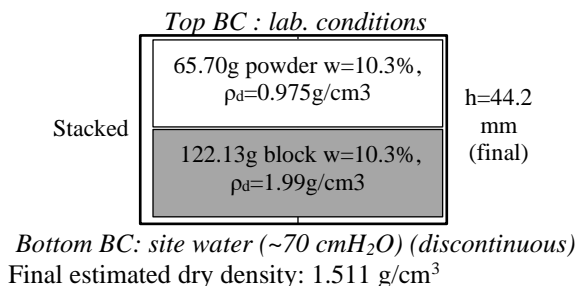
Final estimated  $\rho_d$ : 1.498 g/cm<sup>3</sup>

BEACON\_C 2

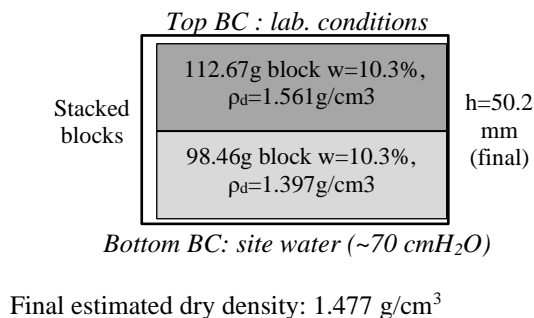


Final estimated dry density: 1.488 g/cm<sup>3</sup>

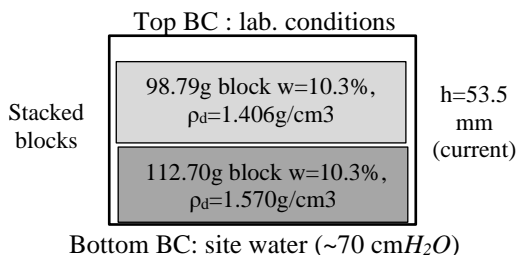
BEACON\_C 3



BEACON\_C 4



BEACON\_C 5



BEACON\_C 6

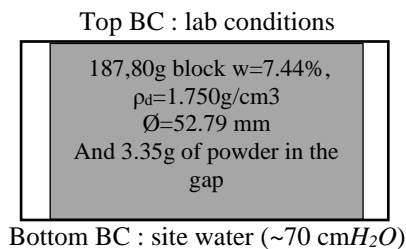
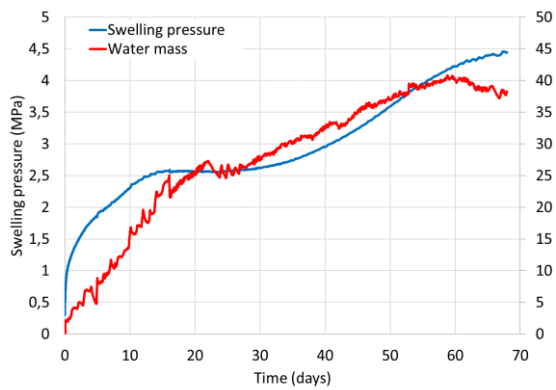
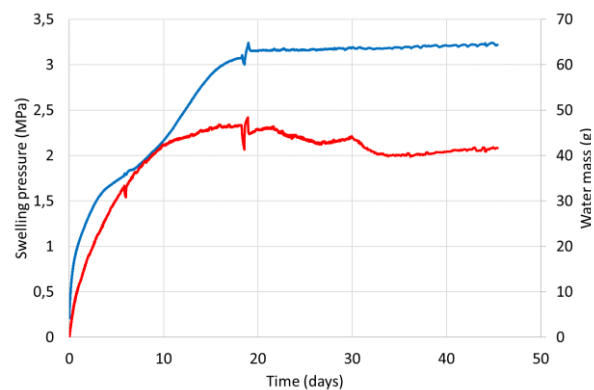


**Figure 5-44. Samples resaturated in the multi-sensor cell**

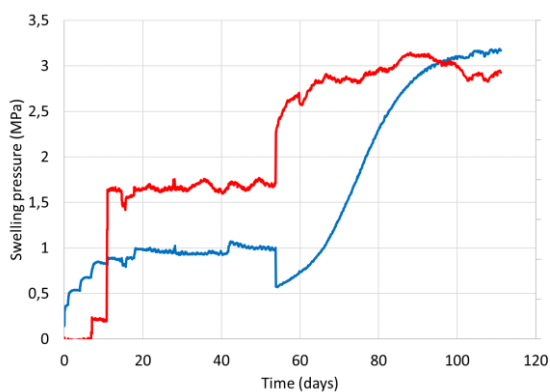
BEACON\_C\_1



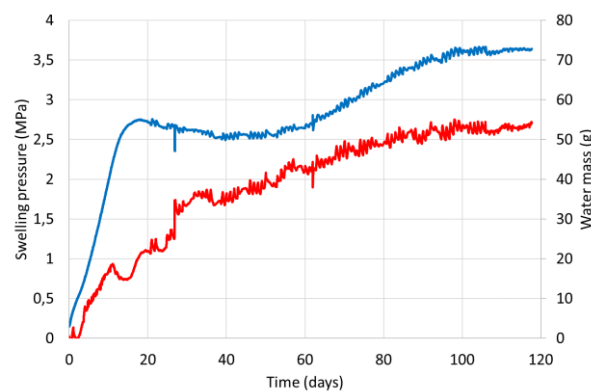
BEACON\_C\_2



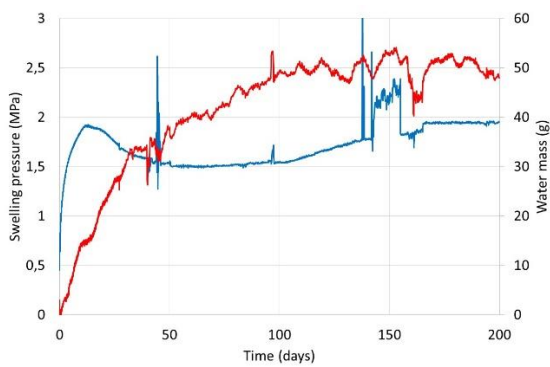
BEACON\_C\_3



BEACON\_C\_4



BEACON\_C\_5



BEACON\_C\_6

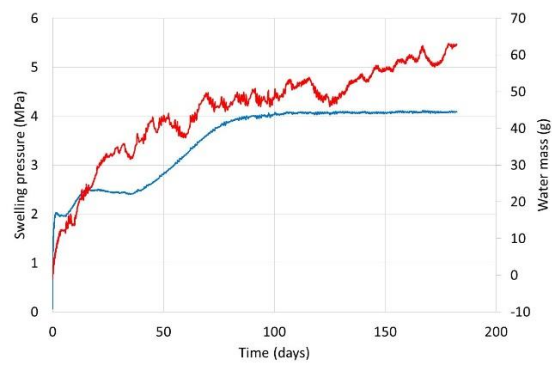


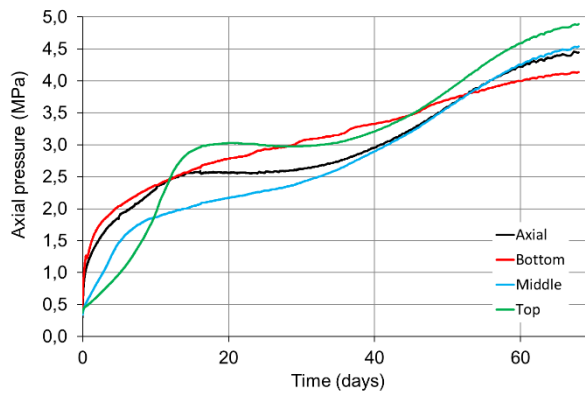
**Figure 5-45. Total injected water mass (red line) and axial swelling pressure measurements (blue line)**

**5.2.3 Stress field evolution**

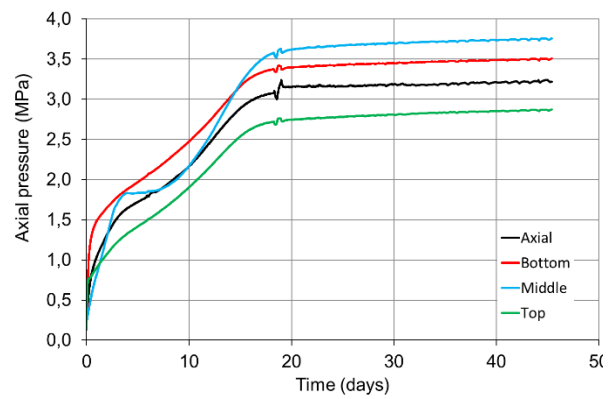
Radial total pressures averaged between the three sensors at the same vertical position (noted bottom, middle, top) are presented below (Figure 5-46) and compared to the axial (top lid) swelling pressure. Single sensor responses are omitted for brevity and are available upon request. A first observation is the similarity of pressure measurements between the average of top radial sensors and the upper axial sensor, especially close to saturation: this seems to indicate an isotropic stress state; small discrepancies are easily explained by the dispersion in local measurements and the different measurement locations. Very high stress heterogeneities

can be observed at early stages of hydration for compacted blocks, where the effect of friction appears more important; swelling pressures at the sample bottom are very partially transmitted to the upper regions. The pellet/powder arrangements do not show such high stress gradients and the effect of friction is much less predominant.

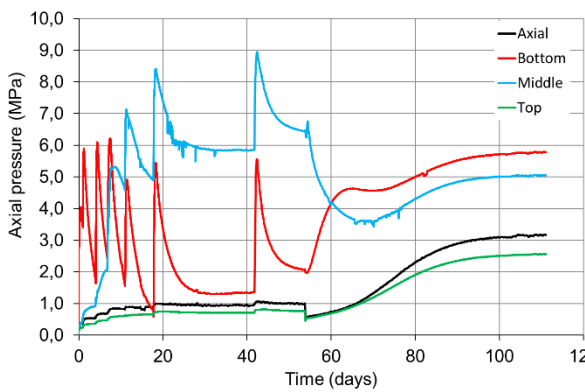
BEACON C 1



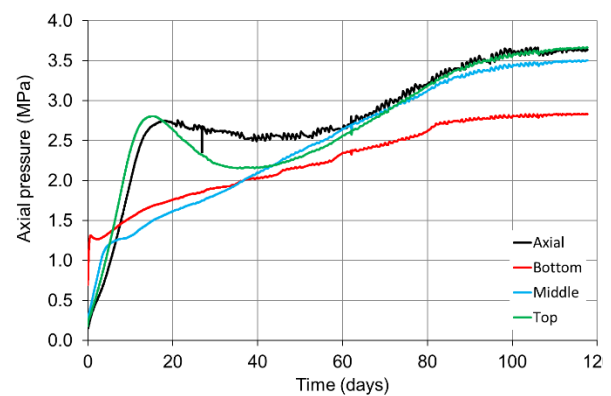
BEACON C 2



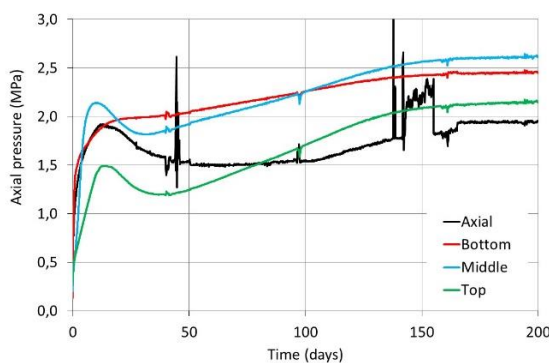
BEACON C 3



BEACON C 4



BEACON C 5



BEACON C 6

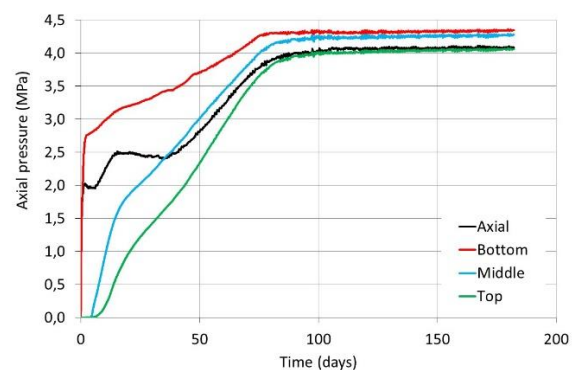


**Figure 5-46. Local stress measurements averaged per height (3 sensors) compared with the axial pressure measurement**

Tests 1, 2 and 4 can be reliably compared since the average parameters of these samples are approximately equal. They differ by the type of hydration (one or two sided) and the type of heterogeneity (pellet powder and stacked blocks). The usual collapse is observed at some point of the hydration process although much more pronounced for the compacted blocks, and only in the regions far from the hydration front; these regions always have higher final swelling pressures.

For pellet-powder samples the hypothesized scenario is that

- The first stages of the hydration process form a saturated low-density region that controls water transport,
- The swelling pressure of this area induces a compaction of far regions (relatively low friction of the granular material allows for rearrangements, filling to macrovoids, etc.),
- At some point the hydration of these far, overly dense areas exerts a sufficient swelling pressure to cause a recompaction of the regions close to the hydration front.

For the blocks the process could be different because of higher initial stiffness, friction and the existing heterogeneity (large top density).

Test C\_3 shows the effect of discontinuous hydration on a very heterogeneous sample (each pressure peak corresponds to a small amount of injected water). The method allowed to progressively release the large stresses in the very dense bottom region by wetting/drying cycles. These cycles seem to accelerate hydration of the upper regions maybe via drying damage acting as channels through the lower areas. The results of test C\_3 are difficult to analyse because of the complexity of the hydration process that leads to a complex succession of drying-wetting cycles.

For all the tests (except for C\_3 where the hydration is discontinuous), the evolution of relative humidity is monotonic (Figure 5-47). The bottom sensor rapidly shows an increase of relative humidity, followed by middle and top sensors. For C\_2 test hydrated by the two faces, the bottom sensor and the top sensor give the same response at the same time. Generally speaking, there is little delay between the responses of the middle and top sensors. The value given by the sensor at the top, when it reaches 100%, indicates clearly the moment when the sample is completely saturated, correlated with the stabilisation of the water mass injected in the sample. In most cases, the hygrometer, even far from the hydration source, is very sensitive to the water inlet.

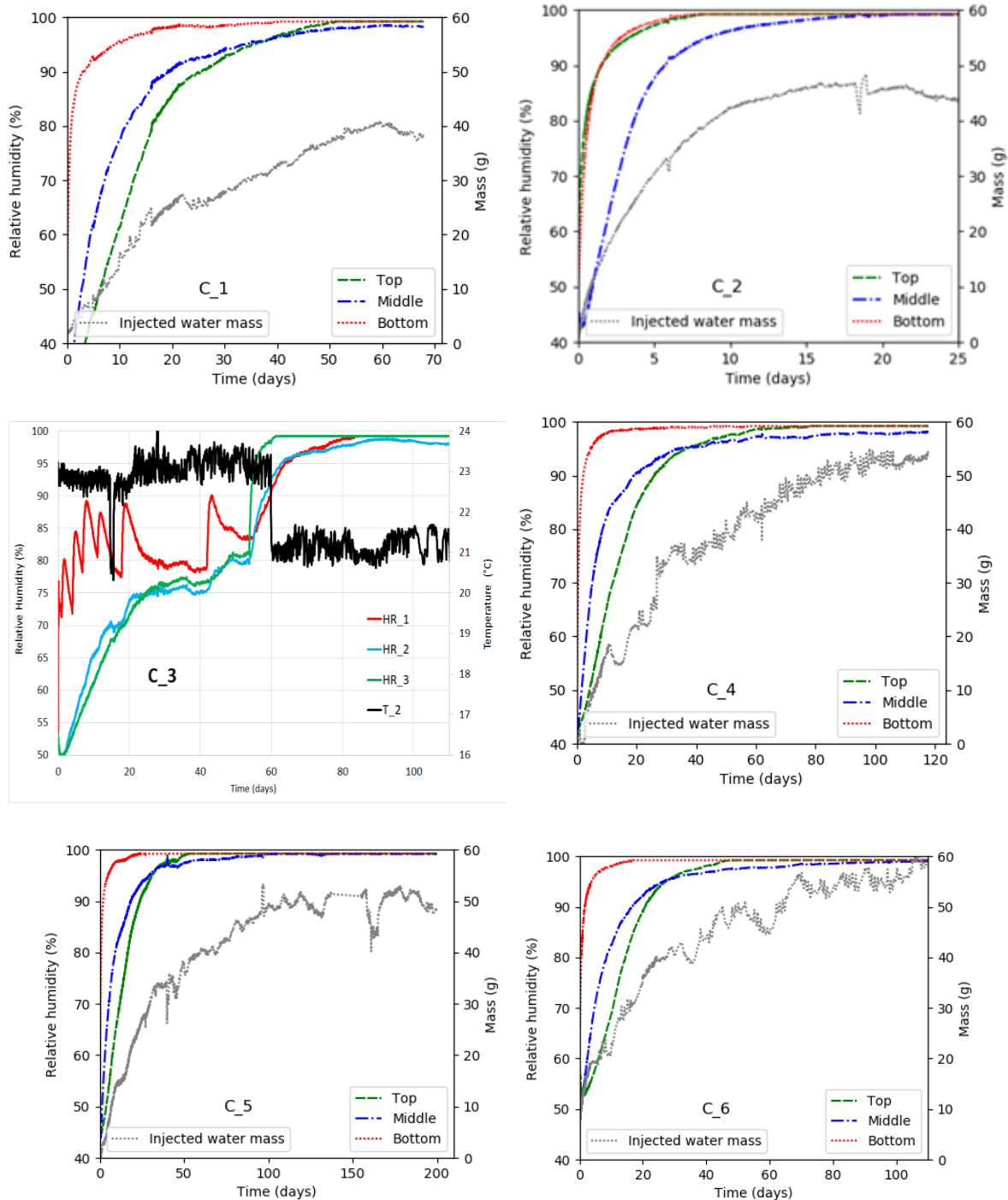


**Figure 5-47. Local Relative Humidity measurements during the hydration phase**

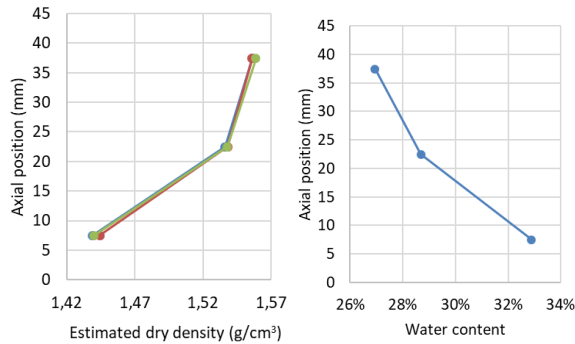
**5.2.4 Characterization of the final states**

Final states have been characterized by cutting samples into 12 equal subvolumes corresponding to positions in front of sensor ports, except with test 4 where the sample also was split along the former block interface (mid section). Water content measurements are carried out using treatment at 105°C for 24h; apparent density measurements are carried out using

hydrostatic weighting in mineral oil. Dry density and water content measurements at dismantling are presented for each sample below (Figure 5-48).

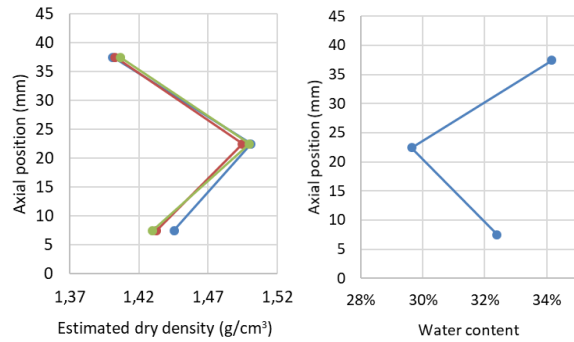
**BEACON C 1**

Av.  $\rho_d=1.511 \text{ g/cm}^3$ ,  $W=29.5\%$  ( $S=95.8\%$ )



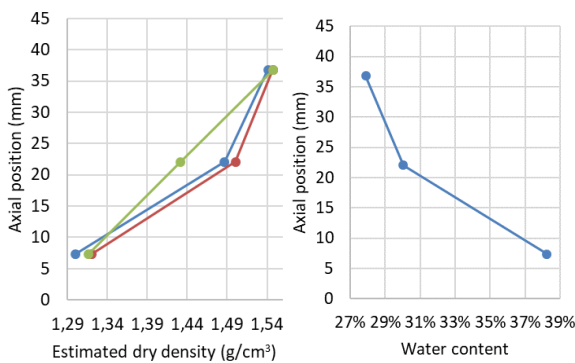
**BEACON C 2**

Av.  $\rho_d=1.446 \text{ g/cm}^3$ ,  $W=32.1\%$  ( $S=102.6\%$ )



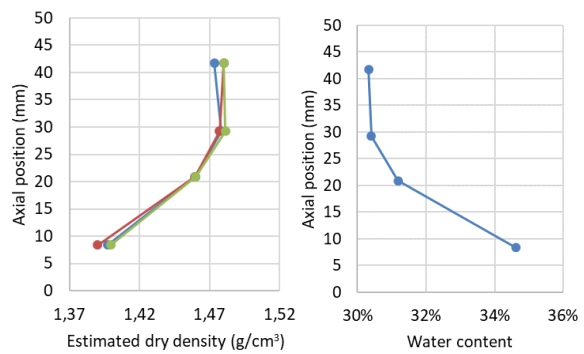
**BEACON C 3**

Av.  $\rho_d=1.444 \text{ g/cm}^3$ ,  $W=32.0\%$  ( $S=106.1\%$ )



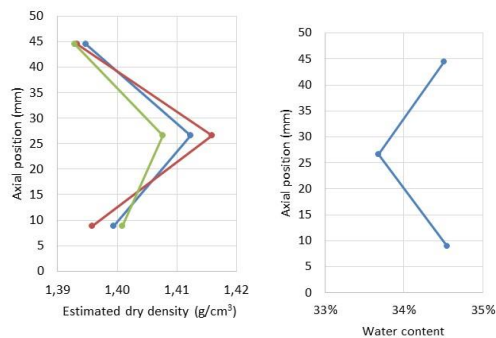
**BEACON C 4**

Av.  $\rho_d=1.453 \text{ g/cm}^3$ ,  $W=31.8\%$  ( $S=100.1\%$ )



**BEACON C 5**

Av.  $\rho_d=1.401 \text{ g/cm}^3$ ,  $W=34.24\%$  ( $S=97.2\%$ )



**BEACON C 6**

Av.  $\rho_d=1.491 \text{ g/cm}^3$ ,  $W=30.22\%$  ( $S=101.6\%$ )

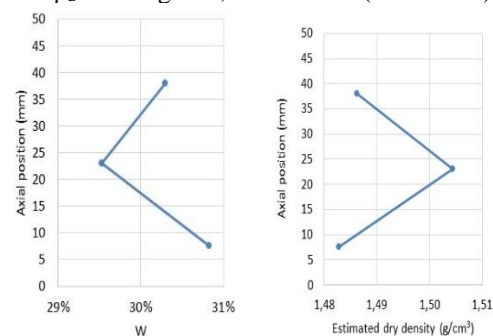


**Figure 5-48. Local dry density and water content measurements**

All final states show similar qualitative features compatible with the observations made previously: a vertical density gradient is observed in the direction of hydration, inversely correlated with water content. In test C\_3, the final density gradient is actually inverted compared to the initial state and is therefore the result of the hydration process and not residual heterogeneity.

Density and water content profiles are presented in Figure 5-49. Vertical positions were normalized to the final height in order to compare very different samples (C\_1 to C\_6, Tomo\_3, C\_3 is not represented). The existence of density gradients in the direction of water flow was observed predominantly for the granular materials (TOMO\_3, C\_1 and C\_2). The C\_4 sample exhibits also a large dry density gradient that may be explained by large bottom porosity allowing initial free swelling in this area. The C\_5 sample initially made with 3 different densities reached finally a homogenous density and water content state, probably because the weak density of the top part allowed the bottom part to swell and progressively provoked an increase of the density of the top part. Considering the C\_6 sample, the swelling was allowed mostly in the radial direction and did not induce significant axial heterogeneities of the final state. Radial stress as a function of local dry density is shown in Figure 5-50.

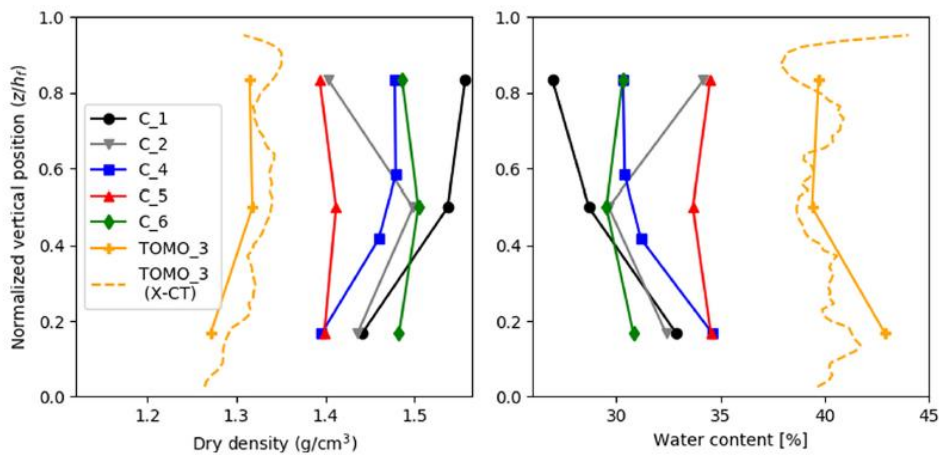


**Figure 5-49. Final dry density and water content profiles for tested configurations. Vertical position in normalized to 1 for comparison**

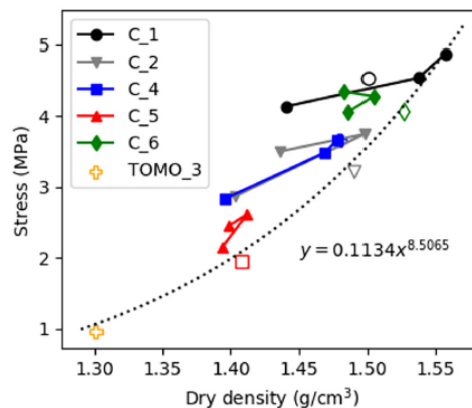


**Figure 5-50. Radial stress vs local dry density (full symbols, probably under-estimated) and axial stress vs average dry density (empty symbols), the dotted line corresponds to a pellets-powder MX-80 power-law fit**

Mercury Intrusion Porosimetry (MIP) measurements were performed on freeze-dried samples taken from tests 1 and 2 and presented below (Figure 5-51), compared with MIP results obtained on pure pellets and pure powder. It mainly shows:

- A main 17 nm mesoporosity characteristic of the intra-aggregate spacing, which appears lower in the injection area,
- A 200 – 400 nm mesoporosity, largely more represented in the injection area,
- A large porosity characteristic of thin microcracking in pellets at 5-10  $\mu\text{m}$ , absent in powder. Larger cracking is observed on freeze-dried samples after hydration up to 50  $\mu\text{m}$ ,
- Intergrain and interpellet spacing starting at approximately 70  $\mu\text{m}$  up to the upper limit of the MIP technique.

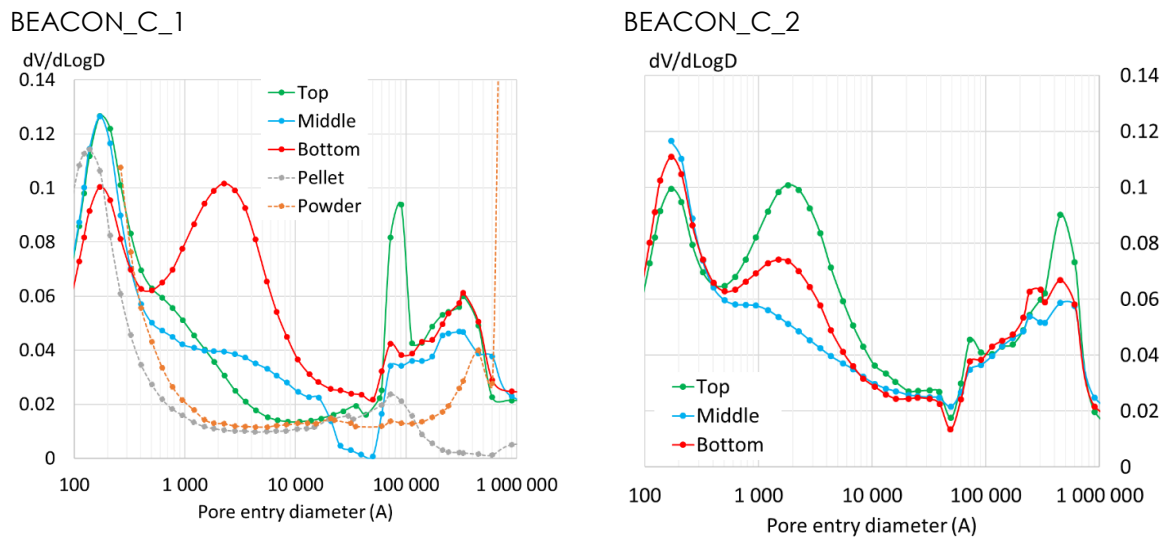


**Figure 5-51. MIP characterization of several samples in tests 1 and 2**

## 5.2.5 Conclusions and perspectives

### 5.2.5.1. Analysis of the hydro-mechanical behaviour of the different experiments

A first analysis of dual density systems resaturated in 1D at constant volume in an instrumented cell has been carried out. Heterogeneities in the final state have been observed which are due mostly to the hydromechanical scenario, due to the coupling between differential stiffness, swelling pressure, friction coefficient and transport properties in several parts of the sample at different suction levels. The dry density gradient observed is qualitatively similar to the REM\_MM experiment (provided as WP3-5 test case 1b) on larger dimensions and time scales.

Considering the evolution of the swelling pressure versus time, all the experiments exhibit a non-monotonous evolution of the axial swelling pressure and of the radial swelling pressure. On the contrary, the thermo-hygrometers provide a monotonous evolution of the relative humidity. The stress state is greatly influenced by local swelling and collapse processes coupled with the moisture transfer through the sample. Considering the high-density areas, the friction along the cell wall adds a degree of complexity.

### 5.2.5.2. Perspectives and improvements suggested for new experiments

In future steps, other types of heterogeneities will be investigated by varying the hydration conditions, average dry density, density gradient and geometry of these dual density systems. Interrupted tests may enable to have access to an intermediary unsaturated state.

Mix of pellets and powder. Understanding the hydro-mechanical behaviour of this kind of mixture is of great importance because it probably will be used to plug boreholes and to fill up the gaps between the EBS made of compacted block and the wall of the galleries. The C\_1 and C\_2 tests differing by the hydration mode (one or two-sided hydration) clearly show the impact of the hydration length on the saturation time. It will be worth checking if that behaviour could be observed with very long sample, for example with a hydration length about 100 mm or more. The main drawbacks when very long sample are studied consist in for one part of the time required for the complete saturation, and for the other part the role of the friction along the cell wall that disturbs the stress evolution especially for small diameters. C\_1 and C\_2 experiments also show that the area saturated at the end of the experiment (far from the hydration source) have the highest dry density. For future experiments, two aspects have to be investigated:

1. The impact of the average initial dry density on the hydration kinetics, and also on the hydro-mechanical behaviour of the mix. The dry density must be chosen between 1.4 and 1.5 g/cm<sup>3</sup> in the realistic range of dry density available for EBS and plugs.
2. The impact of the hydration rate on the final homogenization of the sample. In this work like in many studies the bentonite samples are saturated with liquid water supplied in excess compared to the amount really absorbed by the sample. A quantity of water restricted compared to the flow necessary to hydrate the sample (for example only a half or a quarter of that amount) could lead finally to a different homogenization state. Some teams started to study that interesting subject.

Assembly of blocks with different dry densities. Clearly the dry density of the block or the layer directly in contact with the hydration source influences the transfer of water to the other parts of the bentonite sample. C\_5 test needs a long time to get fully saturated because of the low permeability of the bottom block (high dry density). On the contrary the C-4 experiment needs approximately half-time to get fully saturated. From a realistic point of view, the less compacted parts of the EBS will be in contact with hydration source, and probably will be made of a mix of pellets and powder to fill up the remaining gaps. The most densified parts of the EBS will be placed far from the hydration source.

The future studies need to focus on one type of configuration: a) a low-density area in front of the hydration source, made of a low-density block or a mixture of pellets and powder, or a low-density powder and; b) a high-density area made of a compacted block. The experimental survey will provide more interesting data if the swelling pressure would be measured in two or more level of each area of interest (the low-density zone, and the high-density zone). Regarding the present work, it implies a modification of the device by adding at least two levels of sensors along the sample.

Amid the different parameters to consider for future experiments, some of them need a particular insight:

- The influence of the height and the dry density regarding a homogenous mixture of pellets and powder;
- The influence of the hydration rate for the same type of sample. That means hydrating the sample with a water flow less (1/2 or 1/10) that the flow "naturally absorbed" by the sample when liquid water is supplied with a water column with a constant level.

- The influence of the gradient of density regarding a sample made of two areas with different densities. Considering the same values for either the low-density zone and the high-density zone, it would be interesting to compare two kinds of material to make the low-density area, for example for one hand a mixture of pellets and powder and for the other hand a slightly compacted block. In that configuration, it seems better to place the low-density area in front of the water source.
- The impact of the respective heights of the low-density area and the high-density area on the hydro-mechanical behaviour of the sample.

### **5.3 X-ray tomographic imaging of pellet/powder mixes saturated under isochoric conditions (CEA)**

#### **5.3.1 Objectives and methods**

The goal of in-situ X-ray tomographic imaging (X-CT) of the resaturation of these heterogeneous bentonite assemblies is to provide qualitative and, if possible, some quantitative information on the hydromechanical processes happening inside cells. Indeed, it could provide access to:

- Displacement fields (of solid), through the use of image correlation techniques, providing insights into mass transport of clay and therefore into the homogenization/creation of heterogeneities,
- Water content field, through the use of properly calibrated CT gray levels and displacement fields,
- Dry density fields, through the same analysis.

Through these measurements, access to the global 3D phenomenology of a test as a function of time, such as:

- Evidence of friction phenomena,
- Information on the macroporosity at a scale above several microns and its evolution (interpellet porosity, cracks),
- Etc.

For this purpose, a dedicated experimental apparatus ("Tomobento\_1") has been designed (Figure 5-52), which allows unilateral hydration of bentonite at approximately constant volume, axial swelling pressure measurement and X-ray imaging. It is composed mainly of a PEEK (PolyEtherEtherKetone) cell of internal diameter 57 mm with PE porous injection/exhaust ports, and a standard 25 kN load cell with a spherical contact and displacement locking.

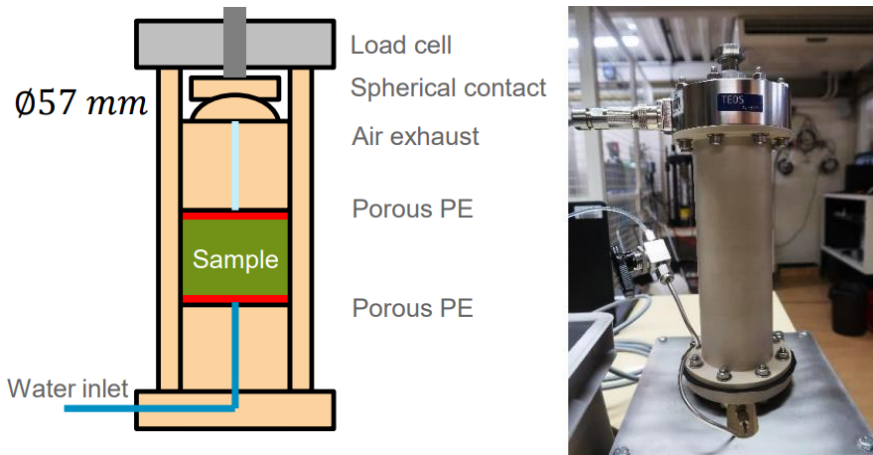


Figure 5-52. Schematic of the “Tomobento\_1” cell and photograph of the experimental apparatus

### 5.3.2 Testing and improvements

#### 5.3.2.1. Experiment TOMO\_1 (Tomobento\_1)

A first validation test (Figure 5-53) was carried out on a single 32 mm pellet sample surrounded by MX-80 crushed pellet powder already used in tests 1 and 2 presented previously. The sample was resaturated using pure water during 44 days and disconnected from their water source for approximately 1h for CT scans (Figure 5-54) carried out at 0h, 1h, 22h, 45h, 6 days, 13 days, 21 days, and 43 days. These correspond to specific time scales on the swelling pressure kinetics. The CT scan was acquired with a GE Phoenix v | tome | x m instrument at 200 kV/185  $\mu$ A and 37  $\mu$ m per pixel using standard cone beam acquisition and reconstruction. As a first approach, gray values were calibrated relatively to each other using a low absorption reference (PEEK) and an internal dense particle (accessory mineral).

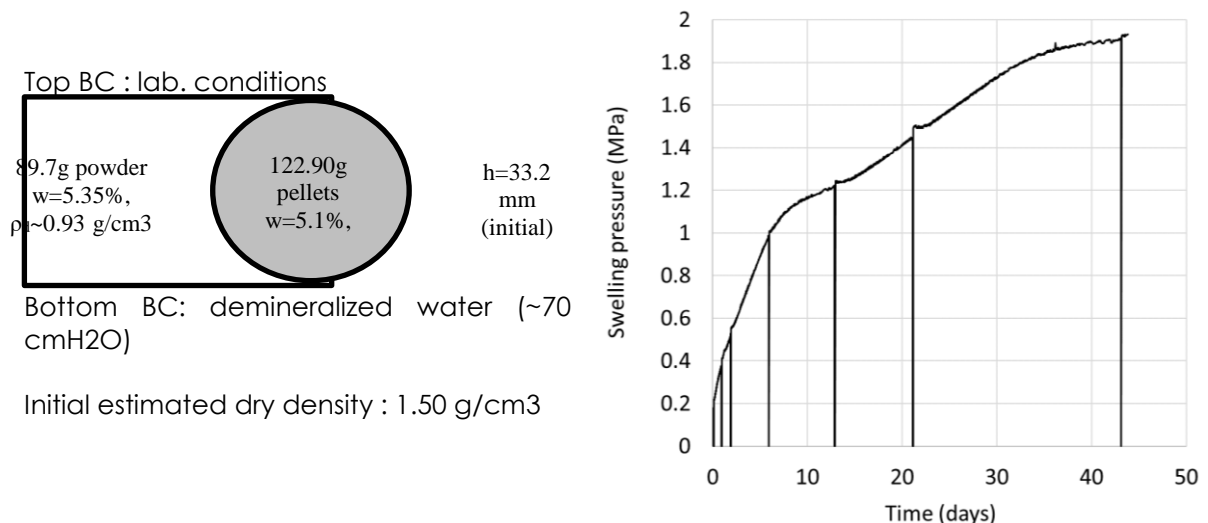
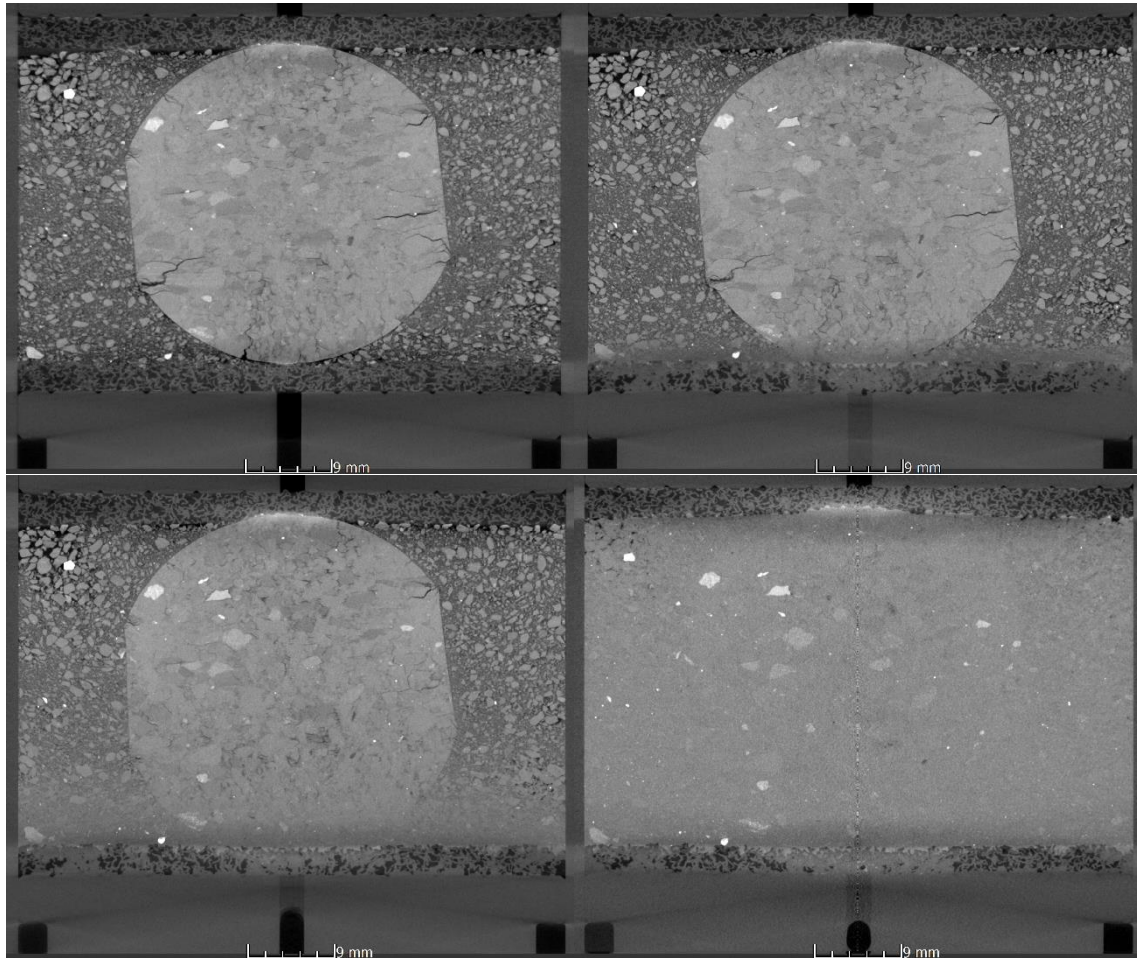


Figure 5-53. TOMO\_1. Sample properties and swelling pressure curve (straight lines indicate X-CT scans)



**Figure 5-54. Vertical slices of the Tomobento\_1 sample at 0h, 1h, 45h and 43 days**

First qualitative observations on this test are:

- A confirmation of the rearrangement and compaction of the powder in the upper regions, and closing of the technological voids due to the initial swelling phase,
- Cracking in the pellet in the area of large humidity gradients, beyond the water front,
- The quick formation of a dense saturated layer controlling transport,
- The reaching of a homogeneous state relatively to X-CT as seen on the final scan.

However, some limits of this method are evidenced, and modifications implemented:

- Large transformations of the material exclude easy displacement measurements by Digital Volume Correlation (DVC) techniques. The mixing with powder of dense marker particles (ZrO<sub>2</sub>) at the scale of 200 µm in diameter allowing the use of particle tracking algorithms.
- Cone beam artefacts induce gray values not representative of the material true absorption in the top and bottom ends of the sample. The use of helical tomography can be used since it is devoid of cone beam artefacts.

### 5.3.2.2. Experiment TOMO\_2 (Tomobento\_2)

This test (Figure 5-55) validates the choice of marker particles and the moderate level of artefacts (Figure 5-56). Some issues with higher beam hardening levels can be solved by using higher tube voltage and additional beam filtering.

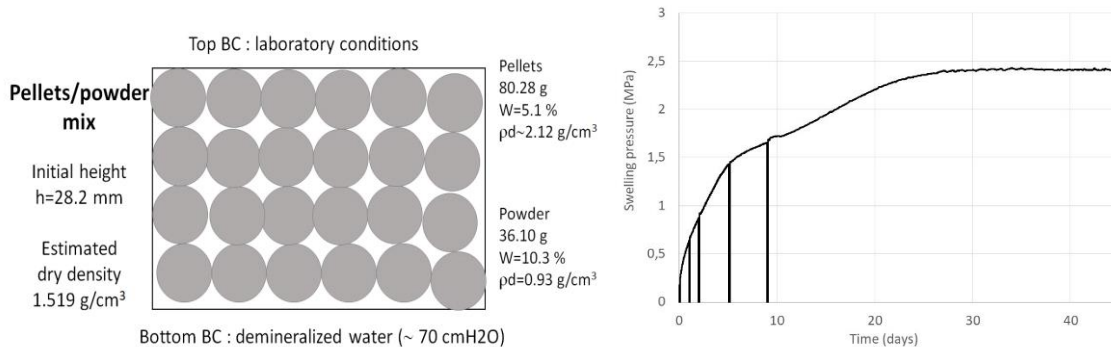


**Figure 5-55. TOMO\_2. Sample properties and swelling pressure curve (straight lines indicate X-CT scans)**

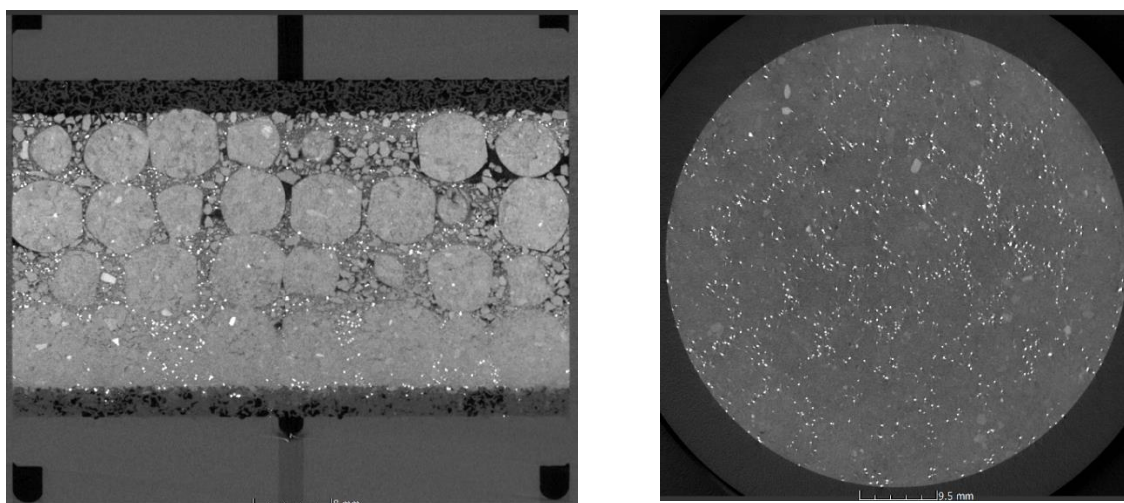


**Figure 5-56. Sample description, vertical slice, and horizontal slice at the midplane of the first pellet layer, for the Tomobento\_2 sample at 1-day hydration**

### 5.3.2.3. Experiment Tomo\_3 (Tomobento\_3)

A third experiment has been conducted on a homogenous sample made of bentonite powder only (in fact crushed pellets), with an initial dry density of 1.365 g/cm<sup>3</sup>. Marker particles with higher density have been incorporated to the sample.

This experiment shows a non-monotonic evolution of the swelling pressure (Figure 5-57). The signal interruptions on the swelling pressure measurements corresponded to the different X-ray scans made during the hydration phase. The value of the swelling pressure does not change after 30 days.

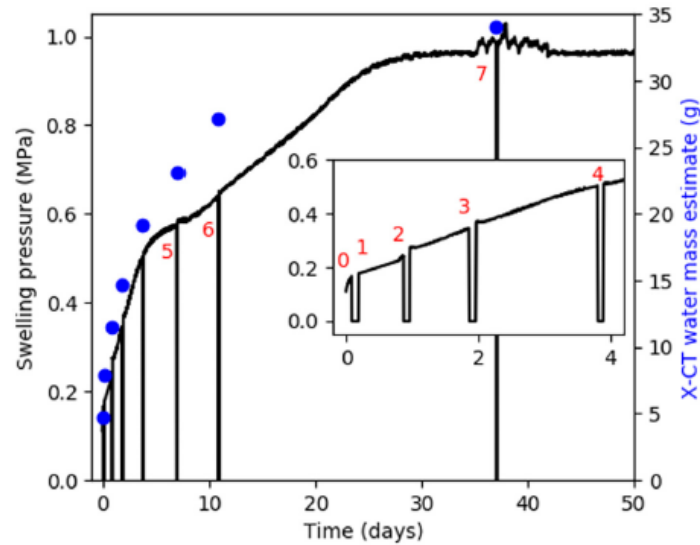


**Figure 5-57. Axial swelling pressure (top lid) measurements and estimation of the water mass absorbed by the sample (calculation from the X-CT images)**

CT scans (Figure 5-58) have been made at seven steps during the hydration phase (initial state and 0.19, 0.87, 1.86, 3.81, 7.02, 10.8 and 37.0 days after the beginning of the hydration). The experiment was stopped at 78 days. The initial image reveals local heterogeneities in the sample which was composed of large powder grains individually resolved and unresolved small powder grains, corresponding to several grey levels. In some regions it can be observed a segregation with a lack of fine powder between large grains. With the flow of water the material becomes homogenous. After 37 days the sample is homogenized. Marker particles clearly appear in all the slides.

Analysis of the results: The whole particle tracking and the grey level analysis procedure make possible the calculation of the 3D water content and dry density fields, as well as the z displacement field, at the different stages of the saturation process. The sample was analysed in an axisymmetric way and the fields were averaged over the angular coordinate theta. The evolution of each of these fields (dry density, water content and z displacement) is presented in the r,z plane (Figure 5-59). Concerning the dry density, the heterogeneity first increased in the vertical direction and finally decreased. The water content depended mostly on z, showing a flat hydration front. The z-displacement is strongly r-dependent because of the friction along the cell wall. Figure 5-60 presents the incremental evolutions of the water content and the dry density. They correspond to the averages over r and theta of the field variations between a time step t and a time step t+1.

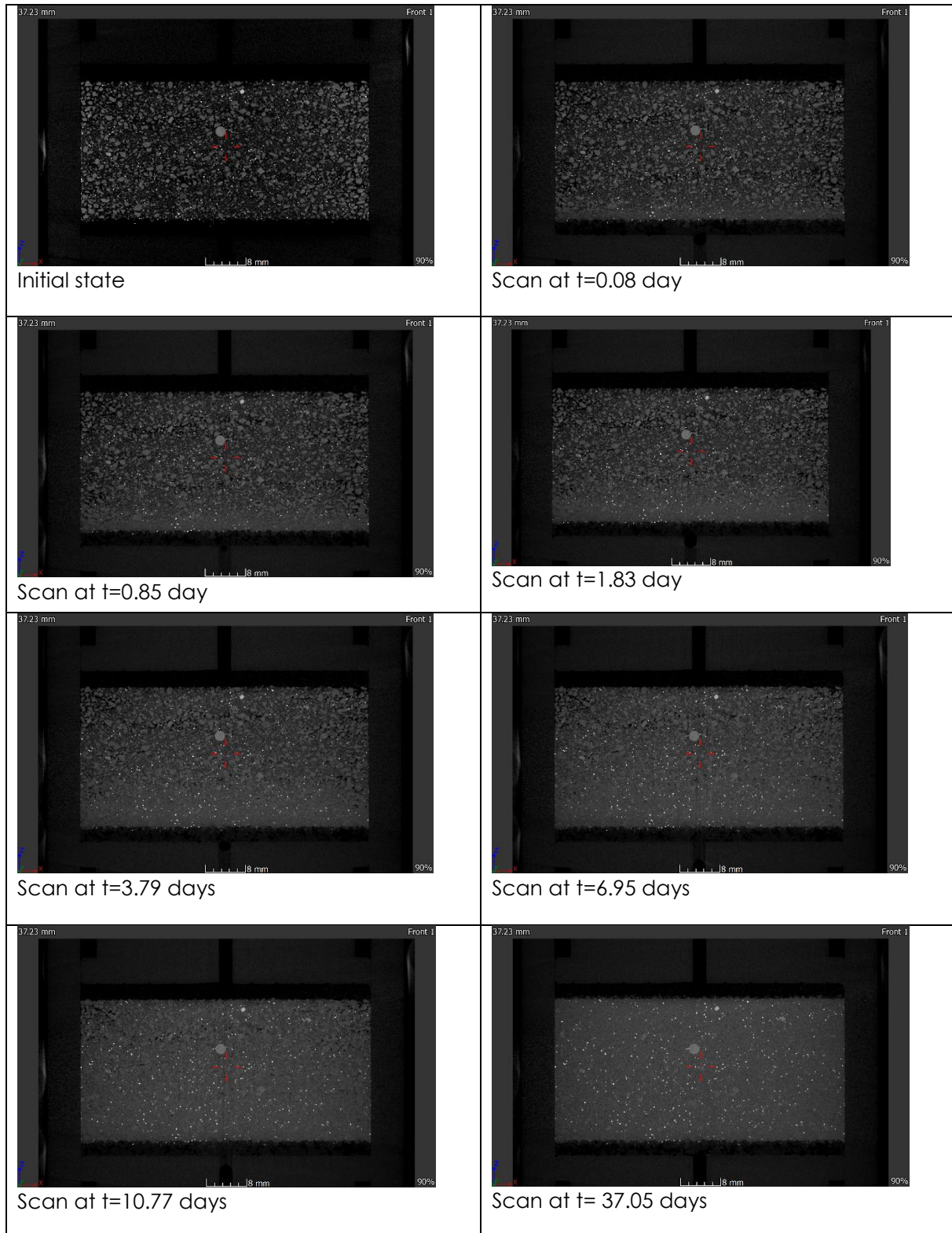


**Figure 5-58. Tomo\_3 experiment: successive X-CT scans**

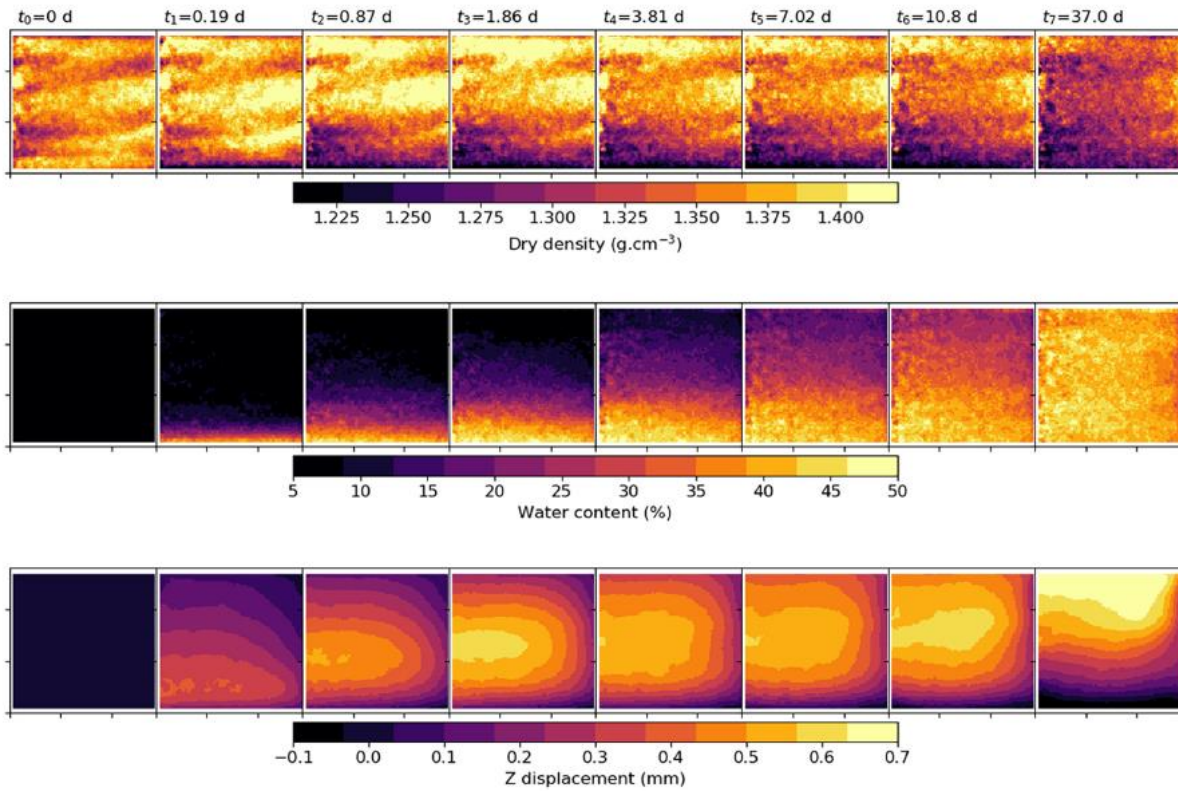


**Figure 5-59. TOMO\_3 experiment. Calculations of the fields of dry density, water content and z-displacement from the X-CT images**

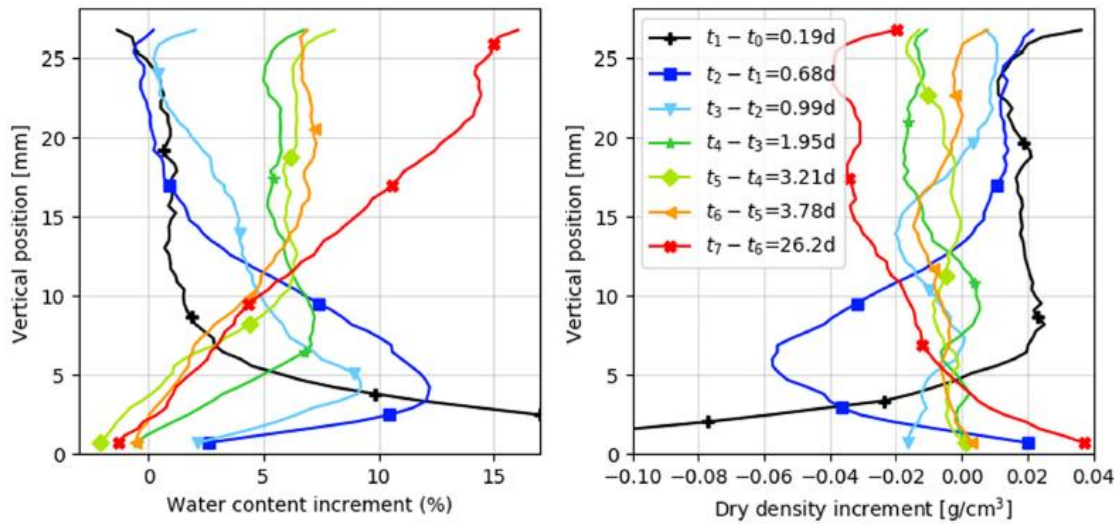


**Figure 5-60. Vertical profiles of the increments of the water content and the dry density between two successive X-CT scans**

### 5.3.3 Conclusions and perspectives

The use of X-CT to perform in-situ observations of the macroscopic phenomena in swelling tests of pellet/powder mixes is validated. The different stages of the homogenization process during the hydration phase are clearly showed. Concerning the TOMO\_3 test, further analysis of the images was made using marking-particles tracking and/or Digital Volume Correlation and a quantitative analysis of the grey levels. The fields of dry density, water content and z-displacement in the r,z plane were obtained at the different steps of the hydration phase (for each X-CT scan). The evolution of the dry density inside the sample is clearly shown. At the beginning the initial heterogeneity of the sample can be observed, because of the segregation of the fine powder particles during pouring. During the hydration phase, the heterogeneities increased in in the vertical direction and finally decreased, showing a reasonably homogenous sample, confirmed by the destructive measurements of dry density and water content at 3 different levels. The evolution of the field of water content along the hydration phase gives a good quantitative estimation. The fields of z-displacement calculated at different steps indicates a strong r-dependency of the z-displacement. The friction along the wall of the cell is clearly demonstrated.

## 6 Influence of the degree of saturation on the shearing behaviour at the bentonite – steel interface (EPFL)

### 6.1 Background

The objective of this experimental study was to determine the shear strength of bentonite in its hygroscopic state and to get insight into the shearing behaviour of bentonite-steel interface at various saturation stages. In order to investigate these processes, a series of direct shear tests were carried out.

### 6.2 Materials and methods

#### 6.2.1 Tested material

The tested material is MX80 bentonite in granular form, and it is described in section 1. Two granulometries (Fuller-type and unifrational) have been tested for shearing behaviour, these are shown in Figure 6-1.

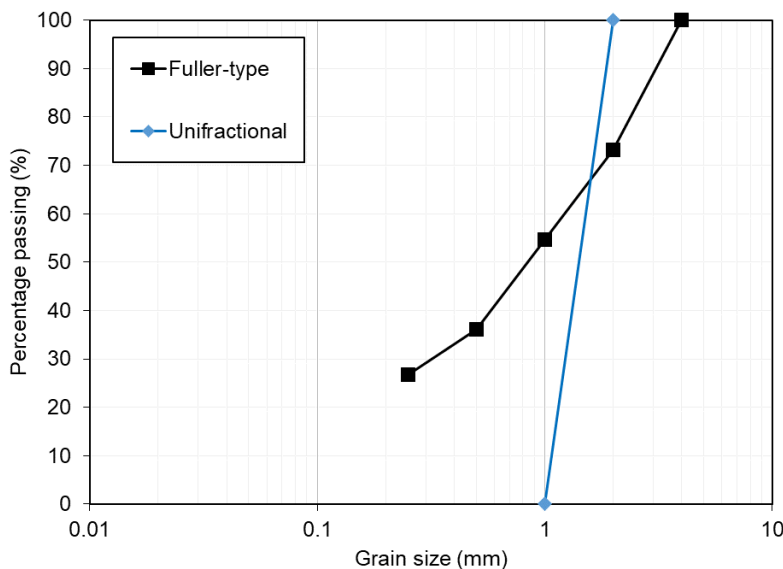


Figure 6-1. Grain size distribution of the tested samples

#### 6.2.2 Experimental setup

##### 6.2.2.1. Experimental set-up for the internal shearing

The tests of internal shearing were conducted using a commercially available direct shear device produced by GDS Instruments™.

Normal and shear forces can be controlled by two electromechanical force actuators, which can be used to pilot the tests in both displacement and force. Two load cells are installed to

measure the vertical and horizontal loads that are applied to the sample. To measure the horizontal and vertical displacements, two LVDTs (Linear Variable Differential Transformers) are used. The maximum vertical and horizontal force attainable is 5 kN, the maximum vertical displacement is  $\pm 12.5$  mm and the maximum horizontal displacement is  $\pm 25.0$  mm. The maximum vertical stress applicable is 2.47 MPa.

### 6.2.2.2. Testing set-up for the interface shearing

To investigate the influence of water content on the interface shearing, a shear box was equipped with a system allowing circulation of water in vapour phase through the sample under testing. The testing set-up is depicted in Figure 6-2. The lower part of the shearing box was replaced by a steel plate of dimensions 105 mm x 60 mm and a height of 16 mm. The roughness of steel plate surface is  $1.6 \mu\text{m}$ . This set-up assures that during all the shearing process the contact area between the specimen and steel surface remain constant. This shear box, which can be seen in Figure 6-3, allows to introduce and circulate the vapour inside the sample. The size of the samples (square base of 30x30 mm and a maximum of 20 mm height), was chosen in order to minimize the time for the samples to reach equilibrium with the imposed relative humidity as well as to achieve a high vertical pressure. With this set up the maximum vertical stress applicable is 5.55 MPa.

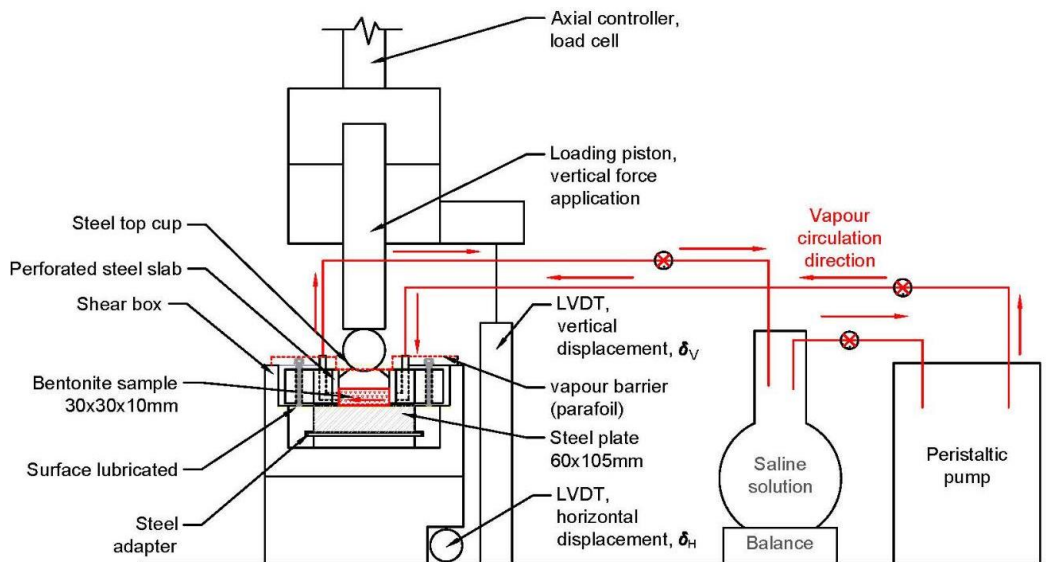


**Figure 6-2. Experimental set-up for the interface shearing**

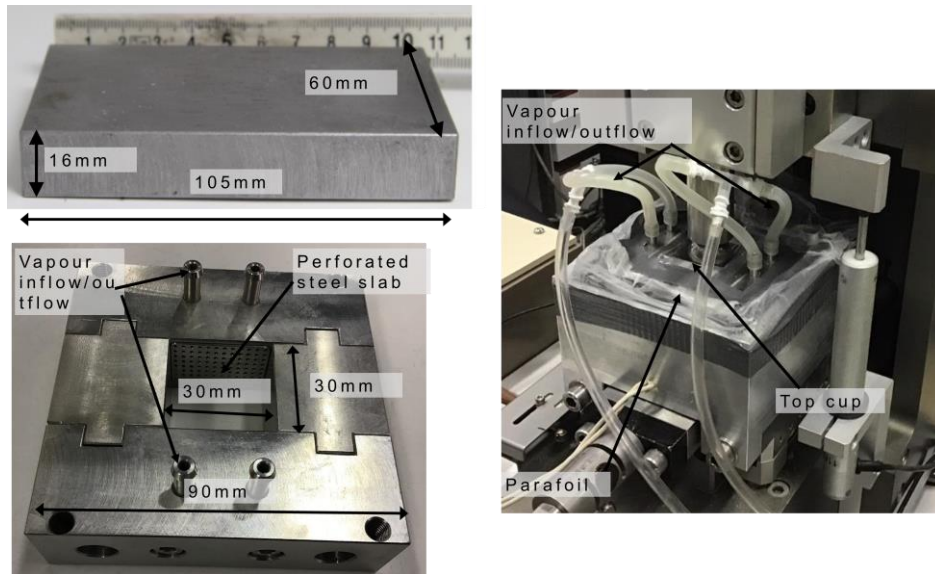


**Figure 6-3. Parts of interface shear apparatus a) steel plate, b) modified upper box of shearing apparatus, c) sealed apparatus**

### 6.2.3 Sample preparation

The granular bentonite was hydrated under free volume conditions in sealed glass containers applying vapour equilibrium technique (Figure 6-4). Total suctions of 11 MPa and 4 MPa were imposed by using respectively KNO<sub>3</sub> and K<sub>2</sub>SO<sub>4</sub> salts. Bentonite was subsequently poured into the direct shear box and compressed up to the desired vertical stress.

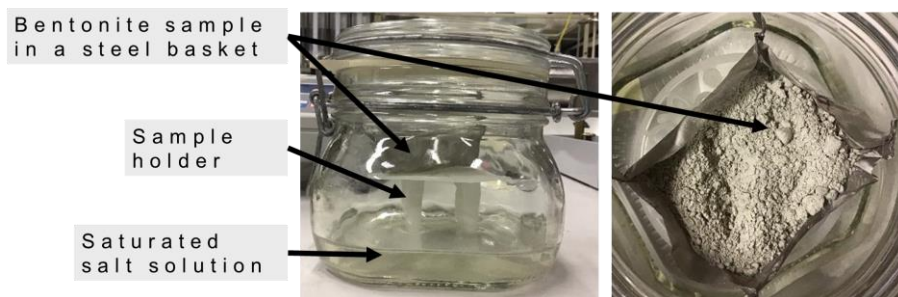


**Figure 6-4. Volumetric free swelling hydration of bentonite applying VET**

All tests were performed in temperature-controlled room where temperature changes were within 1°C, having a negligible impact on the imposed relative humidity.

### 6.2.4 Testing procedure

The first series of test included the internal (bentonite-bentonite) and interface (bentonite-steel) shearing of bentonite characterized by two granulations before hydration (total suction around 150 MPa). The thickness of the samples was of 20±1mm for soil-soil tests and 10mm ±1mm for the interface shearing tests. Table 6-1 summarises the roughness parameters related to these tests. Since two tested granulations present different average grain diameter, the interfaces vary with the relative roughness.

**Table 6-1. Relative roughness of the steel-bentonite interfaces**

Interface	D <sub>50</sub> (mm)	Surface roughness $R_{max}$ (μm)	Relative roughness $R_n(-)$
Steel / Fuller – type GSD	0.8	16	0.0020
Steel / unifractional GSD	1.5		0.0011

After pouring the material inside the shearing box, static compression up to 250 kPa, 500 kPa, 1000 kPa and 2000 kPa was performed for both internal shearing and interface shearing tests. Subsequently the shearing stage was performed.

The second series of tests aimed to study the influence of water content on the behaviour of steel-bentonite interface during shearing. After pouring the wetted granular bentonite into the shear box, the apparatus was connected to the vapour supply system and sealed with parafoil to maintain constant relative humidity during the test. Afterwards, compression was performed up to 250 kPa, 500 kPa, 1000 kPa and 2000 kPa of vertical stress, before proceeding to the shearing stage. The response upon compression is shown in Figure 6-5; reproducibility of sample preparation can be verified by comparison with oedometric compression tests performed by Seiphoori (2014) on the same material.

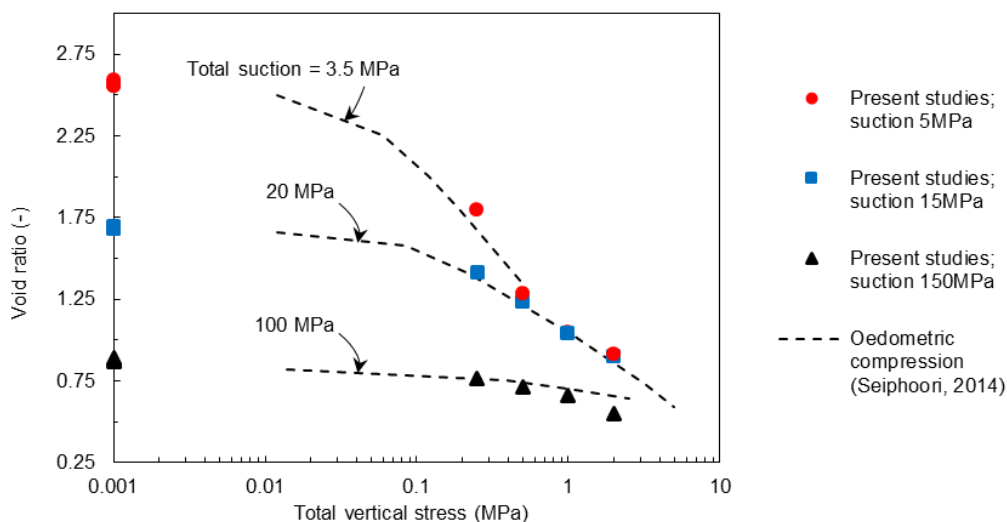


**Figure 6-5. Response of the samples with Fuller-type granulation upon static compaction inside direct shear apparatus, in comparison with the oedometric compression tests performed by (Seiphoori, 2014)**

## 6.3 Results

### 6.3.1 Influence of the granulation on the internal shearing and interface shearing

In Figure 6-6 the results of direct shear test of internal shearing of bentonite characterized by a Fuller-type granulation are shown. Horizontal stress (equivalently shear stress)-displacement curves are shown for each applied vertical stress together with the failure envelope of peak shear strength. The computed peak angle of internal friction is  $\phi_{peak} = 38^\circ$  and the cohesion  $c = 80\text{kPa}$ .

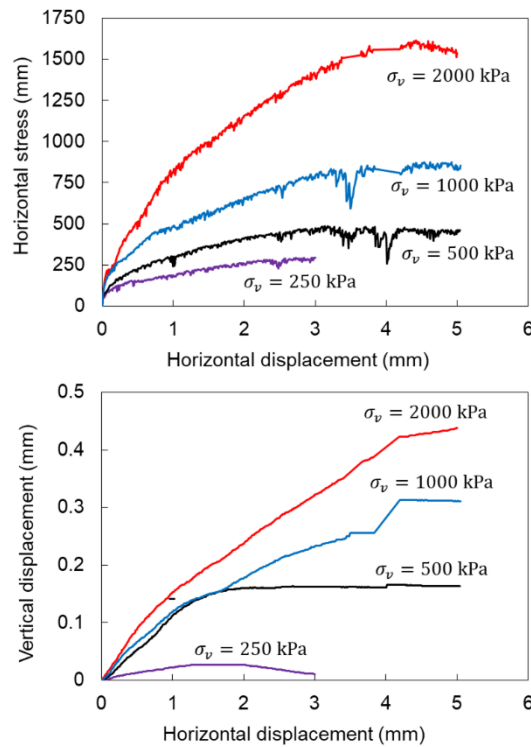


**Figure 6-6. Internal shearing response of MX80 bentonite with Fuller-type granulation at hygroscopic water content**

The contraction behaviour is also presented in terms of vertical displacement versus horizontal displacement curves. Upon shearing, regardless the applied vertical stress all samples contracted. For the samples sheared with vertical stresses up to 1000 kPa, the maximum shear stress remained constant until the test finished. A slight reduction of shear stress (after about 4.5 mm of horizontal displacement) was visible when shearing was performed under a vertical stress of 2000 kPa.

The results of internal shearing of bentonite characterized by a unifractional granulation are presented in Figure 6-7. As in the case of Fuller-type granulation, all samples contracted upon shearing. The maximum value of shear stress was achieved for a displacement of approximately 4 mm and remained constant until the end of the test. The peak angle of internal friction is 27° and the cohesion 83kPa.

In Figure 6-8 and 6-9 the results of the interface shearing of steel-bentonite with Fuller-type granulation and steel-bentonite with unifractional granulation respectively, are presented. Results in both figures were obtained upon shearing the material at hygroscopic conditions. For the two granulations, as in the case of internal shearing, the material contracted upon shearing. The maximum values of shear stress and of axial displacement at corresponding axial stress levels are lower than in the case of interface shearing. The values of the peak angle of interface shearing are  $\delta = 22^\circ$  for the Fuller-type granulation and  $19^\circ$  for the unifractional granulation. A value of interface adhesion of  $c_{ad} = 4$  kPa is obtained by extrapolating the results of the Fuller-type granulation.

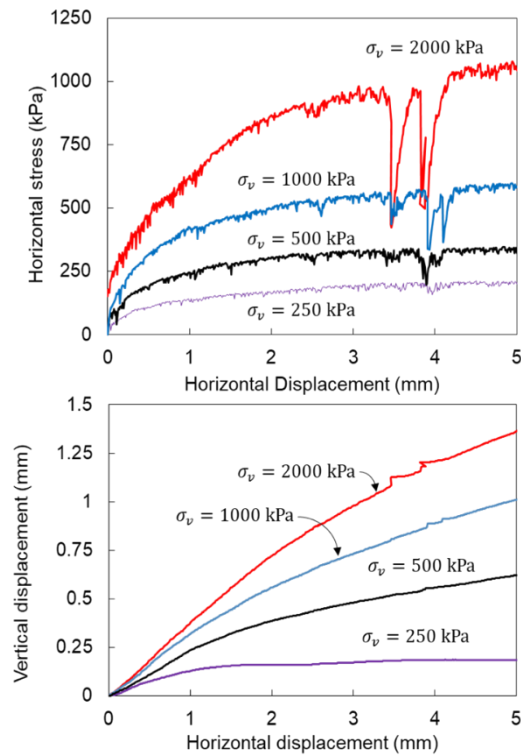


**Figure 6-7. Internal shearing response of MX80 bentonite with unifractional granulation at hygroscopic water content**

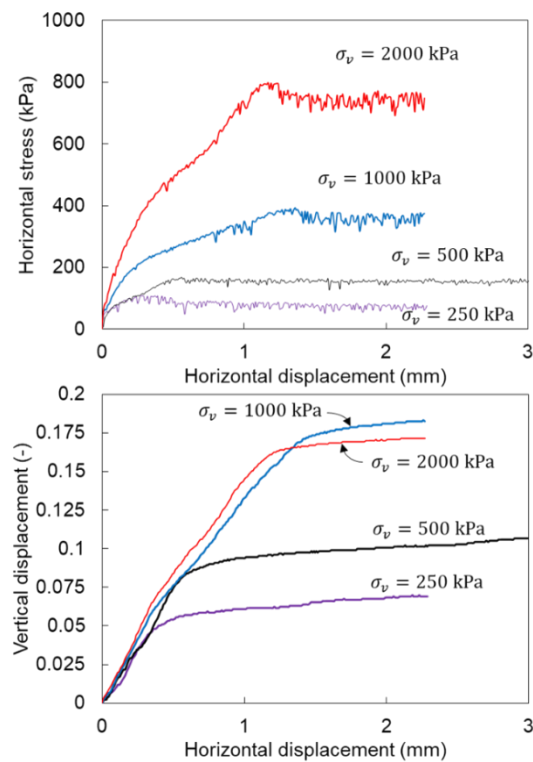


**Figure 6-8. Results of bentonite-steel interface shearing, for granular bentonite with a Fuller-type granulation at hygroscopic conditions**

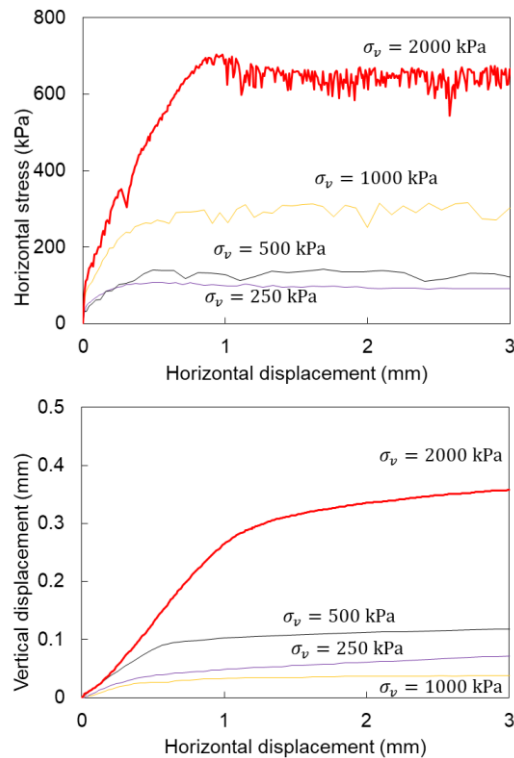


**Figure 6-9. Results of bentonite-steel interface shearing, for bentonite with a unifractional granulations at hygroscopic water content**

### 6.3.2 Influence of water content and suction on the response upon shearing

In Figure 6-10 the results of interface shearing for the samples characterized by initial total suction of 15 MPa and water content of 0.20 are presented. When shearing was performed under 250 kPa and 500 kPa of vertical stress, the maximum value of shear stress was achieved after 1 mm of horizontal displacement and remained constant until the end of the test. For higher values of applied vertical stress, namely 1000 kPa and 2000 kPa, a peak shear stress was reached followed by a reduction to a post-peak stress. The maximum value of the shear stress was obtained at 0.5mm of horizontal displacement for 1000 kPa and 2 mm for 2000 kPa. The sample behaved contractive during all the shearing stage (for pre-peak and post-peak shearing stages). The obtained peak angle of interface shearing is 22° and the interface adhesion is 58 kPa.

In Figure 6-11 the results of interface shearing of samples with initial total suction of 5 MPa and water content of 0.29 are presented. For samples sheared under vertical stresses of 500 kPa, 1000 kPa and 2000 kPa, a peak shear stress was obtained followed by a reduction to a post peak stress. For the sample sheared under a vertical stress of 250 kPa no considerable decrease of shearing stress is noticed. The samples showed contraction during all the shearing stages. The envelope reveals a peak angle of interface shearing of 17° and an interface adhesion of 168 kPa.

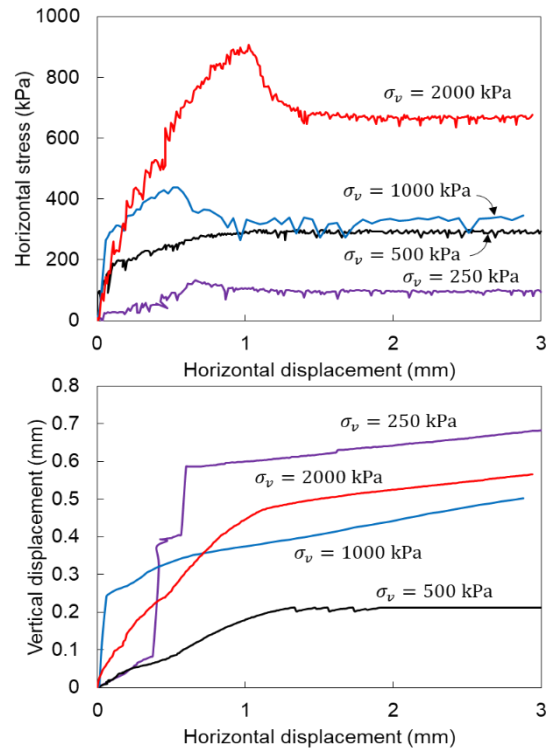


**Figure 6-10. Results of bentonite-steel interface shearing, for bentonite with a Fuller-type granulation with a water content of 0.20 and total suction of 15 MPa**

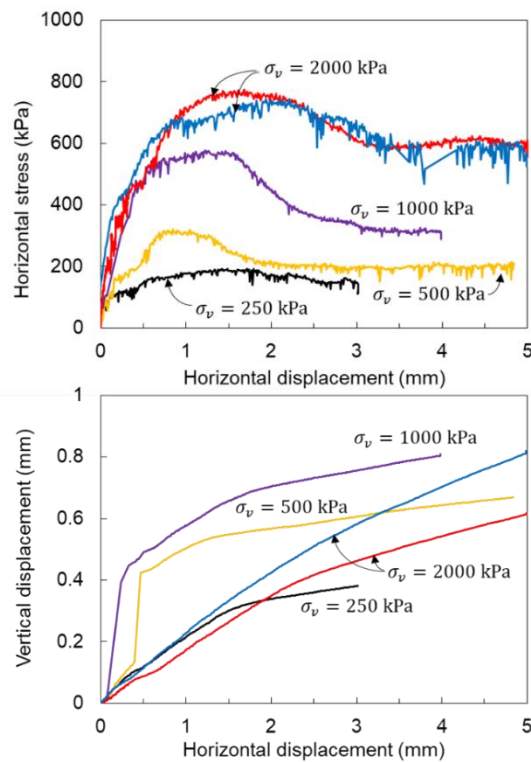


**Figure 6-11. Results of bentonite-steel interface shearing, for bentonite with a Fuller-type granulation with a water content of 0.29 and total suction of 5 MPa**

### 6.3.3 Discussion

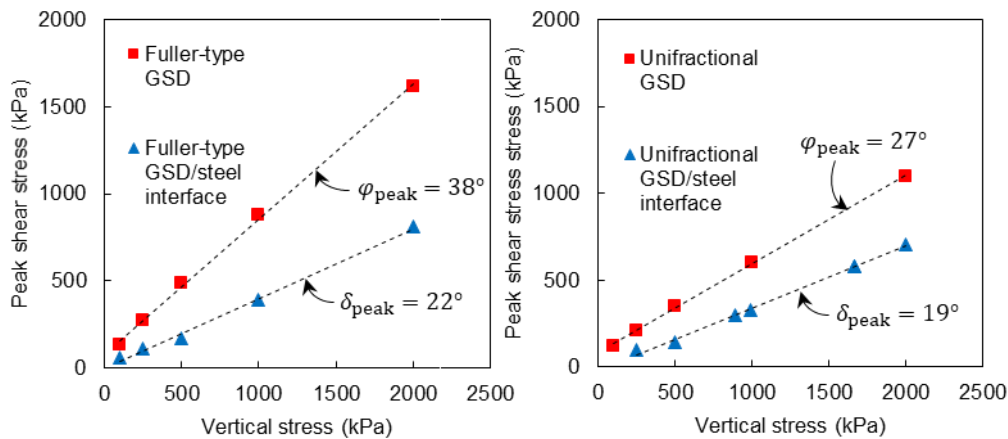
#### 6.3.3.1. Influence of the granulation on the response of the material on internal and interface shearing

Table 6-2 provides a summary of the fitting parameters that are obtained from the envelopes of peak shear strength (maximum horizontal stress) from bentonite at hygroscopic state.

**Table 6-2. Summary of results for shearing at the interface between different materials**

Interface	$\Psi$ (MPa)	$\varphi_{peak}$ OR $\delta_{peak}$ (deg)	C OR $C_{ad}$ (kPa)	$F_r = \frac{\delta_{peak}}{\varphi_{peak}}$ (-)
Fuller-type GSD / Fuller-type GSD	150	38	80	0.6
Steel/Fuller-type GSD		22	10	
Unifractional GSD / unifractional GSD		27	83	0.7
Steel / Fuller-type GSD		19	-	

Failure envelopes for the soil-soil and steel-soil interface shearing for Fuller-type granulation and unifractional granulation are depicted in Figure 6-12. For both granulations, the peak angle of interface friction is lower than the peak angle of internal friction. The friction ratio for the Fuller-type granulation is 0.60 and for the unifractional granulation is 0.70.



**Figure 6-12. Failure envelopes of soil-soil and steel-soil interfaces for the bentonite of Fuller – type GSD (left) and unifractional GSD (right) at hygroscopic conditions**

#### 6.3.3.2. Influence of water content on the response on the interface shearing

The results of direct shear tests are presented in Figure 6-13 in the total normal stress–shear stress plane. In the range of 250-1000 kPa the shearing strength increased with increasing water content, mostly due to the increase of interface adhesion.

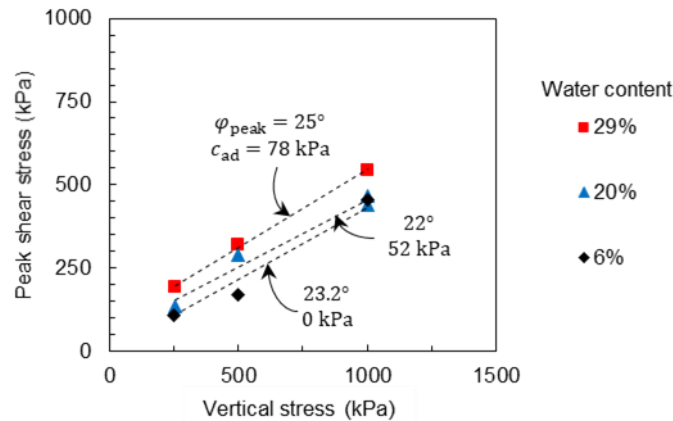


**Figure 6-13. Peak failure at different water content in the net normal stress–shear stress plane from interface direct shear tests, considering interface shearing over the normal stress in the range 250-1000 kPa**

### 6.3.4 Conclusions

The objective of this experimental study was to investigate the internal shearing of granular MX80 bentonite as well as the shearing at steel-bentonite interface. A series of direct shear tests were carried out to determine the internal shearing behaviour of the bentonite at hygroscopic conditions and the impact of the granulation of the soil. Moreover, the influence of water content and suction was investigated.

The following conclusions are drawn from this study:

1. At hygroscopic conditions, samples prepared following an unifractal GSD showed lower values of shear strength parameters in comparison to those prepared with a Fuller-type granulation.
2. For both tested granulations, the interface shearing strength of the material at hygroscopic state was lower than the internal shearing. For samples satisfying Fuller-type granulation, the value of friction ratio presented as a function of relative roughness follows the same trend as effective parameters of sand/steel interfaces shearing found in the literature.
3. All samples tested showed contraction upon shearing.
4. Samples characterized by a higher water content showed a higher peak of shearing strength when compared with samples of lower water content. The increase of strength appears to be governed by the increase of adhesion between steel-bentonite upon hydration.
5. The response upon shearing depends on water content and applied total stress. For samples at hygroscopic conditions, after achieving the maximum value of shear stress, no specific decrease was noted. For samples with water content between 0.2 to 0.29, a peak value of shear strength was followed by a decrease up to post peak value; this was particularly noticeable at high values of vertical stress upon shearing.
6. Peak shear strength increased with increasing water content.

## 7 Conclusions and future work

The objectives of the experimental work performed in Beacon Work Package 4 were to provide input data and parameters for development and validation of models describing bentonite hydro-mechanical behaviour and to reduce uncertainties about conditions and phenomena influencing bentonite homogenisation. The Beacon partners BGS, CEA, CIEMAT, CTU, CU, EPFL, JYU, KIT, and GRS devised and carried out a wide range of experiments to provide the data needed. In this chapter, attempt is made to draw some overall conclusions from this work and to summarize the open questions or issues that need additional in-depth consideration identified by the partners. More detailed respective information of each partner has been given in the previous sections of this report.

### 7.1 Results summary and conclusions

The experiments performed in Beacon WP4 addressed

- the influence of hydro-mechanical path and aggregate size distribution for several macroscopically homogeneous bentonite materials, such as MX-80 (EPFL) and BCV (Cerny vrch bentonite, CU and CTU),
- the gap filling behaviour of swelling bentonite for numerous different configurations and conditions, involving MX-80 (BGS), BaraKade bentonite (JYU), FEBEX bentonite (CIEMAT), BCV (CTU), and Calcigel (KIT/GRS), with instant water contact (BGS) or one-sided hydration (CIEMAT, CTU, JYU, KIT/GRS), including hydration in the vapour phase (CIEMAT),
- the hydration-induced homogenisation of different binary systems like block/pellet (CIEMAT) and pellet/powder as well as block/powder (CEA) systems or systems of two blocks with different initial densities (CU),
- and the shearing behaviour at a bentonite/steel interface (EPFL).

The overall results and conclusions are summarised below.

#### *Macroscopically homogeneous bentonite*

1. Influence of aggregate size distribution: At free swelling, EPFL found a higher volume increase for unifractal samples (MX-80 of 1-2 mm aggregate size) than for bifractal samples (where 20% aggregates of 0.08-1.25 mm were added) which started with a higher dry density. The resulting porosity difference was mainly attached to macroporosity (see 12). The result is in line with gap filling phenomena observed (see 9). The effect was not observed for confined samples.
2. Hydromechanical path dependence: EPFL used granular MX-80 bentonite with a Fuller-type aggregate size distribution to (a) hydrate under constant low stress (nearly free swelling), and subsequent stress increase, or (b) hydration at constant volume conditions, and subsequent stress increase to the same value as in (a). Despite having the same degree of saturation afterwards and being subjected to the same final value of vertical stress, a difference in void ratio of 0.13 (15% of initial void ratio) between the two samples was obtained. This path dependence was also confirmed by CTU using pellet and powder materials (BCV). While having comparable microporosities, the difference is in the macroporosity of the samples undergoing different paths (see 12).

3. Samples of different initial void ratios saturated under different stress tend, however, to arrive at similar states after cycles involving high compressive load, as shown by CU for compacted bentonite and by CTU for pellets and powder (both using BCV).
4. Constant load swelling tests of CU with variable dry density (BCV, homogeneous material of 1.27, 1.6 and 1.9 g/cm<sup>3</sup>), hydraulic path, and confining conditions showed that the water retention behaviour did not seem to be significantly influenced by the initial dry density for bentonite blocks of different densities. The final void ratio of saturated samples under the same load was independent of the initial compaction.
5. Pellet cluster stress evolution: Stress evolution in an instantaneously flooded unifractional pellet cluster (pillow-shaped MX-80 pellets of 16-17 by 8 mm) of GRS was rather complicated and not monotonous (compare 11). Both GRS and CTU observed that the initial stress in a pellet cluster at low density may collapse when water is introduced.

### *Gap filling*

6. A very clear result of the experiments is the high gap filling capacity of the bentonite. In CIEMAT's tests (FEBEX bentonite), voids of 17% - 24% of the sample size were filled; BGS found that even void spaces of 45% of the test cells were filled completely (MX-80). The gap filling capacity will of course depend on the dry density and the type of bentonite.
7. A sample swelling into a gap does not have a homogeneous density distribution afterwards. In those experiments that involved a progressive water supply (JYU, CIEMAT) it was found that density gradients reduced with time and increasing saturation. Once full saturation was reached, however, no further homogenisation could be observed. A decrease of gradients was also observed in BGS' gap filling tests where water was supplied at once. These tests had a duration of 100 days, and in all of them density gradients remained. Lower gradients were obtained with lower overall dry density (due to higher saturated permeability and possibly also due to the lower swelling capacity of low-density materials, which results in less steep gradients in the beginning) and when a greater degree of swelling was allowed to occur (due to the reduction in dry density). Some evidence indicated elevated temperatures may influence the degree of residual density gradients, but more data is required to understand this. Higher fluid salinity was observed to lead to higher gradients, however.
8. A spatially inhomogeneous swelling pressure distribution tends to homogenise with progressing swelling, as shown in BGS' and KIT's experiments (both using MX-80), but there is only a partial homogenisation. Remaining stress gradients in the gap filling tests can be widely explained by the varying local swelling pressure caused by density gradients. Friction may also play a role.
9. A very prominent result is the dependence of density homogenisation on the hydration velocity – for both gap filling setups and binary systems (see 10). In the gap filling case, CIEMAT states that hydration via the gap allows the samples to saturate faster because they swell into the open void and take water very quickly, developing higher internal gradients than when they are saturated from the bentonite side, where no free space is available and a low permeability is maintained (see 10 and 12). If hydration is performed via a vapour phase, higher relative humidity (faster vapour supply) likewise results in faster hydration and larger gradients. This would mean that a lower hydration velocity results in a more homogeneous end product. Higher hydration velocity seems particularly to lead to an increase in the amount of larger pores (see 12).

### *Binary systems*

10. In analogy to the gap filling tests, homogenisation of a granular material/block system used by CIEMAT depended on the hydration direction and kinetics (see 9). CIEMAT used systems of FEBEX bentonite (block and Fuller-type granular material) and MX-80 (block and pellet/powder mixture). A (faster) hydration (via the granular material or because of higher water availability) resulted in larger final density gradients than an intrinsically slower hydration via the block or under restricted water flow. Similar results were obtained by CEA using block/block systems of different block densities. CU also investigated a block/block system and observed the same effect, although the difference due to the hydration direction was rather small. This may be due to the fact that both blocks had a rather high dry density to start with, so that the hydration was slow even when performed via the less dense block.
11. Swelling pressure evolution in binary systems is complicated and not necessarily monotonous, especially in systems with granular material or powder (CIEMAT, CEA) (compare 5).

### *Porosimetry*

12. Many of the experiments performed involved porosimetric characterisation before and after testing, and thus enabled a view on pore size evolution. The results of (1), (2), (9) and (10) all suggest that an initial saturation at low confining stress, possibly with a high hydration velocity, leads to irreversible strains that affect the macrostructure. The subsequent evolution of the system is conditioned by this early evolution. This interpretation is supported by the fact that it is the macropore volume that gets mostly modified as a result of the initial hydration and swelling. Since this effect seems to be persistent, it may be needed to be considered when modelling system evolution. Current dual-porosity models should be suited for this.

### *Influence of the degree of saturation on the shearing behaviour at a bentonite–steel interface*

13. EPFL investigated the internal shearing of granular MX80 bentonite as well as the shearing at a steel-bentonite interface, for a Fuller-type ( $D_{50}=0.8$  mm) and a unifractional aggregate size (1.5 mm) distribution. For both tested granulations, the interface shearing strength of the material at hygroscopic state was lower than the internal shearing. Unifractional samples showed lower values of shear strength parameters in comparison to those prepared with a Fuller-type granulation. Samples characterized by a higher water content showed a higher peak of shearing strength when compared with samples of lower water content. The increase of strength appears to be governed by the increase of adhesion between steel-bentonite upon hydration.

### *New experimental methods*

14. In the Beacon project, new experimental methods were developed and tested, such as particle tracking in combination with X-ray imaging. CEA used X-ray tomography and JYU used X-ray radiography. Another new method is small-scale spatially resolved stress measurement developed by KIT. These methods proved successful and can be used in future investigations. Especially with regard to stress measurement, the inhomogeneous stress distributions found in all test setups with spatially resolved measurement indicate that interpretation of conventional oedometer tests with just

one axial pressure measurement needs care. A more detailed stress measurement and/or control may be advisable for future experiments. A method that is not actually new should be mentioned nevertheless: Using transparent cells provided valuable insight especially into the hydration process in setups involving granular bentonite.

With regard to bentonite homogenisation, the experimental results show that a completely homogeneous system will not be achieved in the short term after hydration, instead, it seems that once full saturation is reached the current status (in terms of dry density distribution) is kept. Although slow processes which are outside the laboratory observation scale may be possible, the results of the natural analogue study performed in the frame of Beacon (Sellin and Villar, 2020) give no hints in this direction. Consequently, the question of the persistence of inhomogeneities in the long term remains unresolved. In any case, bentonite barriers will have to be designed in a way that a sufficient degree of homogeneity will be achieved (or maintained) within the hydration phase, so that the bentonite barrier fulfils the assigned safety functions.

## **7.2 Remaining questions and recommendations for future work**

Although the knowledge of bentonite mechanical evolution has been much furthered by the Beacon project, the experimental programme could not be as comprehensive as to answer all open questions and remove all uncertainties.

While a comparatively high total number of experiments was performed, these could of course not cover all relevant combinations of conditions: the effect of different bentonites (sodium versus bivalent), solutions, textures (blocks, pellets, powder and their combinations) and granulations as well as hydration and stress paths could be investigated in more detail to achieve a more complete database. Observed phenomena, like the apparent influence of hydration velocity on density distribution, should be further investigated. The effect of temperature is not established yet, there were only a few first tests performed. A question that has not been addressed in the experiments is the fate of the air initially contained in the bentonite.

Regarding the design of experimental setups, the inhomogeneous stress distributions found in all test setups with spatially resolved measurement indicate that conventional oedometer tests with just one axial pressure measurement may not be sufficient for an in-depth interpretation. Wall friction is only one of the problems that can occur. Changing from oedometer tests to triaxial stress measurement and control would provide more insight and reduce uncertainty. Sensors at different locations or spatially resolving sensors give even more information.

All experiments presented here are small-scale laboratory tests. It would be advisable to compare the results to existing large-scale experiments in order to get an idea about scale effects.

And finally: Not all the experiments performed were actually used for model simulation. Experiments provide input to model calibration or validation, but on the other hand, modelling an experiment can also help in its interpretation, thus reducing uncertainty about the results and increasing confidence.

## 8 References

- ASTM 2004.** C914-95: Standard test method for bulk density and volume of solid refractories by wax immersion. West Conshohocken, PA, USA: ASTM International.
- ASTM D2435/D2435M-11. 2011.** "Standard Test Methods for One-Dimensional Consolidation Properties of Soils using Incremental Loading." ASTM International: West Conshohocken, PA.
- Baryla, P., Bernachy-Barbe, F., Bosch, J.A., Campos, G., Carbonell, B., Daniels, K.A., Ferrari, A., Guillot, W., Gutiérrez-Álvarez, C., Harrington, J.F., Iglesias, R.J., Kataja, M., Mašín, D., Najser, J., Rinderknecht, F., Schäfer, T., Sun, H., Tanttu, J., Villar, M.V., Wieczorek, K., 2019.** Bentonite mechanical evolution – experimental work for the support of model development and validation. DELIVERABLE (D4.1). Report. 132 pp.
- Bernachy-Barbe, F., Conil, N., Guillot, W., Talandier, J. 2020.** Observed heterogeneities after hydration of MX-80 bentonite under pellet/powder form. *Applied Clay Science* 189: 105542. <https://doi.org/10.1016/j.clay.2020.105542>
- Bian, X., Cui, Y.J., Zeng, L.L., Li, X.Z. 2019.** Swelling behavior of compacted bentonite with the presence of rock fracture. *Engineering Geology* 254: 25-33. <https://doi.org/10.1016/j.enggeo.2019.04.004>
- Brunauer, S., Emmett, P.H., Teller, E., 1938.** Adsorption of gases in multimolecular layers. *Journal of the American Chemical Society* 60: 309–319.
- Bucher, F., Müller-Vonmoos, M., 1989.** Bentonite as a containment barrier for the disposal of highly radioactive wastes. *Applied Clay Science* 4, 157–177.
- Daniels, K.A., Harrington, J.F., Sellin, P. and Norris, S., 2021.** Closing repository void spaces using bentonite: does heat make a difference?. *Applied Clay Science*, 210, p.106124.
- Delage, P., Audiguier, M., Cui, Y. J. & Howat, M. D. 1996.** Microstructure of a compacted silt. *Can. Geotech. J.* 33, No. 1, 150–158.
- Delage, P., Howat, M. D. & Cui, Y. J. 1998.** The relationship between suction and swelling properties in a heavily compacted unsaturated clay. *Engng Geol.* 50, No. 1–2, 31–48.
- Delage, P., Lefebvre, G., 1984.** Study of the structure of a sensitive Champlain clay and of its evolution during consolidation. *Can. Geotech. J.* 21, 21–35. <https://doi.org/10.1139/t84-003>
- Devineau, K., Bihannic, I., Michot, L., Villiéras, F., Masrouri, F., Cuisinier, O., Fragneto, G., Michau, N., 2006.** In situ neutron diffraction analysis of the influence of geometric confinement of crystalline swelling of montmorillonite. *Applied Clay Science* 31 (1–2): 76–84. <https://doi.org/10.1016/j.clay.2005.08.006>
- Dueck, A., Goudarzi, R., Börgesson, L., 2016.** Buffer Homogenisation: Status Report 3. Technical Report, TR-16-04. Svensk Kärnbränslehantering AB (SKB), Stockholm, Sweden.
- ENRESA, 2005.** Engineered barrier emplacement experiment in Opalinus Clay for the disposal of radioactive waste in underground repositories. Final Report. Publicación Técnica ENRESA 02/05. Madrid, 101 pp.
- ENRESA, 2006.** FEBEX Full-scale Engineered Barriers Experiment, Updated Final Report 1994–2004. Publicación Técnica ENRESA 05-0/2006, Madrid, 590 pp.
- Ferrari, A., Favero, V., Laloui, L., 2016.** One-dimensional compression and consolidation of shales. *International Journal of Rock Mechanics and Mining Sciences* 88, 286–300.
- Ferrari, A., Laloui, L., 2013.** Advances in the testing of the hydro-mechanical behaviour of shales, in: *Multiphysical Testing of Soils and Shales*. Springer, pp. 57–68.

- García-Siñeriz, J.L., Villar, M.V., Rey, M., Palacios, B., 2015.** Engineered barrier of bentonite pellets and compacted blocks: state after reaching saturation. *Engineering Geology* 192, 33–45. <https://doi.org/10.1016/j.enggeo.2015.04.002>
- Gens, A., Alonso, E., 1992.** A framework for the behaviour of unsaturated expansive clays. *Canadian Geotechnical Journal* 1013–1032.
- Goldstein, J., 2017.** Scanning electron microscopy and x-ray microanalysis, 4th edition. ed. Springer Science+Business Media, LLC, New York, NY.
- Gutiérrez-Rodrigo, V., Martín, P.L., Villar, M.V. 2021.** Effect of interfaces on gas breakthrough pressure in compacted bentonite used as engineered barrier for radioactive waste disposal. *Process Safety and Environmental Protection* 149: 244–
- Harrington, J. F., K. A. Daniels, A. C. Wiseall, and P. Sellin., 2020** "Bentonite homogenisation during the closure of void spaces." *International Journal of Rock Mechanics and Mining Sciences* 136: 104535.
- Hausmannová, L., Hanusová, I., Dohnálková, M. (2018).** Summary of the research of Czech bentonites for use in the deep geological repository – up to 2018, TZ 309/2018/ENG, SÚRAO
- HITEC, 2021.** HITEC technical report on Material characterisation. Final version of deliverable D7.8 of the HORIZON 2020 project EURAD. EC Grant agreement no: 847593.
- Hoffmann, C., 2005.** Caracterización hidromecánica de mezclas de pellets de bentonita. Estudio experimental y constitutivo. (PhD Thesis), Universitat Politècnica de Catalunya, Barcelona, 387 pp.
- Imbert C, Villar MV, 2006.** Hydro-mechanical response of a bentonite pellets/powder mixture upon infiltration. *Applied Clay Science* 32: 197-209. <https://doi.org/10.1016/j.clay.2006.01.005>
- Juang, C. H. & Holtz, R. D. 1986.** A probabilistic permeability model and the pore size density function. *Int. J. Numer. Analyt. Methods Geomech.* 10, No. 5, 543–553.
- Karnland, O., Olsson, S., Nilsson, U., 2006.** Mineralogy and Sealing Properties of Various Bentonites and Smectite-Rich Clay Materials. Technical Report, TR-06-30. Svensk Kärnbränslehantering AB (SKB), Stockholm, Sweden.
- Karnland, O., Nilsson, U., Weber, H., Wersin, P., 2008.** Sealing ability of Wyoming bentonite pellets foreseen as buffer material – Laboratory results. *Physics and Chemistry of the Earth, Parts A/B/C, Clays in Natural & Engineered Barriers for Radioactive Waste Confinement* 33, S472–S475.
- Kennedy, K., Verfuss, F., Plötze, M., 2004.** Engineered Barrier Emplacement (EB) Experiment in Opalinus Clay: Granular material backfill product documentation. EC contract FKW-CT-2000-00017. Project Deliverable D3c. Mont Terri Technical Note 2004-17, 61 pp.
- Kristensson; O., Börgesson, L., 2015.** Canister Retrieval Test – Final Report. Report TR-14-19, Svensk Kärnbränslehantering AB (SKB), Stockholm.
- Kröhn, K.P. 2005.** New evidence for the dominance of vapour diffusion during the re-saturation of compacted bentonite. *Engineering Geology* 82: 127-132. <https://doi.org/10.1016/j.enggeo.2005.09.015>
- Kröhn, K.-P., 2011.** Code VIPER - Theory and Current Status. Status report, FKZ 02 E 10548 (BMW), Gesellschaft für Anlagen- und Reaktorsicherheit (GRS) mbH, GRS-269, Köln.
- Kröhn, K.-P., 2020.** Checking the consistency of the "two-zone model" for Task 9B – LTDE-SD. Task 9 of SKB Task Force GWFTS – Increasing the realism in solute transport modelling based on the field experiments REPRO and LTDE-SD. SKB-report P-20-02, Svensk Kärnbränslehantering AB (SKB), Solna.

- Lin, B. & Cerato, A. B. 2014.** Applications of SEM and ESEM in microstructural investigation of shale-weathered expansive soils along swelling-shrinkage cycles. *Engng Geol.* 177, 66–74.
- Montes-H, G. 2005.** Swelling–shrinkage measurements of bentonite using coupled environmental scanning electron microscopy and digital image analysis. *J. Colloid Interface Sci.* 284, No. 1, 271–277.
- Plötze, M., Weber, H.P., 2007.** ESDRED: Emplacement tests with granular bentonite MX-80 (No. NAB 07-24), Laboratory results from ETH Zürich. Wettingen, Nagra.
- Pusch, R., 1980.** Swelling Pressure of Highly Compacted Bentonite. Technical Report, 1980-08-20. Svensk Kärnbränslehantering AB (SKB), Stockholm, Sweden.
- Pusch, R., Karnland, O., Hokmark, H., 1990.** GMM - a General Microstructural Model for Qualitative and Quantitative Studies of Smectite Clays. Technical Report, TR-90-43. Svensk Kärnbränslehantering AB (SKB), Stockholm, Sweden.
- Romero, E. 2013.** A microstructural insight into compacted clayey soils and their hydraulic properties. *Eng. Geol.* 165: 3-19. <http://dx.doi.org/10.1016/j.enggeo.2013.05.024>
- Romero, E., Della Vecchia, G. & Jommi, C. 2011.** An insight into the water retention properties of compacted clayey soils. *Géotechnique* 61, No. 4, 313–328.
- Romero, E., Gens, A., Lloret, A., 1999.** Water permeability, water retention and microstructure of unsaturated compacted Boom clay. *Engineering Geology* 54, 117–127. [https://doi.org/10.1016/S0013-7952\(99\)00067-8](https://doi.org/10.1016/S0013-7952(99)00067-8)
- Sánchez M, Gens A, Guimarães L, Olivella, S, 2005.** A double structure generalized plasticity model for expansive materials. *International Journal for Numerical and Analytical Methods in Geomechanics* 29: 751–787. DOI:10.1002/nag.434.
- Seiphoori, A., 2014.** Thermo-hydro-mechanical characterisation and modelling of MX-80 granular bentonite. PhD Thesis. École Polytechnique Fédérale de Lausanne, Switzerland.
- Seiphoori, A., Ferrari, A., Laloui, L., 2014.** Water retention behaviour and microstructural evolution of MX-80 bentonite during wetting and drying cycles. *Géotechnique* 64, 721–734. <https://doi.org/10.1680/geot.14.P.017>
- Sellin, P., Villar, M.V., 2020.** Creep in bentonite – a natural analogue study. DELIVERABLE (D4.3). Report. 12 pp.
- Sing, K.S.W., Everett, D.H., Haul, R.A.W., Moscou, L., Pierotti, R.A., Rouquérol, J., Siemieniowska, T. 1985.** Reporting physisorption data for gas/solid systems with special reference to the determination of surface area and porosity. *Pure and Applied Chemistry* 57(4): 603-619. IUPAC.
- Sridharan, A., Rao, A., Sivapullaiah, P., 1986.** Swelling pressure of clays. *Geotech. Test. J.* 9 (1), 24–33. <https://doi.org/10.1520/GTJ10608J>.
- Sun, H., Mašín, D., Najser, J., Neděla, V. and Navrátilová, E., 2018.** Bentonite microstructure and saturation evolution in wetting–drying cycles evaluated using ESEM, MIP and WRC measurements. *Géotechnique*, pp.1-14.
- Talandier, J. (Ed.) 2019.** Synthesis of results from task 5.1. BEACON Deliverable D5.1.2. 334 pp.
- Tennent, R.M., 1971.** Science Data Book. Oliver and Boyd. ISBN 0 05 002487 6.
- Villar, M.V. 1999.** RESEAL Project. Topical Report on Laboratory Tests. Version 1. Informe Técnico CIEMAT/DIAE/54121/2/99. Madrid, 33 pp.
- Villar, M.V., 2002.** Thermo-hydro-mechanical characterisation of a bentonite from Cabo de Gata. A study applied to the use of bentonite as sealing material in high level radioactive waste repositories. *Publicación Técnica ENRESA 01/2002*, Madrid, 258 pp.

- Villar, M.V., 2007.** Water retention of two natural compacted bentonites. *Clays and Clay Minerals* 55(3): 311-322.
- Villar, M.V.(Ed), 2017.** FEBEX-DP Postmortem THM/THC Analysis Report. NAB 16-017. 143 pp.
- Villar, M.V., Lloret, A. 2001.** Variation of the intrinsic permeability of expansive clays upon saturation. In: Adachi, K., Fukue, M. (Eds.): *Clay Science for Engineering*. A.A. Balkema, Rotterdam, pp. 259–266.
- Villar, M.V., Lloret, A., 2004.** Influence of temperature on the hydromechanical behaviour of a compacted bentonite. *Appl. Clay Sci.* 26, 337–350. <https://doi.org/10.1016/j.clay.2003.12.026>.
- Villar MV, Gómez-Espina R, 2012a.** Long-term Performance of Engineered Barrier Systems PEBS. Permeability tests in samples from the EB experiment at Mont Terri (Borehole EB-B1). Technical Note CIEMAT/DMA/2G210/06/12. Madrid, 15 pp.
- Villar, M.V., Gómez-Espina, R., Gutiérrez-Nebot, L., 2012b.** Basal spacings of compacted bentonite. *Applied Clay Science* 65-66: 95-105.
- Villar, M.V., Gutiérrez-Rodrigo, V., Martín, P.L., Romero, F.J., Barcala, J.M. 2013.** Gas transport in bentonite. *Informes Técnicos CIEMAT 1301*. Madrid, 63 pp. DOI: 10.13140/RG.2.2.14334.28489
- Villar, M.V., Campos, R., Gutiérrez-Nebot, L. 2014.** EB experiment. Laboratory post-mortem analyses report. PEBS Project Deliverable D2.1-7. CIEMAT Technical Report CIEMAT/DMA/2G210/01/2014. Madrid, 34 pp.
- Villar, M.V., Carbonell, B., Martín, PL., Gutiérrez-Álvarez, C., Barcala J.M., 2018.** Gas permeability of bentonite samples of the FEBEX Dismantling Project (FEBEX-DP). *Informe Técnico CIEMAT 1431*. Madrid, 89 pp.
- Villar, M.V., Campos, G., Gutiérrez-Nebot, L., Arroyo, X., 2019.** Effect of prolonged drying at high temperature on the water retention capacity of bentonite (FEBEX-DP samples). *Applied Clay Science* 182: 105290. <https://doi.org/10.1016/j.clay.2019.105290>
- Villar, M.V., Gutiérrez-Álvarez, C., Campos, G., 2021a.** Project BEACON. Laboratory tests on bentonite homogenisation performed by CIEMAT: gap filling. CIEMAT Technical Report CIEMAT/DMA/2G220/1/21. Madrid.
- Villar, M.V., Iglesias, R.J., Gutiérrez-Álvarez, C., Carbonell, B., 2021b.** Pellets/block bentonite barriers: laboratory study of their evolution upon hydration. *Engineering Geology* 106272. <https://doi.org/10.1016/j.enggeo.2021.106272>
- Villar, M.V., Iglesias, R.J., Gutiérrez-Álvarez, C., Carbonell, B., Real, E., 2021c.** Project BEACON. Laboratory tests on bentonite homogenisation performed by CIEMAT: saturation of block/pellets systems. CIEMAT Technical Report CIEMAT/DMA/2G220/2/21. Madrid, 54 pp.
- Yuan, S., Liu, X., Romero, E., Delage, P., Buzzi, O., 2020.** Discussion on the separation of macropores and micropores in a compacted expansive clay. *Géotechnique Letters* 10: 1–7. <https://doi.org/10.1680/jgele.20.00056>